

Synthesis of zirconium disulphide nanomaterials and their nanocomposites with radially aligned nanorutile and polyaniline for room temperature sensing of volatile organic compounds

By

Paul Olawale Fadojutimi

Student no: 2165101

A thesis submitted to the Faculty of Science, University of the Witwatersrand, Johannesburg, in partial fulfilment of the requirements for the award of the degree of PhD in Chemistry.

Supervisor: Dr John Moma

Co-Supervisor: Dr Siziwe Gqoba

Co-Supervisor: Dr Zikhona N. Tetana

University of the Witwatersrand, Johannesburg, August 2022

Abstract

Integration of 2D nanomaterials with a polymer or semiconductor metal oxide could help in the development of low-cost sensors for rapid detection of volatile organic compounds (VOCs) at room temperature.

This study focuses on the fabrication of robust room temperature sensors of pristine radially aligned nanorutile, and zirconium disulphide/polyaniline (PANI) nanocomposites for chemical sensing of VOCs.

ZrS₂ was fabricated using both bottom-up and top-down methods of synthesis. Heat up and hot injection methods were employed to fabricate arrays of morphologies of ZrS₂ nanomaterials using the colloidal method. However, the nanomaterials showed high oxophilicity which was confirmed by both XRD and XPS. The XPS peak of S2p was conspicuously absent while the peak Zr3d was very noticeable in the XPS spectra. XPS and EDS measurements indicated replacement of sulphur atom by the O atom on the surface of the nanomaterials. The stability study showed the nanomaterials were not stable in ambient environment.

Nanoparticles of 11 nm and few layered nanosheets were obtained when bulk crystal samples of ZrS₂ were exfoliated in cyclohexyl-2-pyrrolidone and N-methyl (-2-) pyrrolidone. Isopropanol served as a green solvent for the exfoliation of few-layered ZrS₂ from the bulk crystal sample compared to amide solvents which are not environmentally friendly. However, the pristine ZrS₂ nanomaterials could not sense VOCs at room temperature, this could be as a result of low conductivity and number of layers of the nanomaterials obtained using nanomaterials exfoliated in isopropanol. The sensitivity of raw PANI was greatly enhanced with loading of ZrS₂ nanomaterials. The sensor displayed responses of 0.43, 0.58, 1.04 and 0.34% which correspond to methanol, ethanol, isopropanol, and acetone vapours respectively. The relatively better responses of the sensor were credited to the synergistic effect of ZrS₂/PANI composite structure. The sensor showed good response to low concentrations (7.7 ppm, 11 ppm, 5.8 ppm and 6.1 ppm) which correspond to methanol, ethanol, isopropanol, and acetone respectively. The sensor was more sensitive to isopropanol compared to other alcohols tested for in this work. The behaviour of the sensor changed from p-type to n-type on exposure to ethanol vapour at elevated relative humidity. The sensor displayed good sensitivity, reproducibility, rapid response and recovery times towards alcohols and stability over 60 days.

The hierarchical morphology, high surface area, high porosity and humidity contributed immensely to the titania sensor in the sensing of VOCs at room temperature. The TiO_2 sensor showed high sensitivity with responses of -38.27, -86.75, -9.83 and 1.24% which correspond to methanol, ethanol, isopropanol, and acetone respectively. The sensor is more sensitive to ethanol gas compared to other chemical vapours tested. The sensor displayed good sensitivity, reproducibility, rapid response and recovery times towards alcohols and stability over 45 days.

The surface area of the nanorutile decreased by 35% on loading of ZrS_2 , this could be the main reason there was no response observed when the nanocomposite of TiO_2 - ZrS_2 was tested for chemical sensing at room temperature. The active sites for adsorption of the vapour were not available probably due to the covering of pores of the nanorutile as well as low conductivity of ZrS_2 at room temperature.

Both sensors of nanocomposite of zirconium disulphide and polyaniline as well as titania could find application in breath analysers since the least detection for a breath analyser is reported to be 200 ppm.

Dedication

This work is dedicated to my late parents Mr and Mrs Ebenezer Olakunle Fadojutimi who valued good education and ensured they gave me the best legacy a parent can give to a child.

Acknowledgements

I would like to convey my sincere appreciation to everyone who made this work a success:

- ❖ Unto God be the glory, great things He has done. I would like to thank God Almighty, the Elshadai for provisions and giving me wisdom, good health, and vigour to complete this research.
- ❖ I am indeed grateful to all my supervisors, Dr John Moma, Dr Siziwe Gqoba, Dr Zikhona Tetana and Prof Nosipho Moloto for their guidance, advice and support in this research. Thank you so much for your constructive criticism and for your painstaking effort going through my thesis. I am indeed privileged to learn from the best.
- ❖ A big thanks to all my colleagues in CATMAT group and most especially everyone in labs 117 and 330 for their support and friendly environment provided so far. I would like to thank the following colleagues especially: Dr Rudo Sithole, Dr Pumza Mente, Dr Tumelo Phaahlamohlaka, Dr Victor Mashindi, Mr Clinton Masemola, Miss Boipelo Mathe and Mr Themba Ntuli.
- ❖ Special thanks to every staff member of the Microscopy and Microanalysis Unit (MMU) for the XRD, SEM and TEM training. My special appreciation goes to Dr Rudolph Erasmus for his assistance in Raman spectroscopy analyses and Dr Sanele Nyembe from MINTEK who assisted with AFM analyses.
- ❖ Many thanks to Wits University for funding this research work.
- ❖ Lastly, kudos to my lovely wife Oluwayemisi and my wonderful children Oluwakoretimi and Irenitemi Fadojutimi for your support despite my absence from home.

Presentations

1. Colloidal synthesis of zirconium disulphide (oral presentation), Catalysis and Materials Science group (March 2021).
2. Nanocomposite of rutile titania and zirconium disulphide for room temperature sensing of acetone vapour (Poster presentation) National Young Chemist's symposium (July 2021).
3. Synthesis of zirconium disulphide nanostructures for room temperature sensing of acetone vapours (poster presentation), Wits Nanoscience Young researcher's symposium (October 2021).

Publications

1. Paul Fadojutimi, Siziwe Gqoba, Zikhona Tetana and John Moma. Transition metal dichalcogenides in photocatalytic water splitting. (2022) Journal of Catalysts. Manuscript published.
2. Siziwe S. Gqoba, Rafael Rodrigues, Sharon Lerato Mphahlele , Zakhele Ndala , Mildred Airo , Paul Olawale Fadojutimi , Ivo A. Hümmelgen , Ella C. Linganiso , Makwena J. Moloto and Nosipho Moloto. Hierarchical Nanoflowers of Colloidal WS₂ and Their Potential Gas Sensing Properties for Room Temperature. (2021). J. of Processes, 9, 1491.
3. Paul Fadojutimi, Zikhona Tetana, John Moma, Nosipho Moloto and Siziwe Gqoba Colloidal synthesis of zirconium disulphide nanostructures and its stability against oxidation. (2022). Journal of Chemistry Select. Manuscript published.

Manuscripts to be submitted.

1. Paul Fadojutimi, Siziwe Gqoba, Zikhona Tetana, and John Moma. Hierarchical dandelion rutile titania and their potential gas sensing properties for room temperature sensing methanol and ethanol.
2. Paul Fadojutimi, Siziwe Gqoba, Zikhona Tetana, John Moma and Nosipho Moloto. Nanocomposite of polyaniline and zirconium disulphide for room temperature sensing of primary alcohol.
3. Paul Fadojutimi, Siziwe Gqoba, Zikhona Tetana, Nosipho Moloto, and John Moma. Nanocomposite of polyaniline and titania for room temperature sensing of primary alcohols.
4. Paul Fadojutimi, Siziwe Gqoba, Zikhona Tetana, John Moma and Nosipho Moloto. Few layered synthesis and characterization of zirconium disulphide for optoelectronic application.

Table of Contents

Declaration.....	ii
Abstract.....	iii
Dedication.....	v
Acknowledgements.....	vi
Presentations.....	vii
Publication.....	viii
Table of contents.....	ix
List of figures.....	xv
List of tables.....	xxi
Abbreviation Description.....	xxii
Chapter 1: Introduction and motivation.....	1
1.1 Background and motivation	1
1.2 Problem statement.....	3
1.3 Aim and objectives.....	4
1.4 Thesis outline.....	4
1.5 References.....	6
Chapter 2: Literature review.....	8
2.1 Transition metal dichalcogenides for chemical sensing.....	8
2.2. Exfoliation.....	9
2.3 Gas-Phase method of metal powder production.....	12
2.3.1 Chemical vapour deposition.....	12
2.3.2 Chemical vapour transport	13

2.4 Wet chemical synthesis.....	14
2.4.1 Colloidal synthesis	14
2.4.2 Hydrothermal or solvothermal synthesis.....	19
2.4.3 Sol-gel method.....	20
2.5 Gas sensing mechanism in TMDCs.....	20
2.6 Attributes of a gas sensor.....	21
2.6.1 Response	21
2.6.2 Response and Recovery Time	22
2.6.3 Selectivity/Specificity	22
2.6.4 Detection limits.....	22
2.6.5 Stability	23
2.6.6 Sensitivity and grain size.....	23
2.7 Factors controlling sensitivity.....	24
2.7.1 Receptor.....	24
2.7.2 Transducer.....	24
2.7.3 Utility factor.....	25
2.8 Gas sensing properties of 2D TMDCs and other 2D materials.....	26
2.8.1 Metal doping.....	30
2.8.2 Metal Oxide for sensing VOCs	30
2.8.3 TMDCs with metal oxide composite	32
2.8.4 PANI for chemical sensing.....	34
2.9 References.....	35

CHAPTER 3: colloidal synthesis of zirconium disulphide and its stability against oxidation.....	47
3.1 Introduction.....	48
3.2 Experimental.....	50
3.2 Chemicals and materials.....	50
3.2.2 Synthesis.....	50
3.2.3 Heat up Method.....	50
3.2.4 Hot injection method.....	50
3.3 Material Characterization.....	51
3.4 Results and Discussion.....	51
3.5 Conclusion.....	63
3.6 References.....	64
CHAPTER 4: synthesis of radially aligned nanorutile and its application for chemical sensing of alcohols and acetone.....	67
4.1 Introduction.....	67
4.2 Materials and methods.....	69
4.2.1 Chemicals.....	69
4.2.2 Synthesis of radially aligned nanorutile (RANR).....	69
4.2.3 Sensor fabrication	70
4.2.4 Gas sensing measurement	70
4.3 Characterization of RANR.....	71
4.4 Results.....	72
4.4.1 PXRD OF RANR.....	72

4.4.2 SEM analysis.....	73
4.4.3 TEM analysis.....	74
4.4.4 UV-Vis Spectra analysis.....	76
4.4.5 Thermal analysis of RANR.....	78
4.4.6 BET analysis.....	78
4.5 Gas sensing performance	80
4.6 Methanol vapour sensing.....	81
4.7 Ethanol sensing.....	85
4.8 Isopropanol.....	94
4.9 Acetone.....	96
4.10 Conclusion.....	100
4.11	
References.....	101
Chapter 5: Synthesis and characterization of few-layered zirconium disulphide via liquid exfoliation.....	106
5.1 Introduction	106
5.2 Chemicals and materials.....	107
5.3 Exfoliation of bulk ZrS ₂	107
5.4 Characterization.....	108
5.5 Results and Discussion.....	109
5.5.1 XRD analysis.....	109
5.5.2 UV-Vis spectra analysis.....	110
5.5.3 Raman analysis.....	113

5.5.4 AFM analysis.....	114
5.5.5 SEM analysis.....	116
5.5.6 TEM analysis.....	117
5.5.7 Energy dispersive x-ray spectroscopy (EDS) analysis.....	118
5.5.8 Thermogravimetry analysis.....	119
5.5.9. XPS analysis.....	119
5.6 Conclusion.....	123
5.7 References.....	124
Chapter 6: Polyaniline and zirconium disulphide nanocomposite and its application for chemical sensing of alcohols and acetone.....	127
6.1 Introduction.....	127
6.2 Chemicals and materials.....	128
6.3 Methods.....	129
6.3.1 Synthesis of PANI.....	129
6.3.2 Synthesis of a nanocomposite of zirconium disulphide and polyaniline.....	130
6.3.3 Sensor fabrication.....	130
6.3.4 Gas sensing measurement.....	130
6.4 Characterization.....	131
6.5 Results and discussions.....	131
6.5.1 XRD analysis.....	129
6.5.2 TEM analysis.....	130
6.5.3 BET analysis.....	132
6.6 Gas sensing of PANI-ZrS ₂ nanocomposite.....	136

6.6.1 Primary alcohols and acetone sensing properties.....	135
6.7 Relative Humidity.....	150
6.8 Conclusion.....	151
6.9 References	152
Chapter 7: Titania-zirconium disulphide nanocomposite for sensing acetone vapour.....	155
7.1 Introduction:.....	155
7.2 Chemicals and materials.....	157
7.3 Methods.....	157
7.3.1 Synthesis of nanocomposite of titania with zirconium disulphide	157
7.3.2 Sensor fabrication.....	157
7.3.3 Gas sensing measurement.....	157
7.4 Characterization.....	158
7.5 Results and discussions.....	158
7.5.1 XRD analysis.....	158
7.5.2 Raman analysis.....	159
7.5.3 TEM analysis.....	160
7.5.4 UV-Vis spectroscopy.....	161
7.5.5 Energy dispersive x-ray spectroscopy (EDS) analysis.....	162
7.5.6 BET analysis.....	163
7.5.7 TGA analysis.....	164
7.6 Gas sensing performance of TiO ₂ -ZrS ₂	165
7.7 Conclusion.....	167
7.8 References.....	168

Chapter 8: General conclusions and recommendations for future studies.....	171
8.1 General conclusions.....	171
8.2 Recommendations.....	172
Appendix A.....	174

List of Figures

Figure 2.1: Schematic illustration of sensing mechanism of TMDCs.....	21
Figure 2.2: Schematic illustration highlighting the importance of grain size.....	24
Figure 2.3: Three factors determining the response of a semiconductor gas sensor.....	25
Figure 3.1: PXRD pattern of ZrS ₂ synthesized via the heat up and injection methods.....	52
Figure 3.2: SEM micrographs of ZrS ₂ nanomaterials synthesized by the heat up method...	54
Figure 3.3: SEM micrographs of ZrS ₂ nanomaterials synthesized by the hot injection method.....	54
Figure 3.4: TEM images of ZrS ₂ synthesized by the heat up method.....	55
Figure 3.5: TEM images of ZrS ₂ synthesized by the hot injection method.....	55
Figure 3.6: (a) UV-Vis spectrum and (b) band gap of as-synthesized ZrS ₂ by the heat up method.....	56
Figure 3.7: (a) UV-Vis spectrum and (b) band gap of as-synthesized ZrS ₂ by the injection method.....	57
Figure 3.8: FTIR spectra of (a) raw OA and (b) as-synthesized ZrS ₂ by the heat up method.....	58
Figure 3.9: TGA and DTG thermograms of ZrS ₂ synthesized by the heat up method.....	59
Figure 3.10: (a) and (b) EDS spectra of ZrS ₂ synthesized by the heat up method.....	60
Figure 3.11: High resolution spectra with focus on core levels C1s, O1s, N1s, valence, Zr3d and XPS survey spectrum of ZrS ₂ synthesized by heat up method.....	61

Figure 3.12: Time-dependent study of ZrS ₂ nanomaterials with XRD (a) ZrS ₂ synthesized by heat up method and (b) synthesized by hot injection method.....	62
Figure 4.1: Schematic diagram depicting the synthesis of RANR.....	70
Figure 4.2: Gas sensing set up.....	71
Figure 4.3: PXRD of radially aligned nanorutile.....	73
Figure 4.4: (a) and (b) show the SEM micrographs of the synthesized RANR.....	74
Figure 4.5: (a) and (b) TEM images of RANR	75
Figure 4.6: Mechanism of the synthesis of RANR.....	75
Figure 4.7: Particle size distribution of as-synthesized RANR.....	76
Figure 4.8: The solid-state UV-Vis DRS plot of RANR.....	77
Figure 4.9: The band-gap energy (hν) of RANR.....	77
Figure 4.10: The thermogravimetric and derivative thermogravimetry analysis curves of RANR.....	78
Figure 4.11: Nitrogen adsorption/desorption isotherms of RANR.....	79
Figure 4.12: BJH pore size distributions of the RANR.....	79
Figure 4.13: Response and recovery curves of RANR to methanol at different concentrations.....	82
Figure 4.14: Normalized response of the RANR sensor as a function of methanol vapour concentrations.....	83
Figure 4.15: Repeatability response curves for methanol.....	84
Figure 4.16: Static response characteristic of RANR based sensor towards methanol...85	
Figure 4.17: Static response and recovery curves of RANR to ethanol at different concentrations.....	86
Figure 4.18: Static responses curves of RANR sensor measured under series of ethanol vapour concentration.....	87

Figure 4.19: Normalized response of the RANR sensor as a function of methanol vapour concentrations	87
Figure 4.20: Repeatability response curves for ethanol.....	88
Figure 4.21: Transient response characteristic of RANR based sensor toward 385 ppm of ethanol vapour.....	89
Figure 4.22: Response of RANR towards 77 ppm of ethanol vapour under different humidity conditions at 10, 33,51, 55, 64, 76 and 96%.....	90
Figure 4.23: Stability of RANR sensor towards 77 ppm of ethanol vapour within 45 days.....	94
Figure 4.24: Static responses curves of RANR sensor measured under series of isopropanol vapour concentrations.....	95
Figure 4.25: Normalized response of the RANR sensor as a function of isopropanol vapour concentrations.....	96
Figure 4.26: Static response and recovery curves of RANR toward acetone.....	97
Figure 4.27: Normalized response of the RANR sensor as a function of acetone vapour concentrations.....	98
Figure 4.28: Static responses curves of RANR sensor measured under series of acetone vapour concentrations.....	99
Figure 4.29: Repeatability response curves towards acetone vapour.....	100
Figure 5.1: Exfoliation of bulk crystal of zirconium disulphide.....	108
Figure 5.2: XRD of exfoliated ZrS ₂ nanomaterials.....	110
Figure 5.3: UV-Vis absorption of ZrS ₂	111
Figure 5.4: UV-Vis absorption of ZrS ₂ on exposure to ambient environment for five days...	112
Figure 5.5: Tauc plot of ZrS ₂ (a) Bulk (b) IPA exfol. (c) NMP exfol. (d) CHP exfol.....	113
Figure 5.6: Raman spectra of bulk and exfoliated nanosheets of ZrS ₂ with different thickness.....	114

Figure 5.7: AFM micrographs, height and spectrum of exfoliated ZrS ₂ nanosheets (a) ethanol (b) IPA (c) methanol and (d) water.....	115
Figure 5.8: SEM images of ZrS ₂ (a) and (b) bulk sample (c) IPA exfoliated (d) H ₂ O exfoliated (e) MeOH exfoliated (f) EtOH exfoliated (g) CHP exfoliated (h) NMP exfoliated.....	116
Figure 5.9: TEM and HRTEM images of ZrS ₂ (Ai) and (Aii) CHP exfoliated samples (Bi) and (Bii) NMP exfoliated samples (Ci) and (Cii) IPA exfoliated samples (di) and (Dii) H ₂ O exfoliated samples (Ei) and (Eii) MeOH exfoliated samples F (i) and F (ii) EtOH exfoliated sample.....	117
Figure 5.10: EDS of ZrS ₂ (a) bulk sample (b) NMP sample (c) CHP sample (d) MeOH sample (e) EtOH sample (f) IPA sample (g) H ₂ O sample.....	118
Figure 5.11: Thermogravimetry and derivative thermogravimetry curves of bulk, CHP and IPA exfoliated sample.....	119
Figure 5.12: High resolution core level spectra of NMP exfoliated ZrS ₂ nanosheets with focus on O1S, C1S, S2P+Zr3d, N1s, valence and survey spectrum.....	121
Figure 5.13: High resolution core level spectra of CHP exfoliated ZrS ₂ nanosheets with focus on O1S, C1S, S2P+Zr3d, N1s, valence and survey spectrum.....	122
Figure 5.14: High resolution core level spectra of IPA exfoliated ZrS ₂ nanosheets with focus on O1S, C1S, S2P+Zr3d, N1s, valence and survey spectrum.....	123
Figure 6.1: Schematic diagram of synthesis of PANI.....	129
Figure 6.2: XRD pattern of PANI-ZrS ₂ nanocomposite.....	132
Figure 6.3: TEM image of PANI.....	133
Figure 6.4: TEM images of PANI-ZrS ₂ nanocomposite.....	134
Figure 6.5: (A) Nitrogen adsorption-desorption isotherm for PANI-ZrS ₂ (B): BJH pore size distributions of PANI-ZrS ₂	135
Figure 6.6: (A) Nitrogen adsorption-desorption isotherm for PANI- ZrS ₂ (B): BJH pore size distributions of PANI.....	135
Figure 6.7: Schematic illustration of sensing mechanism of PANI-ZrS ₂	137

Figure 6.8: Dynamic response of PANI-ZrS ₂ towards methanol vapour at RT.....	138
Figure 6.9: (A) Dynamic response curves of PANI-ZrS ₂ towards methanol vapour at RT (B) Response curves of the PANI-ZrS ₂ sensor taken under various methanol vapour concentration.....	139
Figure 6.10: Normalized response of the PANI-ZrS ₂ sensor towards methanol, ethanol, and isopropanol.....	140
Figure 6.11: Typical response and recovery curves of PANI-ZrS ₂ sensor to ethanol at 77 ppm and 385 ppm respectively.....	141
Figure 6.12: Dynamic response and recovery curves of PANI-ZrS ₂ towards ethanol vapour at RT.....	143
Figure 6.13 Response and recovery characteristic curves towards methanol	144
Figure 6.14: Repeatability of the PANI-ZrS ₂ sensor to 385 ppm of ethanol vapour at RT.....	145
Figure 6.15: Dynamic response and recovery curves of PANI-ZrS ₂ towards isopropanol vapour at RT.....	146
Figure 6.16: Comparison of PANI-ZrS ₂ sensor towards methanol, ethanol and isopropanol vapour at RT.....	147
Figure 6.17: Static response and recovery curves of PANI-ZrS ₂ towards acetone vapour at RT.....	148
Figure 6.18 :Normalized response of the PANI-ZrS ₂ sensor towards acetone vapour.....	149
Figure 6.19 :Response of PANI-ZrS ₂ towards (A) 111 ppm of methanol vapour; (B) 77 ppm of ethanol vapour under different humidity conditions at 33, 46,58, 64 and 76% for methanol and at 33, 51, 58, 75 and 96% for ethanol.....	151
Figure 7.1: PXRD of (a) nanocomposite of TiO ₂ -ZrS ₂ and (b) TiO ₂	159
Figure 7.2: Raman of RANR and nanocomposite of ZrS ₂ and with ZrS ₂ -TiO ₂	160
Figure 7.3: TEM of TiO ₂ -ZrS ₂ nanocomposite.....	161

Figure 7.4: HRTEM of TiO ₂ -ZrS ₂ nanocomposite.....	161
Figure 7.5: DRS-UV-Vis of (a) TiO ₂ -ZrS ₂ and (b) TiO ₂	162
Figure 7.6: EDS of TiO ₂ -ZrS ₂ nanocomposite.....	163
Figure 7.7: (a) Nitrogen adsorption/desorption isotherms of TiO ₂ -ZrS ₂ nanocomposite; and (b) BJH pore size distribution of the TiO ₂ -ZrS ₂ nanocomposite.....	164
Figure 7.8: TGA of pristine RANR and TiO ₂ -ZrS ₂ nanocomposite.....	165
Figure 7.9: Static response of pristine RANR towards 122 ppm acetone vapour at RT.....	166
Figure 7.10: Static response of TiO ₂ -ZrS ₂ towards 610 ppm acetone vapour at RT.....	167

List of Tables

Table 1.1: Classification of volatile organic pollutants	1
Table 2.1: TMDCs, metal oxide and its nanocomposite for chemical sensing.....	28
Table 2.2: Comparison of 2D TMDCs with Metal oxide-based sensors.....	33
Table 4.1 Comparison of BET of hierarchical titania.....	80
Table 4.2: Comparison of different MOXs towards VOCs sensing.....	92
Table 6.1: Group IVB TMDCs and TMDCs nanocomposite with polymers for VOC sensing.....	149
Table 7.1: The BET comparison between pristine RANR and nanocomposite of TiO ₂ -ZrS ₂	163

Abbreviation Description

Ammonium persulphate	APS
Polyaniline	PANI
Transition metal dichalcogenides	TMDCs
Interdigitated electrodes	IDEs
Metal oxide semiconductors	MOXs
Room temperature	RT
N,N dimethylformamide	DMF
N-methyl polypyrrolidone	NMF
Part per million	ppm
Relative humidity	RH
Volatile organic compounds	VOCs
Quantum dots	QDs
Polyvinylpyrrolidone	PVP
Printed-circuit board	PCB
World Health Organisation	WHO
Occupational Safety Health and Administration	OSHA
Two-dimensional	2D
Radially aligned nanorutile	RANR
TEM	Transmission electron microscopy

SEM	Scanning electron microscopy
PXRD	Powdered X-ray diffraction
FTIR	Fourier transform infrared spectroscopy
XPS	X-ray photoelectron spectroscopy
DRS	Diffuse reflectance spectroscopy
UV-Vis	Ultraviolet-visible spectroscopy
BET	Branauer-Emmett-Teller (BET)
HAL	Hole accumulation layer
BJH	Barrett Joyner Halenda

CHAPTER 1: INTRODUCTION

1.1 Background and motivation

Volatile organic compounds (VOCs) can be simply defined as chemicals that have the ability to vapourize in ambient environment. These substances are omnipresent in both indoor and outdoor premises. The impact of indoor environmental contamination and pollution arising from VOCs has not been taken very seriously until very recently. The need for monitoring VOCs is very paramount since most people carry out their daily activities in enclosed premises. Statistics from World Health Organization (WHO) shows that close to 4 million of people die yearly due to indoor pollution yearly ¹. Chemicals like acetone, ethanol and formaldehyde have been identified as common indoor pollutants. In a country like the United States of America, the environmental protection agency (EPA) regulates VOCs outdoor due to the possibility of formation of photochemical smog under precise conditions. According to WHO, organic pollutants are classified under three categories: very volatile organic compounds, volatile organic compounds, and semi volatile organic compounds. The classification is shown in **Table 1.1**.

Table 1.1: Classification of volatile organic pollutants (adapted from WHO) ².

Description	Abbreviation	Boiling point range (°C)	Examples of compounds
Very volatile organic compounds	VVOC	<0 to 50-100	Propane, butane, methyl chloride
Volatile organic compounds	VOC	50-100 to 240-260	Formaldehyde, d-limonene, toluene, acetone, ethanol, isopropanol, hexanol
Semi volatile organic compounds	SVOC	240-260 to 380-400	Pesticides, plasticizers, and retardants

VOCs are generally available at home and work; it is inevitable not to be exposed to airborne VOCs. Common sources of VOCs include oil and gas field sites, industrial chemicals, fuel combustion such as petrol, wood, coal, natural gas, printing presses, pharmaceutical plants, and from solvents such as glues and paints. Industrial processes and emission from automobile vehicles have been reported as the main sources of outdoors VOCs.

The era of nanotechnology has paved way for a rapid detection of volatile chemical compounds which have great advantages over the conventional methods of detection of chemical compounds such as gas chromatography (GC), ion mobility spectrometry (IMS) and reaction mass spectrometry. The development of nanotechnology has led to production of nanosensors such as breath analysers, E-nose and wearable nanosensors which provide a quick, affordable, harmless and a portable device for measuring VOCs with high sensitivity, good selectivity, ultra-fast response-recovery times and good repeatability. Chemical sensors find application in the following fields: healthcare-genetics, diagnostics, drug discovery, food processing, environmental and industrial monitoring, quality control, defence and security^{1,3,4}.

Since the discovery of graphene, a two-dimensional (2D) material with great exotic properties and wide applications. But its application is not extended to optoelectronic applications due to lack of band gap. This have resulted into avalanche of other 2D nanomaterials among them are transition metal dichalcogenides (TMDCs)⁵. Fascinating chemical and physical characteristics of 2D materials have made them to be explored in sundry applications such as thermoelectric device, field effect transistors (FET), photodetectors, solar cells, fibre lasers, optics, tribology, electrode materials, catalysis and sensors in the last two decades^{5,6,7,8,9}. TMDCs materials represent a new set of sophisticated class of materials that possess a layered structure just like the clay structure, it may have single or few atoms depending on the thickness of the nanomaterial^{10,11,12,13}. A TMDC has a structure which is quite different from graphene. A monolayer of TMDC is a three atoms stick which is made of a layer of transition metal atoms such as Zr, Hf, Ti, Ta, Mo sandwiched between two planes of chalcogen atoms such as S, Se and Te^{13,14}. These materials have some fantastic characteristics that they exhibit when they exist as mono or few layered materials. 2D nanomaterials have been deployed as sensors because of their layered structures. They possess high surface area and special semiconducting features arising from the manipulation of their band gap makes them suitable in sensor application^{15,16}.

Unlike the group VIB members such as MoS₂, WS₂, MoSe₂ and WSe₂ which have been investigated widely, few works are available on group IVB despite theoretical projections showcased about these nanomaterials as possessing astonishing properties. Theoretical speculation has proved TiS₂ has a good potential for chemical sensing. It is believed that TiS₂ has more active sites for gas absorption than MoS₂ owing to crystal structure and bonding that existed between the metal and the sulphur atoms¹⁷. It was also predicted that monolayer ZrS₂ could find applications in chemical sensing, however ZrS₂ with a defect such as S-vacancies will behave as a better sensor compared to ZrS₂ with no defect¹⁸. Presently, the application of ZrS₂ has been demonstrated as an optical coupled plasmon waveguide resonance (CPWR) sensor but not as a chemiresistive sensor¹⁹.

Decoration of polymers or semiconductor metal oxides with TMDCs could greatly enhance the sensor attributes arising from synergistic effects. Shokouh *et al* fabricated a nanohybrid of TiS₂ and polyvinylpyrrolidone (PVP) for sensing ethanol vapour, the sensor displayed an ultra-fast response-recovery times of 2 s and 60 s respectively. The delayed recovery time that is often associated with TMDCs has been eradicated by forming close interjections between the nanocomposite¹⁷. Qin *et al* made a nanohybrid of TiO₂-WS₂ by loading quantum dots of TiO₂ on WS₂ nanosheets for sensing NH₃ gas. The sensor displayed better response (17 folds) and recovery times, selectivity and stability compared to bare WS₂²⁰.

1.2 Problem statement

The poor or no sensitivity of metal oxide-based semiconductor sensors to chemical vapours or gases at room temperature has prevented their usage in detection of flammable and explosive gases; this has caused a great shift to two-dimensional (2D) nanomaterials. Researchers are now investigating other 2D materials since graphene has properties that make it applicable in gas sensing. The layered structure and large surface-to-volume ratio of 2D nanomaterials make them suitable for gas sensing, with a fascinating good sensor characteristic towards volatile organic compounds. Therefore, these nanomaterials have been explored recently for their gas sensing attributes. However, they still have drawbacks like poor sensitivity and recoverability. Several studies have shown formation of hybrid nanomaterials could greatly improve the performance of transition metal dichalcogenides in gas sensing. The construction of proper close interface between the composite will enhance the electrical and chemical functionalities of the sensor. Integration of TMDCs with metal oxides, polymers and carbon materials will

boost the sensor characteristics of TMDC-based sensors with a geometric advantage of the nanocomposite material.

1.3 Aim and objectives

The aim of this research is to synthesize nanocomposite catalysts of the transition metal dichalcogenide, ZrS₂ with dandelion shaped TiO₂ and polyaniline; and to evaluate their performance in the chemical sensing of volatile organic compounds at room temperature.

To achieve the above-mentioned aims, the following were identified:

1. Colloidal synthesis of ZrS₂ nanomaterials using hot- injection and heat-up methods.
2. Determine the optimal conditions for the synthesis of ZrS₂ nanomaterials by varying the reaction time, coordinating solvents, temperature of reaction and concentration of precursors.
3. Fabrication of few layered ZrS₂ from the bulk crystal sample via liquid exfoliation with green solvents.
4. Synthesis of dandelion shaped TiO₂ by facile hydrothermal method.
5. Synthesis of polyaniline (PANI) using facile chemical polymerization method.
6. Functionalization of both the titania and polyaniline by decorating them with ZrS₂ via ultrasonication.
7. Characterization of the synthesized nanomaterials and heterostructures using techniques such as SEM, TEM, HRTEM, UV-Vis, AFM, FTIR, BET, TGA, Raman spectroscopy, XRD and XPS.
8. Application of pristine and heterostructure nanomaterials in sensing of VOCs at room temperature.

1.4 Thesis outline

Chapter 1: Introduction

This chapter enumerates the details of this research in topics. It provides insight into the background, problem statement, motivation, aim and objectives.

Chapter 2: Literature review

This chapter discusses the current state of research with respect to advances in the synthesis routes of group IVB transition metal dichalcogenides and their nanocomposites with metal oxide or polymer for chemical sensing of volatile organic compounds at room temperature.

Chapter 3: Colloidal synthesis of ZrS₂

The chapter is a journal article submitted to the Journal of Crystal Growth and is currently under review. The article reports on the novel synthesis of ZrS₂ via the colloidal approach. The effects of using different sulphur precursors, different ligand and co-ligands were also investigated. The stability of ZrS₂ was also probed.

Chapter 4: Synthesis of rutile titania

This chapter entails facile fabrication, characterization of radially aligned nanorutile titania and their applications for sensing primary alcohol and acetone gas.

Chapter 5: Synthesis of ZrS₂ nanomaterials

This chapter demonstrates a facile top-down approach of obtaining few-layered ZrS₂ via ultrasonication and its characterization.

Chapter 6: Nanocomposite of PANI-ZrS₂ and its applications in chemical sensing

This chapter describes the fabrication of nanocomposite of ZrS₂ and PANI, characterization and its application for sensing selected primary alcohol and acetone at room temperature.

Chapter 7: Nanocomposite of TiO₂-ZrS₂

In this chapter, the synthesis of ZrS₂ and TiO₂, characterization and its sensing potential towards volatile organic compounds is outlined.

Chapter 8: This chapter presents a general conclusion from the research, as well as recommendation for future work.

1.5 References

1. Conti, P.P., Andre, R.S., Mercante, L.A., Fugikawa-Santos, L. and Correa, D.S., 2021 Discriminative detection of volatile organic compounds using an electronic nose based on TiO₂ hybrid nanostructures. *Sensors Actuators, B Chem.*, 344, pp.130124.
2. McAughey, J.J., Pritchard, J.N. and Black, A., 1990. Risk assessment of exposure to indoor air pollutants. *Environ Technol.*, 1990;11(4), pp.295-302.
3. Sharma, S. and Madou, Marc., 2012. A new approach to gas sensing with nanotechnology. *Royal society*, 370, 2448-2473.
4. Munawar, A., Ong, Y., Schirhagl, R., and Tahir M.A., 2019. Nanosensors for diagnosis with optical, electric and mechanical transducers. *RSC Adv.*, 9, pp.6793-6803.
5. Anichini C., Czepa, W., Pakulski, D., Aliprandi, A., Ciesielski, A., Samorì, P., 2018. Chemical sensing with 2D materials. *Chem Soc Rev.*, 47(13), pp.4860-4908.
6. Pandit, A. and Hamad, B., 2021. The effect of finite-temperature and anharmonic lattice dynamics on the thermal conductivity of ZrS₂ monolayer: Self-consistent phonon calculations. *J Phys Condens Matter.*, 33 (42):1-23.
7. Mattinen, M., Popov, G. and Vehkamäki, M., 2019. Atomic Layer Deposition of Emerging 2D Semiconductors, HfS₂ and ZrS₂, for Optoelectronics. *Chem Mater.*, 15, pp.5713-5724.
8. Wen, Y., Zhu, Y. and Zhang, S. Low temperature synthesis of ZrS₂ nanoflakes and their catalytic activity. *RSC Adv.*, 5(81), pp.66082-66085.
9. Li, L., Lv, R. and Wang., 2019. Optical nonlinearity of ZrS₂ and applications in fiber laser. *Nanomaterials.*, 9(3), pp.315.
10. Choi, W., Choudhary, N., Han, G.H., Park, J., Akinwande, D. and Lee, Y.H., 2017. Recent development of two-dimensional transition metal dichalcogenides and their applications. *Mater Today*, 20, pp.116-129.
11. Tedstone, A. A., Lewis, D.J. and O'Brien, P., 2016. Synthesis, Properties, and Applications of Transition Metal-Doped Layered Transition Metal Dichalcogenides. *Chem Mater.*, 28(7), pp.1965-1974.

12. Shi, Y., and Li, L.J., 2017. Synthesis of transition metal dichalcogenides. In: *2D Materials: Properties and Devices*. Cambridge University Press, pp.344-358.
13. Yan, C., Gan, L., Zhou, X., et al., 2017. Space-Confined Chemical Vapor Deposition Synthesis of Ultrathin HfS₂ Flakes for Optoelectronic Application. *Adv Funct Mater.*, 27(39), pp.1-9.
14. Singh, A.K., Kumar, P., Late, D.J., Kumar, A., Patel, S., and Singh., J., 2018. 2D layered transition metal dichalcogenides (MoS₂): Synthesis, applications and theoretical aspects. *Appl Mater Today.*, 13, pp.242-270.
15. Kumar, R., Goel, N., Hojamberdiev, M., and Kumar, M., 2020. Transition metal dichalcogenides-based flexible gas sensors. *Sensors Actuators, A Phys.* 303, pp.111875.-111892.
16. Lee, E., Yoon, Y.S. and Kim, D.J., 2018. Two-Dimensional Transition Metal Dichalcogenides and Metal Oxide Hybrids for Gas Sensing. *ACS Sensors.*, 3(10), pp. 2045-2060.
17. Hosseini-Shokouh S.H., Fardindoost, S., and Zad, A.I., 2019. A High-Performance and Low-Cost Ethanol Vapor Sensor Based on a TiS₂/PVP Composite. *ChemistrySelect*, 2 4 (21), pp.6662-6666.
18. Nguyen, H.T.T. Hoang, D.Q., Dao, T.P. Nguyen, C.V., Phuc, H.V., Hiew, N.N., Hoat, D.M. Long, H.L., Tong, H.D. and Pham, K.D., 2020. The characteristics of defective ZrS₂ monolayers adsorbed various gases on S-vacancies: A first-principles study. *Superlattices Microstruct.*,140, pp.88-104.
19. Ma, J., Liu, K., Jiang, J., Xu, T., Wang, S. Chang, P., Zhang, Z.,Zhang, J., and Liu, T., 2020. All optic-fiber coupled plasmon waveguide resonance sensor using ZrS₂ based dielectric layer. *Optica*, 28(8), pp.11280-11289.
20. Qin Z., Ouyang, C., and Zhang, J., 2017. 2D WS₂ nanosheets with TiO₂ quantum dots decoration for high-performance ammonia gas sensing at room temperature. *Sensors Actuators, B Chem.*, 253, pp.1034-1042.

CHAPTER 2: LITERATURE REVIEW

2.1 Transition metal dichalcogenides for chemical sensing

Among the new materials for sensor application, much attention is being given to two dimensional (2D) chalcogenide materials which have diverted a great research to explore them in the last few decades ^{1,2,3,4,5,6}. Transition metal dichalcogenides (TMDCs) materials represent a new set of sophisticated class of materials that possess a layered structure just like clay structure, it may have single or few atoms depending on the thickness of the nanomaterial ^{6,7,8,9}. The shift to TMDCs emanated as a result of the exfoliation of graphene about two decades ago, a single-layered carbon with outstanding properties such as conductivity, mechanical, thermal, and electrical properties. Unlike graphene, a TMDC monolayer is three atoms thick consisting of a layer of transition metal atoms such as Zr, Hf, Ti, Ta, Mo sandwiched between two planes of a chalcogen atom such as S, Se and Te ^{9,10}. There are weak van der Waals forces that exist in between the layers and covalent bonds within the materials. These materials have some fantastic characteristics that they exhibit when they exist as mono or few layered materials. 2D nanomaterials have been deployed as sensors as a result of their layered structures. They possess a high surface area and special semiconducting features arising from the manipulation of their band gap making them suitable in sensor application ^{2,3}. TMDCs have some drawbacks which limit their application in gas sensing such as: (i) cross selectivity-the sensor may respond to many gases at a time, without being able to distinguishing one gas from the other (ii) TMDCs sensor response time is very slacking and the recovery time is often partial (iii) oxophilicity of TMDCs which refers to the tendency of the sensor surface to be somewhat topped by oxygen or moisture in ambient environment. This may slowly devalue the activity and stability of the sensor over time.

Numerous methods have been used over the years to eradicate these drawbacks, which include novel metal doping and forming a junction with metal oxide semiconductors ³. In relation with TMDC materials, the monolayers and few-layers of hafnium dichalcogenides have astonishing physical properties speculatively, but are rarely investigated ^{9,12,13,14}. Results have demonstrated that, the calculated room temperature mobility for HfS₂ and HfSe₂ monolayers is about 5.3 and 10.3 times respectively; greater than properly investigated MoS₂ ^{9,15}. They also exhibited greater sheet current densities much higher than that of MoS₂, this remarkable quality makes them valuable materials in FETs application ¹⁵. Notwithstanding these eminence in theoretical projection; correspondingly few experimental results are available presumably due

to the complexity in syntheses methods or as a result of oxophilicity of the nanomaterials^{16,17}. In the few published works, most of the studies use exfoliation method or chemical vapour deposition (CVD) method for their fabrication^{14,18,19,20,21}. The thickness and lateral dimension of the nanosheets cannot be manoeuvred with the use of the mechanical exfoliation method^{15,18,19}. CVD is one the favourite methods of producing the group IVB TMDCs except for TiS₂^{21,22}. The method is economical, easy to carry out and produces a product with high quality; however, the CVD method still has some demerits. Ultrathin 2D TMDCs are mostly synthesized on substrates like mica, sapphire, SiO₂ and hexagonal boron nitride (hBN) which require them to be conveyed to other substrates for further application^{6,11,13,23}. For application purposes, it is better that these nanosheets are in discrete form than to be produced on substrates²⁴. Hence, the solution method is still preferred for the synthesis of 2D TMDCs to CVD method.

There are three common ways of preparing mono or few-layers TMDCs: (a) exfoliation, (b) chemical vapour deposition and (c) wet chemical/solution -based.

2.2. Exfoliation

This method of synthesis can be subdivided into two - mechanical and liquid exfoliation. It is employed in the fabrication of mono and few-layers of 2D layered materials. Mechanical exfoliation is a physical process which requires the use of the scotch-tape technique to separate off from the bulk of the material. The adhesive force of the tape helps to break the van der Waals forces that exist within the layers of the material. The isolated layer can undergo successive peeling to give mono and few-layers sample which is then deposited onto a substrate. This produces high quality single-layered nanosheets though with low output while liquid exfoliation is a solution-based method with great output. The first report on exfoliation of TMDCs from bulk samples was published in 2005 by Novoselov *et al* where mono layers of MoS₂ and NbSe₂ were isolated from the bulk of the material using scotch-tape²⁵. Group IVB TMDCs have been prepared using mechanical exfoliation of the bulk. The group IVB TMDC nanomaterials are easily affected in ambient environment and thus get oxidized^{26,27,28,29}. To prevent their oxidation, exfoliation was carried out in a glove box and vacuum transfer chambers or immediate passivation with protective encapsulation layer was used in the synthesis^{18,30,31}. Chae *et al* fabricated few layers of HfS₂ field effect transistor on a SiO₂/Si substrate inside an integrated vacuum cluster system to prevent ambient oxidation. They realized uniform ambient oxidation of the HfS₂ material, preferentially at defect sites which

resulted to thickness enlargement. The oxidized HfS₂ performed poorly as a field effect transistor compared to the unoxidized sample³⁰. In a similar report Kanazawa *et al* synthesized few layer nanosheets from the bulk using scotch tape on single crystal HfS₂, the small piece that was obtained on the tape, was then cleaved numerous times to obtain thin film of average size of thickness on SiO₂/Si/Al₂O₃ substrate. The Al₂O₃ substrate surface was passivated with hexamethyldisilane (HMDS) before exfoliated HfS₂ was transferred on it³². In another similar work by the same group, HfS₂ flakes were exfoliated on AlO₃ substrate and the exfoliation method used suffered from the difficulty in manipulating the size and thickness of the fabricated TMDCs, as well as not being able to be scaled up for large batch production²⁶.

Liquid exfoliation can be further subdivided into two main types. The one type is simple and does not involve intercalation. The bulk sample is dispersed into the appropriate solvent or surfactant followed by exfoliation through a sonication process. The second type is a two-step process with intercalation preceding the exfoliation process in a solvent^{19,20,33,34}. This method entails insertion of alkali metals into the bulk material with compounds like LiBH₄, n-butyl lithium or organolithium compounds in solvent for 7-14 days at room temperature or at 100 °C for 3-4 days, succeeded by dispersing in an appropriate solvent. Care must be taken to ensure complete exfoliation, if not there is the tendency of generation of metal nanoparticles and Li₂S being precipitated during the process. The lithiated layered material is recovered through a filtration technique and thorough rinsing with solvent such as hexane to eliminate lingering impurities of organic residues and the alkali metal. The intrinsic properties of the dispersing solvent or surfactants is crucial which is to break the cohesive energy that exist in the layered material and also determines the exfoliation output^{33,35}. The surface tension of the solvent needs to match the surface energy of the dissolved bulk sample. It is necessary to use the right solvent for dispersion of the bulk powder as this prevents re-stacking and aggregation of nanosheets in the solvent. Coleman *et al* reported that experimental parameters such as the starting mass of the bulk material, sonication period, centrifugation conditions and nature of solvent determines the concentration, thickness, lateral and broad size of the exfoliated nanosheets produced. An increase in concentration was favoured by increasing the sonication time (200 h) for MoS₂, moreover, the nanomaterial had small lateral sizes and broad size distribution²⁰. The solvents that are commonly used are isopropanol (IP), dimethylformamide (DMF), hexane, N-methyl-cyclohexyl-2-pyrrolidone (NCHP) and N-methyl-2-pyrrolidone (NMP)³⁵. NMP is the most suitable solvent for the fabrication of MoS₂ but due to its toxicity and difficulty in obtaining free standing nanomaterial after sonication, its application is limited.

This has led to the use of other solvents such as aqueous solution or volatile solvents. Coleman *et al* used this method to prepare few-layers of some TMDCs and metal chalcogenides. For a solvent to be suitable for isolation of MoS₂, it was observed its surface tension should be about 40 mJm⁻² ²⁰. However, when water is used as a dispersing agent for a material that hydrolyses in water, the nanomaterial gets oxidized. Traces of water have a tendency to oxidize group IVB TMDCs through hydrolysis, resulting into the production of metal oxides (MOXs) ^{26,27,30,36}. Sherrell *et al* gave an insight to the oxidation of TiS₂. The group synthesized TiS₂ nanosheets by insertion of alkali ions into TiS₂ powder exfoliated in deionized water thereafter. It was observed that the exfoliated nanosheets were quickly destabilized by oxygen. The TiS₂ nanosheet suspension in water was oxidized to oxide of titanium. It first generated TiSO species as the intermediate product, at the same time H₂S gas was liberated to the environment. This was evident, as a colour change was observed in the suspension, it first turned to grey and then to white within 7 days of observation ³⁶. This method is so popular in the synthesis of single layers of MoSe₂, WS₂, MoS₂, WS₂, TaS₂, TiS₂ and ZrS₂ ³⁵. The obtained MoS₂ and WS₂ nanosheets using this method were observed to undergo phase transition, it translated from semiconducting (2H) phase to non-semiconducting (1T) phase. A thermal annealing process was needed to reverse it to the semiconducting phase ³⁷. The use of co-solvents has been developed to enhance the exfoliation process. For this, the use of Hansen solubility parameters (HSP) theory must come into play. Using HSP theory, a variety of a mixture of solvents have been explored to fabricate MoS₂. Zhang *et al* exfoliated MoS₂ nanosheets using a co-solvent of water and ethanol. In a similar way, MoS₂ was also effectively exfoliated using a mixture of chloroform and acetonitrile ³⁸. Kaur *et al* synthesized few-layers of HfS₂ by dispersing the bulk HfS₂ in NCHP and ultrasonicated the solution. For the exfoliation in NCHP, the sheet formed was more stable in air as the solvent shielded the nanomaterial against ambient oxygen for a few days compared to using NMP and DMF as solvents ³⁹. Li *et al* synthesized ZrS₂ nanosheets by dispersing the bulk of the powder in IP, the suspension was then sonicated to give a few layers of ZrS₂ ²⁷.

Zeng's group were the first to report on simplified lithiation using electrochemical lithium intercalation method to produce single layers of MoS₂, WS₂, TaS₂ and TiS₂ by proper adjustment of the amount of lithium intercalated, which was followed by exfoliation in ethanol or water ⁴⁰. In another related experiment, the same group executed a systematic study by manipulating circuit parameters such as voltage and current for the for production of few-

layered inorganic compounds, such as TiS_2 , TaS_2 , WSe_2 , ZrS_2 , NbSe_2 , BiTe_3 , Sb_2Se_2 and BN . They optimized the parameters and produced high quality NbSe_2 and BN nanosheets^{40,41}.

Tandem molecular intercalation (TMI) is an improved method of exfoliation which is a facile single step process that does not involve sonication, operated under safe and mild conditions. This method makes use of Lewis bases (short and long alkylamines or alkoxides) intercalates, in which short initiator molecules will be the first to intercalate, followed by long primary molecules. Group IV and V TMDCs are better synthesized using weak Lewis bases such as alkylamines while alkoxides are more appropriate for the synthesis of group IV TMDCs. Single-layered WSe_2 has been exfoliated by intercalation of an alkali ethoxide and alkali hexanoate in dimethyl sulfoxide (DMSO) with agitation lasting for several hours at room temperature. This process is well accepted for the synthesis of TiS_2 , ZrS_2 , NbS_2 and MoS_2 ⁴². The use of surfactants or polymers has not been well explored like the use of solvents presumably due to the high cost or toxicity of some of these surfactants. Sodium chlorate is the common surfactant that is being used, it helps to coat the sheets in dispersion thus preventing agglomeration⁴³.

2.3 Gas-Phase method of metal powder production

Gas-phase method of synthesis is a bottom-up method of production of materials from unit atoms. Chemical vapour deposition and chemical vapour are gas-phase methods that are commonly being deployed in TMDC synthesis in particular group IVB TMDCs¹⁷.

2.3.1 Chemical vapour deposition

Chemical vapour deposition (CVD) is a methodology that involves decomposition or chemical reactions of gaseous precursors through thermally induced means. Depending on the nature of material or the application, sometimes the use of substrate may be introduced into the furnace onto which the product is formed. CVD is generally deployed as a bottom-up method for synthesis of various 2D materials in the last decade, especially the group IVB TMDCs^{6,11,13,44,45,46,47,48}. In the synthesis, an inert gas (e.g., Ar) and H_2 gas are introduced, which help to eliminate oxidation of the material, at the same time reduce formation of impurities^{9,13,17,23,49,50}.

2.3.2 Chemical vapour transport

There are more reports on the use of chemical vapour transport (CVT) on the synthesis of group IVB TMDCs than mere CVD^{11,51}. CVT requires the use of halogens such as I₂ as the transport gas and is used for bulk single crystal, which takes days for the synthesis to be completed. The synthesized materials are then exfoliated into single or few layered sheets⁵². CVT is also used to synthesize transition metal trichalcogenides (MX₃) which are then subjected to pyrolysis to give MX₂^{27,53}. Wen *et al* synthesized ZrS₂ nanoflakes by reacting a stoichiometric ratio of elemental sulphur (S) and ZrCl₄; S was added in excess due to its ease of evaporation at high temperatures. Various temperatures were evaluated, and in each case, the reaction was held for 1 h. ZrS₃ was formed and later decomposed to ZrS₂ on further heating. The optimal temperature was observed at 800 °C with no traces of impurities.⁵⁰ In a similar manner with little adjustments, Fu *et al* synthesized HfS₂ by using HfCl₄ powder and S powder. Both the metal precursor and S powder were placed upstream of the quartz tubes and heated at a temperature of less than 200 °C while the substrate was inserted in the hot zone at a temperature of about 930 °C. The heating was done simultaneously for a few minutes and then stopped. The unreacted precursors were immediately eliminated with the aid of magnets, after which the furnace was cooled down naturally¹³. Zheng *et al* similarly synthesized HfS₂ nanoforests by placing the substrate in the hot zone; and the metal precursor and chalcogen precursors upstream. The heating was done at the same time, the temperature was set at 950 °C and 160 °C respectively, operated for 10 minutes and then terminated. At the end of the reaction, the furnace was rapidly cooled down⁵⁴. Zhang *et al* comparably reported on synthesis of both ZrS₂ and ZrSe₂ by CVD at elevated temperatures above 800 °C synthesis. The reaction temperature was sustained for about 20 minutes and nanostructures of ZrS₂ and ZrSe₂ were grown on substrates²³. Yan *et al* synthesized HfS₂ nanoflakes using S powder and HfCl₄ or HfO₂ powder as precursors. The precursors were placed upstream and the substrate at downstream and the reaction was operated at 900 °C for just 10 minutes followed by cooling the furnace⁹. Shimazu *et al* synthesized a single crystal of ZrS₂ by heating Zr, S₈ and I₂ in a sealed evacuated quartz operated for 3 days at 800 - 900 °C¹¹. TiS₂ was also prepared by Gao *et al* using three temperature zones in which Ti/NH₄Cl and S powder were placed at upstream where low temperature was applied, and the substrate was placed at downstream operated at 450 °C⁵⁵. CVD is not commonly used for titanium dichalcogenide synthesis, they are often produced through solid-state reaction method. A mixture of titanium powder and sulphur powder are blended together before being transferred and sealed into an ampoule under a

vacuum. It is then calcined using muffle furnace for 12 h at 500 °C. Afterwards, the temperature is elevated to 800°C and maintained for another 24 h after which the reaction is stopped and allowed to cool to room temperature^{56,57,58}. Fabrication of high quality 2D ultrathin TMDCs is very difficult as this method does not allow easy manipulation of reaction parameters.

2.4 Wet chemical synthesis

This method involves the use of surfactants or polymers in the solution during the synthesis process. It is much easier for the fabrication of nanomaterials at low temperatures such as 130 °C and offers better control of kinetic parameters; unlike CVD which requires high temperatures of at least 400 °C and may run for several hours before the reaction gets to completion⁵⁹. The wet chemical synthesis method has four main variations which include colloidal, hydrothermal, sol gel and liquid exfoliation techniques.

2.4.1 Colloidal synthesis

Colloidal synthesis provides favourable merits, such as easy to direct and proper grip of the crystallinity, monodispersity and control over the edges of TMDCs^{60,61,62}. The method has been deployed for the production of quantum dots, metal nanoparticles, nanomaterials, etc. When applied for the synthesis of TMDCs, reaction variables which include reaction time, temperature, nature of the metal precursor, chalcogen precursor and the type of ligand used are crucial in determining the shape and size of the nanomaterial that is formed^{59,63}. This synthesis technique can be further subdivided into two: hot injection and heat-up (one-pot synthesis)^{59,64,65}. Injection synthesis is often used when either or both the reactant(s) is/are solvent(s). The precursor that is in solid form is first dissolved in an organic solvent (ligand), then purged for about 20 minutes. The temperature of the system is raised at a controlled rate to a predetermined temperature, at this point the injection of the other precursor is introduced into the hot system by means of a syringe under vigorous stirring. The injection may be rapid or slow depending on the nature of the product required. One-pot synthesis is a non-injection technique which is commonly used when both metal and chalcogen precursors are solids. In this case the reactants are first mixed with the surfactant at room temperature before heating is introduced under inert conditions. Ligands that are commonly used in the colloidal synthesis of TMDCs include oleylamine (OLA), 1-hexadecylamine (HDA), oleic acid (OA), oleylalcohol (OYA), trioctylphosphine oxide (TOPO), dodecylamine (DDA), squalene, 1-dodecanethiol (1-DDT), stearic acid, octadecylamine (ODA) and 1-octadecene (ODE)^{64,65,66}. The use of ligands in colloidal synthesis helps in controlling the morphology during the

synthesis of semiconductor nano-/micro- crystals by coordinating to the surface of the growing nanoparticles⁶⁶. This method of synthesis is quite popular because of its simplicity. The use of ligands has eased the synthesis of hierarchical structure based morphologies such as comb-like, disk-like, dendrite-like, snow flake-like, rod-like, flower-like and urchin-like structures, which show unique properties by combining the features of micrometer and nanometer building blocks in one crystal^{65,67}.

The colloidal method has been employed in the synthesis of single or few-layered TMDCs. Caution is needed in the synthesis of group IVB TMDCs due to the oxiphilicity nature of single or few-layered nanomaterials to prevent contamination of the nanomaterials with metal oxides. There is a need to strictly avoid water or oxygen in the preparation of precursor solution. The chlorides of group IVB (TiCl_4 , ZrCl_4 and HfCl_4) are commonly used in the synthesis of these nanomaterials. These metal precursors are very hygroscopic; thus, they get hydrolysed while weighing in ambient air. Hence, weighing should be done in a glove box. Prabakar *et al* reported on simple colloidal synthesis of hierarchical structures of TiS_2 using hot injection method by dissolving elemental S in non-coordinating ODE and at 300 °C, TiCl_4 was injected and heated up for 15 minutes. The metal precursor was injected into the system at a lower temperature of 150 °C to produce a flake-like structure unlike the flower-like structure that was observed at the higher temperature⁶⁸. In 2008, Park *et al* synthesized mono layers of nanodisks TiS_2 using OLA in dried form; S powder was dissolved in OLA at 110 °C, the mixture was brought to room temperature. Thereafter, titanium was injected, and the temperature slowly raised to 215 °C under argon gas, the reaction lasted for 12 h. The sample obtained was vacuum dried. On exposure of the nanomaterial to air, the colour changed from black to brown; however, when it was kept refrigerated under nitrogen, the colour remained unchanged. The thickness of the TiS_2 nano-disk was about 0.6 nm and a lateral size of 50 nm. Increasing the concentration of the chalcogen atom with a rapid rate of temperature increase helped control the lateral size of the nano-disks. When the chalcogen concentration was increased by 100%, a decrease in lateral size was observed from 50 nm to 34 nm. At the same time, when the concentration of sulphur was increased by a double fold, there was reduction in the lateral size. However, the synthesized TiS_2 single layer nano-disks were easily destabilised at room temperature, the S atom was displaced by oxygen atom in air. The authors were able to prove this using time independent energy dispersive spectroscopy (EDS) and powder XRD⁶⁹. In related work, Cheon's group synthesized TiS_2 by dissolving TiCl_4 in OLA followed by injection of CS_2 into the reaction mixture. The reaction was maintained for 15 min at 300 °C.

Increasing the concentrations of both metal and chalcogen precursors was so pivotal in controlling the lateral size of nanomaterial formed. When the concentrations were increased to 2.4 times, it produced TiS_2 of lateral size of 40 nm. The group changed the S source to S powder; one pot synthesis was deployed to produce TiS_2 nanocrystals. The authors preferred the use of CS_2 over elemental S based on production of highly reactive radicals by S powder which resulted in structural degradation of the nanocrystals produced. Presumably, it is better to use a chalcogen that contains carbon for the synthesis of group IVB TMDCs as the carbon can react with any traces of metal oxides formed during synthesis. The method was also employed in the synthesis of TiSe_2 by using elemental Se as source of chalcogen. Not much has been reported in open literature on group IVB, in particular on hafnium dichalcogenides. Few reports are available on colloidal synthesis of HfS_2 . Cheon's group reported on its synthesis, in which the reactants HfCl_4 , 1-DDT and OLA were heated up in a reaction flask in an inert atmosphere at $245\text{ }^\circ\text{C}$ for the duration of 10 h⁷⁰. In a similar work, the group also used CS_2 as a S precursor at higher temperature of $320\text{ }^\circ\text{C}$ ⁶⁰. The same group also used a resembling synthesis procedure to synthesize sulphides and selenides nanosheets of the IVB and VB groups. To date, the studies by the Cheon's group are the only ones available on ZrS_2 synthesis^{70,71,72,73}. They distilled and degassed OLA prior to use in order to purify it. However, they did not mention the oxophilicity and the ease of oxidation of group IVB TMDCs. In 2014, Cheon's group demonstrated the use of slow decomposing chalcogen precursors (1-DDT) and H_2S gas in the generation of single-layers nanosheets of Group IVB metal sulphides. At high temperatures (over $150\text{ }^\circ\text{C}$) 1-DDT releases S atoms gradually. In the synthesis of HfS_2 nanosheet a combination of HfCl_4 , OLA and 1-DDT were heated up in a reaction flask in an inert atmosphere at $245\text{ }^\circ\text{C}$ for 10 h. The 1-DDT slowly decomposed to H_2S during the entire synthesis time. Using the same procedure while differing the temperature and time of synthesis, ZrS_2 and TiS_2 nanostructures were also produced. The group also used H_2S gas in a similar set-up; the H_2S was released slowly over 6 h and monolayers of TiS_2 , ZrS_2 and HfS_2 were obtained. A high level of precaution needs to be exercised when using H_2S due to its toxicity which can be fatal. The nanocrystals obtained were of a poorer quality compared with those obtained with the use of 1-DDT⁷⁴. Different S precursors can be used, such as elemental S, 1-DDT, CS_2 , diphenylurea, thiourea and thioacetamide. CS_2 and 1-DDT can be systematically introduced into the heating system using hot injection protocol while other precursors that are in solid form can be dissolved in the solvent prior to heating up with the metal precursor. CS_2 is often used for hot injection as a result of its in-situ hydrogen sulphide generation. A metal chloride is

commonly used as the metal precursor and there is a need to wash the synthesized nanomaterials thoroughly due to lingering impurities such as chloride ions.

Similar to group IVB, not much work has been reported for group VB. Sekar *et al* was the first to report on synthesis of group VB TMDCs. The group synthesized NbSe₂ nanowires using one-pot synthesis. Into a three-neck reaction flask, a mixture of OLA, DDA and the precursors (NbCl₄ and Se) were introduced. Temperature of the reaction was increased to 280 °C under N₂ atmosphere and sustained for 4 h. The reaction vessel was not cooled down and nanomaterials obtained were rinsed with hexane. It was then subjected to heating under N₂ atmosphere at 450 °C for a period of 3 h. The resulting NbSe₂ wires had diameters varying from 2 - 25 nm. When the reaction vessel was cooled to room temperature before washing, nanoplates of NbSe₂ were obtained. The nanoplates had lateral dimensions that range from 500-1000 nm and thickness between 10-70 nm. The authors also varied the reaction parameters in order to achieve different sizes or morphologies, but no changes were observed⁷⁵. Mansouri and Semagina reported on the synthesis of NbS₂ using a mixture of ligands to produce different morphologies varying from nanosheets, nanospheres, nanohexagons and nanorods. Increased amounts of OA in OLA led to more production of the nanosheets, but better morphology and laterally confined 2D nanostructures were obtained with minimal use of OA. Also, of great importance is the timing of the reaction, with 0.25 h of reaction, monolayer of NbS₂ nanosheets were formed with OLA as the sole solvent and as the reaction time was increased few-layers of nanosheets were formed⁶¹. Han *et al* synthesized NbS₂ by a one-pot synthesis method in which stoichiometric ratios of NbCl₅ and 1-DDT were introduced into a three-neck reaction flask containing OLA in a glove box. The use of glove box indicated that the nanomaterial is sensitive to impurities (O₂/H₂O). The reaction was operated for 30 minutes at an elevated temperature of 280 °C after which it was cooled down. The authors do not mention if the reaction was conducted in an inert atmosphere. The synthesized ultrathin triangular NbS₂ nanosheets had a thickness of 3.9 nm which was ascribed to represent five layers³⁷.

A great number of research has been reported on group VIB TMDCs most especially on MoS₂ and WS₂ which have been demonstrated in sensor application. Mahler *et al* synthesized both prismatic 2H-WS₂ and distorted octahedral 1T-WS₂ structures⁷⁶. Hot injection reaction method was deployed, the metal precursor was added to OA in a vial, and the injection was made into a reaction flask containing OLA at 320 °C dropwise for about 0.5 h. Prior to attaining this temperature, CS₂ was injected into the system. This resulted in controlled monolayers by the slow release of the precursors. The addition of HMDS after degassing helped in tuning the

crystal structure of the nanosheets from prismatic to distorted octahedral structure which was flowerlike in shape. In a similar report, Geisenhoff *et al* synthesized WSe₂ using the hot injection method whereby tungsten hexacarbonyl was dissolved in combination with TOPO and OA and selenide precursor⁷⁷. The mixture was injected at 330 °C and the process was completed in half an hour. The ligand mixture helped to adjust the precursor reactivity and an increased amount of OA limited the metal precursor reactivity, resulting in fewer nucleation and thus bigger nanocrystals were formed. Lin *et al* prepared MoS₂ quantum dots by dissolving the single-source precursors, ammonium tetrathiomolybdate ((NH₄)₂MoS₄) in three different capping agents, OLA, OA and ODE⁷⁸. The reaction mixture was purged at 120 °C under vacuum for 2.5 h with stirring. Afterwards the reaction was sustained for 3 h at a temperature of 250 °C under N₂ atmosphere before the reaction was quenched. In a related experiment, Altavilla *et al* prepared both MoS₂ and WS₂ nanosheets using thio-salts of Mo and W by a one-pot synthesis method. The single-source precursor and OLA was first degassed, and then the temperature was raised to 360 °C under N₂ flow for 0.5 to 15 h. Interestingly, as the reaction time increased so did the number of layers produced⁷⁸. Antunez *et al*, in a similar experiment produced WSe₂ nanosheets by injecting di-tertbutyl diselenide (tBu₂Se₂) into a reaction vessel already containing WCl₄ in DDA at a temperature above 100 °C under N₂ gas. The reaction lasted for 6 h under strong magnetic stirring at 225 °C. WCl₄ is not a suitable metal precursor for the synthesis of group VI TMDCs, due to its ease to hydrolyse in air, thus the sample was introduced into a three-neck round-bottom flask in a glove box. It is well established that WCl₄ is easily reduced in the presence of organics if overheated, hence the temperature during heating must be well controlled. The organic solvent (DDA) was not used as supplied but was deoxygenated and distilled before use⁷⁹. Jung *et al*, used a one-pot method to synthesize WSe₂ monolayer nanosheets. W(CO)₆, diphenyl diselenide were dissolved in OA, the system was degassed, and the temperature was raised to 330 °C, the reaction was operated for 12 h. Monolayer nanosheets with a lateral dimension of several nanometres were produced. The group also worked with other surfactants such as OYA and OLA. With OYA, few-layers (2-3) with lateral size of few nanometers were obtained while with OLA multi-layers with smaller lateral size were formed⁸⁰. Zhou *et al* working with mixed surfactants, explored the influence of mixed solvents to produce different layers of the nanostructures of MoS₂ and WS₂ using injection protocols. The authors used Mo(AC)₂ and W(CO)₆, the surfactants stearic acid, TOPO, ODA and squalene under N₂ atmosphere with stirring. The duration of heating was just 1 h before being quenched. In a similar reaction, MoS₂ monolayers were also generated but with a change of surfactants (OA, stearic acid and TOPO). By increasing the concentration of

the chalcogen source and decreasing the concentration of the metal as well as increasing the temperature of the reaction multi-layers (3-5) of WS₂, nanosheets were formed. With little modification, both thioacetamide and Mo precursor were injected into the reaction system at different times to produce few and multi-layers MoS₂ nanosheets ⁸¹.

The mechanism for the formation of single-layered nanosheets of TMDCs is still complex. Three approaches variables have been employed to optimise their formation: firstly, the use of chalcogen precursor that gradually decomposes over a long-time during synthesis or delay injection of reactant for a long period, secondly, the nature of the organic solvent; and lastly the duration of the reaction have been varied.

2.4.2 Hydrothermal or solvothermal synthesis

Hydrothermal or solvothermal method is a versatile and effective synthetic route to produce nanomaterials with a different array of morphologies. Hydrothermal synthesis is one of the most important methods for producing fine powders of metal oxides. The process entails the reactants being dissolved in a solvent, which is then introduced into an autoclave. If the solvent for the reaction is non-aqueous, it is referred as solvothermal; whereas, if the solvent for the reaction media is water, it is termed hydrothermal ⁸². Teflon-lined autoclaves are used in this process; they are preferred over glass and quartz autoclaves, since they can tolerate high temperatures and pressures. Furthermore, they support alkaline solutions as well as being resistant to hydrofluoric acid. The flexibility of the method makes it easier to manipulate reaction parameters to produce nanomaterials with desired properties and quality. It has been extensively used for preparing metal oxide nanoparticles, chalcogenide, and phosphide nanomaterials ^{83,84,85}. Chen and Fan synthesized NiSe₂, NiS₂, CoS₂, FeS₂, MoSe₂ and MoS₂ using hydrothermal synthesis at a low temperature while varying the synthesis parameters. They found that adjusting the reaction variables could extend the method of synthesis to other products ⁸³. The method is commonly used for the synthesis of group VIB TMDCs and their nano composites ^{86,87,88,89,90}. Huang *et al* synthesized MoS₂ nanosheets with a net-like morphology of well linked nanoflakes via the hydrothermal route; the nanoflower material had a thickness of a few nanometres. The prepared material had a large surface area and good conductivity giving it potential for application in high-performance supercapacitors ⁸⁸. Jang *et al* also prepared CdS nano particles using hydrothermal method as well as CdS nano wire/TiO₂ nano particle composite using solvothermal method to produce effective photocatalysts ⁹¹.

2.4.3 Sol-gel method

The sol-gel method is a popular avenue to fabricate metal oxide catalysts such as oxides of Ti and Si composites. A variety of materials which includes nanostructures, nanomaterial nanoparticles, glass, ceramics, and nanocomposite are generally fabricated using this method. This process generally takes place in three steps viz: hydrolysis, condensation, and drying. Sol-gel can be sub-divided into two types: aqueous sol-gel and non-aqueous sol-gel method^{82,92}. To synthesise these colloids, the common precursors are made of metal alkoxides and alkoxysilanes. The use of tetramethoxysilane (TMOS), and tetraethylorthosilicate (TEOS) is most common. There is a need to first make a homogeneous solution of the alkoxides to be used⁹². This method is very suitable for production of group VIB TMDCs and their nanocomposites^{93,94,95,96,97,97}. The method offers some merits such as low synthesis temperatures, high reproducibility, cost effectiveness and products with high purity, porosity, and large surface⁹⁸. A one-step direct sol-gel synthesis method was employed to prepare p-type few-layer MoS₂ films in a large volume via deployment of Mo-containing sol-gel including 1% tungsten⁹⁴. It is very functional and good for large production using spin coating deposition method on a variety of substrates to produce 2H-MoS₂ thin film having uniform surface area at moderate temperatures (300-400 °C) followed by annealing. The thin films MoS₂ produced was of good quality and has great electronic properties with a narrow energy band gap of 1.35 eV which is consistent with the material. The product is of n-type semiconductor which finds application in electronic devices⁹⁵.

2.5 Gas sensing mechanism in TMDCs

Semiconductor metal oxide sensors are popularly known for sensing of gases in the last decades especially toxic and dangerous gases, however the need of elevated temperature for their operation has inhibited their application in detection of flammable and explosives gases. The discovery of graphene, a 2D material for gas sensing has led to the emergence of TMDCs for gas sensing. TMDCs provide good selectivity, high sensitivity at room temperature due to ultrathin nature, high surface areas and adjustable bandgap which can find application in the detection of these gases. The key principle in gas sensing in TMDCs is principally based on charge-transfer activity connecting gas molecules and the immediate environment of the sensor which leads to a change in the electrical conductivity of the sensor. Electrostatic force is responsible for adsorption of gas molecules upon injection of the analyte gas on the 2D material. When air is flushed in the test chamber, desorption of the gas molecules takes place;

in this case there is restoration of the sensor to its original state. **Figure 2.1** shows the mechanism of gas sensing of a typical TMDC with NH_3 gas. The kind of interaction that exists between a gas analyte and sensing material will decide the level of the resistance adjustment. Based on the charge carrier of a semiconductor, it can be categorized as p-type or n-type. With a p-type semiconductor there is an increase in the resistance of the sensor upon interaction with a reducing gas whereas there is reduction in the resistance of the sensor with n-type semiconductor. The charge carriers on a p-type semiconductor are principally holes while it is electrons with n-type semiconductor. Due to high electron mobilities, TMDCs are proficient in sensing at room temperature and do not suffer from constant drift of signal which is typical of metal oxide occasioned by forwards and backwards distortion of oxygen vacancies since there is no oxygen atom present in the matrix of the sensor^{2,3,5}.

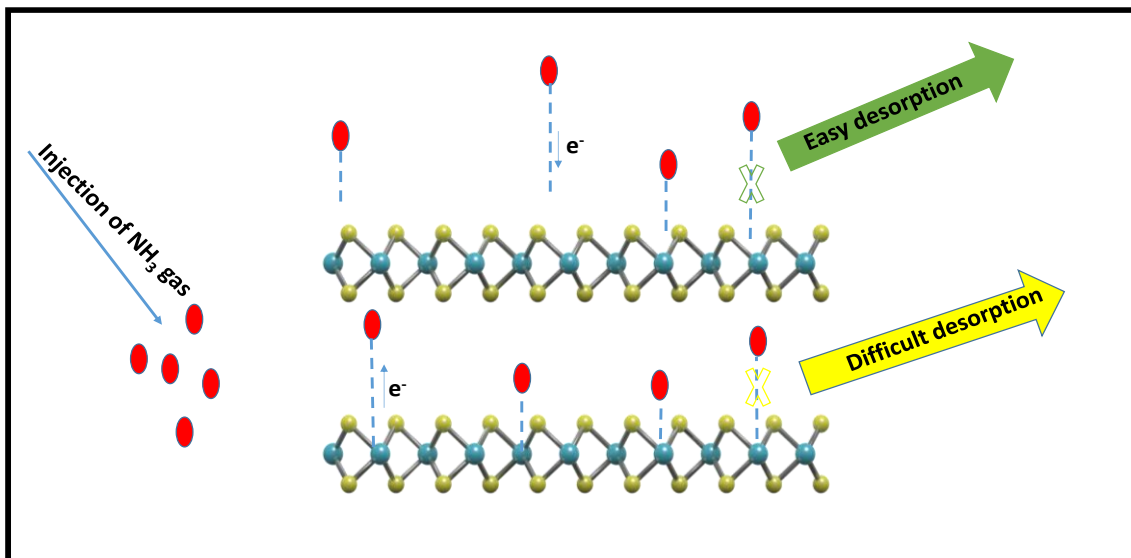


Fig 2.1: Schematic illustration of sensing mechanism of TMDCs. The illustration is adapted from Gqoba *et al*⁹⁹.

2.6 Attributes of a gas sensor

Several parameters are very important in determining the performance of a sensor which include response and recovery time, the 3S (sensitivity, selectivity, and stability of the sensor), operating temperature, concentration of analyte, humidity, and detection limit.

2.6.1 Response

The response is obtained by calculating the ratio of difference in conductance change of the analyte and in air and conductance in air. Mathematically this can be expressed as

$$R = \frac{R_g - R_a}{R_a} = \frac{\Delta R}{R_a} \quad (2.1)$$

$$R = \frac{R_g}{R_a} \quad (2.2)$$

$$R = \frac{R_g - R_a}{R_a} \times 100 = \frac{\Delta R}{R_a} \times 100 \quad (2.3)$$

$$R = \frac{I_o - I_g}{I_g} \times 100 = \frac{\Delta I}{I_g} \times 100 \quad (2.4)$$

Reports have shown that the response and humidity have direct correlation. At extremely high humidity level, water vapour is adsorbed on the surface of the sensor by physisorption which may affect the electronic and ionic conducting properties of the sensor. The adsorbed water layer could serve as a barricade between the sensor surface and the analyte. Thermal treatment can be deployed to eliminate the humidity; however, the heating effect may result into agglomeration of the nanostructures. Reports have shown that acetone sensors perform poorly in terms of response at high temperature arising from thermal ripening of the sensor¹⁰⁰.

2.6.2 Response and Recovery Times

The response time can be defined as the time it takes a sensor to attain 90% saturation upon injection of analyte gas. The recovery time is the time taken to bounce back to 90% of no load upon withdrawal of the analyte gas and consequently blowing dry air to the sensor. A good sensor is expected to have rapid response and recovery times¹⁰⁰.

2.6.3 Selectivity / Specificity

The pragmatic use of a sensor lies on this key parameter, the selectivity of a sensor estimates the preferential ability of a sensor to detect analyte gas of interest in the presence of unwanted gases. The value ranges from 0 to 1, the closer the value to 1 is an indication of high selectivity of the sensor⁹⁹.

2.6.4 Detection limits

This can be defined as minimum concentration that can generate a signal response from a sensor. Two methods are commonly deployed in determination of LOD. Firstly, this is the most widely used method in which repetitive measurements are conducted without any introduction of any analyte gas and with introduction of minimum concentration of the analyte gas.

$$\text{LOD} = \text{LOB} + \text{SD low concentration of analyte} \quad (2.5)$$

Where LOD = Limit of detection

LOB = Limit of blank

SD = Standard deviation

The second method entails obtaining LOD by extrapolation from a linear calibration curve¹⁰¹. A good sensor should be able to detect a very low concentration of gas analyte. This is often reported as part per million (ppm) or part per billion (ppb).

2.6.5 Stability

This is another key factor which determines the reliability and dependability of a sensor. It indicates the effectiveness and consistency of the sensor over a period. A good sensor should have a good stability close to 2-3 years and be recyclable.

2.6.6 Sensitivity and grain size

The size of sensing material plays an important role in its sensing capability. A reduction in the grain size contributes to considerable enlargement in surface area and hence more surface sites for adsorption of analyte to react. This will therefore boost the sensing properties of the sensor¹⁰². No model has been proposed for TMDCs however, three different models have been developed for a metal oxide sensor. Firstly, if the grain size (D) also known as crystallite size is much bigger than space-charge layer (L) $D \gg L$, the large grain does not contribute to improved sensitivity. The electrical conductivity is governed by grain boundaries which control the inner mobile charge carrier and the gas mechanism. The second model suggested that when the grain size reduces, the L moves closer into each of the grain. When grain size is very close to but still higher than 2L, the depletion region around each neck produces conduction channels as shown in **Figure 2.2**. Both the cross-sectional area and grain boundary barriers determine the electrical conductivity. The sensitivity of the gas sensor depends on the grain size when $D \geq 2L$. Thirdly, when the grain size undergoes reduction to 2 folds then $D < 2L$, the entire grain is depleted by the electrons, hence there is reduced conductivity as shown in **Figure 2c**. According to Dmorch *et al* the third model ($D < 2L$) is the most suitable system to improve gas sensing capability. Seal and Shukla reported using SnO₂ as a case study; when the grain size is less than ~10 nm, this leads to better sensitivity for SnO₂ sensor¹⁰². Henceforth, a nanoparticle material is expected to display higher sensitivity compared to coarse-grained peer. Both the

receptor and transducer functions are influenced by grains. Therefore when the crystallite decreases, the higher the sensitivity of the sensor ^{103,100}.

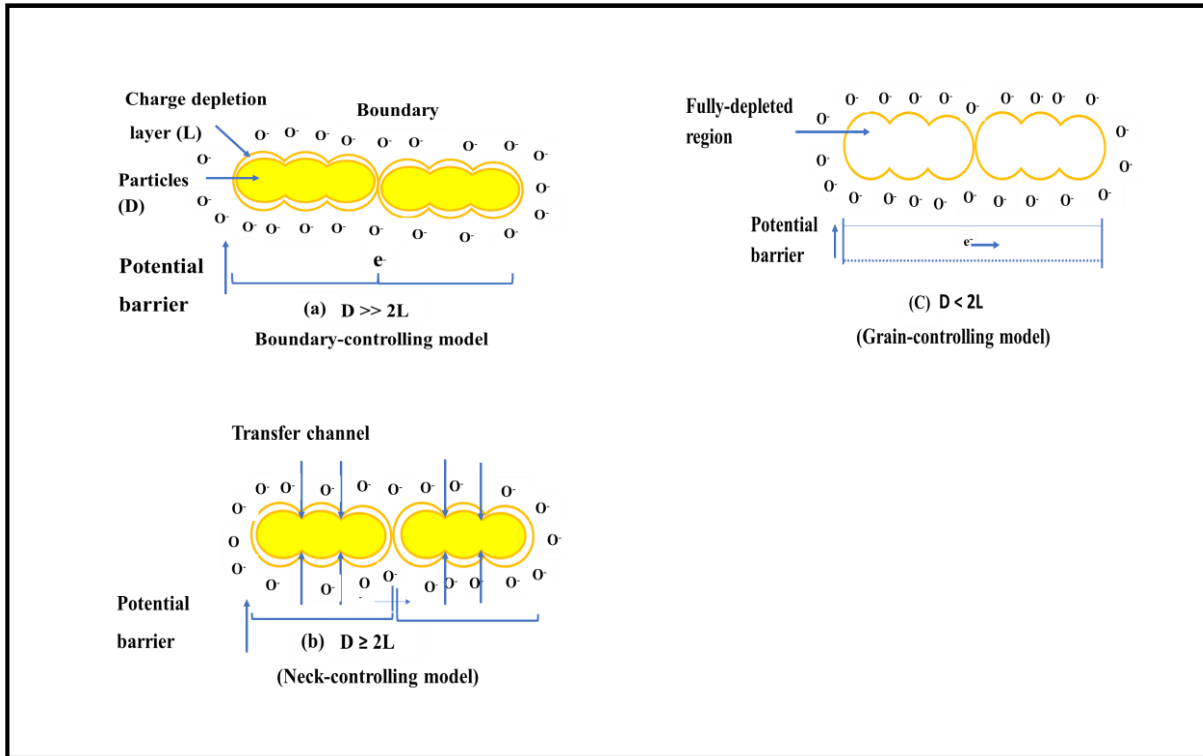


Figure 2.2: Schematic highlighting the importance of grain size. Adapted from Dmorsh *et al* ¹⁰⁰.

2.7 Factors controlling sensitivity

Three important separate characteristics determines the response of a chemical sensor which are receptor, transducer, and utility ¹⁰⁴.

2.7.1 Receptor

This entails how individual grains of a sensor interact with immediate atmosphere accommodating oxygen and target gas, this influences its rate, selectivity, and reversibility. Adsorption only occurs as a result of high reactivity of the sensor surface. The absorption can either be by physisorption and chemisorption ^{104,105}.

2.7.2 Tranducer

A transducer is a device that processes energy from one form to a readable signal. A transducer function shows the capability of the sensor to translate the signal arising from the interactivity occurring on the sensor surface into an electrical signal. A sensing material possesses a receptor and transducer functions, the boundary that exists within the grains plays this role of transducer function¹⁰⁴.

2.7.3 Utility factor

This is related to the diminishing of the response of a sensor arising from factors of diffusion and penetration of the target gas across the pores of the bulk. This explains how the target gas migrates into the inner grains of the sensor material. When the reaction rate is higher compared to diffusion this leads to a decrease in response, this results from the inability of the target gas to reach inner sites of the grains of the sensor material¹⁰⁴. **Figure 2.3** illustrates the relationship that exists among these three factors.

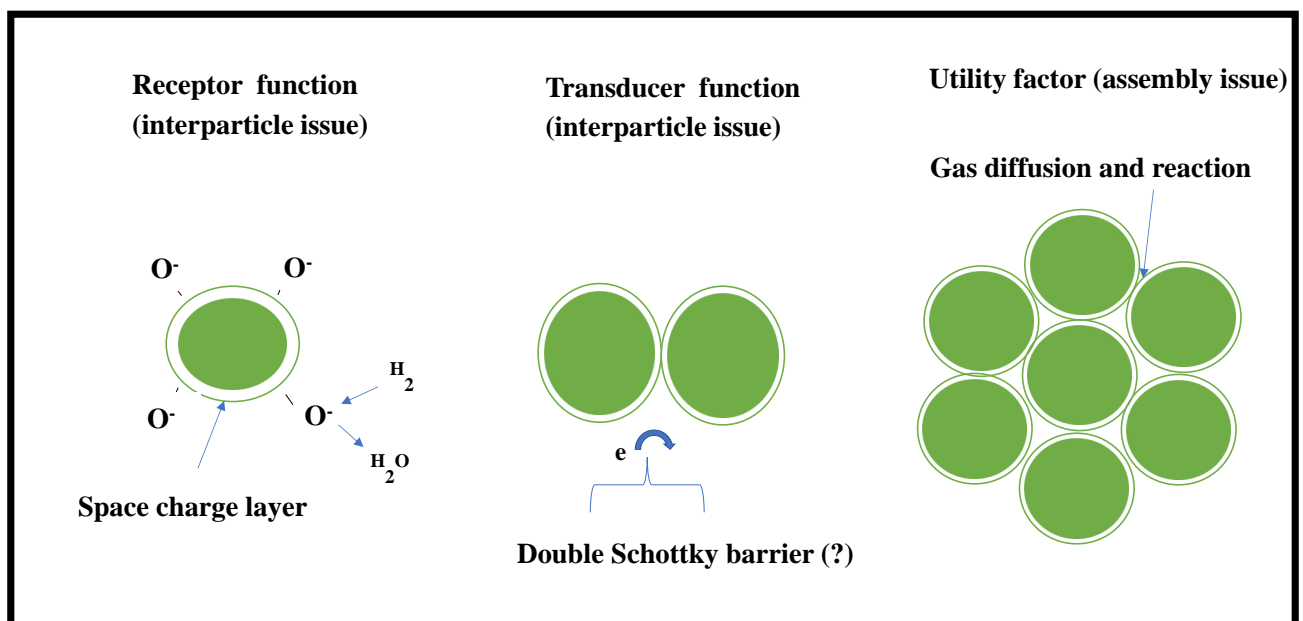


Figure 2.3: Three factors determining the response of semiconductor gas sensor. Adapted from Yamazoe and Shimande¹⁰⁴.

2.8 Gas sensing properties of 2D TMDCs and other 2D materials

The group VI TMDCs are recently being applied in chemical sensing, they have the advantage of being able to respond to chemical vapour at room temperature. More studies have been reported on MoS₂ compared to WS₂. MoS₂ has been demonstrated to sense NO₂, NO, O₂, NH₃ and H₂ at room temperature. Most of the early studies on the use of MoS₂ as chemo-resistive gas sensor were conducted above room temperature.

He *et al* reported on how adjustment of the number of layers can play a key factor in their sensing capabilities. It was observed that the thickness (layer) of the TMDCs plays a key role in determining the response to NO₂ gas. The response of the sensor decreases on exposure to the gas with increasing thickness of MoS₂, this is because of decrease in surface -to-volume ratio of the MoS₂. The authors also reported better response of MoS₂ over rGO based sensor. Integration of Pt nanoparticles with MoS₂ nanosheets improved the sensitivity by a multiple of three¹⁰⁵ Late *et al* provided a contrary view in their studies where the five layered MoS₂ activity was better than fewer layers (2-4). The insight of the mechanism responsible was not properly expantiated; it was merely attributed to electronic structures¹⁰⁶. Cho *et al* vertically grew MoS₂ on SiO₂ substrate using the CVD method. Three different arrangements were fabricated; vertical, horizontal, and mixed alignments. The vertical orientation's performance was better than other alignments; this is ascribed to both the basal plane and edge sites providing more adsorption sites thus, better response¹⁰⁷. Kim *et al* produced microflakes and nanoparticles of MoS₂ using mechanical and liquid exfoliation respectively. The nanoparticles, due to larger surface area and more edge sites than microflakes, produced better response to various O₂ concentrations. The n-type behaviour of the MoS₂ sensor is akin to metal oxide semiconductor in which pre-adsorbed O₂ molecules is very paramount in the sensing mechanism. The sensitivity of the MoS₂ sensor (liquid) for ethanol was high because of enormous physisorption of O₂ molecules on the MoS₂¹⁰⁸.

Qin *et al* exfoliated bulk WS₂ into few layers; the number of the layers plays a key role in the determination of the sensitivity of the sensor. With high number of layers, the response increases but poor recovery. This delay in recovery was expantiated using first principle calculations. With increasing number of layers, the binding energy that exists between the gas molecules and the layer(s) increases hence it leads to longer recovery times (desorption of gas molecules)¹¹⁰. Cha *et al* functionalized surface edges of WS₂ using multiple tubular carbon

nano-fibres (WS_2 @MTCNFs) which resulted into greater specific surface area. The responses increase with increasing concentration of the gas molecules. The sensor sensitivity was quite good toward NO_2 than both NH_3 and C_7H_8 ¹¹¹. Several publications have shown WS_2 sensors are very sensitive to NH_3 vapour: Gqoba *et al* synthesized hierarchical nanoflowers of WS_2 . The selectivity of the sensor toward increasing concentration of NH_3 vapours was good. The response of the sensor towards acetone, ethanol, toluene, and chloroform was quite rapid as well, the hierarchical nanoflowers' morphology provided large surface area for the adsorption of the gas molecule. However, the sensor displayed poor recovery due to delayed desorption of the NH_3 molecules after strong adsorption on the sensor⁹⁹.

Late *et al* demonstrated single layer MoSe_2 for NH_3 sensing at room temperature with quick response (150 s) with increasing concentration of NH_3 vapours but poor recovery (540 s). Despite poor recovery from the sensor, studies showed the performance is far better than some reported work on graphene and MoS_2 sensors for sensing NH_3 and NO_2 at room temperature¹¹². In a related experiment, Guo *et al* exfoliated few layers WSe_2 ; the fabricated sensor exhibited fantabulous sensitivity as low as detecting 0.05 ppm of NO_2 gas with a rapid response time and recovery¹¹³.

SnS_2 is a marvellous 2D material which is not part of the TMDCs, however it has a hexagonal structure akin to TMDCs with a layered structure. The material has a sizeable band gap when in few layers and large electronegativity that seems suitable for gas sensing application. In 2006 Shi *et al* was the first to demonstrate flower-like SnS_2 synthesized using the hydrothermal process; the sensor had good sensitivity and selectivity for NH_3 gas at room temperature with an average response and recovery time of 45 and 110 s respectively¹¹⁴. Xion *et al* produced SnS_2 nanoflowers using the solvothermal method. The hierarchical three-dimensional nanoflowers on exposure to 100 ppm NH_3 produced optimum sensitivity at 150 °C, though with poor response/recovery time, however optimum response/recovery time was gotten at 200 °C. Oxygen catalysed the performance of the sensor; with increasing oxygen content (0-40%) on the sensor, this improved the performance of the sensor in about 3.5 folds. The DFT calculations were used to corroborate on the effect of the increasing oxygen content on the sensor performance. The sensor was able to determine concentrations of NH_3 as low as 0.5ppm and the best selectivity was toward NH_3 over CO_2 , CH_4 , H_2 , $\text{C}_2\text{H}_5\text{OH}$ and CH_3COCH_3 ¹¹⁵. Wang *et al* demonstrated single layer SnS_2 obtained via intercalation liquid exfoliation. The monolayer SnS_2 sensor displayed a quick response (16 s) and good sensitivity towards

ammonia vapour. The response time was excellent, which is quite better compared to other NH₃ gas sensors reported so far however, the author did not report on the recovery time ¹¹⁶.

Guidi *et al* were able to demonstrate the use of CdS and SnS₂ and their metal oxide counterparts for sensing alcohols, acetone, and other chemicals. The CdS and SnS₂ sensors were operated at room temperature with the aid of UV light as well as optimum temperature of 300 °C. The performance of the metal sulphide and SnS₂ sensors outweigh the metal oxide sensors, the CdS sensor displayed great selectivity for alcohols while no selectivity from CdO. The highest selectivity was to butanol, followed by ethanol and methanol was the least. The SnS₂ showed good selectivity to acetone vapour. The operating temperature was maintained at 300 °C. If exceeded, the S atoms and sulphur vacancies in SnS₂ will be displaced with oxygen atoms ¹¹⁷.

Only a few reports are available on chemical sensing of the novel nanomaterials of group IVB TMDCs. Shokouh *et al* reported a fascinating recovery with an ultra-fast response time of 2 s and recovery time of 60 s by fabricating nanohybrids of TiS₂ and polyvinylpolymer (PVP) for ethanol sensing ¹. **Table 2.1** shows some of the TMDCs that have been demonstrated for chemical sensing.

Table 2.1: TMDCs, metal oxides and their nanocomposites for chemical sensing

Material	T °C	Gas (ppm)	Sensitivity (%)	Response time (s)	Recovery time (s)	References
WS ₂ @MTCNFs	25	NO ₂	15	-	-	111
WS ₂ (single layer)	25	NH ₃	-	200	271.5	110
MoS ₂	400	O ₂	-	5700	-	109
MoS ₂	25	NO ₂ (0.1)	-	-	-	108
MoS ₂ (Five layers)	25	NO ₂ /NH ₃	1372/86	-	-	107
MoS ₂ (single layer)	25	NO ₂ (1.2)	-	>1800	>1800	106

WS ₂	25	NH ₃ (240)	-	28	42	99
MoSe ₂	25	NH ₃	-	150	540	112
WSe ₂	25	NO ₂ (0.05)	5.06	50	105	113
SnS ₂	25	NH ₃ (5)	21.6	40-50	100-120	114
SnS ₂	200	NH ₃ (100)	7.4	40.6	624	115
SnS ₂	25	NH ₃ (50)	2.4	-	-	116
SnS ₂ and CdS	300	CH ₃ COCH ₃ and ROH	-	-	-	117
Ag-TiO ₂	25	C ₂ H ₅ OH (5)	4.35	52	63	118
GaN-SnO ₂	25	ROH	-	~100	~100	119
Chitosan	25	C ₂ H ₅ OH	19.35	-	-	120
WO ₃	300	C ₂ H ₅ OH	70	<15	<15	121
NiO-Sn	340	C ₂ H ₅ OH	15.6	17	15	122
MoS ₂ -SnO ₂	25	NO ₂ (5)	18.70	-	-	4
MoS ₂ -SnO ₂	280	C ₂ H ₅ OH	-	-	-	123
MoS ₂ -ZnO	25	NH ₃	46.2	-	-	124
MoS ₂ -TiO ₂	150	C ₂ H ₅ OH	14.20	-	-	125
WS ₂ -TiO ₂	25	NH ₃	43.72	-	174.43	126
TaS ₂ -PANI	25	H ₂ O	97.00	36	49	127
TiS ₂ -PVP	25	C ₂ H ₅ OH(2)	6800	60	2	1

2.8.1 Metal doping

Transition metals which include Fe, Cr, Al, Ni, Sn, and Ce and precious metals such as Pt, Pd and Au can help boost the sensing properties of a semiconductor by enhancing the activity and adjusting the resistance of the sensing material. This improves the overall attributes of the sensor such as 3S (sensitivity, selectivity and stability), response and recovery time; and working temperature especially metal oxide sensors ¹⁰³. Extensive reports have shown that doped ZnO sensors are more effective in sensing acetone vapour over undoped ZnO. Kaur *et al* in their review also showed doped 1- dimensional (D) titanium dioxide with precious metals are very effective in sensing ethanol and acetone compared to undoped titania ⁹⁹. In a similar report, doped SnO₂ sensor showed enhanced sensing capability to VOCs especially acetone unlike the undoped SnO₂. More studies are yet to be available on functionalization of TMDCs with metals and precious metals; however, 2-D materials like graphene sensors doped with precious metals showed better sensing performance over pristine graphene ⁹⁹.

2.8.2 Metal oxides for sensing VOCs

Vast information is available on the sensing mechanism of the metal oxide; thorough research has been conducted on these materials. At ambient temperature, metal oxides exhibit n-type semiconducting features due to propensity for oxygen deficiency which results into development of oxygen vacancies or metal spaces. Metal oxides are principally n-type semiconductors because of oxygen vacancies in the metal oxide lattice. The metal oxide sensing material contains several grains on exposure to atmospheric oxygen. Oxygen e⁻ are adsorbed on the sensing material, the adsorbed oxygen molecules are ionized to oxygen ions, as shown in equation 2.1-2.4; hence there is loss of electrons from the material which results in depletion layer. Upon introduction of reducing gas into the test chamber, the surface of the sensor undergoes redox reactions. The active sites of the metal oxide adsorb the gas molecules which led to change in resistance until the response reaches the optimum level. If a reducing gas is injected, the reducing gas will donate e⁻ which results in further depletion layer (bond) around it, thus resulting in a decrease in resistance. The operating temperature determines the state of form of the adsorbed ion. With temperature exceeding 250 °C, the oxygen molecules dissociate into oxygen ion atom ^{3,103}.





Zhu *et al* produced Ag-TiO₂ sensor by integration of Ag nanoparticles with core-shell nanostructured TiO₂. The performance of the sensor to ethanol at room temperature showed good selectivity, high selectivity (4.35), fast response and recovery of 52 s and 63 s respectively for 5 ppm of ethanol vapour and with a very low detection limit of 0.15 ppm. The authors also demonstrated the raw core-shell TiO₂ nanostructure for sensing of ethanol vapour at room temperature; the high surface provided by the methodology as well as high humidity of about 50% must have been responsible for sensing alcohol at low temperature with a sensitivity of 1.54, fast response of 112 s and recovery of 136 s. The doping with metal nanoparticles improved the sensitivity, response, and recovery time of the sensor by enhancing the electron conduction properties hence improved the sensor capability ¹¹⁸.

Bajpai *et al* fabricated a nanohybrid of nanowire of GaN and nanocrystals of SnO₂ for alcohol sensing at room temperature aided by UV light. The presence of the light permitted the sensor to function at room temperature, the sensor displayed a good response for a wide concentration range (1-5000 ppm) of alcohols. The sensor responses were more favourable to first and second members of primary alcohols compared to other alcohols tested, although this finding is contrary to other work reported by other authors. The responses normally increase with increasing carbon chain for the first to fourth members of alcohols. The response of alcohols depends on the nature of the sensor ¹¹⁹. Ayad *et al* also reported an opposing view; a chitosan film sensor showed high sensitivity for methanol, ethanol and isopropanol with a sensitivity of 7.22, 19.35 and 4.06 respectively. The highest sensitivity of the sensor towards ethanol was ascribed to higher inductive effect of ethyl alcohol to methyl alcohol and isopropanol having the least sensitivity due to steric hindrance of the structure of the molecule ¹²⁰. In a similar report, Chen *et al* produced WO₃ nanoplates which exhibited exceeding sensitivities for methanol, ethanol, isopropanol and butanol at temperature of 300 °C with a quick response and recovery times less than 15 s. The sensitivity increases with increasing carbon chain, the sensor was only tested for a short range of concentration (2-300 ppm) ¹²¹.

Wei *et al* fabricated nanohybrids of mesoporous nickel oxide nanowires by doping with stannum for sensing ethanol at an elevated temperature of 340 °C. A great enhancement of the

sensitivity of the sensor was observed with the doping of the metal oxide which enhanced the surface area of the material by almost 2.5 folds, hence sensitivity improved from 2.16 to 15.6 on exposure to 100 ppm of the gas ¹²².

2.8.3 TMDCs with metal oxide composites

Metal oxide nanostructures have been reported to have good sensitivity, fast response and recovery unlike TMDCs that have a delayed recovery time ¹²². Several metal oxides of various morphologies have been demonstrated towards ethanol sensing in the last decade such as SnO₂, ZnO, TiO₂, α -Fe₂O₃, α -Cr₂O₃, WO₃, InO₃, V₂O₅, ZnFe₂O₄ and CdInO₄ have been tested for sensing VOCs ¹²¹.

The layered structure and large surface-to-volume ratio of TMDCs make them suitable for gas sensing, however they still have drawbacks of poor sensitivity and recoverability. Several studies have shown that formation of hybrid nanomaterials could greatly improve the performance of TMDCs in gas sensing. The construction of proper close interface between the composite will enhance the electrical and chemical functionalities of the sensor. Integration of metal oxides with TMDCs is one of the options to give geometric advantage of the hybrid material. **Table 2.2** shows the merits and demerits of both TMDCs and metal oxide sensors. The orientation of the atoms of the nanomaterials also plays a key role in sensing capability. SnO₂ is probably the most reported metal oxide for gas sensing with ZnO being the next. Han *et al* fabricated MoS₂-SnO₂ heterostructures for sensing oxidizing gas (NO₂) at room temperature. The nanocomposite gas sensor produced a response of 18.7 s on exposure to 5 ppm of the gas. The selectivity was quite good, and stability of the sensor lasted for one month. The heterostructures improved the sensing performance of the sensor compared to raw MoS₂ sensor; and this is attributed to proper p-n heterojunctions formed between the 2D and OD materials ⁴. In a related experiment, Yan *et al* functionalized MoS₂ nanosheets with SnO₂ nanoparticles resulting in enhanced gas sensing performance towards ethanol sensing. The better performance of the nanohybrid was accredited to the enlarged surface area, which provided more active sites which in turn aided proper diffusion of ethanol and quicker electron transfer. Furthermore, there is an internal electric field formed as a result of proper heterojunction formation which quickened the electron transfer. Intensive research has been conducted on ZnO as a sensing material akin to SnO₂ ¹²³. Zhang *et al* reported on MoS₂-ZnO nanocomposite for NH₃ vapour sensing at room temperature. The nanocomposite performance was higher than the raw ZnO with quicker response and recovery times ¹²⁴. Zhao *et al* loaded

MoS₂ nanosheets on TiO₂ nanotubes using the hydrothermal method. The sensor was operated at the optimum temperature of 150 °C. The sensitivity towards ethanol (100 ppm) was fantastic, the response of the nanohybrid outweighed pure TiO₂ by 11 folds. The response to H₂ was minimal and no response to CH₃OH, NO₂ and NH₃¹²⁵.

Qin *et al* fabricated nanohybrid of TiO₂-WS₂ by loading quantum dots of TiO₂ on WS₂ nanosheets for sensing NH₃ gas. The sensor displayed better response (17 folds) and recovery times, selectivity and stability compared to bare WS₂¹²⁶.

Table 2.2: Comparison of 2D TMDCs with metal oxide based sensors

TMDCs	Metal oxides
Advantages	
High electron mobility at room temperature	Rapid response time
Low energy consumption	High sensitivity
High gas response	Affordability
Good compatibility	Long-term stability
Mechanical flexibility	Easy fabrication
Disadvantages	
Low selectivity	Limited selectivity
Sluggish recovery	Low electron mobility at low temperature
High cost	High operating temperature
Lack of long-term stability	High power consumption
Lack of scalable fabrication	Constant drift of the signal
	Poor life-time

2.8.4 PANI for chemical sensing

Polyaniline is commonly known as a good conducting polymer for sensing volatile organic vapours (VOCs), hazardous gases, humidity and warfare agent stimulants at room temperature¹²⁷. Athawale and Kulkarni demonstrated the use of PANI and other polymers for sensing of alcohols. The PANI sensor exhibited good sensitivity towards methanol, ethanol, propanol, butanol and heptanol vapours. The sensitivity of the sensor decreases as the carbon chain length increases. Methanol was reported to have the highest sensitivity being the lightest member of the alcohols, there is ease for its interaction and diffusion within the matrix of the polymer in comparison to other alcohols¹²⁷.

PANI based sensors do have shortcomings such as poor selectivity, low reproducibility, and stability. Functionalization with metals/precious metals or incorporation with metal oxides, carbon compounds, TMDCs and polymers provides integrative performance. PANI nanocomposites have shown outstanding sensing response towards vapours of NH₃, H₂, HCl, NO₂, H₂S, CO, CO₂, SO₂, VOCs and liquefied petroleum gas (LPG). Jiang *et al* reported very short response and recovery times of 5 s and 7 s by loading Au nanoparticles on PANI nanobowls for sensing NH₃ vapour¹²⁸ Tai and his cohorts have illustrated a nanohybrid of PANI/TiO₂ for sensing NH₃ vapour with a good sensitivity, quick response and recovery times¹²⁹. Manjunata *et al* demonstrated nanocomposites of polyaniline and titanium disulphide (PANI/TaS₂) for humidity sensing with good sensitivity, rapid response, and recovery times¹³⁰.

2.9 References

1. Hosseini-Shokouh, S.H., Fardindoost, S. and Zad, A.I., 2019. A High-Performance and Low-Cost Ethanol Vapor Sensor Based on a TiS₂/PVP Composite. *ChemistrySelect*, 4(21), pp. 6662-6666.
2. Kumar, R., Goel, N., Hojamberdiev, M., and Kumar, M., 2020. Transition metal dichalcogenides-based flexible gas sensors. *Sensors Actuators, A Phys*, 303, pp. 111875.
3. Lee, E., Yoon, Y.S. and Kim, D.J., 2018. Two-Dimensional Transition Metal Dichalcogenides and Metal Oxide Hybrids for Gas Sensing. *ACS Sensors*, 3(10), pp.2045-2060.

4. Han, Y., Ma, Y. and Liu, Y., Xu, S., Chen, X. Meng, M., Hu, N., Su, Y., Zhou, Z. and Yang, Z., 2019. Construction of MoS₂/SnO₂ heterostructures for sensitive NO₂ detection at room temperature. *Appl Surf Sci*, 493, pp.6
5. Yang, W., Gan, L., Li, H. and Zhai, T., 2016. Two-dimensional layered nanomaterials for gas-sensing applications. *Inorg Chem Front*, 3(4), pp.433-451.
6. Choi, W., Choudhary, N. Han, G.H., Park, J., Akinwande, D. and Lee Y.H., 2017. Recent development of two-dimensional transition metal dichalcogenides and their applications. *Mater Today*, 20(3), pp.116-130.
7. Tedstone, A.A., Lewis, D.J. and O'Brien P., 2016. Synthesis, Properties, and Applications of Transition Metal-Doped Layered Transition Metal Dichalcogenides. *Chem Mater*, 28 (7), pp.1965-1974.
8. Shi, Y. and Li, L.J., 2017. Synthesis of transition metal dichalcogenides. In: *2D Materials: Properties and Devices*. Cambridge University Press, pp.344-358.
9. Yan, C., Gan, L., Zhou, X., Guo, J., Huang, W., Huang, Jin, B., Xiong, J. Zhai, T. and Li, Y., 2017. Space-Confined Chemical Vapor Deposition Synthesis of Ultrathin HfS₂ Flakes for Optoelectronic Application. *Adv Funct Mater*, 27(39), pp.1-9.
10. Singh, A.K., Kumar, P., Late, D.J., Kumar, A., Patel, S. and Singh, J., 2018. 2D layered transition metal dichalcogenides (MoS₂): Synthesis, applications and theoretical aspects. *Appl Mater Today*, 13, pp.242-270.
11. Shimazu, Y., Fujisawa, Y., Arai, K., Iwabuchi, T. and Suzuki, K., 2018. Synthesis and Characterization of Zirconium Disulfide Single Crystals and Thin-Film Transistors Based on Multilayer Zirconium Disulfide Flakes. *ChemNanoMat.*, 4(10), pp.1078-1082.
12. Kang, M., Rathi S. and Lee I., 2015. Electrical characterization of multilayer HfSe₂ field-effect transistors on SiO₂ substrate. *Appl Phys Lett*, 106 (14), pp 143108.
13. Fu, L., Wang, F. and Wu, B., 2017. Van der Waals Epitaxial Growth of Atomic Layered HfS₂ Crystals for Ultrasensitive Near-Infrared Phototransistors. *Adv Mater*, 29 (32), pp.1-8.
14. Wang, D., Meng, J. and Zhang, X., 2018. Selective Direct Growth of Atomic Layered

- HfS₂ on Hexagonal Boron Nitride for High Performance Photodetectors. *Chem Mater*, 30 (11), pp. 3819-3826.
15. Kang, M., Rathi, S. and Lee, I., 2015. Electrical characterization of multilayer HfSe₂ field-effect transistors on SiO₂. *Phys Lett.*, 106, pp.143108.
 16. Cruz, A., Mutlu, Z., Ozkan, M. and Ozkan, C.S., 2018. Raman investigation of the air stability of 2H polytype HfSe₂ thin films. *MRS Communication*, 8(3) pp. 1191-1196.
 17. Brooks, D.J., Douthwaite, R.E., Brydson, R., Calvert, C., Measures M.G. and Watson, A., 2006. Synthesis of inorganic fullerene (MS₂, M ≤ Zr, Hf and W) phases using H₂S and N₂/H₂ microwave-induced plasmas. *Nanotechnology*, 17(5), pp.1245-1250.
 18. Mañas-Valero ,S., García-López, V., Cantarero, A. and Galbiati, M., 2016. Raman spectra of ZrS₂ and ZrSe₂ from bulk to atomically thin layers. *Appl Sci*, 6(9), pp.264.
 19. Xu, K. Wang, Z., Wang, F., Huang, Y., Wang, F., Yin, L., Jiang, C and He, J.,2015. Ultrasensitive Phototransistors Based on Few-Layered HfS₂. *Adv Mater*, 27(47), pp. 7881-7887.
 20. Coleman, J.N., Lotya, M. and O'Neill, A., Bergin, S.D., King, P.J., Khan, U., Young, K., Gaucher, A., De, S., Smith, R.J. and Shvets, I.V.2011. Two-dimensional nanosheets produced by liquid exfoliation of layered materials. *Science*, 331(6017), pp. 568-571.
 21. O'Brien, M., McEvoy, N., Hallam, T., Kim, H-Y., Berner, N.C., Hanlon, D., Lee, K., Coleman, J.N., and Duesberg, G.S., 2014. Transition metal dichalcogenide growth via close proximity precursor supply. *Sci Rep*, 4, pp. 1-7.
 22. O'brien, M., Mcevoy, N., Hanlon, D., Hallam, T., Coleman, J.N. and Duesberg G.S., 2015. Mapping of Low-Frequency Raman Modes in CVD-Grown Transition Metal Dichalcogenides: Layer Number, Stacking Orientation and Resonant Effects. *Scientific reports*, 6, pp.7493.
 23. Zhang, M., Zhu, Y. and Wang, X., 2015. Controlled Synthesis of ZrS₂ Monolayer and Few Layers on Hexagonal Boron Nitride. *J Am Chem*, 137 (22) : 7051-7054.
 24. Liu, Y., Zeng, X., Hu, X. and Hu, J., and Zhang X., 2019. Two-dimensional nanomaterials for photocatalytic water disinfection: recent progress and future

- challenges. *J Chem Technol Biotechnol*, 94 (1), pp.22-37.
25. Novoselov, K.S, Jiang, D., Schedin, F., Booth, T.J., Khotkevich, V.V., Morozov, S.V. and Geim, A.K. 2005. Two-dimensional atomic crystals. *Proc Natl Acad Sci U S A*, 102 (30), pp. 10451-10453.
 26. Kanazawa, T., Amemiya, T. Upadhyaya, V., Ishikawa, A., Tsuruta, K., Tanaka, T. and Miyamoto, Y., 2017. Performance Improvement of HfS₂ Transistors by Atomic Layer Deposition of HfO₂. *IEEE Trans Nanotechnol.*, 16(4), pp.582-587.
 27. Li, L., Fang, X., Zhai, T., Liao, M., Guatam, U.K., Wu, X., Koide, Y., Bando, Y., and Goldberg, M., 2010. Electrical transport and high-Performance photoconductivity in individual ZrS₂ nanobelts, *Adv Mater*, 22(37), pp. 4151-4156.
 28. Mirabelli, G., McGeough, C., Schmidt, M., McCarthy, E.K., Monaghan, S., Povey, I.M., McCarthy, M., Nagle, R., Hughes, G., Cafolla, A., Hurley, P.K., and Duffy, R., 2016. Air sensitivity of MoS₂, MoSe₂, MoTe₂, HfS₂, and HfSe₂. *J Appl Phys*, 120(12) pp.1063-1069.
 29. Mattinen, M., Popov, G. and Vehkamäki, M., 2019. Atomic Layer Deposition of Emerging 2D Semiconductors, HfS₂ and ZrS₂, for Optoelectronics. *Chem Mater*, 31(15):5713-5724.
 30. Chae, S.H., Jin, Y. and Kim, T.S., 2016. Oxidation effect in octahedral hafnium disulfide thin film. *ACS Nano.*, 10 (1):1309-1316.
 31. Mleczko, M.J., Zhang, C., and Lee, H.R. 2017. HfSe₂ and ZrSe₂: Two-dimensional semiconductors with native high-κ oxides. *Sci Adv.*, 3(8), pp.1126-1135.
 32. Kanazawa, T., Amemiya, T. and Ishikawa, A., 2016. Few-layer HfS₂ transistors. *Sci Rep.*, 6 pp.1-9.
 33. Grayfer, E.D., Kozlova, M.N., Fedorov, V.E., 2017. Colloidal 2D nanosheets of MoS₂ and other transition metal dichalcogenides through liquid-phase exfoliation. *Adv Colloid Interface Sci.*, 245, pp. 40-61.
 34. Li, L., Lv, and Wang, R., 2019. Optical nonlinearity of ZrS₂ and applications in fiber laser. *Nanomaterials*, 9(3), pp.315.

35. Jana, M.K. and Rao, C.N.R., 2018. Transition Metal Dichalcogenides and Other Layered Materials. *2D Inorg Mater beyond Graphene*, pp.1-65.
36. Sherrell, P.C., Sharda, K. and Grotta, C., 2018. Thickness-Dependent Characterization of Chemically Exfoliated TiS₂ Nanosheets. *ACS Omega*, 3(8), pp.8855-8662.
37. Han, J.H., Kim, H.K. and Baek, B., 2018. Activation of basal plane in Transition Metal Chalcogenide Nanostructures. *J Am Chem Soc.*,140(42) 13663-13671.
38. Zhang, S.L., Jung, H., Huh, J.S., Yu, J.B. and Yang, W.C., 2014. Efficient exfoliation of MoS₂ with volatile solvents and their application for humidity sensor. *J Nanosci Nanotechnol*, 14 (11), pp.8518-8522.
39. Kaur, H., Yadav, S. and Srivastava, A.K., 2018. High-yield synthesis and liquid-exfoliation of two-dimensional belt-like hafnium disulphide. *Nano Res.*, 11(1), pp.343-353.
40. Zeng, Z., Yin, Z., and Huang, X., 2011. Single-Layer Semiconducting Nanosheets: High-Yield Preparation and Device Fabrication. *Angew Chemie Int Ed.*, 50(47), pp.11093-1109.
41. Zeng, Z., Sun, T., and Zhu, J., 2012. An effective method for the fabrication of few-layer-thick inorganic nanosheets. *Angew Chemie - Int Ed*, 51(36), pp. 9052-9056.
42. Jeong, S., Yoo, D., Ahn, M., Miro, P., Heine, T. and Cheon, J., 2015. Tandem intercalation strategy for single-layer nanosheets as an effective alternative to conventional exfoliation processes. *Nat Commun*, 6(1), pp.1-7.
43. Zhang, X., Lai, Z., Tan., C. and Zhang, H., 2016. Solution-Processed Two-Dimensional MoS₂ Nanosheets: Preparation, Hybridization, and Applications. *Angew Chemie Int Ed.*, 55(31), pp.8816-8838.
44. O'Brien, M., McEvoy, N., Hanlon, D., Hallam, T., Coleman, J.N. and Duesberg, G.S. 2016. Mapping of Low-Frequency Raman Modes in CVD-Grown Transition Metal Dichalcogenides: Layer Number, Stacking Orientation and Resonant Effects. *Sci Reports*, 6(1), pp.1-11.
45. Xiong, Y., Chen, H.W., Zhang, D.W., and Zhou, P., 2019. Electronic and Optoelectronic Applications Based on ReS₂. *Phys status solidi – Rapid Res Lett*, 13

- (6), pp.1800-1810.
46. Liu, E., Fu, Y. and Wang, Y., 2015. Integrated digital inverters based on two-dimensional anisotropic ReS₂ field-effect transistors. *Nat Commun.*, 6(1), pp.1-7.
 47. Pawbake, A.S., Pawar, M.S. Jadhkar, S.R. and Late DJ., 2016. Large area chemical vapor deposition of monolayer transition metal dichalcogenides and their temperature dependent Raman spectroscopy studies. *Nanoscale*, 8(5), pp.3008-3018.
 48. Zhang, Z., Yang, P. and Hong, M., 2019. Recent progress in the controlled synthesis of 2D metallic transition metal dichalcogenides. *Nanotechnology*, 30, pp.182002.
 49. Zhu, Y., Wang, X., Zhang, M., Cai, C. and Xie, L., 2016. Thickness and temperature dependent electrical properties of ZrS₂ thin films directly grown on hexagonal boron nitride. *Nano Res.*, 9(10), pp.2931-2937.
 50. Wen, Y., Zhu, Y. and Zhang, S., 2015. Low temperature synthesis of ZrS₂ nanoflakes and their catalytic activity. *RSC Adv.* 5(81), pp. 66082-66085.
 51. Muhammad, Z., Mu, K. and Lv, H., 2018. Electron doping induced semiconductor to metal transitions in ZrSe₂ layers via copper atomic intercalation. *Nano Res.*, 11(9) pp. 4914-4922.
 52. You, J., Hossain, M.D. and Luo, Z., 2018. Synthesis of 2D transition metal dichalcogenides by chemical vapor deposition with controlled layer number and morphology. *Nano Converg.*, 5(1), pp. 2567-2573.
 53. Tenne, R., 2003. Advances in the synthesis of inorganic nanotubes and fullerene-like nanoparticles. *Angew Chem Int Ed Engl.*, 4(42), pp. 5124-5132.
 54. Zheng, B., Wang, Z. and Qi, F., 2018. CVD growth of large-area and high-quality HfS₂ nanoforest on diverse substrates. *Appl Surf Sci.*, 435, pp.563-567.
 55. Gao, Z., Ji, Q. and Shen, P.C., 2018. In Situ-Generated Volatile Precursor for CVD Growth of a Semimetallic 2D Dichalcogenide. *ACS Appl Mater Interfaces*, 10(40), pp.34401-34408.
 56. Parvaz, M., Ahmed, S., Khan, M.B., Rahul, A.S. and, Khan Z.H., 2018. Synthesis of TiS₂ nanodiscs for supercapacitor application. *AIP Conf Proc.* 2018;1953 (1), pp.8-13.

57. Parvaz, M., Khan, M.B., Azam, A., Khan, Z.H., 2019. Synthesis, characterization, and photocatalytic properties of CuO-TiS₂ nanocomposite. *Mater Res Express*, 6 (12), pp.125054.
58. Hu, Z., Tai, Z. and Liu, Q., 2019. Ultrathin 2D TiS₂ Nanosheets for High Capacity and Long-Life Sodium Ion Batteries. *Adv Energy Mater.* 9(8), pp.1803210.
59. Tan, C. and Zhang, H., 2015. Wet-chemical synthesis and applications of non-layerstructured two-dimensional nanomaterials. *Nature communication*, 6, pp.7873-7880.
60. Jeong, S., Yoo, D., Jang, J.T., Kim, M. and Cheon, J., 2012. Well-defined colloidal 2-D layered transition-metal chalcogenide nanocrystals via generalized synthetic protocols. *J Am Chem Soc*, 134(44), pp.18233-18236.
61. Mansouri, A. and Semagina, N., 2018. Colloidal Synthesis Protocol of Shape- and Dimensionally-Controlled Transition-Metal Chalcogenides and Their Hydrodesulfurization Activities. *ACS Appl Nano Mater.*, 1(9), pp.4408-4412.
62. Razgoniaeva, N., Yang, M., and Garrett, P., 2018. Just Add Ligands: Self-Sustained Size Focusing of Colloidal Semiconductor Nanocrystals. *Chem Mater*, 30 (4), pp.1391-1398.
63. Gqoba, S., Airo, M. and Ntholeng, N. 2015. Evolution of In₂S₃ Nanoplates with Time. *Mater Today Proc.* 2(7), pp.3901-3908.
64. Van Embden, J., Chesman, A.S.R. and Jasieniak J.J., 2015 .The heat-up synthesis of colloidal nanocrystals. *Chem Mater.*, 27(7). pp. 2246-2285.
65. Qiao, L., and Swihart, M.T., 2017. Solution-phase synthesis of transition metal oxide nanocrystals: Morphologies, formulae, and mechanisms. *Adv Colloid Interface Sci.*, 244, pp.199-266.
66. Mourdikoudis, S. and Liz-Marzán, L.M., 2013. Oleylamine in nanoparticle synthesis. *Chem Mater.* 25(9), pp.1465-1476.
67. Wang, Q, Lian J, and Li, J., 2015. Highly Efficient Photocatalytic Hydrogen Production of Flower-like Cadmium Sulfide Decorated by Histidine Open. *Nat Publ Gr.*,5, pp.13593-13600.

68. Prabakar, S., Bumby, C.W., and Tilley, R.D., (2009). Liquid-Phase Synthesis of Flower-like and Flake-like Titanium Disulfide Nanostructures. *Chem.matter*, 21 (8), pp.1725-1730.
69. Park, K.H, Choi, J, Kim, H.J, Oh, D.H, Ahn, J.R, Son, S.U., 2008. Unstable single-layered colloidal TiS₂ nanodisks. *Small*. 4(7), 945-950.
70. Yoo, D., Kim M, Jeong S, Han J., and Cheon J., 2014. Chemical Synthetic Strategy for Single-Layer Transition-Metal Chalcogenides. *J Am Chem Soc.*, 36(42), pp.14670-14673.
71. Jeong, S. Yoo, D., Jang, J., Kim, M. and Cheon, J., 2012. Well-Defined Colloidal 2-D Layered Transition-Metal Chalcogenide Nanocrystals via Generalized Synthetic Protocols Scheme 1. Schematic Illustration of 2-D Layered Nanomaterials a. *J Am Chem Soc.*, 13, pp.8233-18236.
72. Jang, J.T., Jeong, S., and Seo, J.W. 2011. Ultrathin zirconium disulfide nanodiscs. *J Am Chem Soc.*133(20), pp.7636-7639.
73. Miró, P., Han, J.H., Cheon, J. and Heine, T., 2014. Hexagonal Transition-Metal Chalcogenide Nanoflakes with Pronounced Lateral Quantum Confinement. *Angew Chemie Int Ed.*, 53 (46), pp 12624-12628.
74. Sekar, P., Greyson, E.C., and Barton, J.E., 2005. Odom TW. Synthesis of nanoscale NbSe₂ materials from molecular precursors. *J Am Chem Soc.* 2127(7), pp.2054-2055.
75. Mahler, B., Hoepfner, V., Liao, K. and Ozin, G.A., 2014. Colloidal Synthesis of 1T-WS₂ and 2H-WS₂ Nanosheets: Applications for Photocatalytic Hydrogen Evolution. *J Am Chem Soc.*, 136 (40), pp.14121-14127.
76. Geisenhoff, J.Q, Tamura, A.K., Schimpf, A.M. and Li, R., 2019. Chemcomm , Communication C. Using ligands to control reactivity, size and phase in the colloidal synthesis of WSe₂ nanocrystals †. *Chem Commun.*, 55 (60), pp.8856-8863.
77. Lin, H., Wang, C., Wu, J., Xu, Z., Huang, Y. and Zhang, C., 2015. Colloidal synthesis of MoS₂ quantum dots: Size-dependent tunable photoluminescence and bioimaging. *New J Chem.*, 39 (11) pp. 8492-8497.
78. Antunez, P.D, Webber, D.H, and Brutchey, R.L., 2013. Solution-phase synthesis of

- highly conductive tungsten diselenide nanosheets. *Chem Mater.*, 25 (12) pp.2385-2387.
79. Jung, W., Lee, S., and Yoo, D., 2015. Colloidal Synthesis of Single-Layer MSe₂ (M = Mo, W) Nanosheets via Anisotropic Solution-Phase Growth Approach. *J Am Chem Soc.*, 137(23), pp.7266-7269.
 80. Zhou, W. Yin, Z, and Du, Y., 2013. Synthesis of Few-Layer MoS₂ Nanosheet-Coated TiO₂ Nanobelt Heterostructures for Enhanced Photocatalytic Activities. *Small*, 9(1), pp.140-147.
 81. Rao, B.G., Mukherjee, D., and Reddy, B.M., 2017. Novel approaches for preparation of nanoparticles. In: *Nanostructures for Novel Therapy: Synthesis, Characterization and Applications*. Elsevier Inc., 1, pp.1-36.
 82. Chen, X. and Fan, R., 2001. Low-temperature hydrothermal synthesis of transition metal dichalcogenides. *Chem Mater.*,13(3) pp.802-805.
 83. Rajamathi, M. and Seshadri, R., 2016. Oxide and chalcogenide nanoparticles from hydrothermal/solvothermal reactions. *Curr Opin Solid State Mater Sci.*9, pp. 806.
 84. Zhao, J., Wang, S., Run, Z, Zhang, G., Du, W. and Pang, H., 2015. Hydrothermal Synthesis of Nickel Phosphate Nanorods for High-Performance Flexible Asymmetric All-Solid-State Supercapacitors. *Part Part Syst Charact*, 32(9), pp.880-885.
 85. Rahmanian, E., Malekfar, R. and Pumera, M., 2018. Nanohybrids of Two-Dimensional Transition-Metal Dichalcogenides and Titanium Dioxide for Photocatalytic Applications. *Chem - A Eur J.*,24(1), pp.18-31.
 86. Swain, G. Sultana, S., Moma, J. and Parida, K., 2018. Fabrication of Hierarchical Two-Dimensional MoS₂ Nanoflowers Decorated upon Cubic CaIn₂S₄ Microflowers: *Inorg Chem.*, 57(16) pp.10059-10071.
 87. Huang, K.J., Zhang, J.Z., Shi, G.W., and Liu, Y.M.,2014. Hydrothermal synthesis of molybdenum disulfide nanosheets as supercapacitors electrode material. *Electrochim Acta*, 132, pp.397-403.
 88. Wang, C., Lin, H., Xu, Z., Cheng, H. and Zhang, C., 2015. One-step hydrothermal synthesis of flowerlike MoS₂/CdS heterostructures for enhanced visible-light

- photocatalytic activities. *RSC Adv*, 5(20), pp.15621-15626.
89. Ramasubramanian, P.A., Thangavel, S., and Nallamuthu, G. 2018. A novel MoS₂ structures for electrochemical detection of 4-aminophenol. *J Mater Sci Mater Electron*, 29(7), pp.5696-5701.
 90. Jang, J.S., Kim., H.G., Joshi, U.A., Jang, J.W. and Lee, J.S., 2008. Fabrication of CdS nanowires decorated with TiO₂ nanoparticles for photocatalytic hydrogen production under visible light irradiation. *Int J Hydrogen Energy*, 33(21), pp.5975-5980.
 91. Rajput N., 2015. Methods of preparation of nanoparticles-a review. *IJAET*, 7 (5), pp.1806-1811.
 92. Therese, H.A., Li, J. Kolb, U. and Tremel, W., 2005. Facile large scale synthesis of WS₂ nanotubes from WO₃ nanorods prepared by a hydrothermal route. *Solid State Sci.*, 7(1), pp.67-72.
 93. Zheng, W., Lin, J. and Feng, W., 2016. Patterned Growth of P-Type MoS₂ Atomic Layers Using Sol-Gel as Precursor. *Adv Funct Mater.*, 26(35) pp.6371-6379.
 94. Nardi, M. V., Timpel, M. and Ligorio, G., 2018. Versatile and Scalable Strategy to Grow Sol-Gel Derived 2H-MoS₂ Thin Films with Superior Electronic Properties: A Memristive Case. *ACS Appl Mater Interfaces*, 10(40), pp. 34392-34400.
 95. Firmiano, E.G.S. Cordeiro, M.A.L. Rabelo, A.C., Dalmaschio, C.J., Pinheiro, A.N. and Pereira E.C., 2012 Graphene oxide as a highly selective substrate to synthesize a layered MoS₂ hybrid electrocatalyst. *Chem Commun.*, 48(62):7687-7689.
 96. Ramsha, K., Adeel, R., Sofia, J., Rahim, J., Muhammad, A.A. and Mohammad M., 2018. Synthesis and characterization of MoS₂/TiO₂ nanocomposites for enhanced photocatalytic degradation of methylene blue under sunlight irradiation. In: *Key Engineering Materials*, 778, pp.137-143.
 97. Thiagarajan, S., Sanmugam, A., and Vikraman, D., 2017. Facile Methodology of Sol-Gel Synthesis for Metal Oxide Nanostructures. In: *Recent Applications in Sol-Gel Synthesis*. InTech, (10), pp.68708-68713.
 98. Gqoba, S.S, Rodrigues, R., Mphahlele, S.L., Ndala, Z., Airo, M., Fadojutimi P.O. Hümmelgen, I.A., Liganiso, E.C., Moloto, M.J. and Moloto, N., (2021). Hierarchical

- nanoflowers of colloidal WS₂ and their potential gas sensing properties for room temperature detection of ammonia. *Processes*, 9(9), pp.1491-1495.
99. Kaur, N., Singh, M., Moumen, A, Duina ,G., and Comini, E. 2020. 1D titanium dioxide: Achievements in chemical sensing. *Materials*, 13(13), pp1-21.
 100. Drmosh, Q.A., Olanrewaju, A., Alade, I., Qamar, M., and Akbar, S., 2021. Zinc Oxide-Based Acetone Gas Sensors for Breath Analysis: A Review. *Chem - An Asian J.*,16 (12), pp.1519-1538.
 101. Loock, H.P., and Wentzell, P.D., 2012. Detection limits of chemical sensors: Applications and misapplications. *Sensors Actuators, B Chem.*,173, pp.157-163.
 102. Seal, S. and Shukla, S., 2002. Nanocrystalline SnO gas sensors in view of surface reactions and modifications. *Jom.*, 54(9), pp.35-38.
 103. Franke, M.E., Koplin, T.J., and Simon, U., 2006. reviews Metal and Metal Oxide Nanoparticles in Chemiresistors : Does the Nanoscale Matter? *Small*, 2(1):36-50.
 104. Yamazoe, N. and Shimano, K., 2009. Receptor Function and Response of Semiconductor Gas Sensor. *Hindawi sensor*, 2009, pp.10.875704.
 105. He, Q., Zeng, Z., and Yin, Z., 2012. Fabrication of flexible MoS₂ thin-film transistor arrays for practical gas-sensing applications. *Small*. 8(19), pp.2994-2999.
 106. Late, D.J., Huang, Y.K. and Liu, B., 2013. Sensing behavior of atomically thin-layered MoS₂ transistors. *ACS Nano.*, 7(6) pp.4879-4891.
 107. Cho, S.Y., Kim, S.J., and Lee, Y., 2015. Highly Enhanced Gas Adsorption Properties in Vertically Aligned MoS₂ Layers. *ACS Nano.*, 29(9), pp.9314-9321.
 108. Kim, Y.H., Kim, K.Y., and Choi, Y.R., 2016. Ultrasensitive reversible oxygen sensing by using liquid-exfoliated MoS₂ nanoparticles. *J Mater Chem A*. 4(16), pp.6070-6076.
 109. Qin, Z., Zeng, D. and Zhang J., 2017. Effect of layer number on recovery rate of WS₂ nanosheets for ammonia detection at room temperature. *Appl Surf Sci.*, 414, pp.244-250.
 110. Cha, J.H., Choi, S.J., Yu, S. and Kim, I.D., 2017. 2D WS₂-edge functionalized multi-channel carbon nanofibers: Effect of WS₂ edge-abundant structure on room

- temperature NO₂ sensing. *J Mater Chem A.*, 5(18), pp.8725-8732.
111. Late, D.J., Doneux, T. and Bougouma, M., 2014. Single-layer MoSe₂ based NH₃ gas sensor. *Appl Phys Lett.*,105(23): pp, 3-7.
 112. Guo, R., Han, Y., and Su, C., 2019. Ultrasensitive room temperature NO₂ sensors based on liquid phase exfoliated WSe₂ nanosheets. *Sensors Actuators, B Chem.* 300 (2), pp.127013-127019.
 113. Shi, W., Huo, L., Wang, H., Zhang, H., Yang, J. and Wei, P., 2006. Hydrothermal growth and gas sensing property of flower-shaped SnS₂ nanostructures. *Nanotechnology*, 17(12), 2918-2924.
 114. Xiong, Y., Xu, W. and Ding, D., 2018. Ultra-sensitive NH₃ sensor based on flower-shaped SnS₂ nanostructures with sub-ppm detection ability. *J Hazard Mater.*, 341, pp.159-167.
 115. Wang, H. and Xu, K. and Zeng, D., 2015. Room temperature sensing performance of graphene-like SnS₂ towards ammonia. *IEEE SENSORS - Proc.*, 2015, pp.5-8.
 116. Guidi, V., Fabbri, B., and Gaiardo, A., 2015. Metal Sulfides as a New Class of Sensing Materials. *Procedia Eng.*,120, pp.138-141.
 117. Zhu, Z., Kao, C.T., and Wu, R.J., 2014. A highly sensitive ethanol sensor based on Ag@TiO₂ nanoparticles at room temperature. *Appl Surf Sci.*,320, pp.348-355.
 118. Bajpai R., Motayed, A. and Davydov, A. V. 2012. UV-assisted alcohol sensing using SnO₂ functionalized GaN nanowire devices. *Sensors Actuators, B Chem.*,171(172), pp.499-507.
 119. Ayad, M.M., Salahuddin, N., and Minisy, I.M., 2014. Detection of some volatile organic compounds with chitosan-coated quartz crystal microbalance. *Des Monomers Polym.*,17(8), pp.795-802.
 120. Chen, D., Hou, X. and Wen, H. 2010. The enhanced alcohol-sensing response of ultrathin WO₃ nanoplates. *Nanotechnology*, 21(3), pp.035501.
 121. Wei, J., Li, X., and Han, Y., 2018. Highly improved ethanol gas-sensing performance of mesoporous nickel oxides nanowires with the stannum donor doping.

Nanotechnology, 29(24), pp.245501-245508.

123. Yan, H., Song, P., Zhang, S., Yang, Z., and Wang, Q., 2015. Dispersed SnO₂ nanoparticles on MoS₂ nanosheets for superior gas-sensing performances to ethanol. *RSC Adv*, 5(97), pp.79593-79599.
124. Zhang, D., Jiang, C., and Sun Y., 2017. Room-temperature high-performance ammonia gas sensor based on layer-by-layer self-assembled molybdenum disulfide/zinc oxide nanocomposite film. *J Alloys Compd.*, 698, pp. 476-483.
125. Zhao, P.X., Tang, Y., and Mao, J., 2016. One-Dimensional MoS₂-Decorated TiO₂ nanotube gas sensors for efficient alcohol sensing. *J Alloys Compd.*, 674:, 52-58.
126. Qin, Z., Ouyang, C., Zhang, J., 2017. 2D WS₂ nanosheets with TiO₂ quantum dots decoration for high-performance ammonia gas sensing at room temperature. *Sensors Actuators, B Chem.*, 253, pp.1034-1042.
127. Athawale, A.A. and Kulkarni, M.V., 2000. Polyaniline and its substituted derivatives as sensor for aliphatic alcohols. *Sensors Actuators, B Chem.*, 67(1): pp.173-177.
128. Jiang, S., Chen, J., Tang, J., Jin, E., Kong, L., Zhang, W. and Wang, C., 2009. Au nanoparticles-functionalized two-dimensional patterned conducting PANI nanobowl monolayer for gas sensor. *Sensors and Actuators B: Chemical*, 140(2), pp. 520-524
129. Tai, H., Xie, G., Yu, J., Ying, Z. and Chen, X., 2008. Comparative NH₃-sensing characteristics studies of PANI/TiO₂ nanocomposite thin films doped with different acids. *Sixth International conference in thin film Physics and applications*, 6384, pp. 556-570.
130. Manjunatha, S., Machappa, T. and Ravikiran, Y.T., 2019. Chethan B. and Sunilkumar A. Polyaniline based stable humidity sensor operable at room temperature. *Phys B Condens Matter.*, 561, pp.170-178.

CHAPTER 3: COLLOIDAL SYNTHESIS OF ZIRCONIUM DISULPHIDE AND ITS STABILITY AGAINST OXIDATION

Abstract

The need to exploit the exotic properties of ZrS₂ synthesized via colloidal means is imperative. For almost a decade now there has been no literature on the colloidal synthesis of ZrS₂ nanomaterials. Meanwhile, several publications are available on other methods of synthesis mostly chemical vapour transport (CVT) and chemical vapour deposition (CVD). The synthesized bulk material from the CVT method is further subjected to exfoliation (mechanical or liquid) to obtain mono or few-layers of ZrS₂. With the colloidal method, there is a possibility of the oxide being formed during the synthesis of ZrS₂ and likely destabilization of the nanomaterial after synthesis on exposure to ambient environment. In this study, both the heat up and hot injection methods were employed to fabricate various morphologies of ZrS₂ nanomaterials. The metal and sulphur precursors were dissolved in a mixture of octadecene (ODE) and oleic acid (OA); and refluxed at a temperature of 290 °C in the presence of nitrogen gas. ODE served the role of non-coordinating solvent, while OA served as the capping agent. Nanorods, nanospheres and nanosheets were obtained from the heat up method. Meanwhile, the hot injection approach produced nanosheets and nanospheres with well noticeable hollow centres. X-ray diffractometer (XRD) validated the formation of ZrS₂ hexagonal phase with traces of oxides of zirconium, ZrO₂ as well. The peak of S2p was conspicuously absent while the Zr3d peak was well noticeable in the XPS spectra. XPS and EDS measurements indicated replacement of sulphur atom by the O atom on the surface of the nanomaterials. Only one exciton peak was observed for the absorption spectra of both the heat up and hot injection method; and thermal thermogravimetry analysis (TGA) revealed three plateaux of decomposition of the nanomaterials.

Keywords: Zirconium disulphide, nanostructures, oxidation, structural properties, stability.

3.1 Introduction

Zirconium disulphide is a member of the group IVB transition metal dichalcogenides (TMDCs) with a layered structure of the cadmium iodide type (CdI_2). Adjacent layers are held together only by relatively weak van der Waals forces with an octahedral arrangement¹. ZrS_2 is a 2D layered material with fantabulous attributes when in mono or few layers; which include fast electron transport, high carrier mobility and sizeable band gap. The abundant nature of zirconium in the earth's crust could be well harnessed in materials science unlike rare earth metals which are not cost effective and very limited in nature. The ZrS_2 nanomaterial is highly sought after due to its application in solar cells, field effect transistors (FETs), thermoelectric devices, photodetectors, fiber lasers, optics, sensors, tribology, electrode materials and catalysis^{2,3}.

Till date, publications on colloidal synthesis of ZrS_2 are very limited except for publications by the Cheon Group^{4,5}. Proper investigations showed that traces of impurities (moisture, oxygen) prior to the synthesis of group IVB transition metal dichalcogenides will inevitably lead to the formation of oxides of the metal or mixed phases (TMDC and oxides of the metal). To eradicate any traces of impurities in this case becomes a herculean task^{2,6,7,8}. The metal precursor (ZrCl_4) that is preferably used has been reported to be very hygroscopic, thus the use of a glove box may be necessary. The organic solvents that are commonly used in colloidal synthesis are not totally free from impurities. Oleylamine (OLA) technical grade is about 70% purity, oleic acid 90% purity and octadecene (ODE) is 90% purity. The presence of impurities in OLA must have necessitated the Cheon group to degas and distil OLA for several hours prior to use. Colloidal synthesis of other 2D nanomaterials is much more available, the Moloto group have fabricated several 2D nanomaterials using the colloidal method of synthesis which includes InSe , In_2S_3 , AuSe , MoSe_2 and WS_2 among many others⁹⁻¹³. The colloidal method of synthesis has provided the Moloto group an avenue to fabricate hierarchical nanostructures in the form of nanoflowers of MoSe_2 , NbSe_2 and WS_2 by varying the reaction parameters.

Chemical vapour transport (CVT) has been the most common method used in the synthesis of this nanomaterial¹⁴⁻¹⁶. Exfoliation of the bulk ZrS_2 via (mechanical or liquid) has also been reported for the fabrication of mono or few-layered ZrS_2 . This nanomaterial is not stable at temperatures above 300 °C and is easily oxidizable in the presence of impurities such as air, moisture, oxygen and oxides of carbon. The thin film of ZrS_2 nanomaterials has also been synthesized using atomic layer deposition and spray pyrolysis^{2,17}. The reaction of zirconium

with sulphur can form a variety of sulphide phases such as ZrS, Zr₂S, ZrS₂, ZrS₃, Zr₂S₃, ZrS₄ and ZrOS depending on the reaction parameters ⁷.

Mattinen *et al*, gave a thorough insight on this in which ZrS₂ and HfS₂ films were synthesized by atomic layer deposition. It was observed that oxides of zirconium were being produced over the zirconium disulphide. The following oxidants identified could have been the source of the oxidation: (a) H₂O, O₂ and CO₂ (b) impurities in metal precursor or sulphur precursor and (c) adsorbed gases on the wall of the reactor. Until every source of impurities was eliminated, it was then that ZrS₂ film was fabricated by adopting the following measures: (a) metal precursor was stored in a glove box (b) a gas purifier was connected to the sulphur source and carrier gas and (c) pre-evacuation and pre-annealing of the reactor ². The formation of oxides is ascribed to the hydrolysis of ZrCl₄ resulting from absorption of moisture at ambient environment. When the metal precursor is subjected to heating at a temperature of about 270-300 °C, further hydrolysis occurs where oxychlorohydroxides are being formed as the intermediate product, which further decompose to produce zirconium oxide ⁶. It is very paramount to totally steer clear of any iota of humidity prior to the synthesis of ZrS₂; if not, ZrO₂ will be formed which is very stable and considered to be the thermodynamic end product in Zirconia chemistry.

Purity of a material is a sine qua non parameter to ascertain its true chemical composition, but this cannot be said of group IVB TMDCs. The nanomaterials are most often contaminated with oxides of the metal as well as the trisulphide of the metal ^{2,3,18}. However, this could be well harnessed in materials science as this could produce heterostructures of ZrS₂-ZrO₂ or ZrS₂-ZrS₃ or ZrS₂-ZrS₃-ZrO₂. Vapour phase methods of synthesis are the most preferred methods for producing ZrS₂ using CVT. In this method, single crystals (bulk) are produced which take about 5-6 days for the synthesis to be completed. This method is commonly deployed for the synthesis of group IVB TMDCs over wet methods due to the difficulty in producing group IVB TMDCs with high purity. Even with CVT or CVD there is a possibility of traces of trisulphide and/or oxide of the metal being formed. The optimum temperature for operating the reaction has been reported to be at about 800 °C ³. This study illustrates ligand controlled synthesis protocols using both the heat up and hot injection methods for the synthesis of ZrS₂ nanomaterials. We observed that the as-synthesized nanomaterials were not stable in ambient environment.

3.2 Experimental

3.2.1 Chemicals and materials

Zirconium tetrachloride [99%, $ZrCl_4$, Sigma-Aldrich], thiourea [99%, $CS(NH_2)_2$ Sigma-Aldrich], sulphur powder [99.9%, S, Sigma-Aldrich], thioacetamide [99%, Sigma-Aldrich], 1-octadecene [90%, ODE, Sigma-Aldrich], oleic acid [90%, OA, Sigma-Aldrich], toluene [99%, ACE associated chemical enterprises], oleylamine [70%, OLA, Sigma-Aldrich], 1-dodecanethiol [98%, 1-DDT, Sigma-Aldrich] oleylalcohol [90%, OYA, Sigma-Aldrich], octaclamine [99.9%, Sigma-Aldrich] and isopropyl alcohol [99%, MK Chemicals, IPA], were used as received without further purification.

3.2.2 Synthesis

3.2.2.1 Heat up method

In a typical synthesis, 0.163 g of $ZrCl_4$ and 0.105 g of thiourea were introduced into a three neck flask containing a mixture of 9 ml ODE and 4 ml OA that have been degassed for 20 min at 120 °C. Subsequently, the temperature was raised to 290 °C and maintained for 3h. Thereafter, the heating was stopped and the reaction flask was cooled to room temperature. The synthesized nanomaterials were washed with toluene via centrifugation to remove impurities and later washed with isopropanol multiple times and allowed to dry in open air. It is noteworthy to state that during synthesis there were no distinct colour changes as it is commonly observed in a typical colloidal synthesis. However, bubbling and foaming accompanied by intermittent squirting were noticed during the reaction. The resulting nanomaterials had a colour of light brown to yellowish. The reaction was also conducted in 9 ml of raw ODE only and a mixture of 9 ml of ODE and 0.5 ml of 1-DDT.

3.2.4 Hot injection method

The setup is the same as described for the heat up method. However, in the hot injection method the metal precursor is injected with the aid of a syringe at 290 °C into a mixture of 9 ml ODE, 0.75 ml OA and thiourea; and heating was maintained for 3 h before quenching. The final product was obtained by centrifugation and rinsed with toluene and isopropanol multiple times and allowed to dry in open air.

3.3 Material characterization

Powder X-ray diffraction (PXRD) analysis was performed using a Bruker D2 phaser (D2-205530) diffractometer with Cu K α 1 radiation ($\lambda = 1.54060 \text{ \AA}$) at 30 kV and 10 mA. Measurements were taken using a glancing angle of the incident detector at an angle of 2° over 2θ angle range of $5\text{--}90^\circ$ in steps of 0.026° with a step time of 5 s at ambient temperature. X-ray photoelectron spectroscopy (XPS) analysis was conducted using ESCALab 250Xi spectrometer model. Transmission electron microscopy (TEM) (Jeol JEM-2100F 200 kV) was used to analyze the morphology of the as-synthesized ZrS₂ nanomaterials. TEM samples were prepared by dissolving the nanomaterials in IPA, sonicated for 10 min, after which they were deposited on a copper grid and allowed to dry at room temperature before analysis. The surface morphology was studied by scanning electron microscopy (SEM) using a ZEISS GeminiSEM 560 instrument with sub 1 kV resolution below 1 nm. The infrared spectra of ZrS₂ were obtained using Fourier transform infrared (FTIR) spectroscopy on a PerkinElmer Spectrum 100 instrument. The thermal stability of ZrS₂ was monitored using a PerkinElmer 6000 thermogravimetric analyzer.

3.4. Results and Discussion

ODE as the only organic solvent looked very promising for the synthesis of ZrS₂. From **Figure 3.1a**, the (001), (101), (003), (111), (103), (200), (201), (004), (202), and (210) peaks were observed which match card no. 010605262 of hexagonal ZrS₂. The peak (001) at diffraction angle of 15.20° (2θ) is an indication of the formation of ZrS₂. Similarly, peaks of the oxide of zirconium were also observed which are indicated on the XRD diffraction pattern as asterisk. This corresponds to the findings in literature, pointing to the possibility of formation of ZrOx during the synthesis of ZrS₂^{2,6,7,8}. The metal precursor is very hygroscopic, it absorbs moisture during weighing at ambient environment and the impurities in the organic solvent may have probably contributed to the formation of ZrO₂. It is important to note that no nucleation occurs when oleic acid is used in excess of 4 ml as co-solvent with ODE. The mixture of 4 ml OA and 9 ml ODE was the optimized volume for the synthesis in this study. Different sulphur sources were experimented with such as sulphur powder, thioacetamide, thiourea and ethane-1,2-diol to determine which sulphur source is most appropriate for the colloidal synthesis of ZrS₂; this can be found in the **Figure S1**. In the same way, different capping agents such as OLA, 1-DDT, oleyl alcohol, octadecylamine (ODA), OA and ODE were solely used as solvent, reducing agent and ligand. Details can be found in the supplementary information. However, with raw 1-DDT,

amorphous peaks of ZrO_2 was formed). ODE, a non-coordinating solvent showed evidence of the synthesis of the ZrS_2 when thiourea was used as the source of sulphur, while with elemental sulphur, the reaction solution turned black within 15 minutes of the reaction, oxide of zirconium was formed, likewise with thioacetamide.

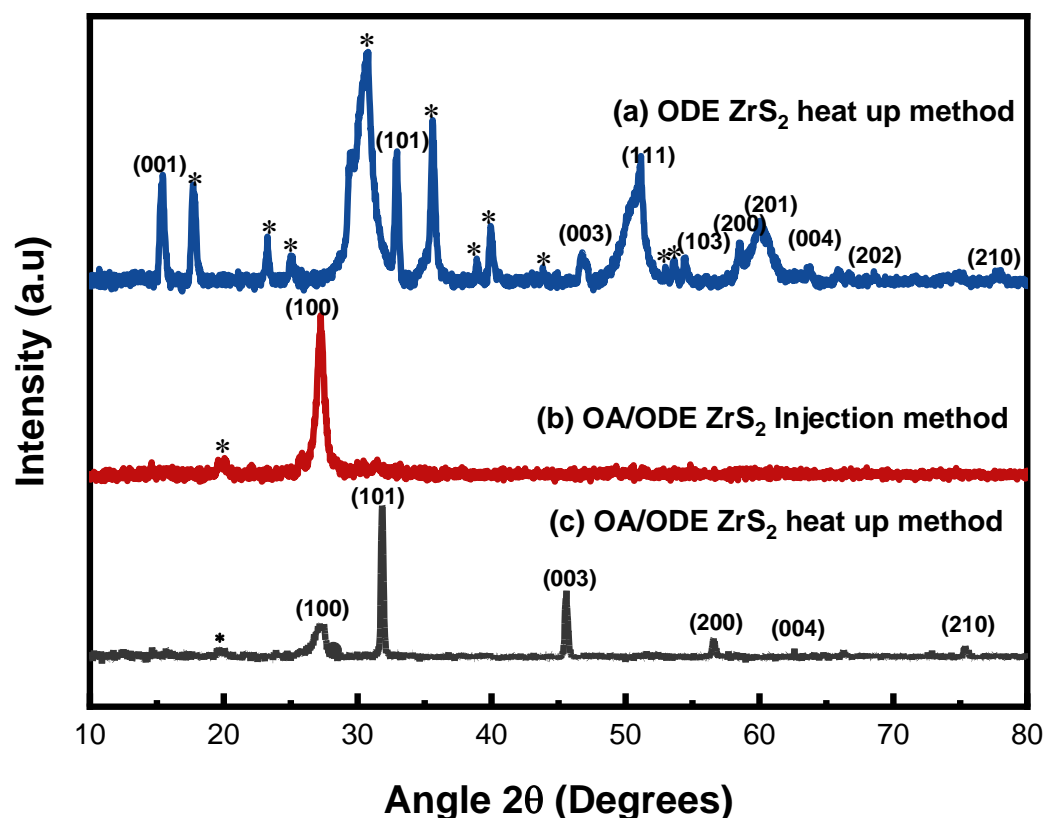


Figure 3.1: PXRD patterns of ZrS_2 synthesized via the heat up and injection methods.

Figure 3.1 (c) clearly shows the diffraction patterns of ZrS_2 obtained via the heat up method. The (100), (101), (003), (200) (004), and (210) peaks were observed and indexed to the card no of 010605262 of hexagonal ZrS_2 . While for the hot injection method as shown in **Figure 3.1b**, only one peak was noticed which is indexed to (100) peak. The (100) peak is very sharp and well elongated suggesting that the as-synthesized ZrS_2 is highly crystalline.

The nanocrystals obtained with the mixture of ODE and 1-DDT gave the following peaks from the PXRD diffractograms: (100), (002), (101), (003), (110), (111) and (200) which match the card no. 010605262 of hexagonal ZrS_2 . This can be found in the **Figure S4**. However, the

reproducibility of this method using ODE and 1-DDT proved very difficult unlike the mixture of ODE and OA. Synthesis of ZrS₂ using wet methods of synthesis seems not to be too favourable. Krishnakumar *et al*, synthesized ZrS₂ using the hydrothermal method. From the XRD results, the authors reported the formation of both phases of ZrS₂ and ZrO₂ with a very intense peak at about 30.14° (2 Θ). The peak at about 35.00° (2 Θ) also indicated the diffraction peak of zirconium oxide. Other diffraction peaks were also observed at 50.33°, 59.87° and 62.66° (2 Θ). It should be noted that both ZrS₂ and ZrO₂ have similar diffractograms at some points such as the peaks at about 30.00°, 50,33° and 62.66° (2 Θ). However, a very pronounced peak at about 30.14° suggested a peak of ZrO₂ but the authors attributed it to ZrS₂⁸. The Cheon group have reported on the use of OLA as well as 1-DDT for the synthesis of ZrS₂^{4,5}. In this study, no product was formed after several hours of reaction when OLA, OA, OYA and ODA were used individually as solvents for the synthesis.

The SEM micrographs of ZrS₂ nanomaterials are shown in the Figures 3.2 and 3.3 revealed significant differences in the morphology produced by the two different methods deployed. With the heat up method, nanorods and nanospheres of ZrS₂ nanomaterials were formed. Meanwhile, with the hot injection method arrays of morphologies were formed such as nanospheres, hollow nanospheres and hollow nanospheres with a beeswax-like pattern which resembles nano-hexagons with facets on the edges, as seen in **Figure 3.3**.

Figures 3.2a, 3.2b, 3.2c and 3.2d show great striking resemblance in which nanospheres and nanorods are the main morphologies formed with the heat up method. Concurrently, with hot injection, the morphologies in **Figures 3.3a, 3.3b and 3.3c** are quite similar in which the hollow hexagonal morphology is beeswax-like, while **Figure 3.3d** shows a whole sphere, a broken sphere and hollow hemisphere morphologies.

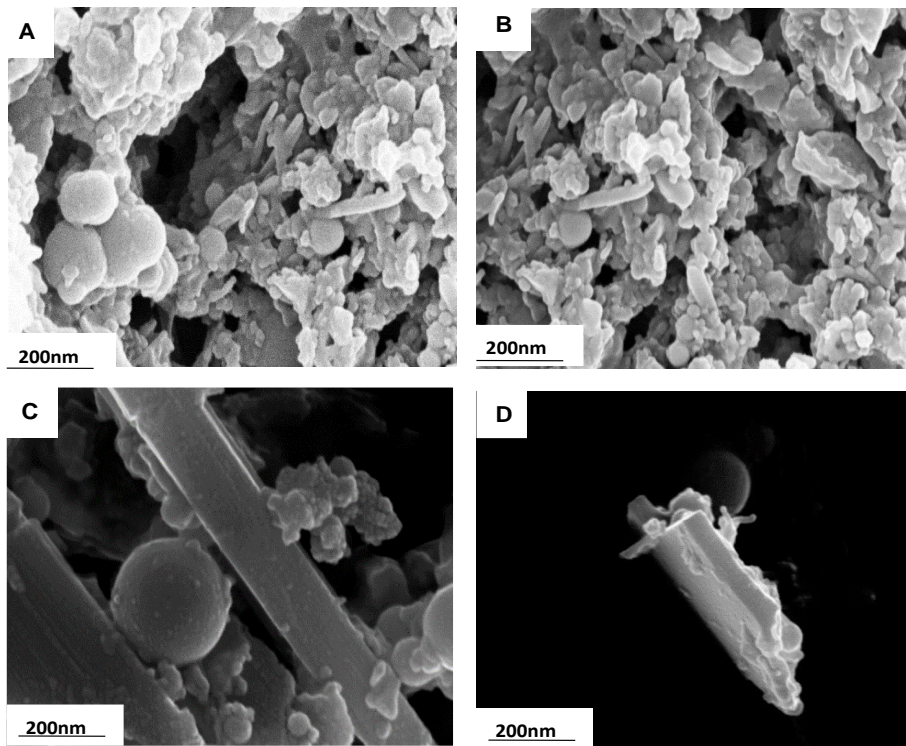


Figure 3.2: SEM micrographs of ZrS_2 nanomaterials synthesized by the heat up method.

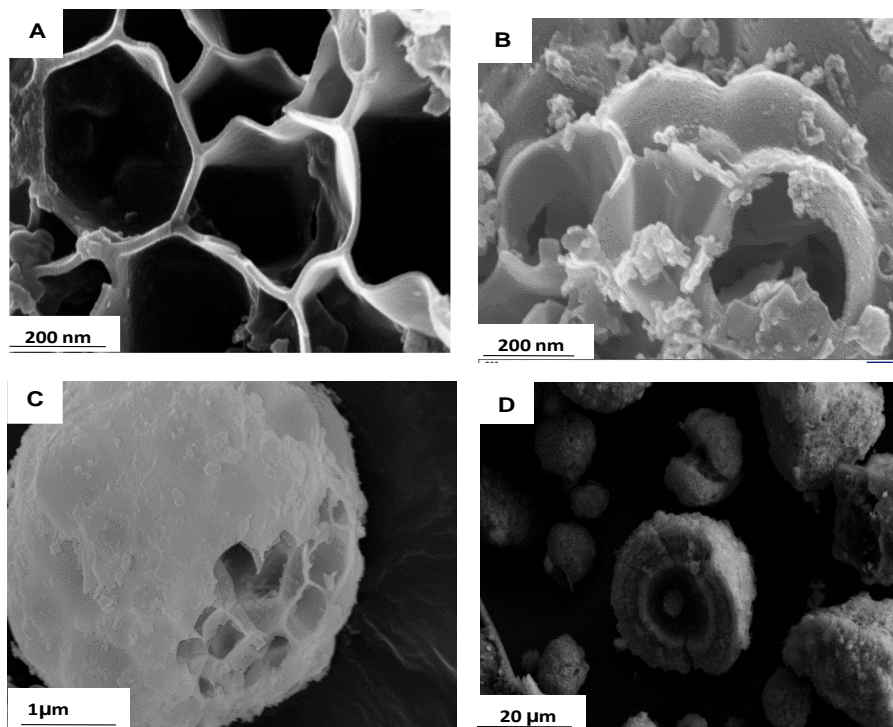


Figure 3.3: SEM micrographs of ZrS_2 nanomaterials synthesized by the hot injection method.

Figures 3.4 and 3.5 represent TEM images of ZrS₂ nanomaterials. Patterns of morphologies ranging from nanosheets, nanorods and nanospheres which exist in few layers are observed with the heat up method as already seen from the SEM micrographs.

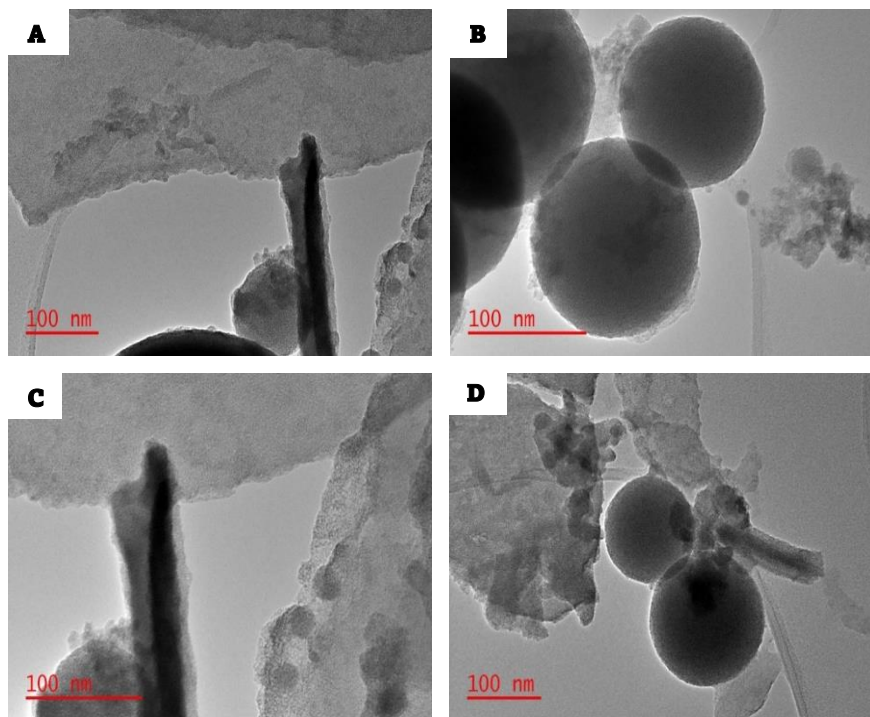


Figure 3.4: TEM images of ZrS₂ synthesized by the heat up method.

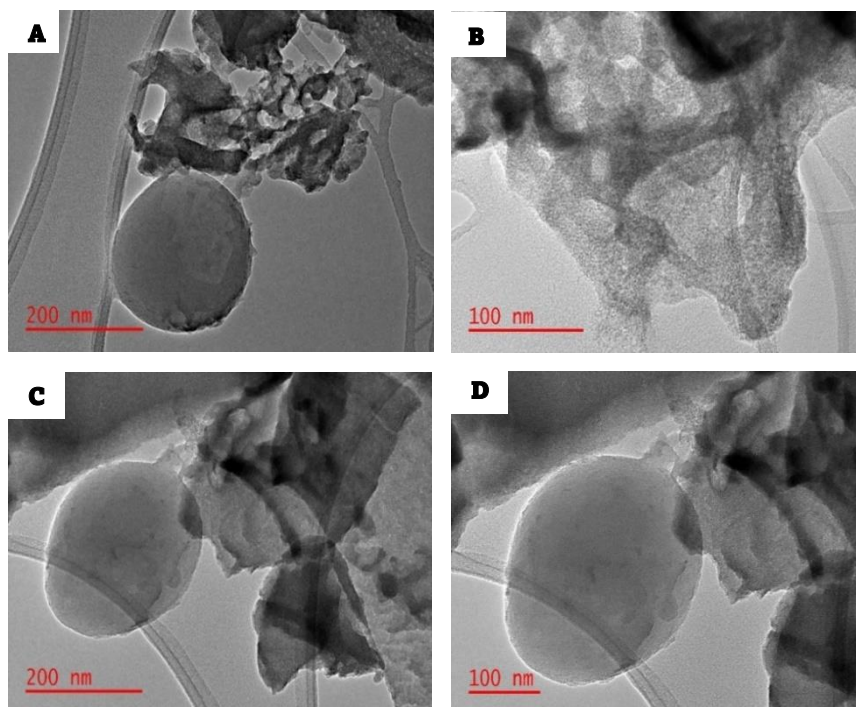


Figure 3.5: TEM images of ZrS₂ synthesized by the hot injection method.

Arrays of morphologies ranging from nanosheets with bees-wax morphology, nanospheres and hollow nanospheres are formed. The TEM results corroborate with the SEM results in which similar morphologies are observed in both analyses. However, TEM showed nanosheets morphology while SEM micrographs do not reveal the nanosheet morphology. The HRTEM can be found in **Figure S6 and S7**.

From **Figures 3.6a** and **3.7a**, only one absorption peak was observed at about 325 nm, this is similar to what Wen *et al.*, also observed in their report. ZrS₂ nanoflakes synthesized by CVD had two absorption peaks at about 245 nm and 280 nm³. Zhou *et al.*, also reported two absorption peaks at about 282 nm and 336 nm for quantum dot ZrS₂ obtained through solvent exfoliation of the bulk material via sonication¹⁹. From **Figures 3.6b** and **Figure 3.7b**, the band gaps of the nanomaterials were extrapolated to be 2.82 eV and 2.87 eV for heat up and hot injection methods respectively. This shows that the nanostructures of the ZrS₂ material were blue-shifted from the bulk material which has been reported to be at about 1.70 eV. The Tauc plot indicated the presence of a direct band gap in the synthesized nanostructure of ZrS₂. The values obtained are in good harmony with literature³.

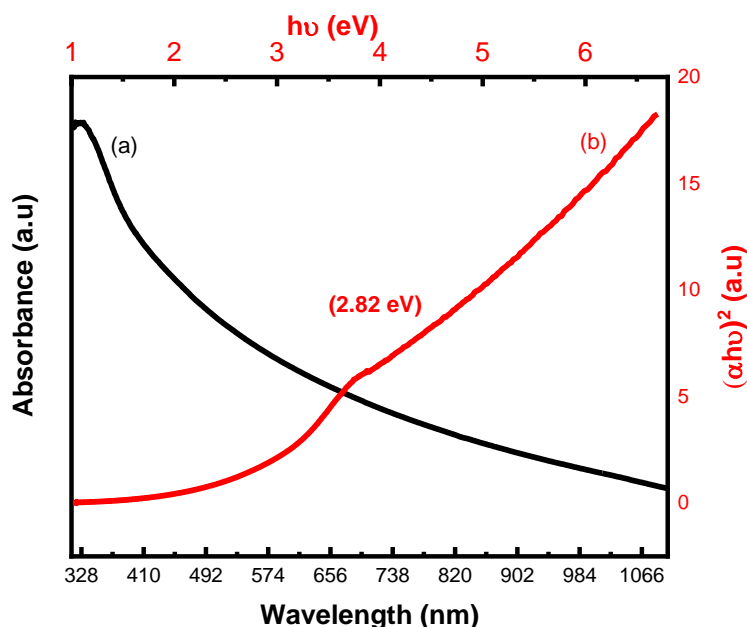


Figure 3.6: (a) UV-Vis spectrum and (b) band gap of as-synthesized ZrS₂ by the heat up method.

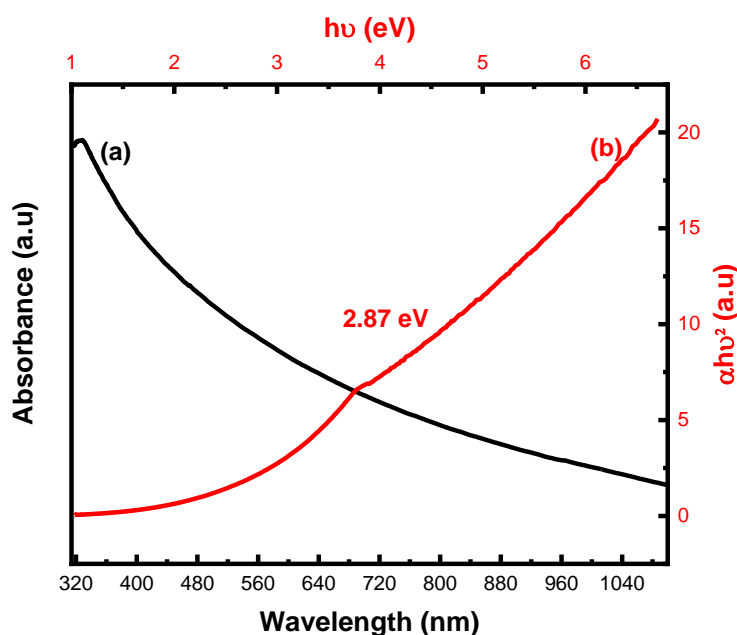


Figure 3.7: (a) UV-Vis spectrum and (b) band gap of as-synthesized ZrS₂ by the injection method.

In **Figure 3.8a**, the spectrum of pristine oleic acid, the symmetric and asymmetric CH₂ stretching is located at about 2854 and 2923 cm⁻¹ respectively. The asymmetric C=O bond has the highest intensity at 1714 cm⁻¹ and C-O stretching at about 1285 cm⁻¹. From the spectra in Figures 8a and 8b, similar stretching vibration peaks could be observed for the pure OA and as-synthesized nanomaterial except for wide chemical shift that were noticed. The C=O stretching vibration which is a feature of OA was observed at 1714 cm⁻¹ for the raw OA, however the vanishing of this peak on the nanomaterials has been reported by other authors as an indication of strong binding that exist between the ligand and the nanomaterials^{11, 20}. Two extra bands were observed at about 1599 and 1526 cm⁻¹, this could be attributed to asymmetric and symmetric COO⁻ stretching. This is attributed to complexation that existed between the metal atoms and the carboxylic group of oleic acid²¹. The FTIR of the as-synthesized ZrS₂ using mixture of ODE and 1-DDT can be found in supporting information (**Figure S8**).

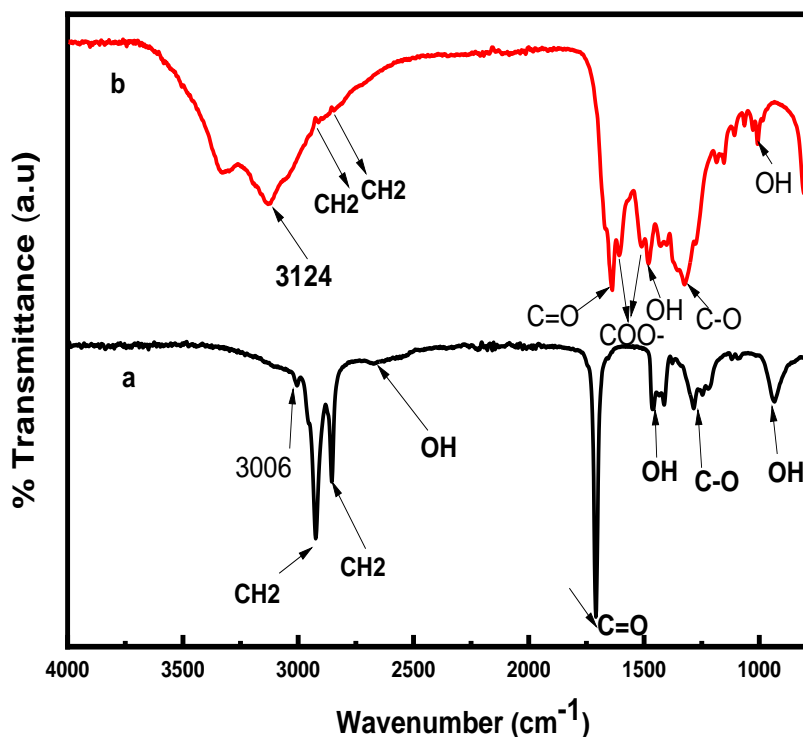


Figure 3.8: FTIR spectra of (a) raw OA and (b) as-synthesized ZrS₂ by the heat up method.

The thermogravimetric analysis of the ZrS₂ nanomaterials under N₂ showed three plateaus as depicted in Figure 3.9, about 5% loss was observed at the first plateau below 100 °C and a massive loss of about 40 % at about 270 °C and a further loss of weight was noticed at about 485 °C. The initial loss is ascribed to the decomposition of water adsorbed due to the oxophilicity nature of the nanomaterials. The second effect is attributed to the loss of sulphur which was easily released due to the weak van der Waals forces that existed within the layered nanomaterial and/or organic materials. The third effect is suggested to be the loss of S or O that is in plane covalently bonded to the Zr atom. The residue is Zr metal which is about 35%.

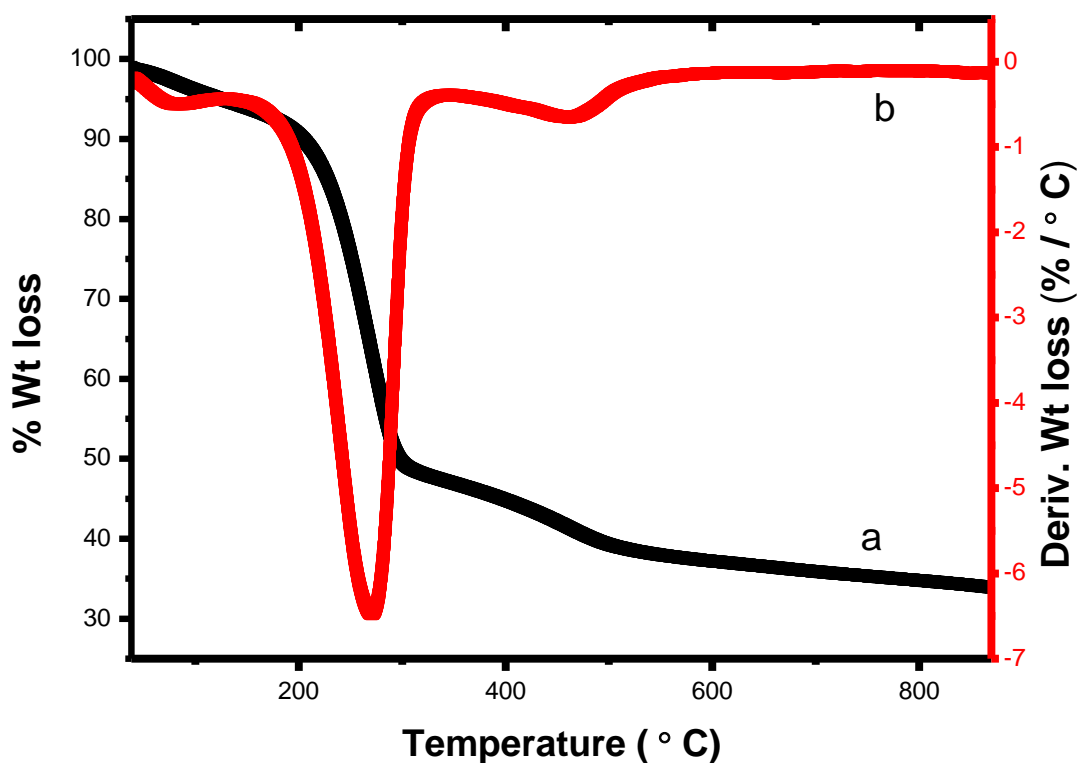


Figure 3.9: TGA and DTG thermograms of ZrS_2 synthesized by the heat up method.

Figure 3.10 shows the EDS of the as-synthesized nanomaterials obtained by the heat up method were not close to stoichiometry of pure ZrS_2 , the main impurity being oxygen and about 2% chlorine content was also detected. In **Figure 11b**, no traces of S were found in the as-synthesized ZrS_2 ; the S atom had been displaced by O atom. Marttinen *et al.*, provided an extensive report on surface oxidation of ZrS_2 film synthesized; it was reported that the surface of the film of ZrS_2 contained high levels of O_2 arising from the surface oxidation of the film ². The following materials are reported to be generally unstable, namely the group IVB TMDCs, TiS_2 , $TiSe_2$, ZrS_2 , $ZrSe_2$, HfS_2 , $HfSe_2$, black phosphorus and perovskites ¹⁸.

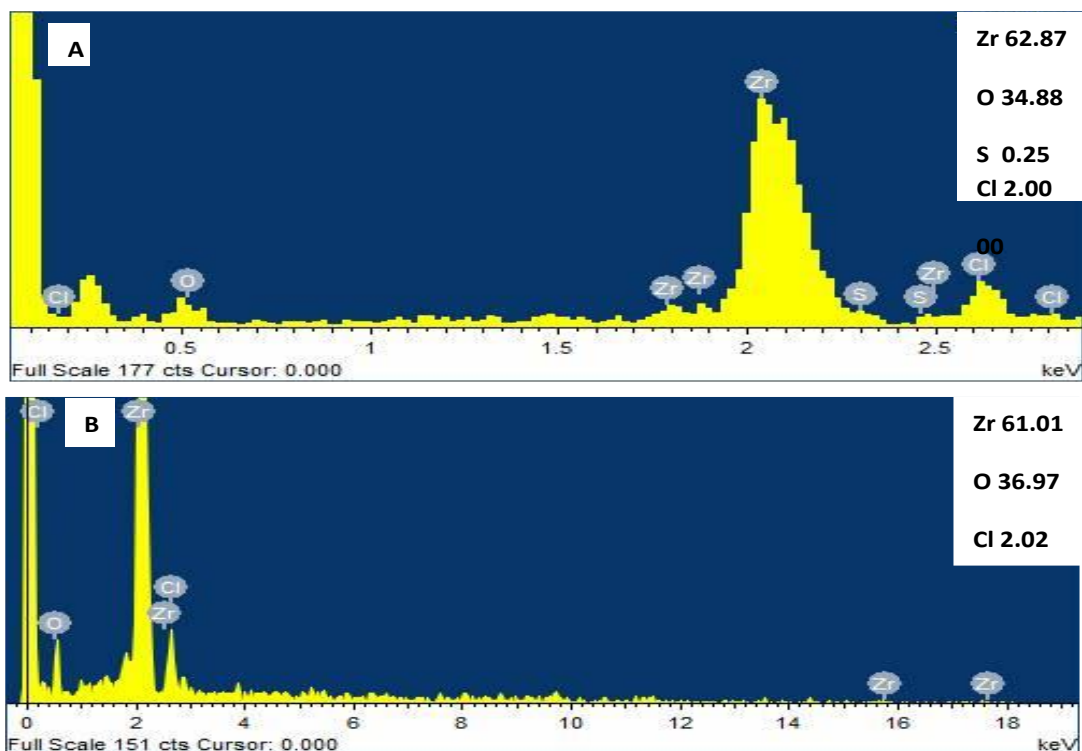


Figure 3.10: (a) and (b) EDS spectra of ZrS_2 synthesized by the heat up method.

The disparity in energy between ZrS_2 and ZrO_2 has been reported to be minimal²³, the $\text{Zr}3d$ orbital is associated with both ZrS_2 and ZrO_2 . The peaks at 184.8 eV and 182.4 eV corresponding to $\text{Zr}3d_{3/2}$ and $\text{Zr}3d_{5/2}$ respectively are expected for ZrO_2 while for ZrS_2 , $\text{Zr}3d_{3/2}$ and $\text{Zr}3d_{5/2}$ should be located at about 183.2 eV and 180.9 eV²¹. The $\text{O}1s$ spectrum in Figure 3.11 clearly indicated a significant amount of impurities attributed to the total displacement of the S atom by the oxygen atom. For ZrS_2 , $\text{S}2p_{3/2}$ and $\text{S}2p_{1/2}$ peaks are expected at about 163 eV and 162 eV respectively^{14,23}, rather it was peak of $\text{Zr}3d_{5/2}$ and $\text{O}1s$ at 182.3 eV, 530.3 eV respectively that were observed. This is in accordance with literature for ZrO_2 , $\text{Zr}3d_{5/2}$ and $\text{O}1s$ peaks are observed for ZrO_2 at about 182.3 eV, 530.3 eV respectively²⁴. As expected, long exposure of ZrS_2 to air normally leads to surface oxidation of ZrS_2 . Zemignani *et al* also observed $\text{O}1s$ peak of ZrO_2 from the XPS spectrum, this was attributed to surface oxidation of the material due to oxiphilicity nature of ZrS_2 . ZrS_2 is reportedly only very stable when in bulk but not in few layers²³. To the best of our knowledge, XPS of ZrS_2 synthesized by colloidal method has not been reported as to compare the result of the XPS with another work conducted by colloidal method. The $\text{O}1s$ consists of three parts, the metal oxide peak at 330.3 eV, C-O and C=O at 531.9 eV and 533.1 eV respectively. The surface oxidation of TMDCs have been

reported by many authors, the other oxygen peaks can be ascribed to the oxidation of the ligand used for the synthesis. A similar finding has been reported in our group^{11,13}. The C1s peak also has 3 peaks at 284.6 eV, 286.3 eV and 288.1 eV which are ascribed to C-C, C-O and O-C=O respectively. The highest peak is C-C bonds from the alkyl group of OA, the C-O and O-C=O are as a result of the oxidation of the ligand. This is also an indication as well that the material is being capped by the capping agent as the C1s had the highest composition of the sample which is about 53.3% of the sample analysed. The N1s also corroborates the capping of the material as the binding energy was obtained at 399.3 eV.

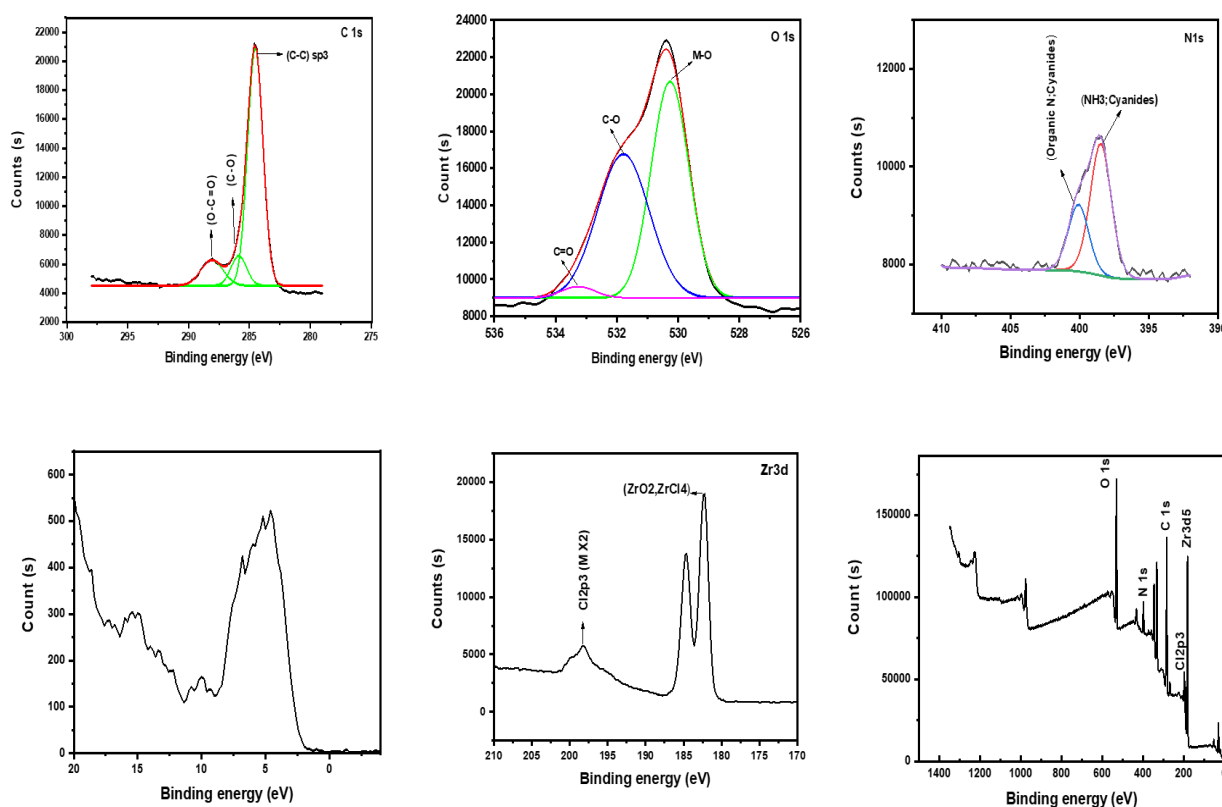


Figure 3.11: High resolution spectra with focus on core levels C1s, O1s, N1s, valence, Zr3d and XPS survey spectrum of ZrS₂ synthesized by heat up method.

Within few days of storage in ambient environment, elevated oxidation was observed with EDS spectra showing sulphur levels being less than 1%. The stability study was conducted with XRD time dependent study as shown in **Figure 12**. The several peaks observed for the heat up method disappeared within 5 days on exposure to ambient environment except for the (100) peak. After 20 days of exposure, the (100) peak disappeared too, while for the hot injection the

(100) peak was not detected after 5 days of exposure to ambient environment. Park *et al.*, also made similar observations when monolayer TiS_2 destabilized at room temperature after few days of synthesis ²⁵. Similar observation was made with the as-synthesized ZrS_2 ; the nanomaterials were not stable at ambient environment. Sherrell *et al* extensively studied the oxidation of TiS_2 nanosheets produced via exfoliation means using following techniques potential (ZP), UV-Vis spectroscopy and PXRD measurements. The surface charge of TiS_2 exfoliated in water was (-40 mV) which was higher than the surface charge of both nanosheets of MoS_2 and WS_2 exfoliated in water. The disparity in electronegativity between S (2.58) and Ti (1.54) in TiS_2 is greater compared to WS_2 and MoS_2 , resulting in a stronger partial negative charge on the S atoms. The UV-Vis spectrum of freshly exfoliated TiS_2 exhibited two main absorption peaks at 294 nm, 600 nm and a minor peak at 369 nm. After 5 days of exposure to ambient environment, a decrease in intensity of the absorbance at 600 nm was noticed, at the same time there was a blue shift of the 294 nm peak close to 266 nm. This peak shift is accounted to the oxidation of TiS_2 to TiO_2 . XRD analysis also confirmed the oxidation of TiS_2 nanosheets with a lateral size of 20 nm. The (002) and (003) peaks disappeared and a substantial reduction in intensity of the (001) peak was observed over 5 days ²⁶.

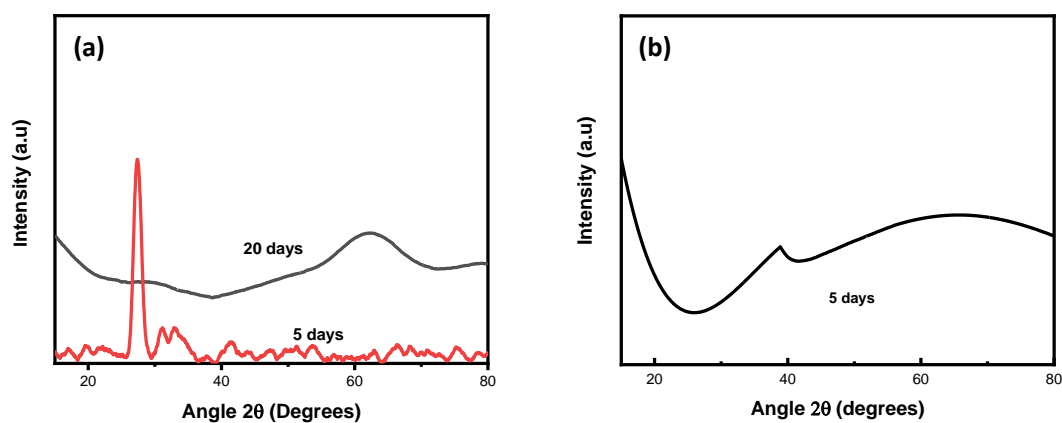


Figure 3.12 : Time-dependent study of ZrS_2 nanomaterials with XRD (a) ZrS_2 synthesized by the heat up method and (b) synthesized by the hot injection method.

3.5 Conclusion

In conclusion, ZrS₂ nanomaterials with various morphologies obtained via both heat up and hot injection methods were prepared for the first time using octadecene and oleic acid. The different morphologies obtained with both methods prove that one can use a certain type of synthesis to easily direct the morphology by manipulating the reaction parameters. XRD showed both phases of ZrS₂ and ZrO₂ were formed with peaks of zirconium disulphide dominating. The stability study conducted using time-dependent XRD studies showed that the nanomaterials are unstable even at room temperature. Further analysis by XPS confirmed the instability of ZrS₂ nanomaterials as the S atom had been completely replaced by the O atom.

3.6 References

1. Ho, C.H., Yen, P.C., Huang, Y.S., and Tiong, K.K., 2002. Photoreflectance study of the excitonic transitions of rhenium disulphide layer compounds. *Phys Rev B - Condens Matter Mater Phys.*, 66(24),pp.1-5.
2. Mattinen, M., Popov, G. and Vehkamäki, M., 2019. Atomic Layer Deposition of Emerging 2D Semiconductors, HfS₂ and ZrS₂, for Optoelectronics. *Chem Mater.* 31(15), pp. 5713-5724.
3. Wen, Y., Zhu, Y. and Zhang, S., 2015. Low temperature synthesis of ZrS₂ nanoflakes and their catalytic activity. *RSC Adv.*, 5(81), pp.66082-66085.
4. Jang, J.T., Jeong, S., Seo, J.W., 2011. Ultrathin zirconium disulfide nanodiscs. *J Am Chem Soc.*, 133(20), pp.7636-7639.
5. Yoo, D., Kim, M., Jeong, S., Han, J. and Cheon, J., 2014., Chemical synthetic strategy for single-layer transition-metal chalcogenides. *J Am Chem Soc.*, 136 (42), pp.14670-14673.
6. Fang, Z. and Dixon, D.A., 2013. Hydrolysis of ZrCl₄ and HfCl₄: The initial steps in the high-temperature oxidation of metal chlorides to produce ZrO₂ and HfO₂. *J Phys Chem C.*,117(15), pp.7459-7474.
7. Kaminskii, B.T., Prokof'eva G.N., Plygunov, A.S, and Galitskii, P.A., 1973. Manufacture of zirconium and hafnium sulfide powders. *Sov Powder Metall Met Ceram.*, 12(7), pp.521-524.

8. Krishnakumar, B., Imae, T., Miras, J. and Esquena, J., 2014. Synthesis and azo dye photodegradation activity of ZrS₂-ZnO nano-composites. *Sep Purif Technol.*, 132, pp. 281-288.
9. Airo, M.A., Rodrigues, R., Gqoba, S., 2016. Colloidal InSe nanostructures: Effect of morphology on their chemical sensitivity to methanol and formaldehyde fumes. *Sensors Actuators, B Chem.*, 236, pp.116-125.
10. Gqoba, S., Airo, M., Ntholeng, N., Machogo, L.F.E., Moloto, M.J., Sithole, R., Wyk, J-V., and Moloto, N., 2015. Evolution of In₂S₃ with time. *Materials Today: Proceedings.*, (2), 3901-3908.
11. Machogo, L.F.E., Sithole, R.K., Phao, N, et al., 2021. Probing the structure and functionalized surface of colloidal AuSe. *Mater Sci Eng B Solid-State Mater Adv Technol.*, pp.114878.
12. Ndala, Z., Shumbula, N., Nkabinde, S, Kolokoto, T., Nchoe, O, Shumbula, P., Tetana, Z.N., Langaniso, E.C., Gqoba, S.S., and Moloto, N., 2020. Evaluating the effect of varying the metal precursor in the colloidal synthesis of mose₂ nanomaterials and their application as electrodes in the hydrogen evolution reaction. *Nanomaterials*, 10 (9), pp.1-14.
13. Gqoba, S.S., Rodrigues, R., Mphahlele, S.L. Ndala, Z.,Airo, M. Fadojutimi P.O. Hümmelgen, I.A. , Langaniso, E.C.Moloto, M.J. and Moloto, N., 2021. Hierarchical nanoflowers of colloidal WS₂ and their potential gas sensing properties for room temperature detection of ammonia. *Processes*, 9(9), pp.1491.
14. Shimazu, Y., Fujisawa, Y., Arai, K., Iwabuchi, T. and Suzuki K., 2018. Synthesis and Characterization of Zirconium Disulfide Single Crystals and Thin-Film Transistors Based on Multilayer Zirconium Disulfide Flakes. *ChemNanoMat.*, 4(10), pp.1078-1082.
15. Tenne, R., 2003. Advances in the Synthesis of Inorganic Nanotubes and Fullerene-Like Nanoparticles. *Angew Chemie Int Ed*, 42(42), pp.5124-5132.
16. Kanazawa, T., Amemiya, T., Upadhyaya, V., Ishikawa, A., Tsuruta, K., Tanaka, T. and Miyamoto, Y., 2017. Performance Improvement of HfS₂ Transistors by Atomic Layer Deposition of HfO₂. *IEEE Trans Nanotechnol.*, 16 (4), pp.582.

17. Thiagarajan, R., M. Mahaboob, B. and M. Anusuya., 2017. Nano structural characteristics of zirconium sulphide thin films. *Journal of Americal Science*, 16(4), pp.582-587.
18. Chae, S.H. Jin, Y., Kim, T.S, Chung, D.S., Na, H., Nam, H., Kim, H., Perello, D.J., Jeong, H.Y., Ly, T.H. and Lee, Y.H., 2016. Oxidation effect in octahedral hafnium disulfide thin film. *ACS Nano*.10(1), pp.1309-1316.
19. Zhou, L.L, Wu, H.B., Li, X.M., Tang, L., Bin, Guo ,W. and Liang J., 2019 ZrS₂ quantum dots: Preparation, structure, and optical properties. *Wuli Xuebao/Acta Phys Sin.*, 68(14), pp 75-80.
20. Burnham, P. Dollahon, N., Li, C.H., Viescas, AJ, and Papaefthymiou, G.C. 2013. Magnetization and Specific Absorption Rate Studies of Ball-Milled Iron Oxide Nanoparticles for Biomedicine. *J Nanoparticles*, 2013, pp.1-13.
21. Ibarra, J., Melendres, J., Almada, M., Burboa, M.G., Taboada, P., Juarez, J. and Valdez, M.A., 2015. Synthesis and characterization of magnetite/PLGA/chitosan nanoparticles. *Mater Res Express.*,2(9), pp 95010-95017.
22. Zhang, M., Zhu, Y., Wang, X., Feng, Q., Qiao, S., Wen, W., Chen, Y., Cui, M. and Zhang, J., 2015. Controlled Synthesis of ZrS₂ Monolayer and Few Layers on Hexagonal Boron Nitride. *J Am Chem Soc.*, 137 (22), pp.7051-7054.
23. Zemignani, G.Z., Och, M. and Casari, C.S., 2019. Chemical vapour deposition of zirconium disulphide thin films (Unpublished master dissertation). (Politecnico di milano)
24. Liu, J. Liao, M., Imura, M., Tanaka, A., Iwai, H. and Koide, Y., 2014. Low on-resistance diamond field effect transistor with high-k ZrO₂ as dielectric. *Sci Rep*. 4, pp.2-6.
25. Park, K.H. Choi, J., Kim, H.J, Oh, D., Ahn, J.R. and Son, S.U., 2008. Unstable Single-Layered Colloidal TiS₂ Nanodisks. *Small*. 4(7), pp. 945-950.
26. Sherrell, P.C., Sharda ,K., Grotta, C., Ranalli, J., Sokolikova, M.S., Pesci, F.M., Palcynski, P., Bemmer, V.L. and Mattev, C., 2018. Thickness-Dependent Characterization of Chemically Exfoliated TiS₂ Nanosheets. *ACS Omega*, 3(8), pp.

8655-8662.

CHAPTER 4: SYNTHESIS OF RADIALY ALIGNED NANORUTILE AND ITS APPLICATION FOR CHEMICAL SENSING OF ALCOHOLS AND ACETONE

4.1 Introduction

Titanium dioxide, being a versatile material has found applications in photocatalysis, solar cells, filters, medicine, optical wave guides, opacifier, isolator, switches, pigment and photovoltaics^{1,2,3}. TiO₂ is also employed in gas sensing due to its fantabulous physical and chemical properties, cheap production, and availability. Several strategies have been employed to improve the sensing capability of TiO₂ by fabricating it with various patterns. The need for cheap, miniature, adequate and dynamic sensing devices has led to the development of TiO₂ nanostructures among which one-dimensional (1D) nanostructures TiO₂-based chemical sensors have been demonstrated in the last decade as very effective means in gas/chemical sensing. This have found applications in environmental monitoring and health care purpose to meet the present industrial and technological development. Non-functionalized 1D TiO₂ based gas sensors have been effectively utilized for the detection of the following vapours : acetone, carbon (iv) oxide, formaldehyde, isopropanol, hydrogen, oxygen, and methane⁴. Fabrication of materials in various patterns such as thin films and nanostructures has helped to improve the sensing capability of metal oxides. The wide gap of metal oxides (MOXs) like TiO₂ coupled with outstanding electrical properties have afforded them opportunities in the fabrication of transparent electronic devices. SnO₂ with various nanostructure morphologies is the most researched material in chemical/gas sensing. Meanwhile, 1D nanostructures such as nanowires, nanofibers, nanobelts, nanotubes are the most investigated materials in chemical/gas sensing due to the following attributes: (i) fast electron transport (ii) large surface area (iii) firm absorption ability and (iv) plethora active sites. Considerable research is needed to be deployed into three-dimensional (3D) morphology such as flower-like, urchin-like, etc for chemical sensing. This morphology provides distinctive attributes as a result of the properties afforded by the micrometre and nanometre building blocks within the crystal. Considering the dandelion morphology, the radial nanorods provide a high aspect ratio with large surface area and an ordered mesoporous structure. The tips of the rods give a curved surface; at the same time, the cylindrical nature of the nanorods gives a curvature. The large surface area and porous structures makes them a preferred choice over P 25 the commercial titania in photocatalytic reactions. This provides more active sites for adsorption to take place which could make them find application in chemical sensing.⁵ The rutile phase is most thermodynamically stable among the allotropes of titania⁶.

This morphology can be fabricated using methods such as hydrothermal, solvothermal, sol gel, Kirkendall effect, reversed micelle and chemical vapour deposition method.⁷ Among these methods, the hydrothermal method seems to be the easiest for the production of nanorutile titania with architectural 3D patterns due to facile approach of synthesis and is very economical. This reaction is very exothermic; hence the use of an ice/cold water bath is needed. The metal precursor is introduced drop wise in a flask containing distilled water already immersed in an ice/cold water. The resulting solution is then refluxed at a temperature ranging from 150 -200 °C for several hours to 24 h. The TiO₂ formed is then subjected to multiple washing using hot distilled water via centrifugation to eradicate unwanted recalcitrant Cl⁻. The process involves many stages (i) nucleation and precipitation of nanoparticles (ii) the formation of immature nano rods (iii) continuous growth of the nanorods and (iv) The nanorods aggregate to produce dandelions resembling a flower-like TiO₂.

In 2015 Baloyi synthesized dandelion like TiO₂ using the hydrothermal method; the average diameter of each nanorod was about 17 nm. The author reported on a pilot scale, the industrial method of fabricating rutile dandelion-like TiO₂ in which a large volume of the metal precursor was used (60 ml) and the reaction was conducted at 100 °C and the reflux was conducted for 24 h. Several publications are available on this synthesis, only Baloyi *et al* reported on the synthesis at a lower temperature.⁷ In our group, only nanorods were formed at this temperature. In a related experiment, Dziike *et al* synthesized RANR using the hydrothermal method; the radii was about 1.2-1.6 µm with an average width of 9 nm at 200 °C for 24 h and thereafter dried in an oven⁶. In a similar report, Barrett *et al* produced RANR using the hydrothermal method by conducting the reaction at 160 °C for 16 h⁵.

Musavi and Mohammed synthesized RANR using a mixture of TiCl₄, HCl, NaCl and distilled water was transferred into autoclave and reaction conducted at 180 °C for a short period of 4 h⁸. The white precipitate formed was washed multiple times with deionized water and ethanol. The use of salt in this reaction is to regulate the pH of the reaction. In a related experiment, Bai *et al* also used hydrothermal method to synthesize RANR by using TiCl₃ precursor instead of commonly used TiCl₄ precursor. Mixture of TiCl₃, HCl, NaCl and NaOH were introduced into autoclave reactor and reaction conducted at 190 °C for 2h. The resulting solution was washed several times with ethanol. The time of the reaction was short and NaOH was added to the reaction to regulate the pH of the solution⁹. Yi *et al* similarly fabricated titania with a dandelion morphology using the hydrothermal method. RANR was fabricated on SnO₂ as a template; a mixture of SnO₂, toluene, titanium (iv) butoxide and hydrochloric acid were introduced into

autoclave and reaction lasted for 4h at 180 °C. The resulting solution was washed multiple times with ethanol and dried in air. This method is not that economical since so many chemicals are needed for the synthesis of titania ¹⁰.

The operating temperature is an important feature that determines the gas-sensing attributes of a metal oxide. The morphology, surface structure of RANR were studied at room temperature for sensing the vapours of methanol, ethanol, isopropanol, and acetone. TiO₂ is an n-type chemiresistive sensor. The conductance increases on exposure to a reducing gas and recovers upon exposure to dry air. There is change in conductance upon increase in vapour concentration ¹¹.

Few reports are presently available on TiO₂ based sensor for sensing VOCs at room temperature, most of the research conducted were performed above room temperature. Adjustment of metal oxide by doping with precious metals, metals, forming hybrid with 2d materials like graphene, transition metal dichalcogenides and conducting polymers, as well as boosting with ultraviolet light (UV) are the means developed over the years to make metal oxide sense at room temperature ¹¹. It is very appealing to scientists to fabricate chemiresistive sensors at low temperature preferably at room temperature. This has the following advantages: (i) it saves energy (ii) long span of the sensor (iii) it allows for easy upgrade of the device and (iv) it prevents explosion ¹². Perillo and his group demonstrated TiO₂ nanotubes in sensing ethanol, ammonia, toluene and chloroform at room temperature with rapid sensitivity ^{13,14,15}.

4.2 Materials and methods

4.2.1 Chemicals

Titanium tetrachloride (TiCl₄) (99 %) was obtained from Sigma Aldrich and was used without further purification. Interdigitated electrodes (IDE's) of electroless nickel immersion gold (ENIG) (18 pairs), length of 7.9 nm and 0.1 nm wide apart.

4.2.2 Synthesis of radially aligned nanorutile (RANR)

The fabrication of nanorutile was accomplished using the hydrothermal technique. About 12 ml of TiCl₄ was introduced in drops into a round bottom flask containing about 160 ml of distilled water submerged in an ice bath with vigorous stirring. Subsequently about 100 ml of distilled water was added to the slurry and the reaction was refluxed for 24 h at 190 °C with constant stirring. The white powder formed was centrifuged and rinsed several times with hot

distilled water to eradicate recalcitrant Cl⁻. The product was dried at room temperature for one day. The schematic illustration of the synthesis is shown in **Figure 4.1** below.

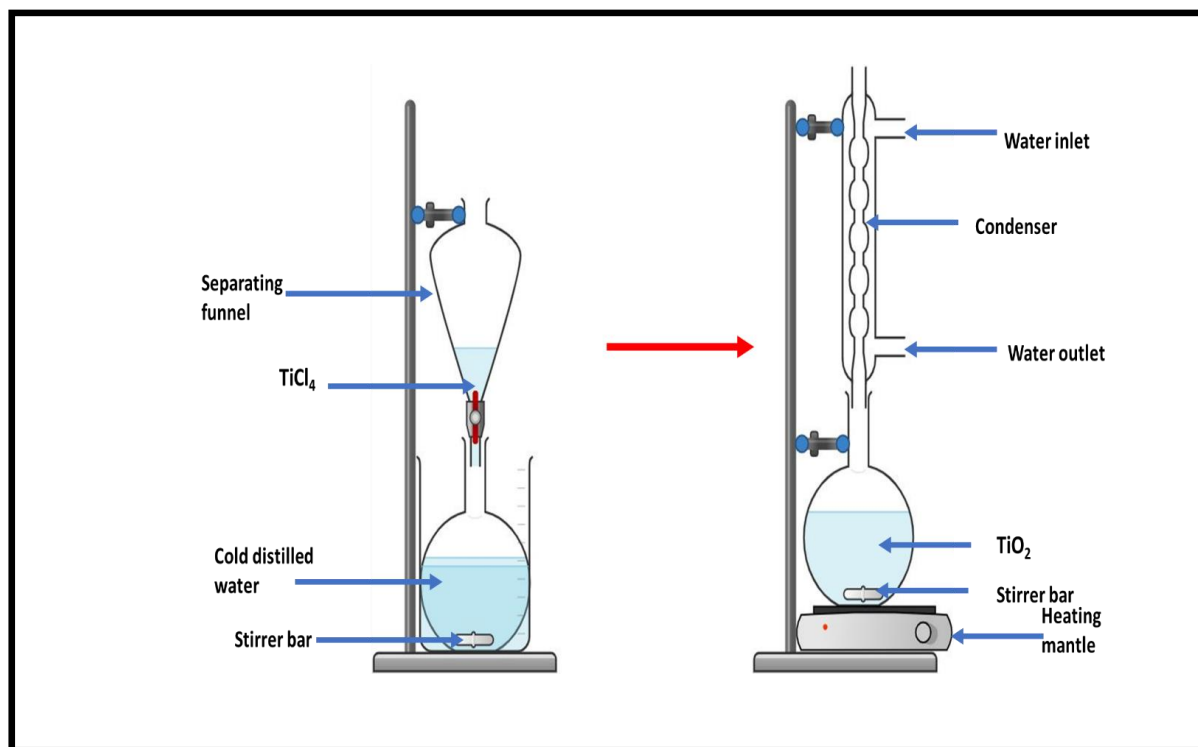


Figure 4.1: Schematic diagram depicting the synthesis of RANR.

4.2.3 Sensor fabrication

The TiO₂ based sensor was prepared on a printed circuit board (PCB) FR4 substrate. Interdigitated electrodes were patterned on the rectangular shape PCB consisting of electroless nickel immersion gold electrodes of 18 pairs with length of 7.9 mm and a space of 0.1 mm between each electrode. The sensing film was prepared by drop casting 20 μL of the film that was prepared by sonicating for 10 mins 3 mg of TiO₂ in 500 μL of methanol.

4.2.4 Gas sensing measurement

All electrical measurements were conducted at about 25 °C. An LCR-6300, 10Hz – 300 KHz precision LCR meter coupled with a computer. The frequency and voltage were set at 10 KHz and 1.00 V respectively. The system was allowed to stand for a few minutes before any measurements were done. **Figure 4.2** shows the set-up of the gas sensing experiment. The vapour sensing experiment was conducted at room temperature and the response values were recorded using a data logger (LCR). The vapour sensing properties were explored by injecting a measured volume of anhydrous alcohol (methanol) into a closed glass chamber (5 L) via a

glass syringe. The concentration of the methanol vapour in the test chamber can be evaluated in ppm by using the following equation:

$$C = \frac{224\rho TV_s}{273MV} \times 100 \quad (3.0)$$

Where C represents the concentration of methanol vapour (ppm), ρ is the density of the solvent (gML^{-1}), T is the temperature in Kelvin, Vs is the volume of the solvent, and M is the molecular weight of the solvent. The response of the sensor is obtained as $S = (R_a - R_g)/R_a \times 100$, where R_a and R_g represented resistance in air and methanol vapour respectively. The time required by a sensor to complete 90% of the resistance change is known as response/recovery time. The TiO_2 sensor was exposed to methanol vapour at various concentrations. To ensure the vapour reaches saturation point upon injection of the gas, the sensor was allowed to interact with the analyte gas for 300 s for proper adsorption and 200 s for the desorption of the vapour (recovery). The same procedure was conducted for ethanol, isopropanol, butanol, and acetone.

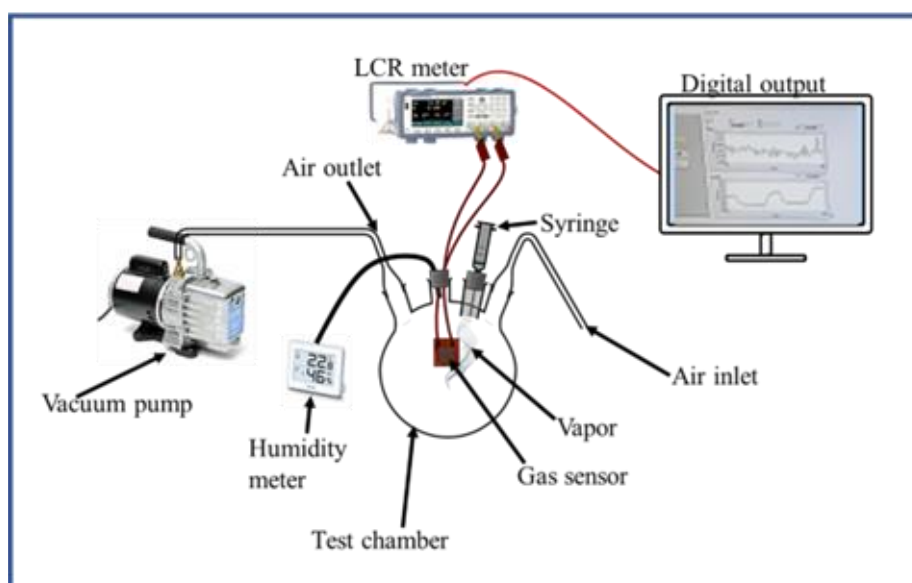


Figure 4.2: Gas sensing set up.

4.3 Characterization of RANR

Powder X-ray diffraction (PXRD) analysis was performed using a Bruker D2 phaser (D2-205530) diffractometer with $\text{Cu K}\alpha 1$ radiation ($\lambda = 1.54060 \text{ \AA}$) at 30 kV and 10 mA. Measurements were taken using a glancing angle of the incident detector at an angle of 2° over 2θ angle range of $5-90^\circ$ in steps of 0.026° with a step time of 5 s at ambient temperature. Transmission electron microscopy (TEM) (FEI Technai G2 Spirit 120 kV) was used to analyse

the morphology of the synthesized titania nanomaterials. TEM samples were prepared by dissolving the RANR in ethanol, sonicated for 10 min, after which they were deposited on a copper grid and allowed to dry at room temperature before analysis. The surface morphology was studied by scanning electron microscopy (SEM) using a ZEISS GeminiSEM 560 instrument with sub 1 kV resolution below. The thermal stability of as-synthesized RANR was monitored using a PerkinElmer 6000 thermogravimetric analyzer. The surface area and porosity were measured using Micromeritics RS232 and porosity analyzer instrument. The surface area measurements were performed via N₂ adsorption/desorption and calculated by the Brunauer Emmett and Teller (BET) analysis method. The diffuse reflectance (DR) UV–vis spectra were obtained in the range of 200–800 nm using a Cary 500 spectrophotometer equipped with a Praying Mantis diffuse reflectance accessory.

4.4 Results

4.4.1 PXRD OF RANR

The as-synthesized RANR exhibited diffractions at 27.5, 36, 39, 42, 43, 54, 56, 63, 64, 69 and 70° which correspond to the (110) (101) (200) (111) (210) (211) (220) (002) (310) (301) and (112) peaks respectively; and can be indexed to the tetragonal rutile phase (JCPDS No. 21-1276). No iota of impurity or phase of other allotropes of TiO₂ was noticed, this indicates the probity of the material. This is consistent with literature, only peaks of rutile are formed at temperature less than 200 °C, moreover at temperatures exceeding 200 °C the formation of anatase and rutile phases will be produced^{5,6}. The sharp peaks as shown in **Figure 2** show high crystallinity of the as-synthesized RANR.

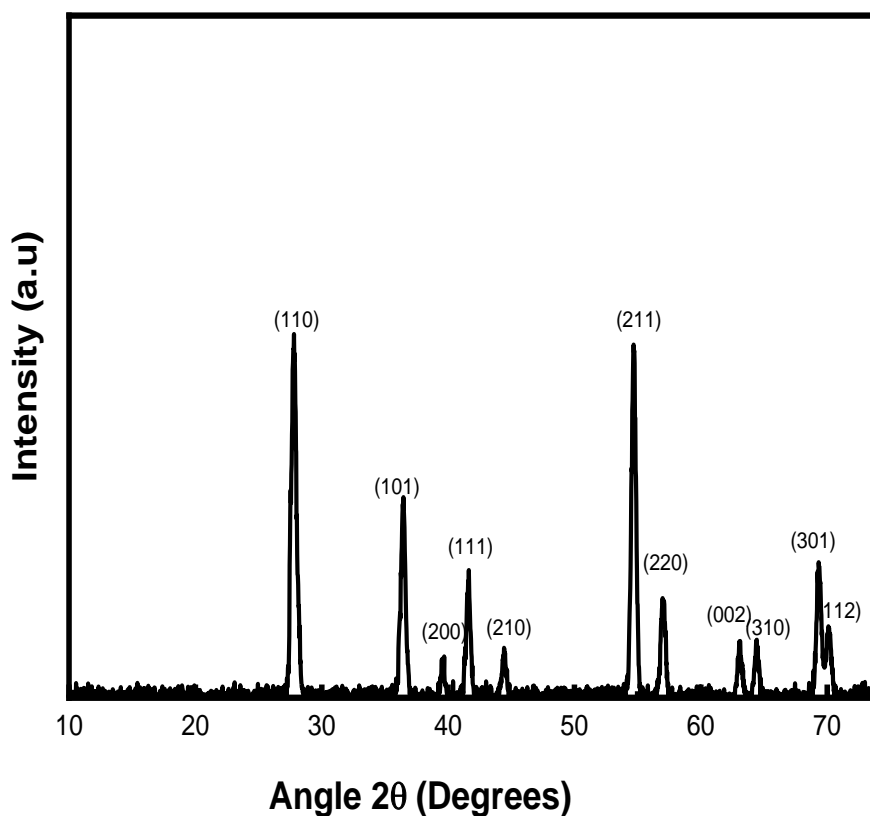


Figure 4.3: PXRD of radially aligned nanorutile.

4.4.2 SEM analysis

Figures 4.4a and **4.4b** show nanospheres of the as-synthesized RANR, the nanorods are properly bundled together to look like a flower/sphere. The uniform distribution of spherical-shaped dandelion can be seen from the micrographs, the nanorods were homogenously distributed to form densely packed spheres with various sizes of a 3D morphology.

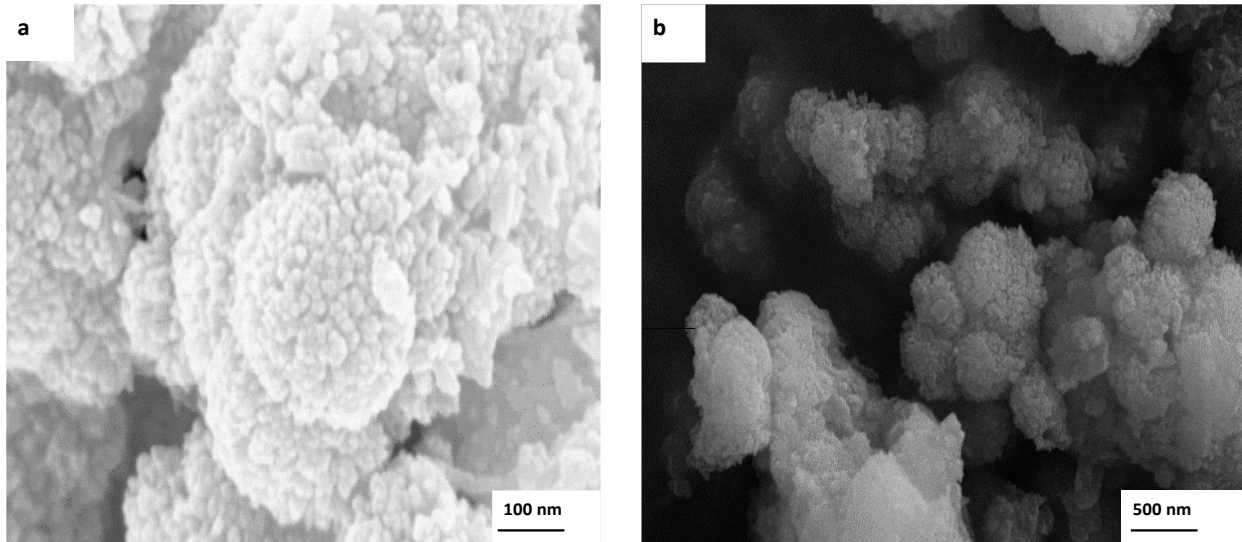


Figure 4.4: (a) and (b) show the SEM micrographs of the synthesized RANR.

4.4.3 TEM analysis

Figures 4.5a and **4.5b** show the dandelion morphology of the nanorutile. Several authors have unanimously reported that homogeneous nucleation of TiO_2 is the initial step in the formation of the flower-like pattern. The second step involves the formation of nanorods, this can be evidently seen in **Figure 4a**, and thirdly the nanorods self-assemble resulting into quarter and half-dandelions; this as well can be seen in **Figure 4.5a** and lastly the half-dandelions grow further to form well packed dandelion-like patterns. **Figure 4.6** illustrates the mechanism of the formation of the RANR. The average diameter distribution of the material was 575 ± 62 nm (**Figure 4.7**) measured by image J, and it ranges from 350 to 750 nm.

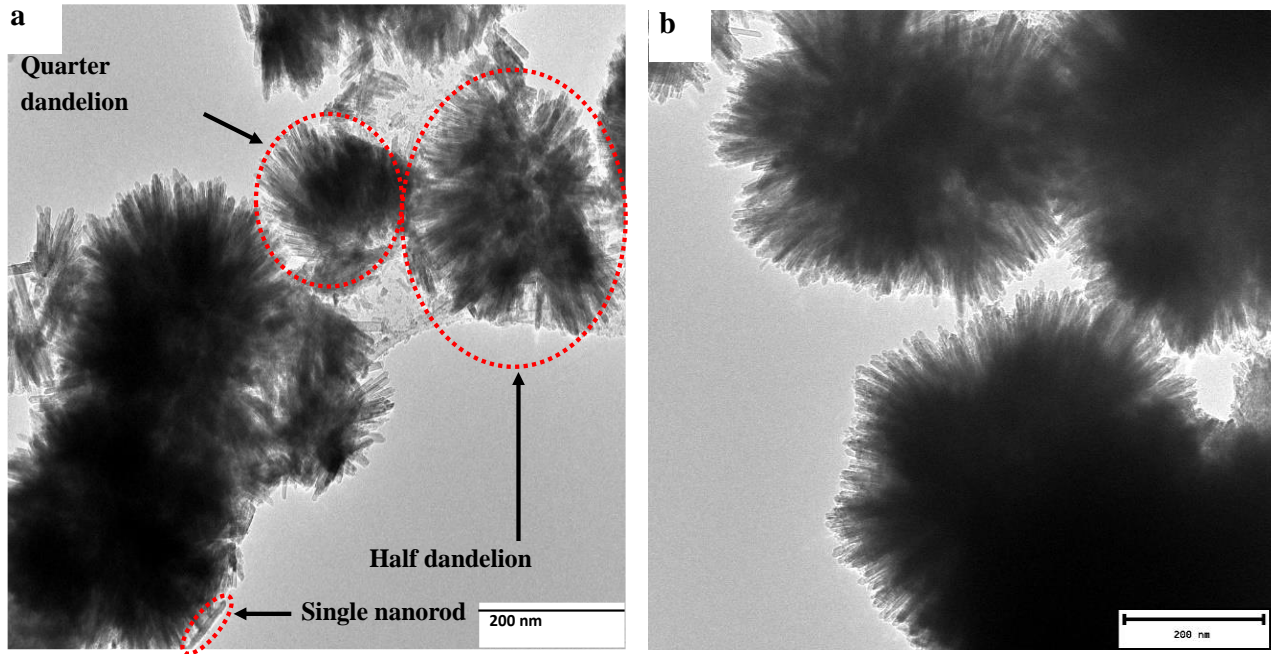


Figure 4.5: (a) and (b) TEM images of RANR.

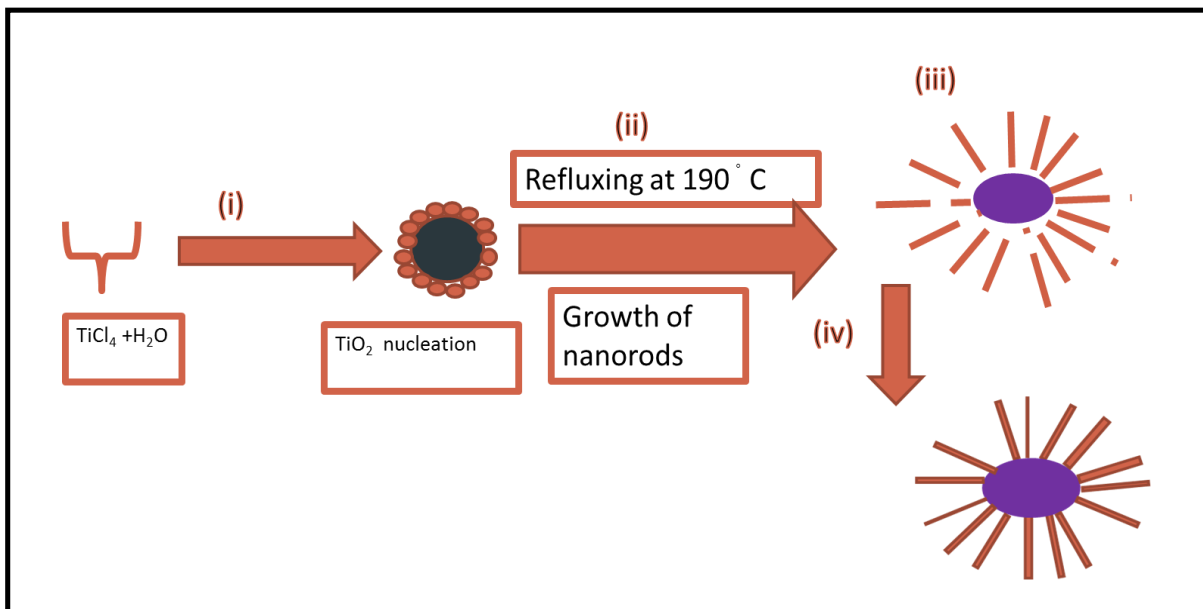


Figure 4.6: Mechanism of the synthesis of RANR adapted from Baloyi, *et al*⁷.

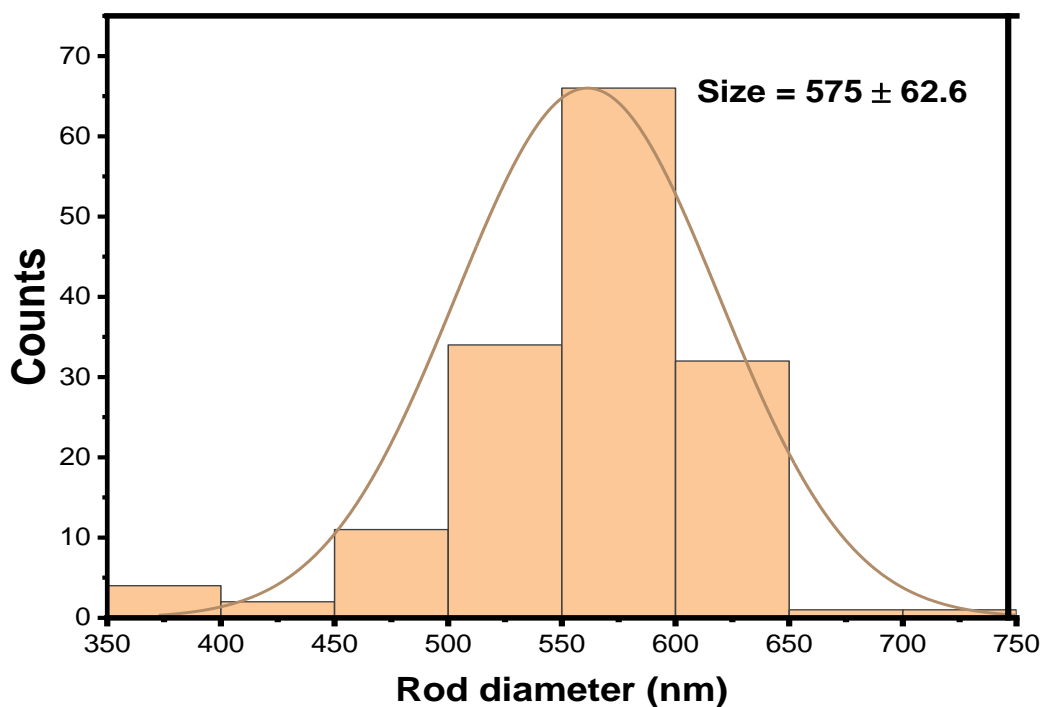


Figure 4.7: Particle size distribution of as-synthesized RANR.

4.4.4 UV-Vis spectra analysis

The solid-state UV-Vis DRS plot of RANR absorbance varies from 200-800 nm with a small and large absorption at about 350 and 417 nm respectively as shown in **Figure 4.8**. This is in concordance with many authors who also reported absorption below or at about 400 nm^{16,17}. The band gap of the material was extrapolated using the Tauc plot (**Figure 4.9**) to be 3.150 eV, similar values were also obtained by other authors^{6,16,17,18}.

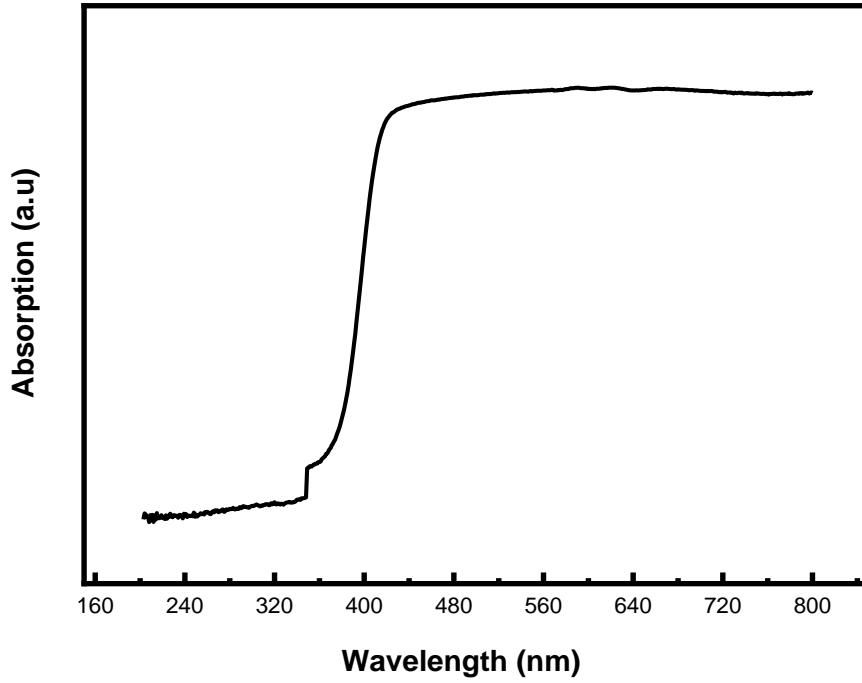


Figure 4.8: The solid-state UV-Vis DRS plot of RANR.

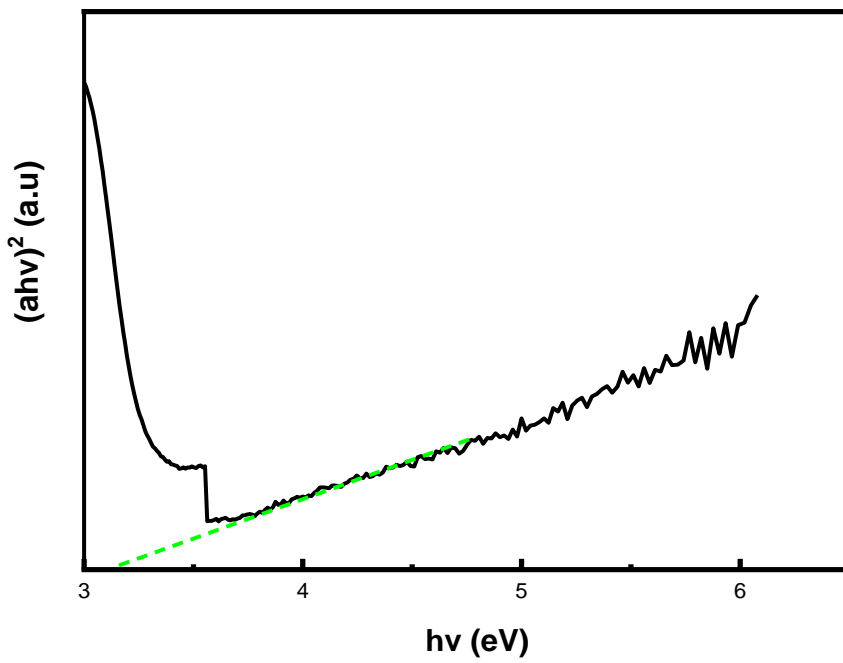


Figure 4.9: The band-gap energy (hv) of RANR.

4.4.5 Thermal analysis of RANR

From the thermogram in **Figure 4.10**, two plateaus can be observed: the first stage from 0-360 °C, there is sustained decomposition (mass loss) of about 7%. This can be attributed to loss of moisture from the material. The second stage from 360-500 °C, this loss is marginal at < 1 % loss. This is in concordance with the literature that rutile is very stable at elevated temperatures.

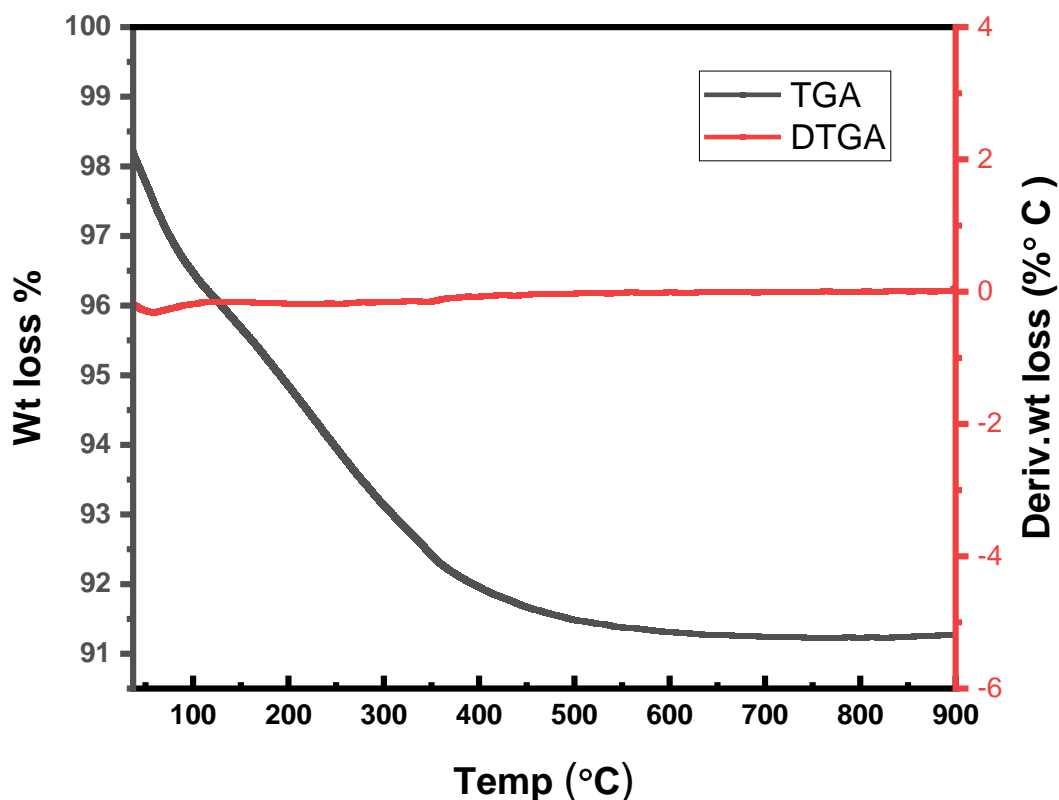


Figure 4.10: The thermogravimetric and derivative thermogravimetry analysis curves of RANR.

4.4.6 BET analysis

Textural attributes of the synthesized RANR show that titania has a high surface area of 99.0 m²/g which is very high compared to some of the work reported in literature. **Table 4.1** shows the pore volume and surface area of some published work on 3D TiO₂. **Figures 4.11** and **4.12** show nitrogen-desorption curves and pore-size distribution respectively. The N₂ adsorption - desorption isotherm of the material can be classified as type-IV, this shows the material is mesoporous (2-50 nm) ⁷.

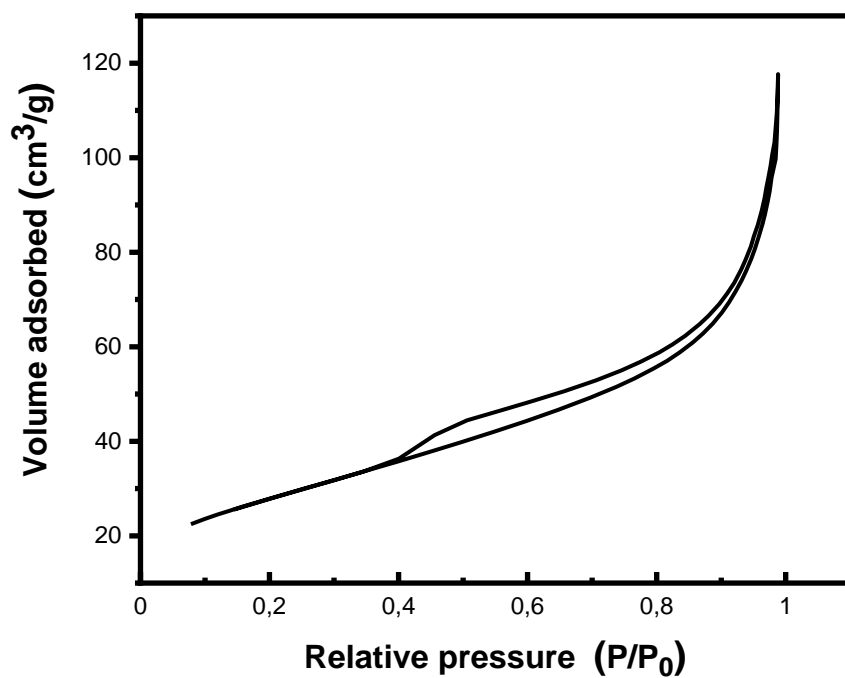


Figure 4.11: Nitrogen adsorption/desorption isotherms of RANR.

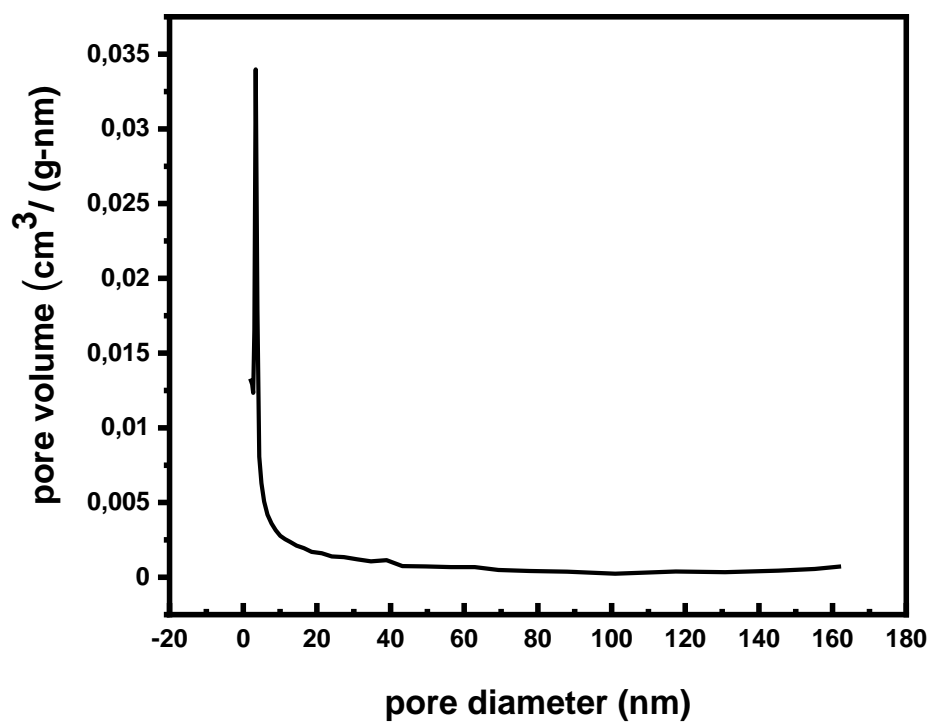


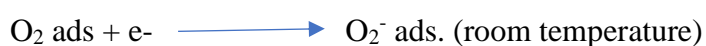
Figure 4.12: BJH pore size distributions of the RANR.

Table 4.1: Comparison of BET of hierarchical titania.

Sample	BET surface area (m ² g ⁻¹)	Pore size (nm)	Reference
RANR	81	3.2	7
RANR	46	44	10
RANR	81	3	19
RANR	50	0.22	6
RANR	100	-	5
Titania (anatase)	96.3	18.9	20
P25	48		23
RANR	99	7.09	This work

4.5 Gas sensing performance

Gas sensing is an occurrence that takes place on the surface of the sensor. With TiO₂ being an n-type semiconductor; on exposure to atmospheric oxygen, chemisorption of oxygen takes place on the surface to produce oxygen species. The operating temperature determines the kind of oxygen ions (O⁻, O₂⁻, O²⁻) that will be available on the sensing material. Since the experiment is conducted at room temperature O₂⁻ is the oxygen species that will be present on the TiO₂ sensor²¹.



The chemisorbed oxygen receives electrons from the TiO₂ surface, hence there is loss of electrons from the titania surface which results in depletion layer. When a reducing gas such as any of the alcohols and acetone is exposed to the sensor, oxidation of the gas occurs via the chemisorbed oxygen. This puts the electron back onto the surface of the titania resulting in further depletion layer, hence a change in the resistance is observed. The (001) crystal facet is very key in chemical sensing of TiO₂. Reports have shown that (001) crystal facets possess the

maximum surface energy which ease the decomposition of vapour molecules on interplay with the sensor to generate excellent response ^{21,22}. Wang *et al* also reported similar observations, the enhanced response of the hydrogenated titania towards methanol was as a result of the (001) crystal facet which contains a robust density of unsaturated TiSc atoms. This is the site where the gas adsorption normally takes place ¹¹.

4.6 Methanol vapour sensing

The recommended maximum exposure to methanol is given by Occupational Safety Health and Administration (OSHA) as 200 ppm for 8 h per day. Short time exposure to high concentration of methanol can causes blindness, headaches, drowsiness, irritation of the eyes and difficulty in breathing, dizziness, ataxia, nausea, vomiting, heart and respiratory failure and death ²³. Methanol monitoring is of serious concern globally since methanol is a common adulterant of illicit alcohol supply. Methanol poisoning has caused several deaths in many countries over the years.²⁴ The morphology of a nanostructure is an important factor in gas sensing; the dandelion morphology of the nanorutile helped in the gas sensing of alcohols. As shown by **Figure 4.13**, with an increase in concentration of methanol vapour from 111 ppm – 666 ppm, the response curves also increase. The sensor displayed a rapid response at room temperature. This is likely ascribed to the dandelion pattern of the nanorutile consisting of nanorods that resulted to 3D morphology providing a plethora of active sites for the adsorption of vapour molecules.

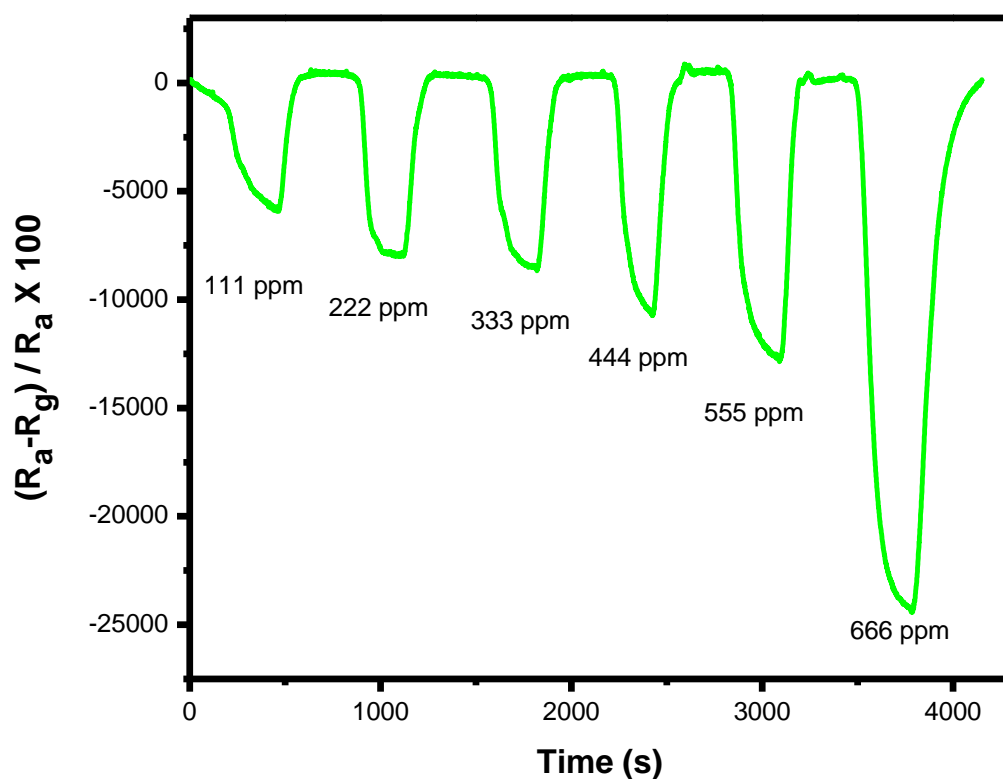


Figure 4.13: Response and recovery curves of RANR to methanol at different concentrations.

From the linear fitted plots in **Figure 4.14**. It can be observed that with an increase in concentration, the response increases; this indicates the response of a sensor depends largely on the concentration of the vapour molecules that interacts with the sensor. The conductance of the titania sensor diminished with adsorption of methanol molecules; this is evident with the negative response from the normalized response graph. This shows the sensor is an n-type, it received more of holes than electrons. The sensitivity of the sensor toward methanol was extrapolated from the linear fitted plots of the response to be -38.3%.

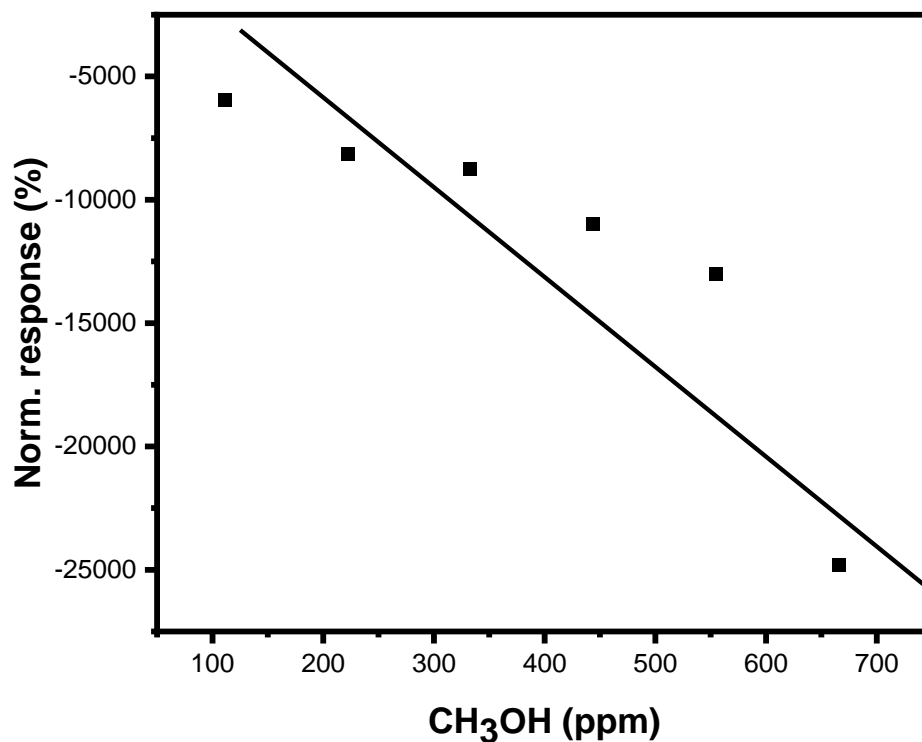


Figure 4.14: Normalized response of the RANR sensor as a function of methanol vapour concentrations.

The reproducibility of a sensor is a key factor, as this determines the reliability of the chemical sensor for practical purposes. **Figure 4.15** depicts the reproducibility nature of the TiO₂ film sensor to 555 ppm vapour at RT with four repetitive response-recovery curves. The sensor demonstrated a clear response-recovery output and stable four repetitive response-recovery curves for methanol vapour sensing.

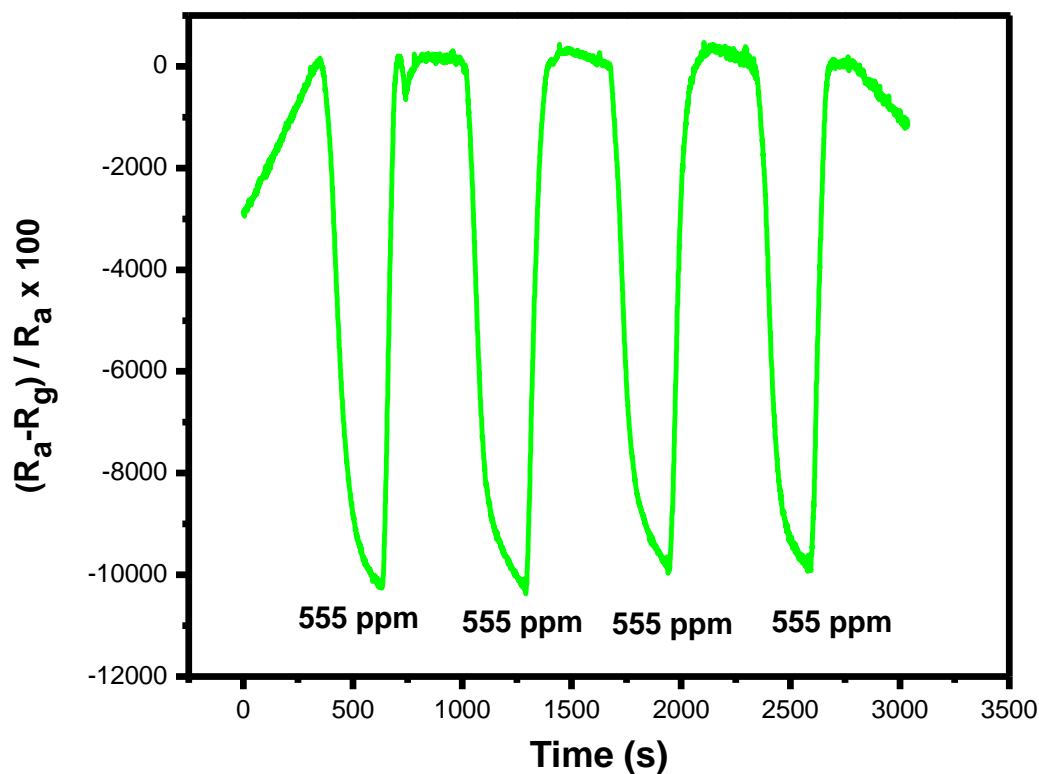


Figure 4.15: Repeatability response curves for methanol.

Figure 4.16 shows a quick response and recovery time of 81 and 84 s respectively of RANR to 555 ppm of methanol vapour. The detected response measured for methanol vapour in this work was much higher than what Mabrook and Hawkings observed with TiO_2 in a polymer matrix for sensing methanol vapour. The authors observed disparity in response-recovery time with increasing and decreasing concentration of methanol vapour. The sensitivity of the sensor was very poor ²⁵.

Hazra *et al* also developed nanotubes of titania for efficient sensing of methanol and ethanol at room temperature, the sensor showed more sensitivity to methanol compared to ethanol which is in contrast to this work, the sensor is more sensitive to ethanol in comparison to methanol vapour ²⁶. Sun *et al* also demonstrated thin film of titania toward methanol and ethanol at room temperature with higher sensitivity towards methanol compared to ethanol with response-recovery time of 60 and 80 s respectively ²⁷. The sensitivity of the RANR sensor is higher than the work reported by the group and the sensitivity was more towards ethanol compared to their findings however, the response and recovery time is very comparable.

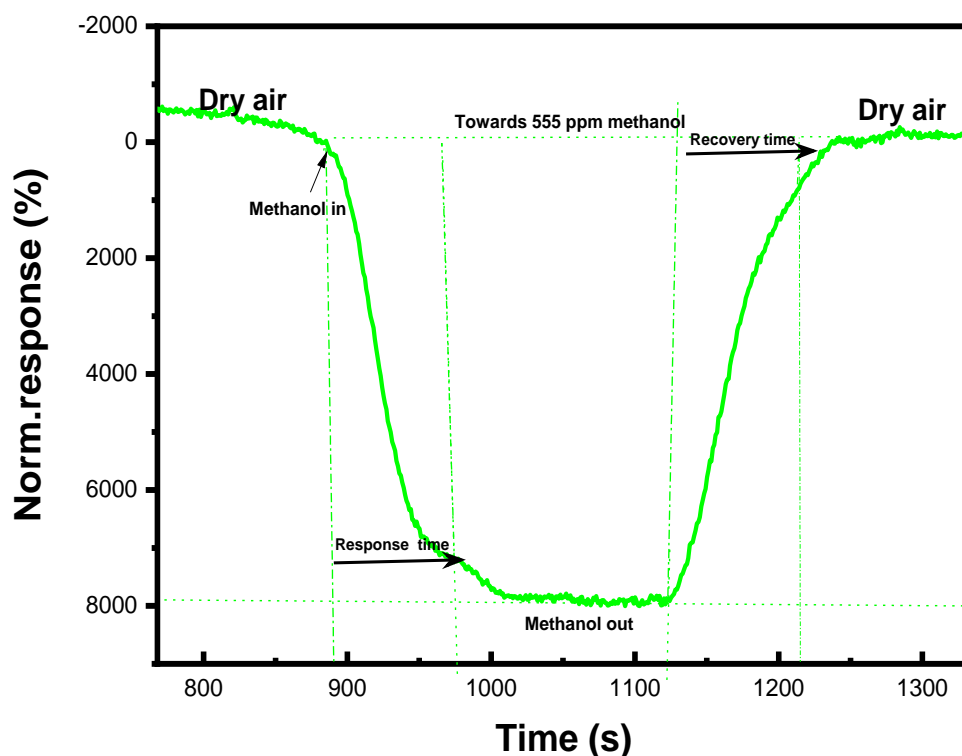


Figure 4.16: Transient response characteristic of RANR based sensor towards methanol.

4.7 Ethanol sensing

The recommended maximum exposure to ethanol is given by the Occupational Safety Health and Administration (OSHA) as 1000 ppm. Protracted exposure to high concentration of ethanol can cause health issues such as harm to liver, headaches, drowsiness, irritations of eyes and difficulty in breathing^{28,29}. More publications are available on ethanol and acetone vapours compared to other VOCs using 1D TiO₂ sensor for VOCs sensing^{3,30}. 1D TiO₂ has been more investigated in chemical sensing towards VOCs compared to other morphologies. A recent study shows that 3D TiO₂ having the advantage of large surface area, a plethora of mesopores and can be effectively deployed to chemical sensing of VOCs. The RANR sensor exhibited n-type sensing behaviour. Upon exposure of RANR to reducing gas such as ethanol, more holes are accumulated and thus leading to hole-accumulation layer (HAL). As more holes are produced in the HAL this leads to decrease in resistance. This is the expected trend for MOXs,

however few reports have shown TiO_2 or TiO_2 nanocomposites with other MOXs that behaved as p-type sensor^{11,31}.

Similar to methanol vapour, the results in **Figure 4.17** show that the response curves rise with an increasing vapour concentration. **Figure 4.18** shows the curves of the TiO_2 measured at different ethanol concentrations (77-308 ppm). The measurement was conducted from low vapour concentration to high vapour concentration and vice versa from high vapour concentration to low concentration. A distinct rise in the sensor response is noticed with the increasing vapour concentration. This is illustrated with the linear fitted plots (**Figure 4.19**).

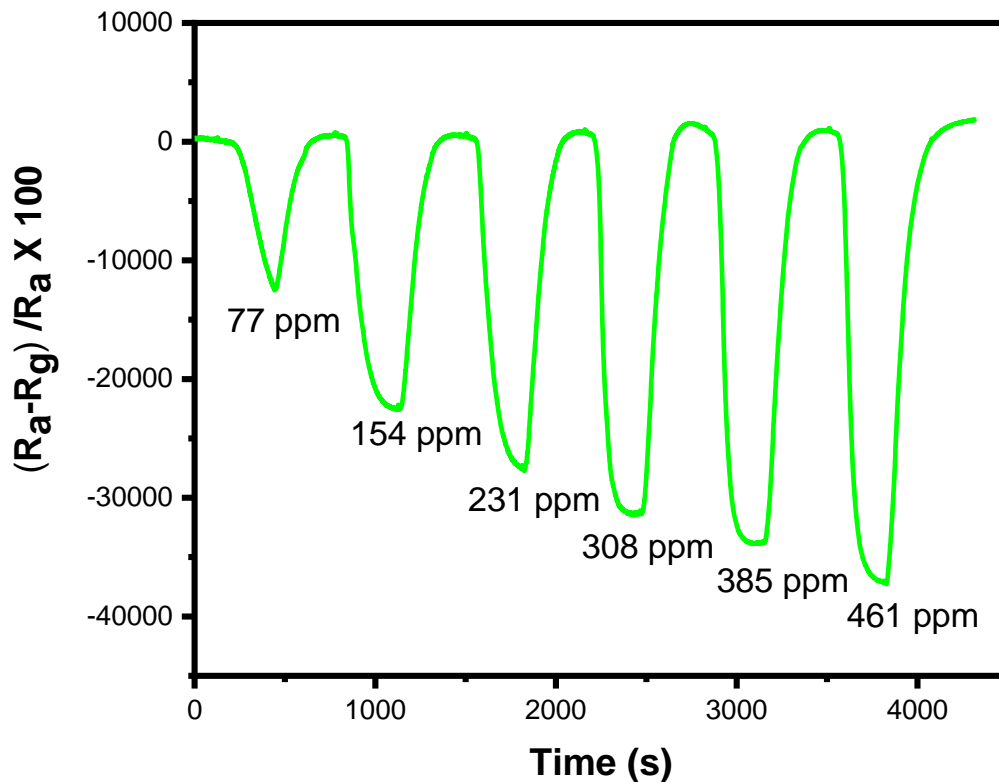


Figure 4.17: Static response and recovery curves of RANR to ethanol at different concentrations.

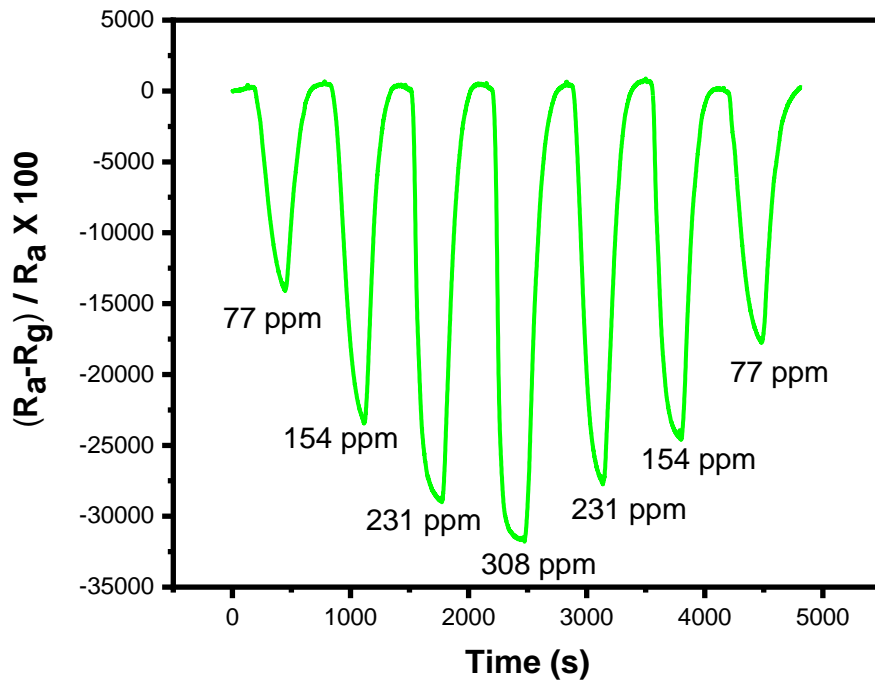


Figure 4.18: Static response curves of RANR sensor measured under a series of ethanol vapour concentrations.

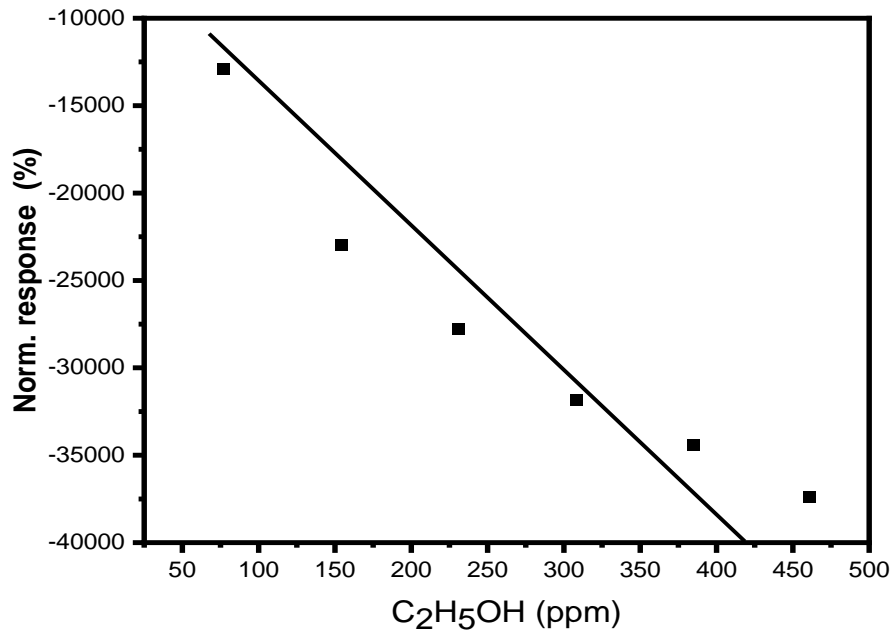


Figure 4.19: Normalized response of the RANR sensor as a function of methanol vapour concentrations.

Figure 4.20 depicts repeatability nature of the TiO₂ film sensor to 385 ppm vapour at RT with four repetitive response-recovery curves. The sensor demonstrated a clear response-recovery

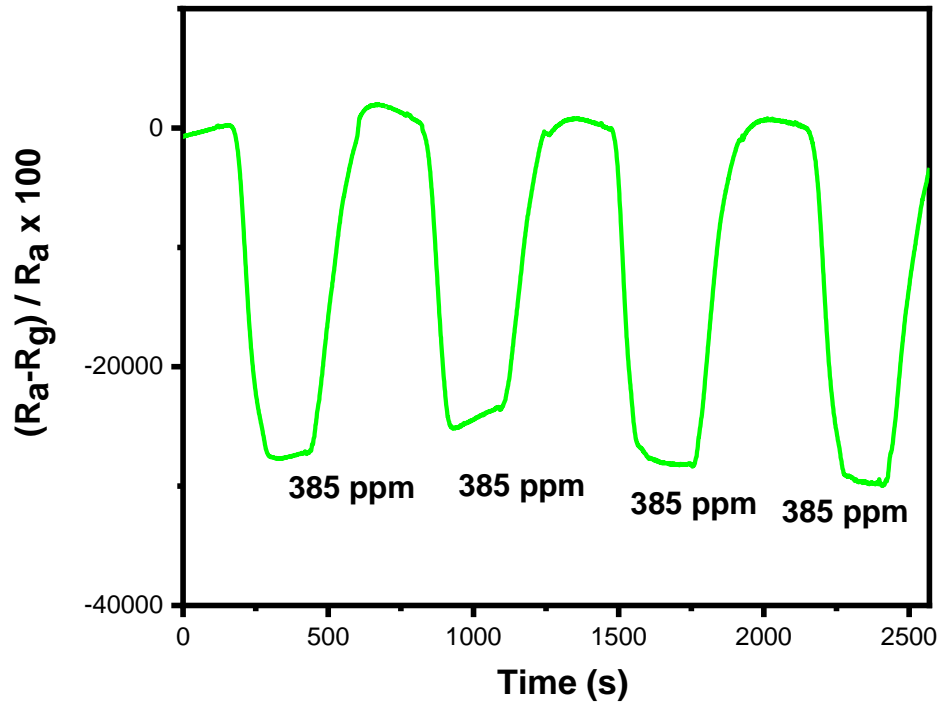


Figure 4. 20: Repeatability response curves for ethanol.

output and stable four repetitive response-recovery curves for ethanol vapour sensing.

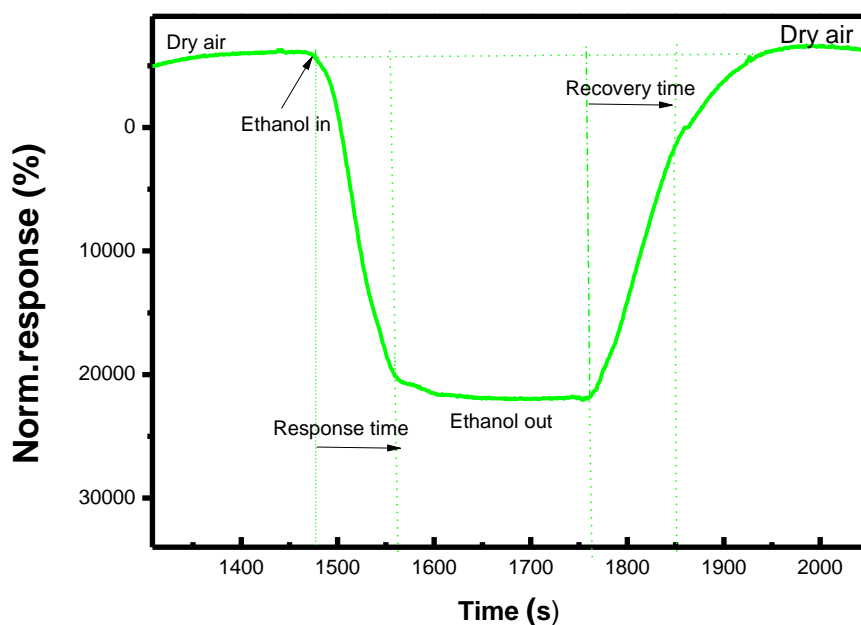


Figure 4.21: Transient response characteristic of RANR based sensor toward 385 ppm of ethanol vapour.

The sensor showed a rapid response and recovery time of 76 s and 89 s respectively to 385 ppm of ethanol vapour (Figure 4.21). Shooshtari *et al* synthesized TiO₂ nanowires (NWs) with good sensitivity (15%) towards ethanol vapour at room temperature however, elevating the temperature by the order of 7.2 times (180 °C) improved the response by almost two times. The sensor response was boosted when the relative humidity (RH) increased from 10 - 60%. However, as the RH increased from 60 - 90% the response diminished due to the variation in mechanisms of synergy of the titania with moisture and ethanol molecules ¹. A similar observation was made with the RANR sensor; the moisture content served as a promoter and the response increased when the RH increased from 10 -55%. Figure 4.22 illustrates the effects of RH on chemical sensing of ethanol vapour with RANR sensor.

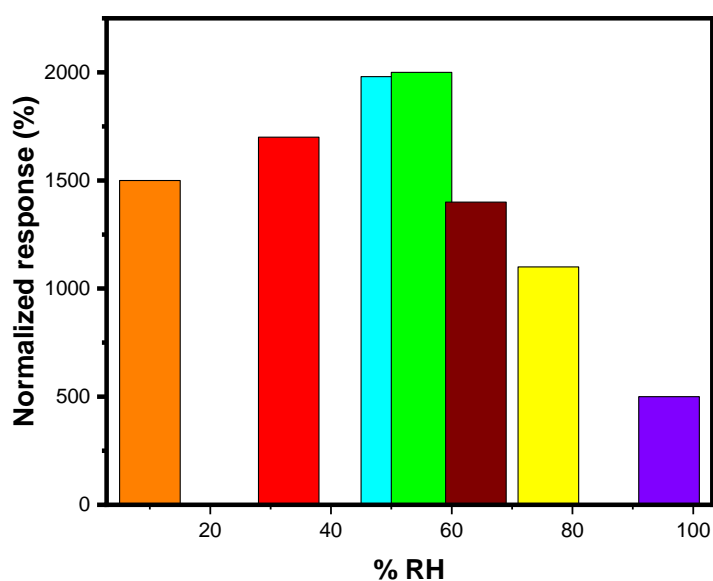


Figure 4.22: Response of RANR towards 77 ppm of ethanol vapour under different humidity conditions at 10, 33, 51, 55, 64, 76 and 96%.

The effect of humidity on ethanol sensor was maximum at about 55%, then as the RH increased from 55-98% the response decreased. According to Shooshtari *et al* two classifications of OH group is available, a rooted OH with an oxygen lattice and one bounded with titanium lattice. With increase in humidity there is a difference in hydroxyl group which is lesser compared to that of oxygen on the surface, hence this leads to increase in response, however at a very high humidity the hydroxyl group spreads over the surface and reduces the oxygen adsorption thus a decline in response. A similar observation was also reported with RH increasing from 26-72%, nanorods of ZnO showed an increase in response towards ethanol sensing³². The performance of the RANR sensor is higher than the one reported by Perillo and Rodriguez, the first authors who demonstrated TiO₂ nanostructures for sensing ethanol at room temperature in which the sensor displayed a delayed response of about 13 min¹³. Hazra *et al* produced TiO₂ nanotubes with variations in length and thickness for ethanol sensing at room temperature (27 °C) and elevated temperature²⁶. The sensor showed a good response of 80% to 1000 ppm of ethanol with response and recovery times of 11 and 117 s respectively at 150 °C²⁶. Kilinc *et al* demonstrated TiO₂ nanotubes for sensing 5000 ppm of alcohols (methanol, ethanol, and isopropanol) at 200 °C. Moreover, the sensor displayed a weak response for ethanol (16%) and methanol (10%) with very sluggish response and recovery times of 720 s and 1800 s respectively³³. Wang *et al* also demonstrated 3D anatase titania having several nanopetals

forming flower-like patterns for the sensing of methanol, ethanol and acetone. The sensor was more sensitive to ethanol with sensitivity of 2.25 and 1.33 % for ethanol and methanol respectively. Indium oxide hollow nanorods were fabricated by Tao *et al* for-sensing ethanol gas at 200 °C, the sensor displayed ultrafast response and recovery (3 s and 4 s respectively) with a high selectivity towards ethanol. The sensor displayed a long range of sensing from 5-1000 ppm with a good response at a low concentration ³⁴. The response-recovery time were ultrafast compared with this work, despite the experiment was conducted above room temperature. Shankar *et al* fabricated ZnO nanorods using electrospinning method. The sensor displayed an outstanding response of 26.4% towards 500 ppm of ethanol vapour. At the same time the sensor showed response and recovery time of 23 s and 43 s respectively for 100 ppm of ethanol. The response time of the sensor is faster than the recovery time towards ethanol vapour; a similar observation was also made in this work. This can be attributed to the ease of the chemisorption of ethanol gas on the sensor surface compared to its desorption of ethanol from the sensor. The duration of dissociation of oxidative compounds such as ethanol from MOXs sensor have been reported to be slightly delayed ³². Despite SnO₂ sensors have been reported as the most developed sensor among the MOXs, information is scarcely available on their sensitivity towards alcohols at room temperature. Ying *et al* synthesized SnO₂ nanowhiskers and demonstrated the sensor towards ethanol gas at 300 °C with response time of 23 s and a very sluggish recovery value of almost 600 s ³⁵. Their response-recovery time were far less compared to this work despite their reaction was conducted at elevated temperature. Zeng *et al* reported one of the best response value of MOXs by increasing the oxygen concentrations of the SnO₂; the sensor produced response value of 120.3% to 300 ppm of ethanol at a temperature of 190 °C compared to pure SnO₂ that gave a response value of 36.90% ²⁹.

Pandeeswari *et al* developed TiO₂ nanoparticles for sensing ethanol vapour at room temperature with an outstanding sensitivity value of 535% towards 50 ppm of ethanol vapour and rapid response and recovery time of 5 s and 52 s respectively which is far higher than the sensitivity in this work ²⁸. Rella *et al* reported on TiO₂ nanoporous towards ethanol and acetone vapours with the sensor being more sensitive to ethanol compared to acetone vapour at elevated temperatures ³⁰. Most of the work reported higher duration of recovery time compared to response time, this can be attributed to the very fact that the sensing operation was done at room temperature ²⁸. **Table 4.2** shows the comparison of the RANR sensor in this study with other MOX sensors.

Table 4.2: Comparison of different MOXs towards chemical sensing and relative humidity.

Sensor	Temperature (°C)	Vapour (ppm)	Sensitivity (%)	Response (s)	Recovery (s)	Reference
TiO ₂ nanotubes	RT	ethanol (1000)	45.7	-	-	26
		methanol (1000)	60.2	-	-	
TiO ₂ nanotubes	RT	ethanol (400)	-	780	-	13
TiO ₂ nanowires	RT	ethanol (100)	15			1
ZnO nanorods	RT	ethanol (100)	23.0	26	43	32
TiO ₂ nanotubes	200	ethanol	16	720	1800	33
		methanol (5000)	10			
TO ₂ nanoparticles	RT	ethanol (5)	5	52	535	28
TiO ₂	RT	propanol	-	-	-	36
TiO ₂ nano tubes	RT	acetone 10-50	-	-	-	37
TiO ₂	370	acetone	25.97	13	8	38
		ethanol	11.19			
		methanol	9.86			

			isopropanol	5.35			
			(500)				
TiO ₂ nanoparticles	350	ethanol	240	180			30
	400	acetone					
		(100)					
SnO ₂ nano ring	250	Isopropanol	6.8	38.6	7.27		39
TiO ₂ powder	RT	Methanol	120 and	-	-		25
		Ethanol	360				
RANR titania	RT	Methanol	38.3	81	84		This work
		Ethanol	86.75	76	89		

The stability study showed that sensor towards ethanol is stable for 45 days. This is shown in **Figure 6.20**. Stability indicates the level to which sensor characteristics remain constant over

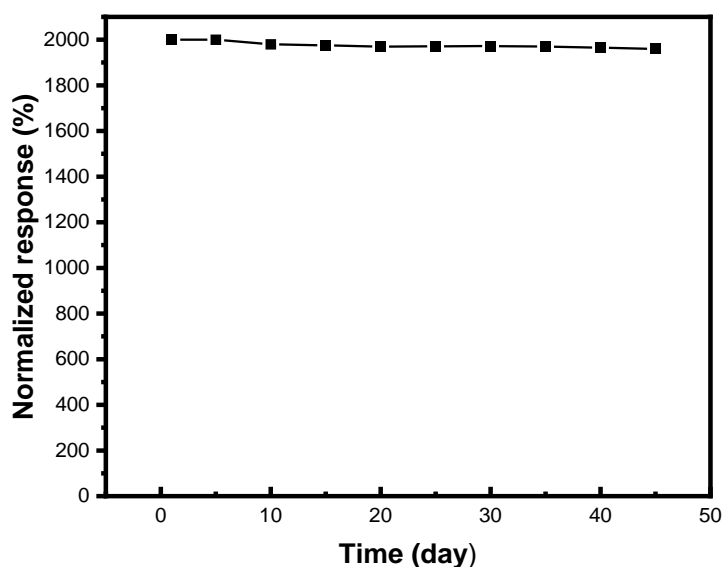


Figure 4.23: Stability of RANR sensor towards 77 ppm of ethanol vapour within 45 days.

time, any changes in stability is termed drift which results from the following: (i) aging of the components (ii) decrease in response value of components and/or (iii) a change in the signal to noise ratio.

4.8 Isopropanol sensing

Upon exposure to low concentration of isopropanol (< 400 ppm) it may cause irritation of the eyes, nose, mouth and throat but at high exposure to it may cause the following: dizziness, low blood pressure, stomach pain, nausea, rapid heart rate, or tachycardia, low body temperature, slurred speech, slow breathing, vomiting, Unresponsive reflexes, throat pain or burning, seizure and coma³⁹. Figure 4.22 depicts the response of the sensor towards isopropanol vapour, the response of the sensor increases with an increase in concentration (58-231 ppm) and vice versa. In a related experiment, Gaidan *et al* also demonstrated TiO₂ sensor to large variations of propanol vapour at room temperature with good sensitivity³⁶.

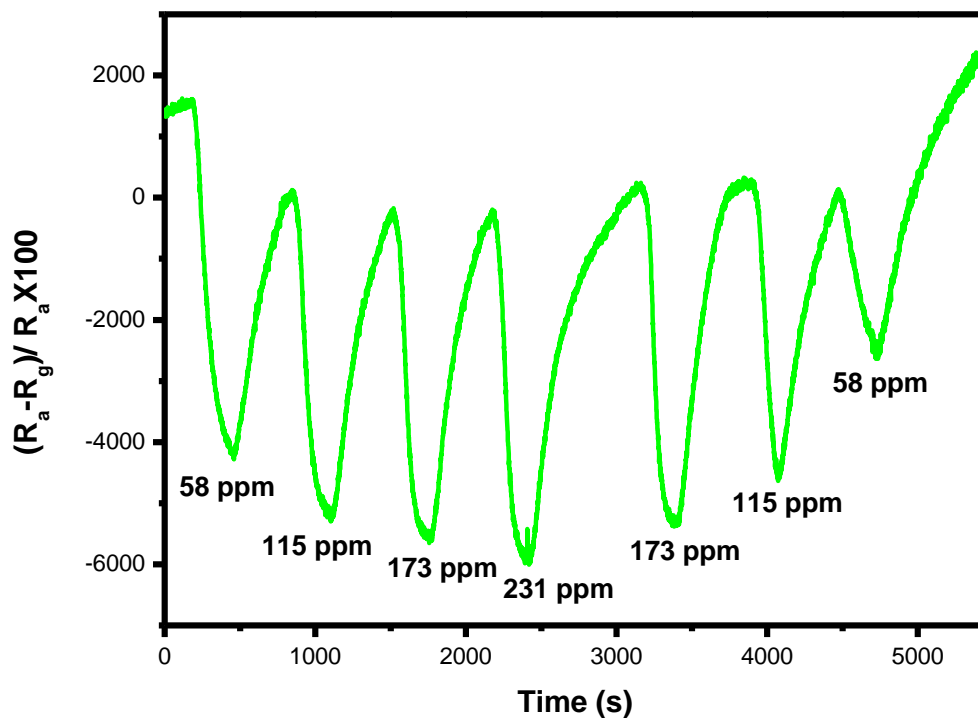


Figure 4.24: Static response curves of RANR sensor measured under a series of isopropanol vapour concentrations.

Figure 4.25 shows the linear fitted plots of the sensor. This indicates that with increasing concentration, the sensor was able to absorb more vapour molecules on the plethora of active sites of the TiO_2 sensing film hence, an increase in response is observed. The sensitivity obtained in this research is higher than what Chen *et al* observed when the TiO_2 sensor was operated at 370°C towards 500 ppm of acetone vapour; the sensitivity was 5.35%. Reports on room temperature sensing of isopropanol vapour using MOXs are scarcely available³⁸. Li *et al* developed SnO_2 nanorings for sensing of isopropanol at 250°C , the sensor showed good sensitivity of 7.27% with response-recovery times of 6.8 and 38.6 s respectively They also demonstrated the importance of morphology in chemical sensing, the performance of the nanorings was far better than nanopowder in isopropanol sensing at the set temperature³⁹. The RANR morphology seems to resemble the nanorings as they are both spherical which allows for large surface area for adsorption of gas molecules and rapid response.

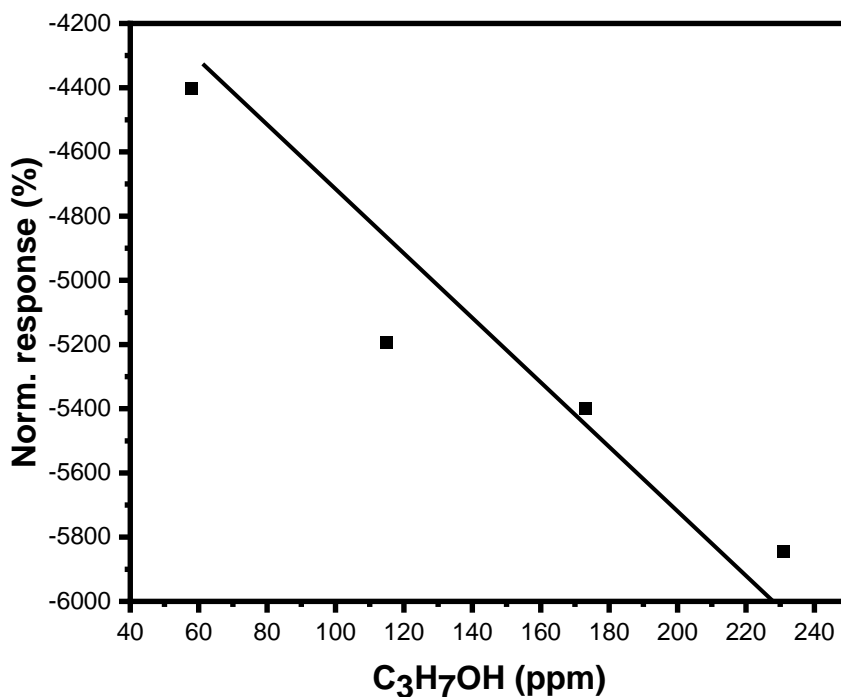


Figure 4.25: Normalized response of the RANR sensor as a function of isopropanol vapour concentrations.

4.9 Acetone sensing

Monitoring acetone vapour is very important since VOCs are the primary sources of environmental pollutants. Acetone finds applications in industrial processes. It can affect the central nervous system (CNS) which will impart a serious threat. At concentration above 173 ppm, it can cause damage to parts of sense organs and CNS. At higher concentration it may results into change of moods, nausea, respiratory tract irritation, dizziness and weakness and the possibility of explosion because of its high flash point ³⁸.

The response curves rise with increasing concentrations of acetone vapour as shown in **Figure 4.26**. This shows the response of the sensor relies on the interactions of the sensing material with the concentrations of analyte molecule. The more acetone vapour is introduced into the test chamber the more the active sites available on the TiO₂ sensing film will absorb the gas molecules until it reaches a saturation point.

Figure 4.27 displays the linear dependency of the sensor as shown by the linear fitted plots of the response. The conductance of the titania sensor increased with adsorption of acetone

molecules, this is evident with the positive response from the normalized response curves. The sensitivity of the sensor towards acetone was extrapolated from the linear fitted plots of the response to be 1.24%. Most reports available on titania sensor for sensing acetone vapour were conducted at temperature above RT.

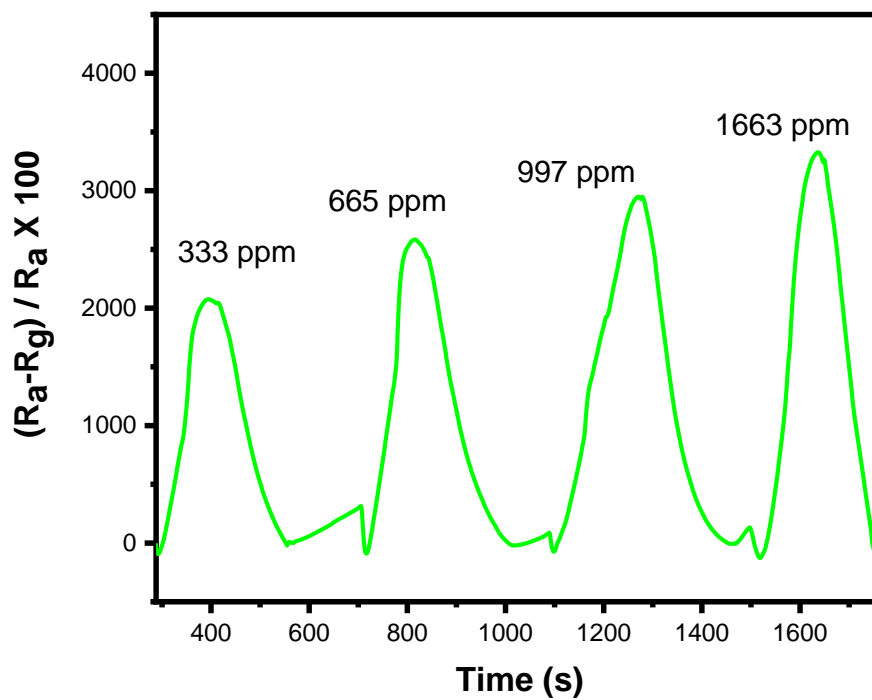


Figure 4.26: Static response and recovery curves of RANR towards acetone.

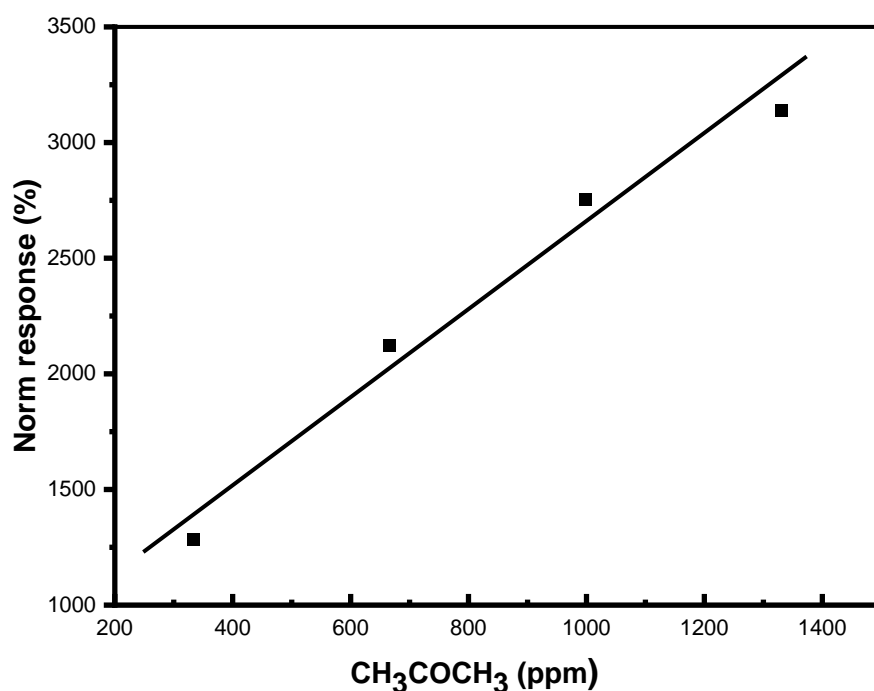


Figure 4.27: Normalized response of the RANR sensor as a function of acetone vapour concentrations.

Figure 4.28 displays the response curves of the sensor under various acetone concentrations from 66 -1663 ppm and the test was then alternated from high concentration to low concentration (1663-665 ppm). A distinct surge in the sensor response was observed with increasing vapour concentrations and a descending trend in response on decreasing the vapour concentration. A very recent study conducted by Kumar *et al* showed that the sensor displayed a good response towards acetone vapour with better response when the reaction was conducted in a visible light over non irradiated with light ³⁷.

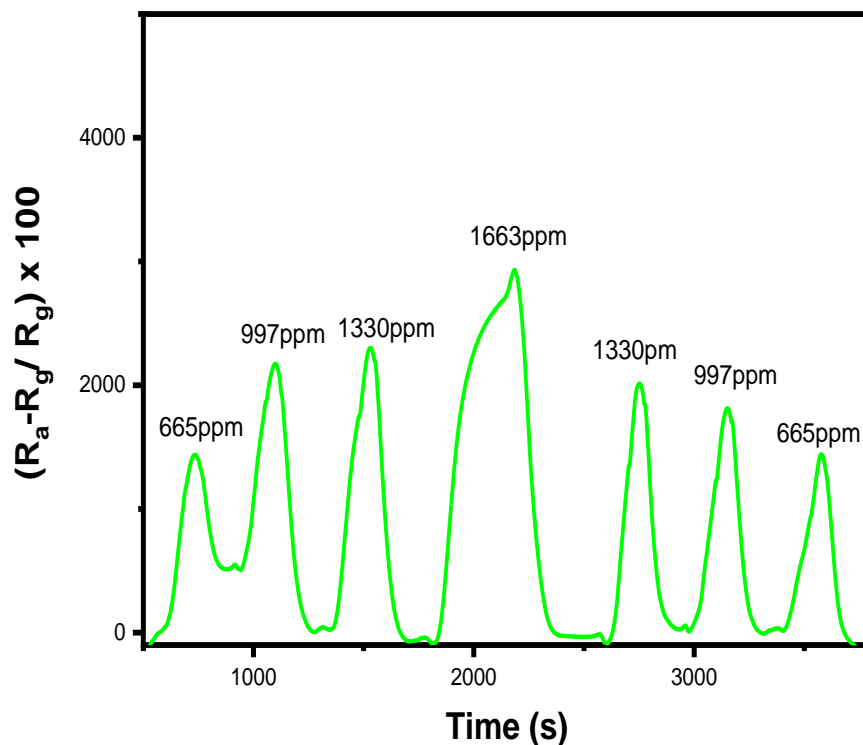


Figure 4.28: Static response curves of the RANR sensor measured under a series of acetone vapour concentrations.

Figure 4. 29 shows the repeatability of the sensor towards 333 ppm of acetone vapour at room temperature. It has been communicated by many authors that TiO₂ nanostructures or hybrid-based sensors have shown poor sensitivity, response/recovery time toward acetone vapour even above room temperature.^{30,40,41,42} However, Chen *et al* demonstrated one of the best responses of titania-based sensor in the chemical sensing of acetone vapour at 370 °C with quick response and recovery times of 13 s and 8 s respectively and a sensitivity of 25.97%³⁸. Rella *et al* disclosed chemical sensing of TiO₂ nanoparticles towards 200 ppm of acetone vapour at 400 °C with response-recovery time of 240 s and 180 s respectively³⁰.

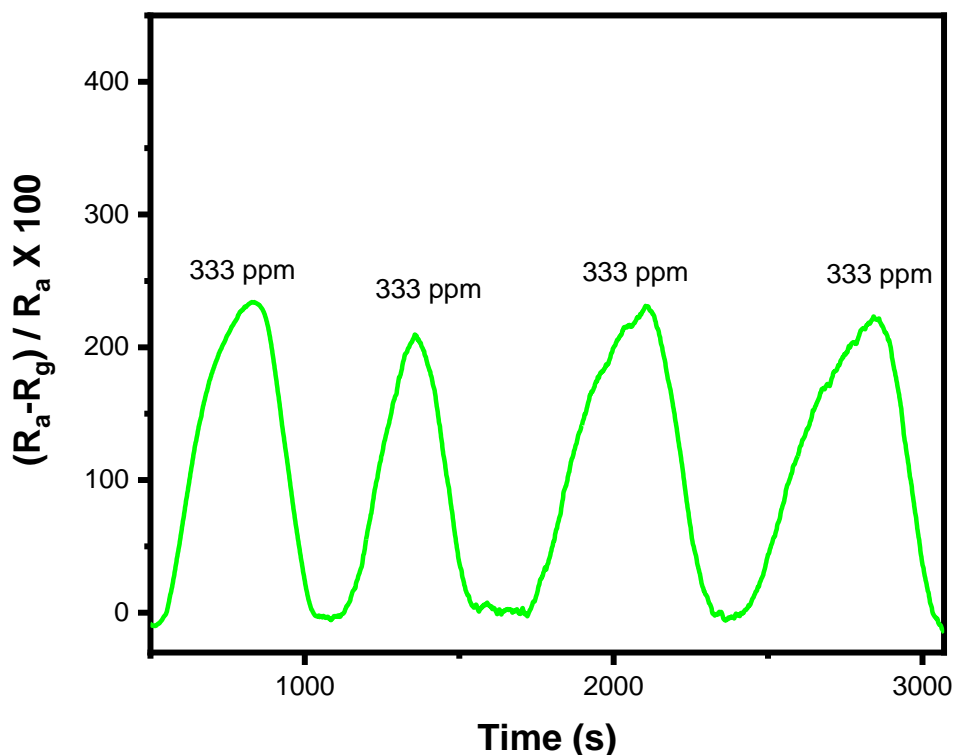


Figure 4.29: Repeatability response curves towards acetone vapour.

4.10 Conclusion

The radially aligned nanorutile was fabricated by the facile hydrothermal method. The gas sensing performances showed that the hierarchical morphology, high surface area, high porosity and humidity played a vital role in sensing of VOCs at room temperature. Humidity served as promoter of reaction up to 55% RH, whereas as at humidity beyond 55% the response reduces. The TiO₂ sensor showed high sensitivity with responses of -38.27, -86.75, -9.83 and 1.24% which correspond to methanol, ethanol, isopropanol, and acetone respectively. The sensor may find application in breath analysers since the least detection for a breath analyser is reported to be 200 ppm. The sensor displayed good sensitivity, reproducibility, rapid response and recovery times towards alcohol and stability over 45 days. The sensitivity and selectivity of the sensor can be improved at room temperature by doping with precious metals, 2D materials, carbon and polymers.

4.11 References

1. Shooshtari, M. and Salehi, A., 2021. Vollebregt S. Effect of temperature and humidity on the sensing performance of TiO₂ nanowire-based ethanol vapor sensors. *Nanotechnology*, 2(32), pp.325501-325508.
2. Lee, E., Yoon, Y.S. and Kim, D.J., 2018. Two-Dimensional Transition Metal Dichalcogenides and Metal Oxide Hybrids for Gas Sensing. *ACS Sensors*, 3(10), pp.2045-2060.
3. Kaur, N., Singh, M., Moumen, A. and Duina, G., 2020. Comini E. 1D titanium dioxide: Achievements in chemical sensing. *Materials*, 13(13), pp. 1-21.
4. Tian, X., Cui, X., and Lai, T., 2021. Nano Materials Science Gas sensors based on TiO₂ nanostructured materials for the detection of hazardous gases : A review. *Nano Mater Sci.* 2021;3(4), pp.390-403.
5. Barrett, D.H., Scurrall, M.S, Rodella, C.B, Diaz, B., Billing, D.G. and Franklyn P.J., 2016. Achieving nano-gold stability through rational design. *Chem Sci.*,7(11), pp.6815-6823.
6. Dziike, F., Franklyn, P.J., Durbach, S.H, Maubane, M., and Hlekelele, L., 2018. Synthesis of radially aligned nano-rutile modified with Au and Ni for the photodegradation of methyl orange. *Mater Res Bull.*, 104, pp.220-226.
7. Baloyi, J., Seadira, T., Raphulu, M. and Ochieng A., 2015. Preparation, Characterization and Growth Mechanism of Dandelion-like TiO₂ Nanostructures and their Application in Photocatalysis towards Reduction of Cr(VI). *Mater Today Proc.* 2(7), pp.3973-3987.
8. Gharavi, P.S.M. and Mohammadi, M,R., 2015. The improvement of light scattering of dye-sensitized solar cells aided by a new dandelion-like TiO₂ nanostructures. *Sol Energy Mater Sol Cells*, 137, pp.113-123.
9. Bai, Y.L., Wu, X.Y. and Liu, Y.S., 2020. Dandelion-clock-inspired preparation of core-shell TiO₂@MoS₂ composites for high performance sodium ion storage. *J Alloys Compd.*, 815, pp.152386-152395.
10. Yi, J., Liu, Y., Wang, Y., Li, X., Hu, S., and Li, W., 2012. Synthesis of dandelion-

- like TiO₂ microspheres as anode materials for lithium ion batteries with enhanced rate capacity and cyclic performances. *Int J Miner Metall Mater.*, 19(11), pp.1058-1062.
11. Wang, M., Zhu, Y., Meng, D., Wang, K., and Wang C., 2020. A novel room temperature ethanol gas sensor based on 3D hierarchical flower-like TiO₂ microstructures. *Mater Lett.*, 277, 128372-128385.
 12. Song, Y., Chen, F. and Zhang, Y., 2018. Sensors and Actuators B : Chemical Fabrication of highly sensitive and selective room-temperature nitrogen dioxide sensors based on the ZnO nano flowers. *Sensors Actuators B Chem.*, 287, pp.191-198.
 13. Perillo, P.M, and Rodríguez D.F., 2012. The gas sensing properties at room temperature of TiO₂ nanotubes by anodization. *Sensors Actuators, B Chem*, 171(172), pp.639-643.
 14. Perillo, P.M., and Rodríguez, D.F. and Boggio, N.G., 2014. TiO₂ Nanotubes for Room Temperature Toluene Sensor .*Scientific research*, 2014:1(7) pp.4236-4242.
 15. Perillo, P.M, and Rodríguez, D.F. A room temperature chloroform sensor using TiO₂ nanotubes. *Sensors Actuators, B Chem*, pp.193:263-266.
 16. Ba-Abbad, M.M., Kadhum, A.A.H., Mohamad, A.B., Takriff, M.S. and Sopian K., 2012. Synthesis and catalytic activity of TiO₂ nanoparticles for photochemical oxidation of concentrated chlorophenols under direct solar radiation. *Int J Electrochem Sci.*,7(6), pp.4871-4888.
 17. Huang, C.W. and Wu ,M.C., 2020. Photocatalytic degradation of methylene blue by UV-assistant TiO₂ and natural sericite composites. *J Chem Technol Biotechnol.*, 95 (10) pp. 2715-2722.
 18. Nwankwo, U., Bucher, R., Ekwealor, A.B.C., Khamlich, S., Maaza, M., and Ezema, F.I., 2019. Synthesis and characterizations of rutile-TiO₂ nanoparticles derived from chitin for potential photocatalytic applications. *Vacuum*, 161, pp.49-54.
 19. Zhou, J., Zhao, G., Song, B., Han, G., Solvent-controlled synthesis of three-dimensional TiO₂ nanostructures via a one-step solvothermal route. *CrystEngComm*. 2011;13(7): pp.2294-2302.

20. Tshabalala, Z.P, Mokoena, T.P., Hillie, K.T, Swart, H.C. and Motaung, D.E., 2021. (Improved BTEX gas sensing characteristics of thermally treated TiO₂ hierarchical spheres manifested by high-energy {001} crystal facets. *Sensors Actuators, B Chem.* 338, pp.129774-129872.
21. Tshabalala, ZP, Mokoena, T.P, and Jozela, M., 2021. TiO₂ Nanowires for Humidity-Stable Gas Sensors for Toluene and Xylene. *ACS Appl Nano Mater.*, 4(1): pp.702-716.
22. Pal, R., Goyal, S.L. and Sharma, S., 2019. Facial synthesis of polyaniline and its nanocomposites for room temperature methanol sensors. *AIP Conf Proc.* 215 (1), pp.030217-030220.
23. Manning, L. and Kowalska, A., 2021. Illicit alcohol: Public health risk of methanol poisoning and policy mitigation strategies. *Foods*,10(7):1-16.
24. Mabrook, M., and Hawkins, P., 2001. A rapidly-responding sensor for benzene, methanol and ethanol vapours based on films of titanium dioxide dispersed in a polymer operating at room temperature. *Sensors Actuators, B Chem.* 75(3), pp.197-202.
25. Hazra, A., Bhowmik, B., Dutta, K., Chattopadhyay, P.P. and Bhattacharyya, P., 2015. Stoichiometry, length, and wall thickness optimization of TiO₂ nanotube array for efficient alcohol sensing. *ACS Appl Mater Interfaces*, 7(18), pp.9336-9348.
26. Sun, L. and Huo, L. and Zhao, H., Gao, S. and Zhao J., 2006. Preparation and gas-sensing property of a nanosized titania thin film towards alcohol gases. *Sensors Actuators, B Chem.*, 114(1), pp.387-391.
27. Pandeewari, R. Karn, R.K. and Jeyaprakash, B.G., 2014. Sensors and Actuators B : Chemical Ethanol sensing behaviour of sol – gel dip-coated TiO₂ thin films. *Sensors Actuators B Chem.*, 194, pp.470-477.
28. Zeng, Q, Cui, Y., Zhu, L., and Yao, Y., 2020. Materials Science in Semiconductor Processing Increasing oxygen vacancies at room temperature in SnO₂ for enhancing ethanol gas sensing. *Mater Sci Semicond Process*, 111, 104962.-104974.
29. Rella, R., Spadavecchia, J. and Manera, M.G., 2007. Acetone and ethanol solid-state gas sensors based on TiO₂ nanoparticles thin film deposited by matrix assisted pulsed

- laser evaporation. *Sensors Actuators, B Chem.*, 127 (2), pp.426-431.
30. Wu, H. Kan, K. and Wang, L., 2014. Electrospinning of mesoporous p-type $\text{In}_2\text{O}_3/\text{TiO}_2$ composite nanofibers for enhancing NO_x gas sensing properties at room temperature. *CrystEngComm.*, 16 (38), pp.9116-9124.
 31. Shankar, P., Bosco J. and Rayappan B., 2017. Room temperature ethanol sensing properties of ZnO nanorods prepared using an electrospinning. *Mater.Chemistry*, 5, pp. 10869-10880.
 32. Kılınç, N., Şennik, E. and Öztürk Z.Z., 2011. Fabrication of TiO_2 nanotubes by anodization of Ti thin films for VOC sensing. *Thin Solid Film*, 520 pp.953-958.
 33. Tao, K., Han, X., Yin, Q., Wang, D., Han, L. and Chen, L., 2017. Metal-Organic Frameworks-Derived Porous In_2O_3 Hollow Nanorod for High-Performance Ethanol Gas Sensor. *ChemistrySelect*, 2(33):10918-10925.
 34. Ying, Z., Wan, Q., Song, Z.T. and Feng, S.L., 2014. SnO_2 nanowhiskers and their ethanol sensing characteristics. *Nanotechnology*. 15 (11), pp.1682-1684.
 35. Gaidan, I., Asbia, S., Brabazon, D. and Ahad, I.U., 2017. TiO_2 gas sensor to detect the propanol at room temperature. *AIP Conf Proc.* 2017;1896 (1) , pp.1063-1069.
 36. Kumar, K.G., Avinash, B.S, Rahimi-Gorji, M., and Majdoubi, J., 2020. Photocatalytic activity and smartness of TiO_2 nanotube arrays for room temperature acetone sensing. *Molecular liquids*, 300, pp.112418-112427.
 37. Chen, N., Li, Y. and Deng, D., 2017 Acetone sensing performances based on nanoporous TiO_2 synthesized by a facile hydrothermal method. *Sensors Actuators, B Chem.*, 238, pp.491-500.
 38. Li ,S.H., Chu, Z. and Meng, F.F., 2016. Highly sensitive gas sensor based on SnO_2 nanorings for detection of isopropanol. *J Alloys Compd.* 2016;688:pp.712-717.
 40. Wang, X, Sang Y, Wang D, Ji S. and Liu H., 2015. Enhanced gas sensing property of SnO_2 nanoparticles by constructing the SnO_2 - TiO_2 nanobelt heterostructure. *J Alloys Compd.*, 639, pp.571-576.
 41. Bian, H., Ma, S., and Sun, A., 2015. Characterization and acetone gas sensing

- properties of electrospun TiO₂ nanorods. *Superlattices Microstruct.*, 81, pp.107-113.
42. Epifani, M, Comini E, Siciliano P, Faglia G. and Morante, J.R., 2015. Evidence of catalytic activation of anatase nanocrystals by vanadium oxide surface layer: Acetone and ethanol sensing properties. *Sensors Actuators, B Chem.* 217, pp.193-197.

CHAPTER 5: SYNTHESIS AND CHARACTERIZATION OF FEW- LAYERED ZIRCONIUM DISULPHIDE VIA LIQUID EXFOLIATION

5.1 Introduction

Direct exfoliation of bulk of crystals of transition metal dichalcogenides (TMDCs) in a solvent is one of the facile methods in which mono or few layers of group IVB TMDCs are prepared recently.^{1,2} Mono or few layer zirconium disulphide finds application in the following: thermoelectric device, field effect transistors (FET), photodetectors, solar cells, fibre lasers, optics, tribology, electrode materials, catalysis and sensors^{3,4,5,6,7,8,9}.

Over the time, amide solvents such as N-cyclohexyl-2-pyrrolidone (CHP), N-methyl-2-pyrrolidone (NMP) and dimethylformamide (DMF) are the common solvents deployed in effective exfoliation of layered materials such as graphene and TMDCs. The choice of the solvent plays a very key role here, the nearness of the surface tension of the solvent to that of the dissolved layered bulk material is very paramount in this process. With the amide solvent, few minutes/hours are required for the exfoliation of the bulk material into nanomaterials with a possibility of quantum dots, nanoparticles and mono or few layers. However, the cost, high boiling point, toxicity and difficulty in obtaining free standing nanomaterials after sonication limits the use of this solvent¹⁰. This has paved way for other solvents such as alcohols and water which are more environmentally safe among them is isopropanol (IPA). Alcohols such as methanol, ethanol and isopropanol have low boiling points of 66 °C, 78 °C, and 80 °C respectively. IPA has been extensively used recently in exfoliation of many 2D layers^{6,11,12,13}.

Yin *et al* exfoliated nanosheets of HfS₂ via liquid exfoliation, the bulk crystal was converted to fine powder by ball milling for 4 h followed by sonication in IPA for 10 h using a non-contact sonicator². Similarly, Yang *et al* fabricated nanosheets of ZrS₂ by dissolving a sample of bulk crystal of ZrS₂ in IPA and the solution was sonicated for several hours¹². Ma *et al* gave a fascinating report by obtaining two layers of ZrS₂ nanosheets via ultrasonication of the bulk sample in IPA. However, details such as the duration of sonication, spectroscopical and morphological methods were not mentioned except for SEM analysis⁹. Very recently, Li *et al* also fabricated nanosheets of ZrS₂ by sonicating the bulk powder in IPA for 5 h⁶. In a related experiment, Kaur *et al* exfoliated bulk crystal of HfS₂ by dispersing the sample in N-cyclohexyl-2-pyrrolidone (CHP) and sonicated for 2 h in a bath sonicator. The resulting solution was then centrifuged at low speed to remove the unexfoliated material. The exfoliated nanomaterial was then centrifuged at high speed for several minutes to remove remnant CHP.

It is necessary to remove remnant CHP, since CHP has a high boiling point and is not easily dried at room temperature. The material was then further suspended in toluene and centrifuged at high speed to remove remnant CHP still left in the nanomaterial¹. Similarly, Li *et al* also prepared nanosheets of HfS₂ by exfoliating the crystal bulk of the material in CHP for just 2 h¹⁴. The use of water as a solvent is very economical and environmentally safe but may result in slight oxidation of group IV TMDCs. Pang *et al* prepared nanosheets of HfS₂ by exfoliating the bulk crystal of the sample in deionized water for the duration of 5 h¹⁴. Likewise, Ahmad fabricated nanosheets of HfS₂ from the bulk sample by sonicating for 10 h¹⁵. Ethanol has been well explored in the exfoliation of graphene and group VIB however, not much is reported on group IVB¹⁶. Sometimes the use of a surfactant like sodium chlorate is deployed to reduce the high surface energy of water and to prevent agglomeration. Vega-mayoral *et al* fabricated few layers of TiS₂ by exfoliating the bulk sample in a mixture of water and sodium chlorate and the solution was sonicated for 1 h¹⁷. So recently, Li *et al* exfoliated nanosheets of 2-3 layers of ZrS₂ using NMP via intercalations of short amines.¹⁸ In this work, the bulk sample was exfoliated in CHP, NMP, ethanol, methanol, isopropanol and water.

5.2 Chemicals and materials

Zirconium disulphide [99%, ZrS₂, C.C. Imelmann (pty) ltd], N-cyclohexyl-2-pyrrolidone (CHP) [99%, Sigma-Aldrich], N-methyl-2-pyrrolidone (NMP) [99.9%, Sigma-Aldrich] isopropyl alcohol (IPA) [99%, MK Chemicals, IPA], ethyl alcohol (EOH) [99%, MK Chemicals,] and methyl alcohol (MeOH) [99%, MK Chemicals,], were used as received without further purification. A mortar and pestle, a PS-20A sonicator bath with power of 100 W were used.

5.3 Exfoliation of bulk ZrS₂

The bulk sample of about 1 g was ground for about 2 h and 5 mg of the sample was transferred to a vial. A volume of 12 ml of IPA was introduced and the vial was covered and wrapped with parafilm. The solution was then transferred to a bath sonicator and sonicated for 24 h. The temperature was maintained at about 25 °C by introducing ice into the bath sonicator at regular intervals. The same procedure was followed for other solvents except for amide solvents for which the reaction was allowed to run for about 2 h. The set-up of the reaction is shown in Figure 5. After exfoliation, the resulting solution was centrifuged at 2000 rpm for 45 minutes to separate the exfoliated from the unexfoliated sample. The supernatant was collected and centrifuged for 30 minutes at 1500 rpm. The low speed of centrifugation is needed at this time

to effectively separate the exfoliated and non-exfoliated nanomaterials. From the insets of Figure 5.1 it can be observed that the bulk sample was pecan brown before grinding and the colour changed to light brown during grinding in ambient environment; this may be ascribed to possible slight oxidation of the sample. The exfoliated nanosheets of ZrS₂ dispersion in IPA produced a homogeneous solution with good dispersion of yellow colouration.

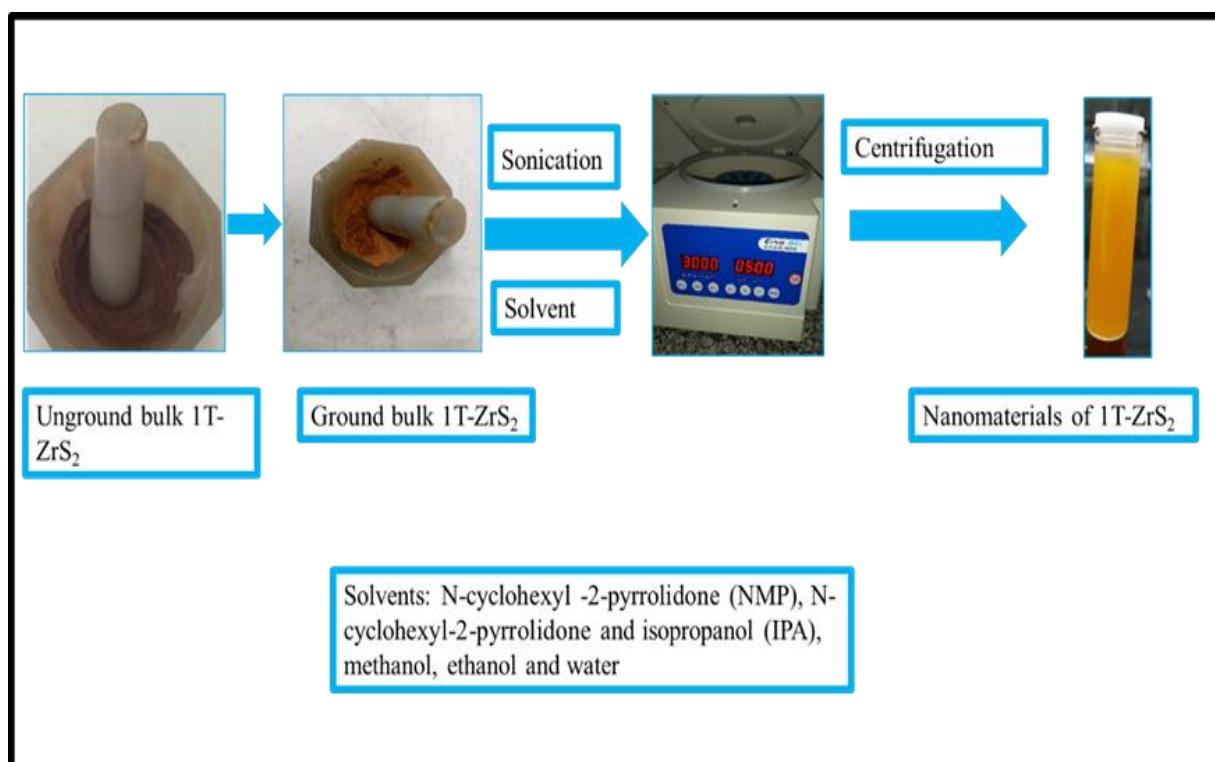


Figure 5.1: Exfoliation of bulk crystal of zirconium disulphide.

5.4 Characterization

Powder X-ray diffraction (PXRD) analysis was performed using a Bruker D2 phaser (D2-205530) diffractometer with Cu K α 1 radiation ($\lambda = 1.54060 \text{ \AA}$) at 30 kV and 10 mA. Measurements were taken using a glancing angle of the incident detector at an angle of 2° over 2θ angle range of $5\text{--}90^\circ$ in steps of 0.026° with a step time of 5 s at ambient temperature. X-ray photoelectron spectroscopy (XPS) analysis was conducted using ESCAlab 250Xi spectrometer model. Transmission electron microscopy (TEM) (Jeol JEM-2100F 200 kV) was

used to analyse the morphology of the a-synthesized ZrS₂ nanomaterials. TEM samples were prepared by dissolving the RANR in ethanol, sonicated for 10 min, after which they were deposited on a copper grid and allowed to dry at room temperature before analysis. The surface morphology was studied by scanning electron microscopy (SEM) using a ZEISS GeminiSEM 560 instrument with sub 1 kV resolution below. AFM (Nanoscale: Bruker) was used to analyse the roughness of the samples. The thermal stability of as-synthesized RANR was monitored using a PerkinElmer 6000 thermogravimetric analyzer. Raman spectra were obtained using a Horiba LabRAM HR Raman spectrometer with an Olympus BX41 microscope attachment and the 514.5 nm line of a Lexel argon-ion laser as the excitation source. UV-vis absorption was conducted using a Varian Cary Eclipse (Cary 50) UV-Vis spectrophotometer.

5.5 Results and Discussion

5.5.1 XRD analysis

Figure 5.2 shows the XRD diffraction patterns of the bulk and exfoliated samples. Diffraction patterns of all exfoliated samples have fewer peaks compared to the bulk that have several diffraction peaks. A similar observation was made by Liang-Liang *et al* when a bulk sample of ZrS₂ was exfoliated in NMP; only two peaks belonging to (101) and (103) crystal planes were observed, and the nanomaterials were amorphous. Meanwhile, all the samples exfoliated in this work are crystalline¹⁹. They all show diffraction peaks indexed to crystal plane (001). The bulk sample shows traces of impurities of ZrS₃, represented by asterisks (*). The NMP and CHP exfoliated samples show similar diffraction peaks of (001), (100), (101), (102) and (110). The IPA exfoliated sample shows two weak diffraction peaks indexed to (001) and (101). The XRD results obtained for methanol, ethanol and water also showed the bulk material has been exfoliated to few layers. A similar observation was also reported by Li *et al* in which fewer diffraction peaks with less intensity compared to the bulk sample were obtained¹⁸.

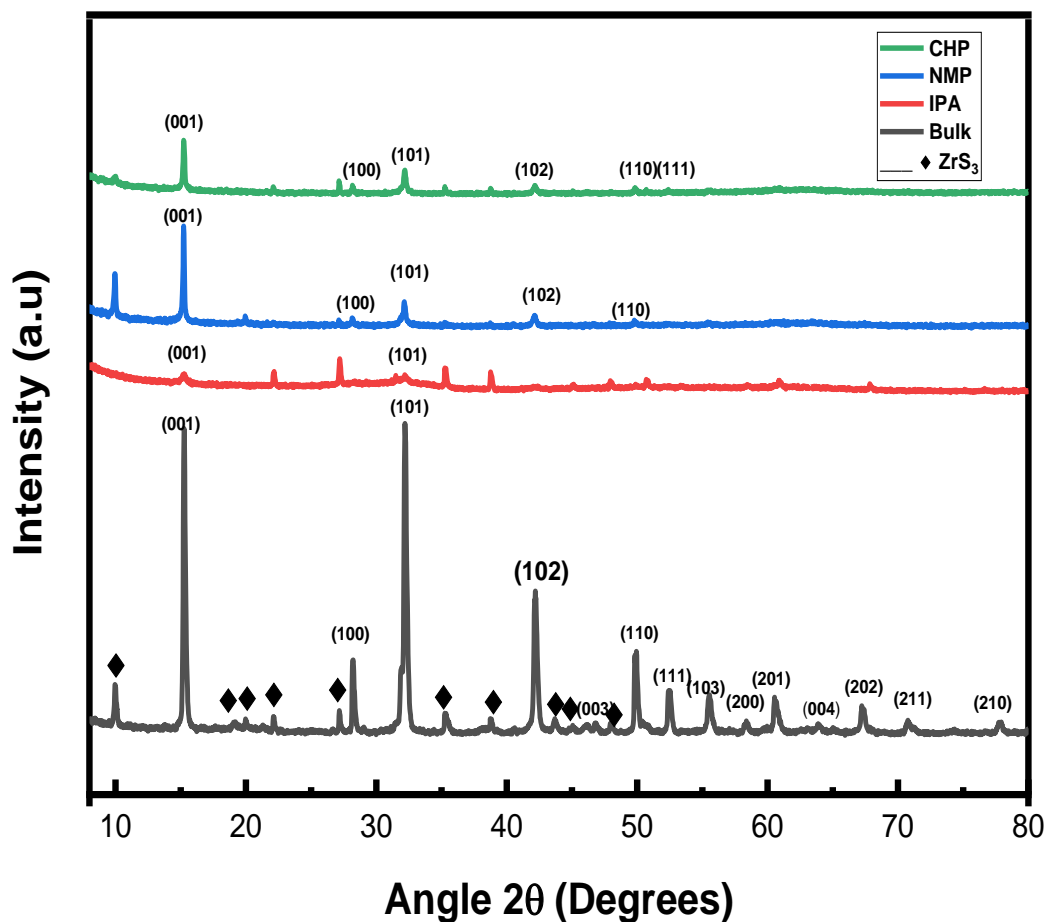


Figure 5.2: XRD of exfoliated ZrS₂ nanomaterials.

5.5.2 UV-Vis spectra analysis

The three exfoliated samples show similar absorptions at about 420 nm and 510 nm as observed in Figure 5.3. The intensity of the absorption peaks is highest with CHP compared with other solvents used. Liang-Liang *et al* observed two absorptions peaks also but at lower absorption wavelengths of 283 and 336 nm respectively¹⁹. Likewise, Yan *et al* also observed two absorption peaks at lower absorption wavelengths of 245 and 280 nm⁵. Thiayagarajan *et al*, in their work did not observe any sharp absorption peak with ZrS₂ thin film; and the absorption decreased as the wavelength increased²⁰.

The intensity of the UV-Vis absorption of the ZrS₂ (IPA) (**Figure 5.4**) reduced after the first day of exfoliation however, there was no observable shift of absorption peaks; this could be ascribed to slight oxidation of the nanomaterials. Close observation by Sherrell *et al* revealed a decrease in the intensity of the absorption of the exfoliated TiS₂ after 5 days of exposure in ambient environment ²¹.

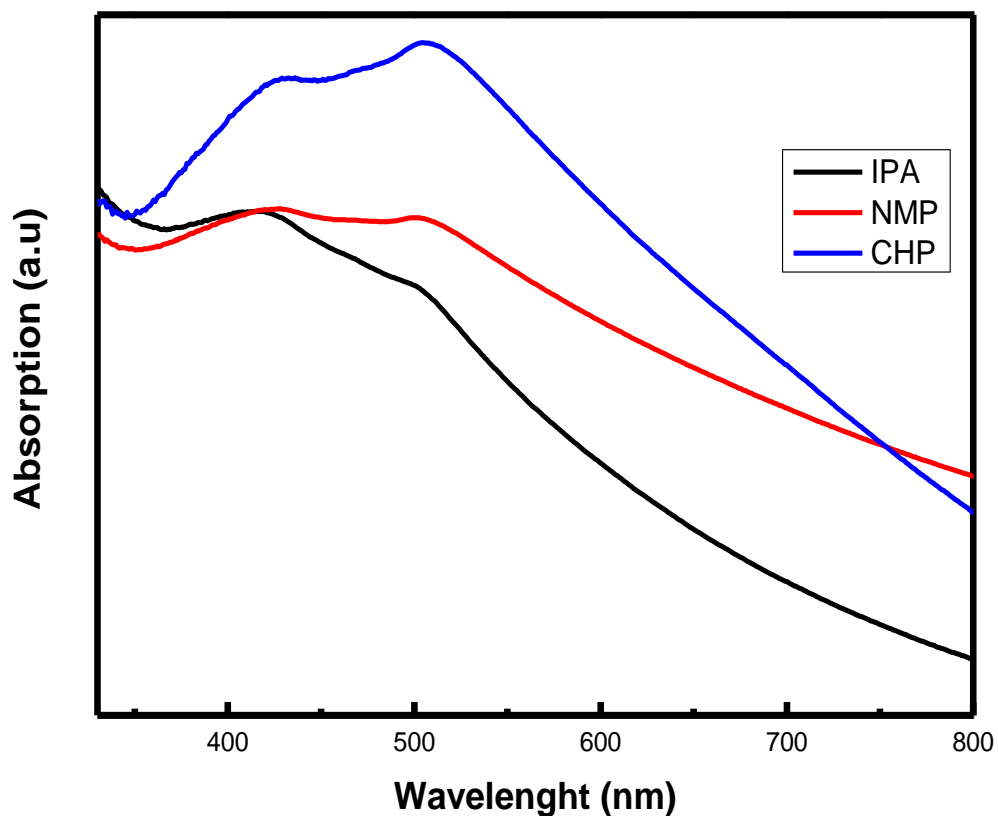


Figure 5.3: UV-Vis absorption spectra of ZrS₂.

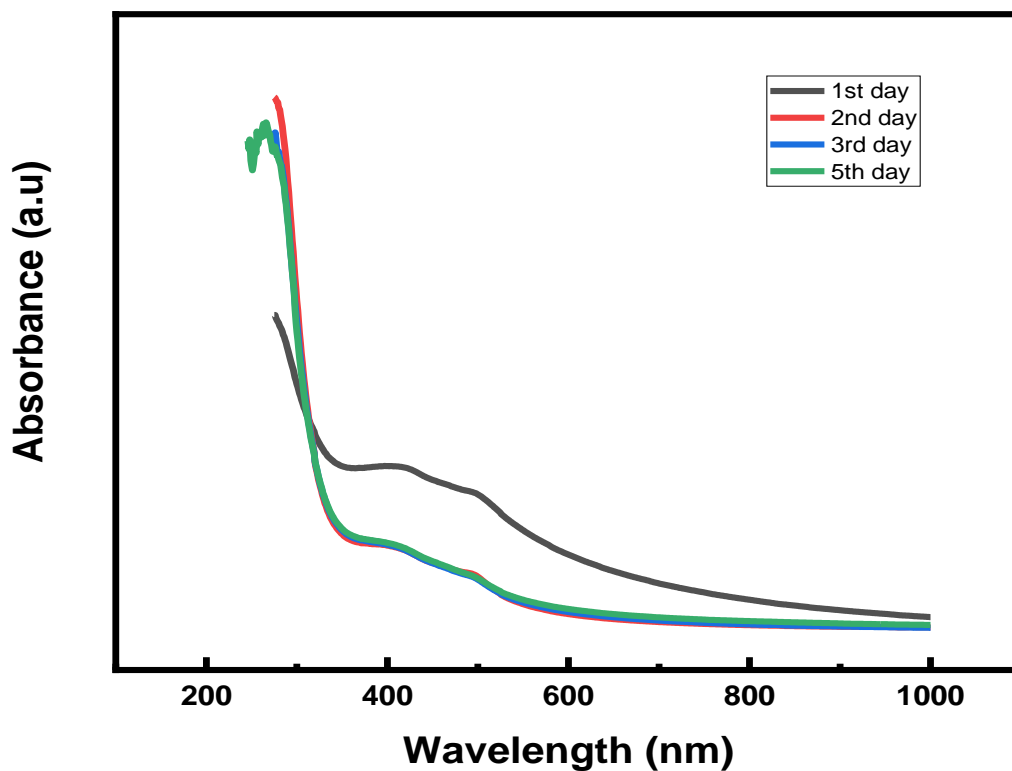


Figure 5.4: UV-Vis absorption spectra of ZrS₂ on exposure to ambient environment for five days.

Figure 5.5 shows the band gap of the bulk and exfoliated samples. The bulk has a band gap of about 1.98 eV, this is slightly higher than what is reported in literature (1.70-1.80 eV)²². IPA, NMP and CHP exfoliated samples exhibited band gaps of about 2.45, 2.55 and 2.60 eV respectively, it can be deduced that exfoliated nanomaterials exhibited direct band gaps as result of quantum confinement. Liang-Liang *et al* obtained a higher value of 3.15 eV in their report¹⁹.

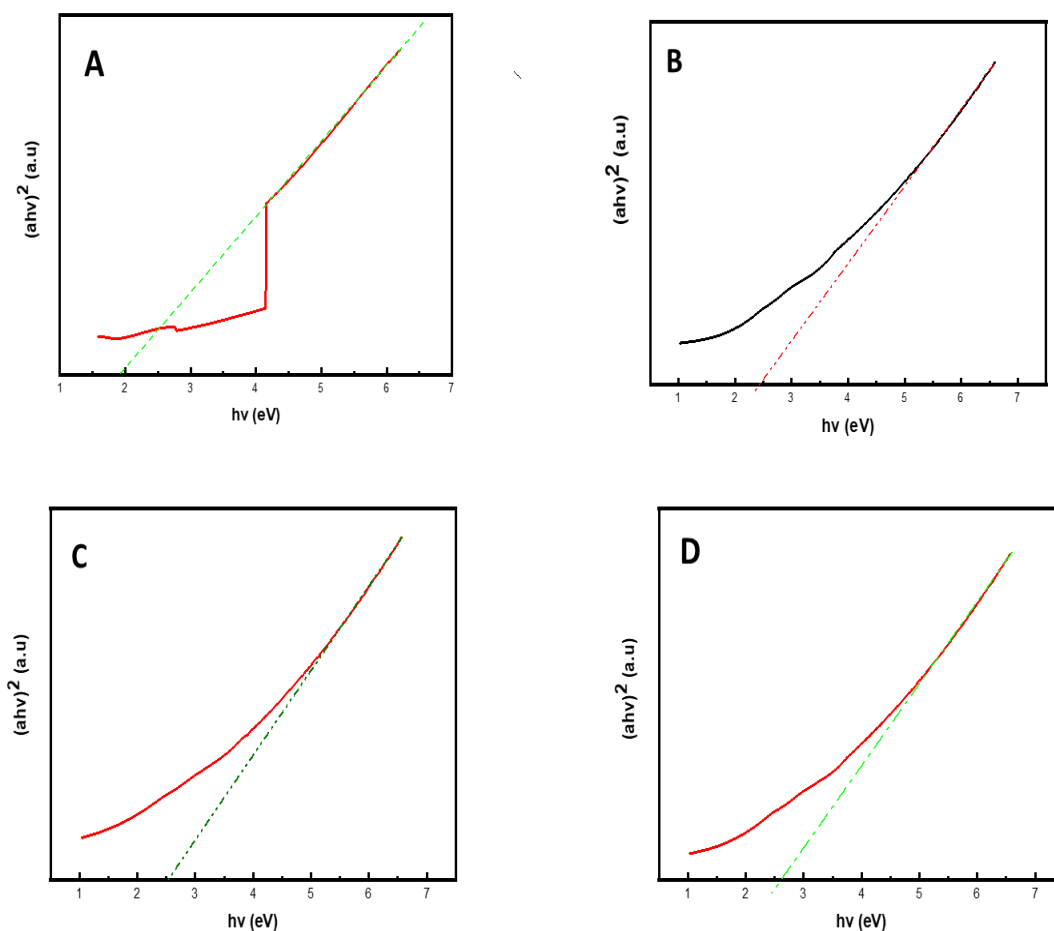


Figure 5.5: Tauc plot of ZrS₂ (a) Bulk (b) IPA exfoliated (c) NMP exfoliated (d) CHP exfoliated.

5.5.3 Raman analysis

Raman spectroscopy was conducted to confirm the finger prints of the nanomaterial as shown in Figure 5.6. The Raman peaks of the bulk in-plane mode (E_g) and the out of plane mode (A_{1g}) are not pronounced, and this is in contrast with literature.²³ The intensity of the A_{1g} mode at about 313 cm^{-1} is expected to increase with increasing number of layers. For the IPA exfoliated, the weak E_g mode at about 247 cm^{-1} is observed whereas this mode is absent in the NMP, and CHP exfoliated samples. The dominant A_{1g} mode is observed at about 331 cm^{-1} in the IPA exfoliated sample, as well for the CHP exfoliated; however, a shift was observed for the NMP exfoliated sample. The broadening of the A_{1g} peak was observed at about 314 cm^{-1} as a result of non-harmonic effects while many authors have ascribed the observed shoulder to the infrared (IR) Azu mode^{23,24}. The A_{1g} vibration mode is also observed at about 520 cm^{-1} for IPA

exfoliated sample; however, a slight shift is observed in the CHP exfoliated sample. The peaks at about 109 cm^{-1} , 148 cm^{-1} and 216 cm^{-1} are also observed in IPA exfoliated but only peak at about 109 cm^{-1} is observed for NMP and CHP exfoliated; these peaks are attributed to the density of two phonon states of ZrX_2 .

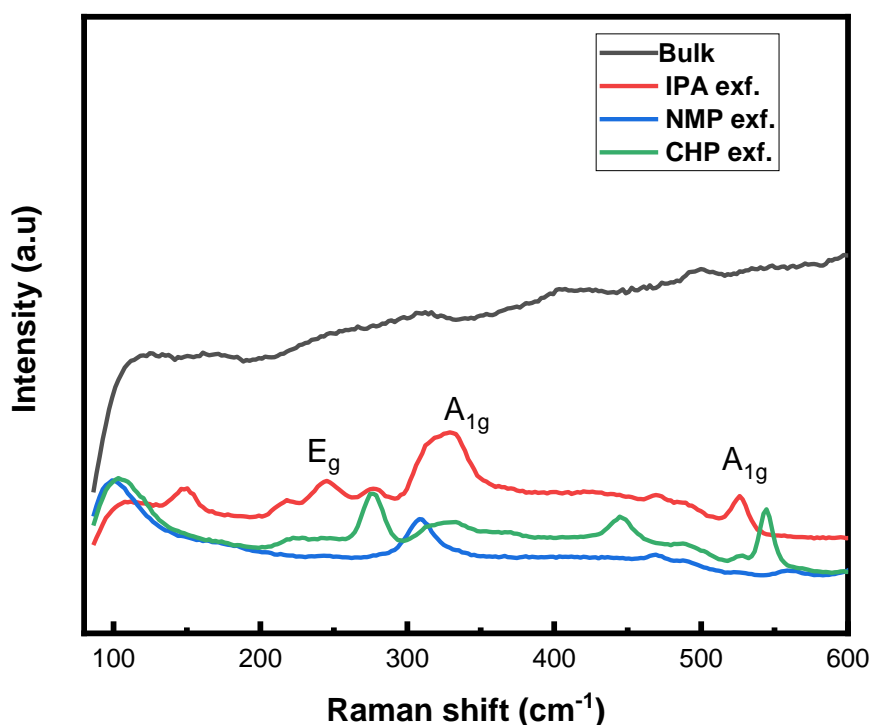


Figure 5.6 Raman spectra of bulk and exfoliated nanosheets of ZrS_2 with different thickness.

It should be noted that the observed peak at about 275 cm^{-1} is the A_{1g} mode of ZrS_3 present in the sample. Li *et al* also observed 2 peaks of E_{1g} and A_{1g} at 247 and 313 cm^{-1} respectively for IPA exfoliated nanosheets ⁶. Liang-Liang *et al* reported two vibration modes of in-plane and out-of plane vibration modes at 507 cm^{-1} and 520.1 cm^{-1} respectively for ZrS_2 quantum dots exfoliated with NMP ¹⁹.

5.5.4 AFM analysis

AFM was conducted to determine the surface roughness and morphology of the nanosheets as shown in Figure 5.7. Among primary alcohol solvents used, ethanol provided the best roughness, next was IPA, followed by methanol while with H_2O it was difficult to observe the

roughness with AFM analysis. The result obtained also corroborates the TEM results; the IPA has less layers compared to ethanol, methanol, and water. According to literature, a monolayer of ZrS_2 exfoliated using mechanical exfoliation had a thickness of about 0.9-1.0 nm and bilayer thickness of about 1.6 nm^{23,25}. There is a possibility that the thickness of nanosheets with liquid exfoliation may be higher than mechanical exfoliation since mechanical exfoliation produces good quality nanosheets compared to liquid exfoliation. The thickness of IPA, ethanol and methanol exfoliated sheets have thicknesses of 31.25 nm, 58.59 nm and 97.66 nm respectively, which may correspond to 30-39 layers, 59-73 layers and 97-122 layers respectively.

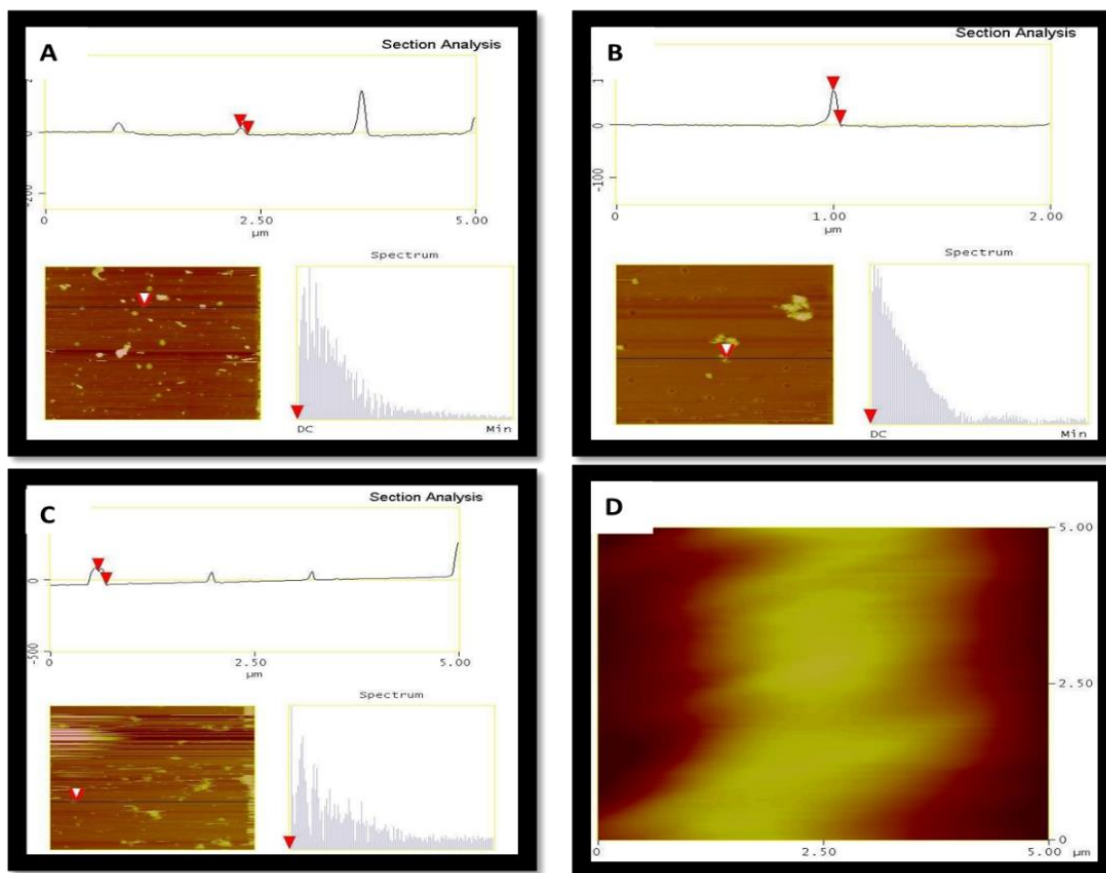


Figure 5.7: AFM micrographs, height, and spectrum of exfoliated ZrS_2 nanosheets (a) ethanol (b) IPA (c) methanol and (d) water.

5.5.5 SEM analysis

SEM revealed the surface morphological details of the nanomaterials; various morphologies were observed. **Figures 5.6a** and **5.6b** represent the micrographs of the bulk examples. It revealed the hexagonal morphology of ZrS_2 with multilayers. Figure 5.6c shows the homogeneous distribution of the nanomaterials with good dispersion. Figure 5.6d also shows a layered structure of the sample with a proper dispersion. Figures 5.6e and 5.6f show the nanomaterials with a layered structure. IPA exfoliated nanosheets seemed more homogenous with good dispersion over other alcohols used; this may be ascribed to IPA having a higher surface energy than the other alcohol members. Figures 5.8g and 5.8h showed good dispersion and homogeneous distribution of the nanomaterials. Amide solvents seemed more effective in exfoliation compared to other solvents; however, the toxicity and high boiling point of amide solvents has necessitated researchers to look for a greener route of synthesis by using alcohols, water or a mixture of alcohol with water.

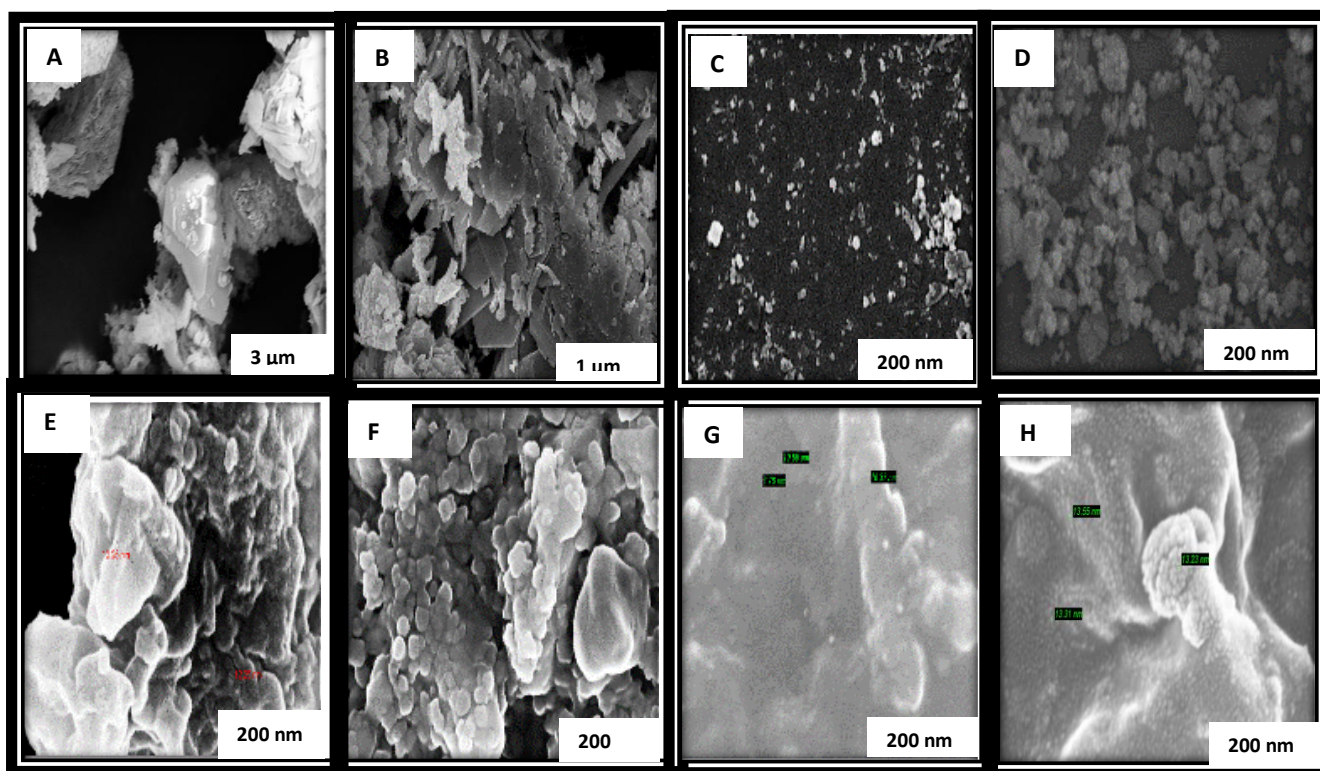


Figure 5.8: SEM images of ZrS_2 : (a) and (b) bulk sample (c) IPA exfoliated (d) H_2O exfoliated (e) MeOH exfoliated (f) EtOH exfoliated (g) CHP exfoliated (h) NMP exfoliated.

5.5.6 TEM analysis

Figure 5.8 A (i)- F(ii) show the different morphologies obtained by using several solvents. Figure 1A (i)-(ii) show CHP is very effective in the exfoliation of 2D materials, nanoparticles with a size of about 11 nm was determined with image J. The size corroborates what was obtained with SEM images. This is an indication that it will be a facile approach to obtain quantum dot morphology if the duration is slightly increased say up to 2.5 h. Figure 5.8B (i-ii) show properly exfoliated nanosheets with very few layers. Figure. 5.7C(i-ii) show nanosheets with many layers with IPA exfoliation. Figure. 5.7D (i-ii) show water can also be as effective in the exfoliation of 2D materials; however, small pore-like pattern can be easily seen on the nanosheets which may be because of water adsorption on the surface of the material. Figure 5.9E (i-ii) show that methanol is the least effective in exfoliation of the bulk sample, the layers are not distinct compared to other solvents used in this study. In Figure 5.9F (i-ii), ethanol seemed to be effective as well in the exfoliation of ZrS₂ bulk materials.

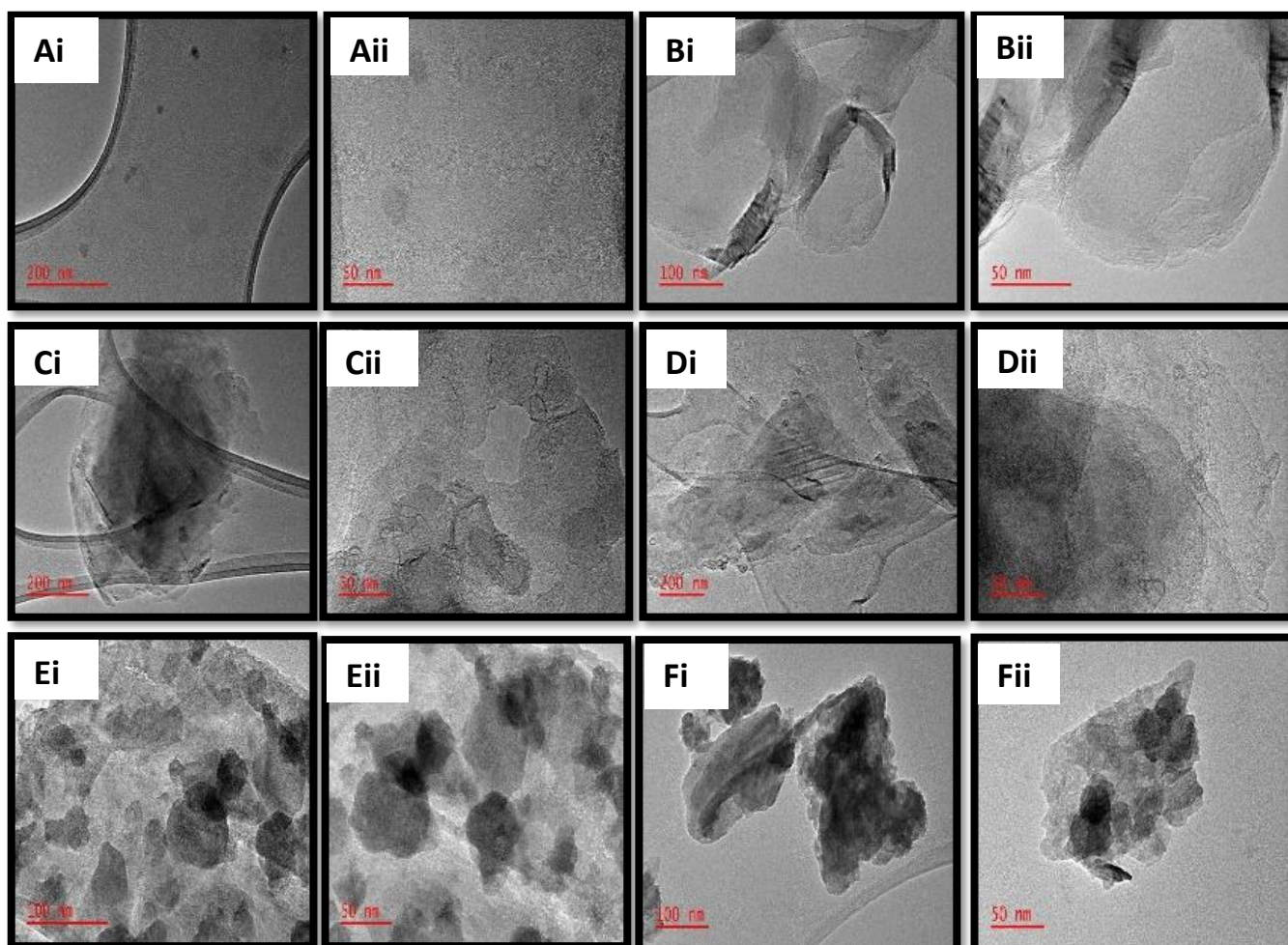


Figure 5.9: TEM and HRTEM images of ZrS₂ (Ai) and (Aii) CHP exfoliated samples (Bi) and (Bii) NMP exfoliated samples (Ci) and (Cii) IPA exfoliated samples (di) and (Dii) H₂O

exfoliated samples (Ei) and (Eii) MeOH exfoliated samples F (i) and F (ii) EtOH exfoliated sample.

5.5.7 Energy dispersive x-ray spectroscopy (EDS) analysis

The chemical composition of bulk and exfoliated samples was conducted with SEM-EDS.

The SEM-EDS showed that bulk ZrS_2 is very stable at ambient environment with no traces of oxidation. The weight of the elements as shown in **Figure 5.10** revealed Zr: 59.57 % and S: 40.43, the values obtained are in harmony with those in literature. However, partial oxidation of the material has been reported by many authors when ZrS_2 exists in few or monolayer²³. From Figures 5.10 (b) –(g) it can be observed that the nanomaterial undergoes oxidation in ambient environment.

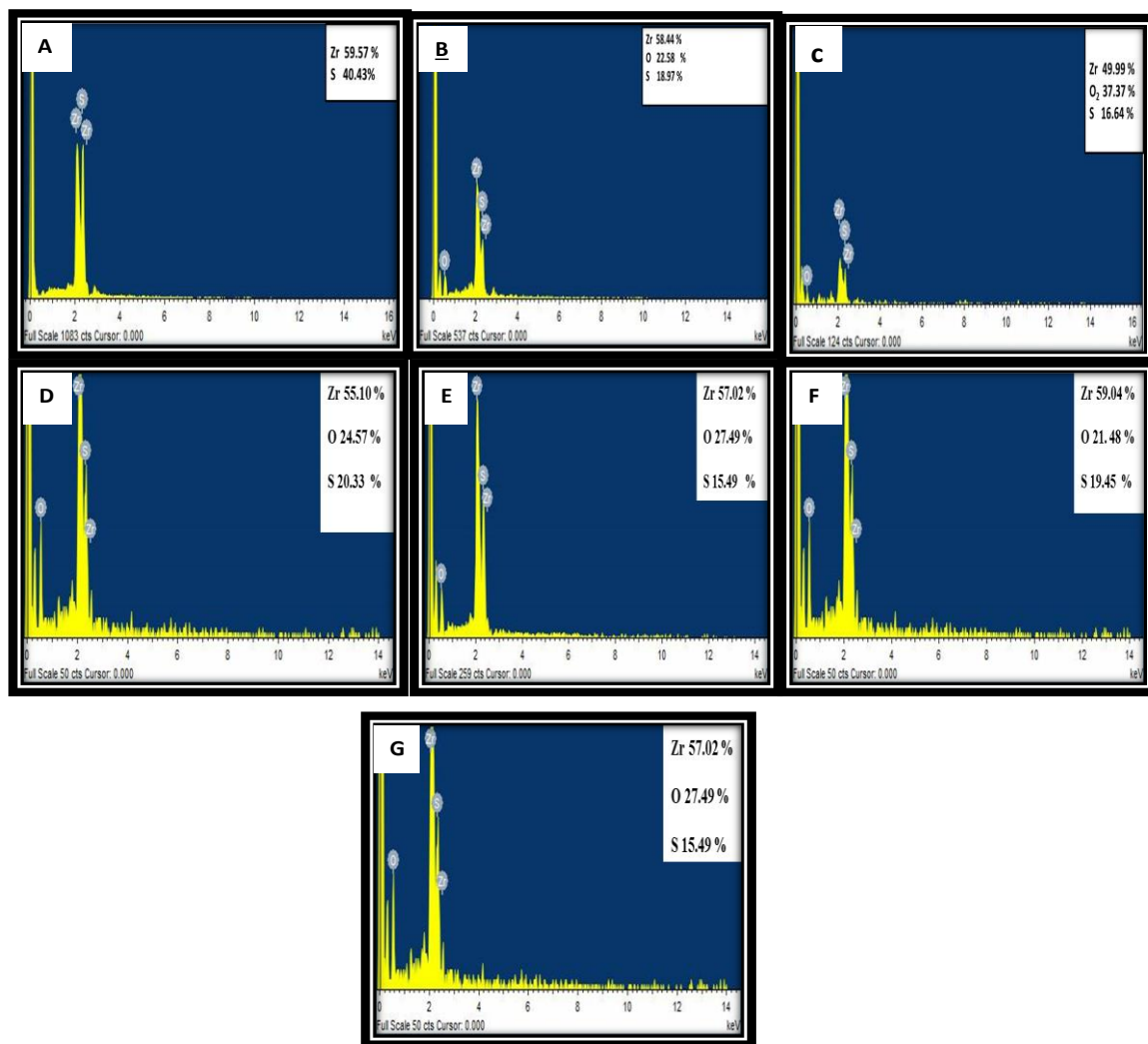


Figure 5.10: EDS of ZrS_2 (a) bulk sample (b) NMP sample (c) CHP sample (d) MeOH sample (e) EtOH sample (f) IPA sample (g) H_2O sample.

5.5.8 Thermogravimetry analysis

The thermogravimetry analysis of the ZrS₂ nanomaterials under N₂ shows four plateaus for IPA exfoliated nanosheets while bulk and CHP exfoliated show two plateaus each as shown in **Figure 5.11** For IPA loss of water at about 130 °C, the second mass loss at about 240 °C; this is ascribed to the loss of sulphur due to weak van der Waals forces within the material or organic materials resulting from organic solvent used for the exfoliation. Decompositions observed at 470 °C and 730 °C can be attributed to further decomposition of sulphur that is covalently bonded to Zr atoms.

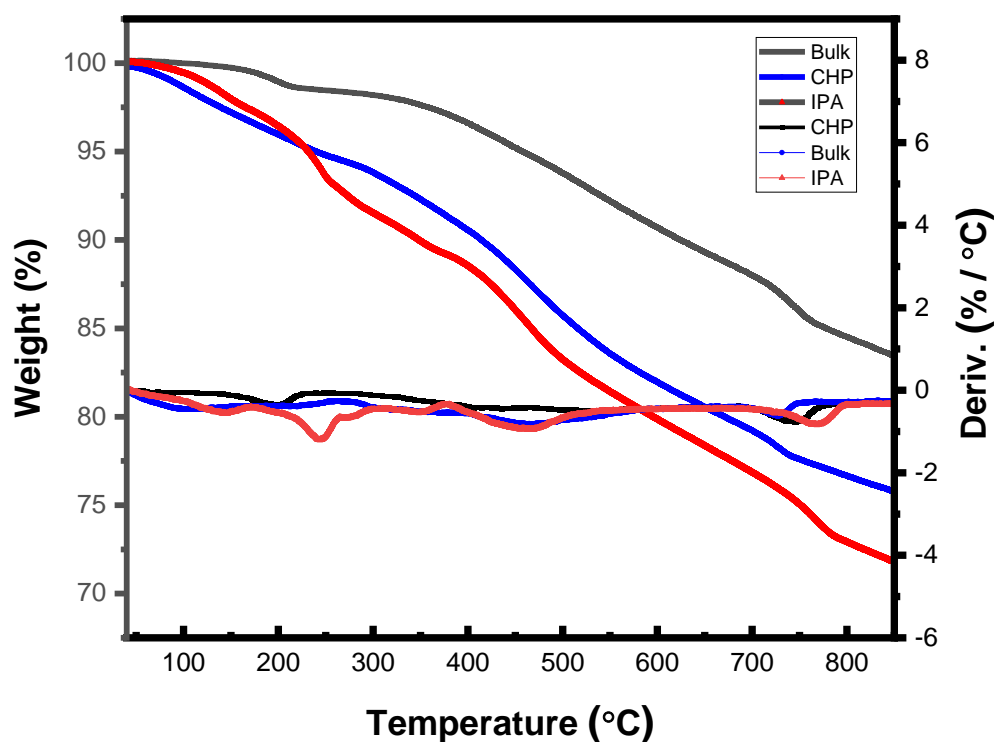


Figure 5.11: Thermogravimetry and derivative thermogravimetry curves of bulk, CHP and IPA exfoliated sample.

5.5.9. XPS analysis

From all the results as shown in Figures 5.12-5.14, the O1s peaks are made of three parts; firstly, metal oxide peak at 530.3 eV, 530.2 eV and 530.5 eV; C-O peaks at 531.8 eV, 531.8 eV and 532.1 eV and C=O peaks at 533.1 eV, 533.1 eV and 533.2 eV for NMP, CHP and IPA exfoliated samples respectively. The Zr3d orbital peaks correlated to both ZrS₂ and ZrO₂.

Additionally, due to possible contamination of ZrS₂ nanomaterials as a result of oxiphilicity nature of group IV TMDCs, oxidation is well noticed on the surface of the material; the O1s peak of ZrS₂ were observed in all the XPS spectrum can be ascribed to the molecules from the atmosphere. The Zr3d_{5/2} peaks for ZrO₂ and peaks ZrS₂ are located at 182.40 ,182.3 and 182.7 eV for NMP, CHP and IPA exfoliated samples respectively. The 3d_{3/2} peaks are positioned at 184.8, 184.7 and 182.7 eV respectively. It can be observed that a meagre disparity in the binding energy of IPA exfoliated sample from amide exfoliated samples exists, the peak Zr3d_{3/2} for IPA is slightly lower compared to other two samples. The values are consistent with literature²⁶. The S2p_{1/2} peaks are positioned at 162.1, 161.8 and 162.20 eV for NMP, CHP and IPA exfoliated samples respectively. The S2p_{3/2} peaks are found at about 160.7, 160.8 and 161.0 respectively. This is consistent with the literature for ZrS₂, S2p_{3/2} and S2p_{1/2} peaks are expected to be observed at about 163 eV and 162 eV respectively²⁷. As a result of oxidation and possible hydration of the material the S2p_{2/1} and S2p_{3/2} peaks belonging to sulphate anions are positioned at 169.8 eV, and 168.7 eV, 169.8 eV and 168.5 eV, 170.2 eV and 169.0 eV for NMP, CHP and IPA exfoliated nanomaterials. Similar observations have been reported in the literature²⁶. Likewise, the C1s peak also has 3 peaks at 284.6 eV, 286.3 eV and 288.7 eV for NMP sample; at 284.3 eV, 286.3 eV and 288.6 eV for CHP sample; and at 284.7 eV, 286.2 eV and 288.7 eV for IPA sample which are ascribed to C-C, C-O and O-C=O correspondingly.

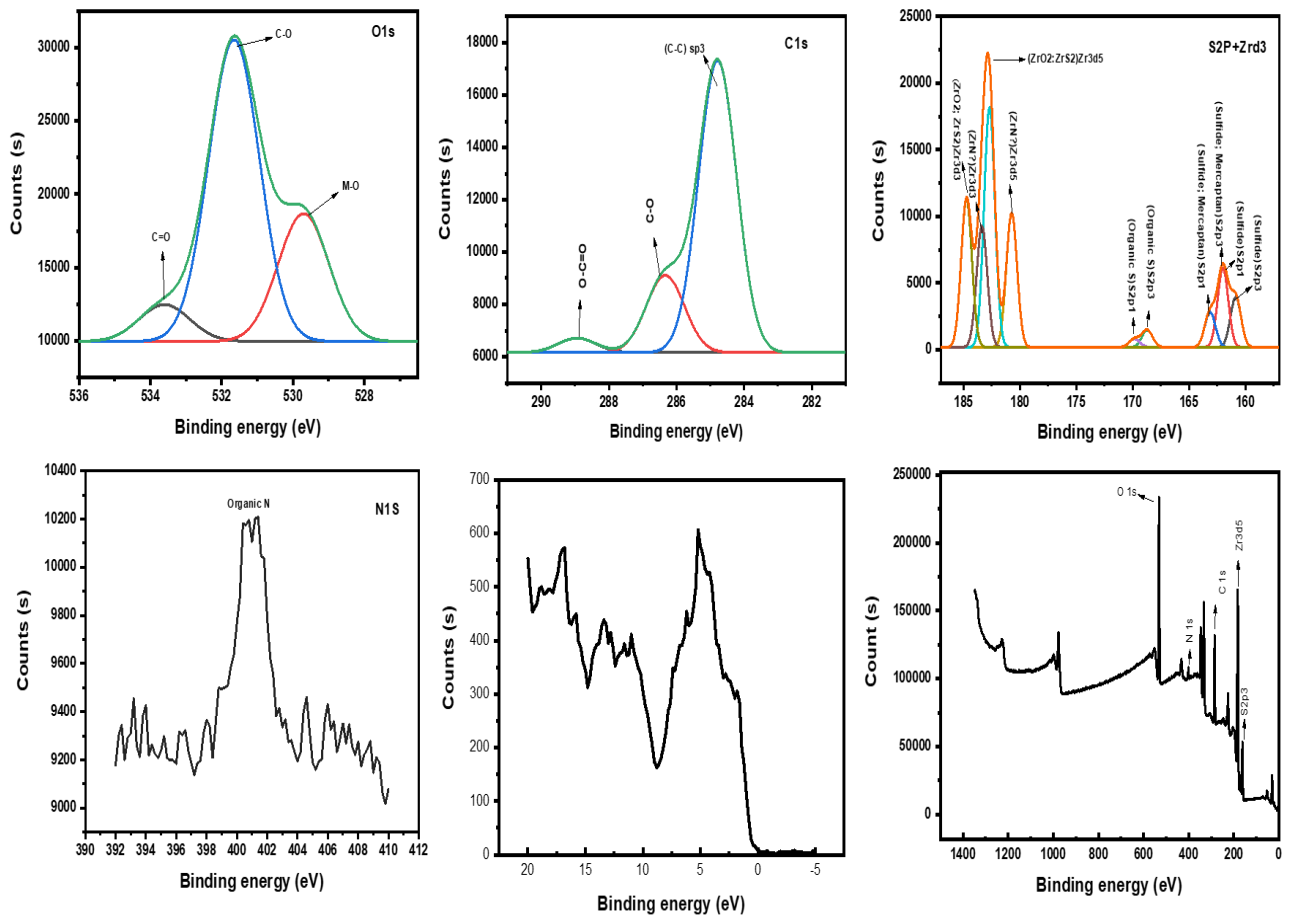


Figure 5.12: High resolution core level spectra of NMP exfoliated ZrS₂ nanosheets with focus on O1s, C1s, S2p+Zr3d, N1s, valence and survey spectrum.

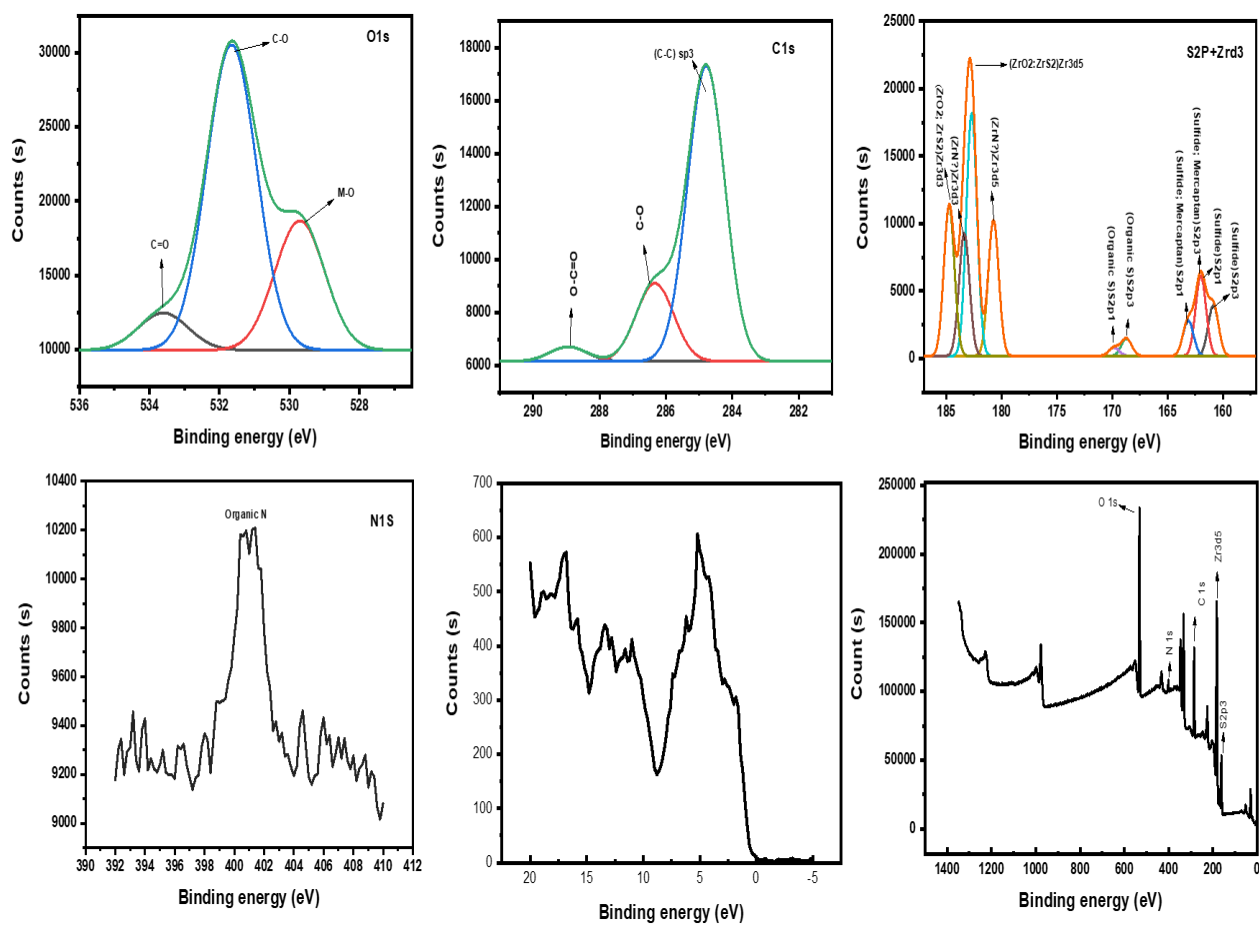


Figure 5.13 High resolution core level spectra of CHP exfoliated ZrS₂ Particles with focus on O1s, C1s, S2p+Zr3d, N1s, valence and survey spectrum.

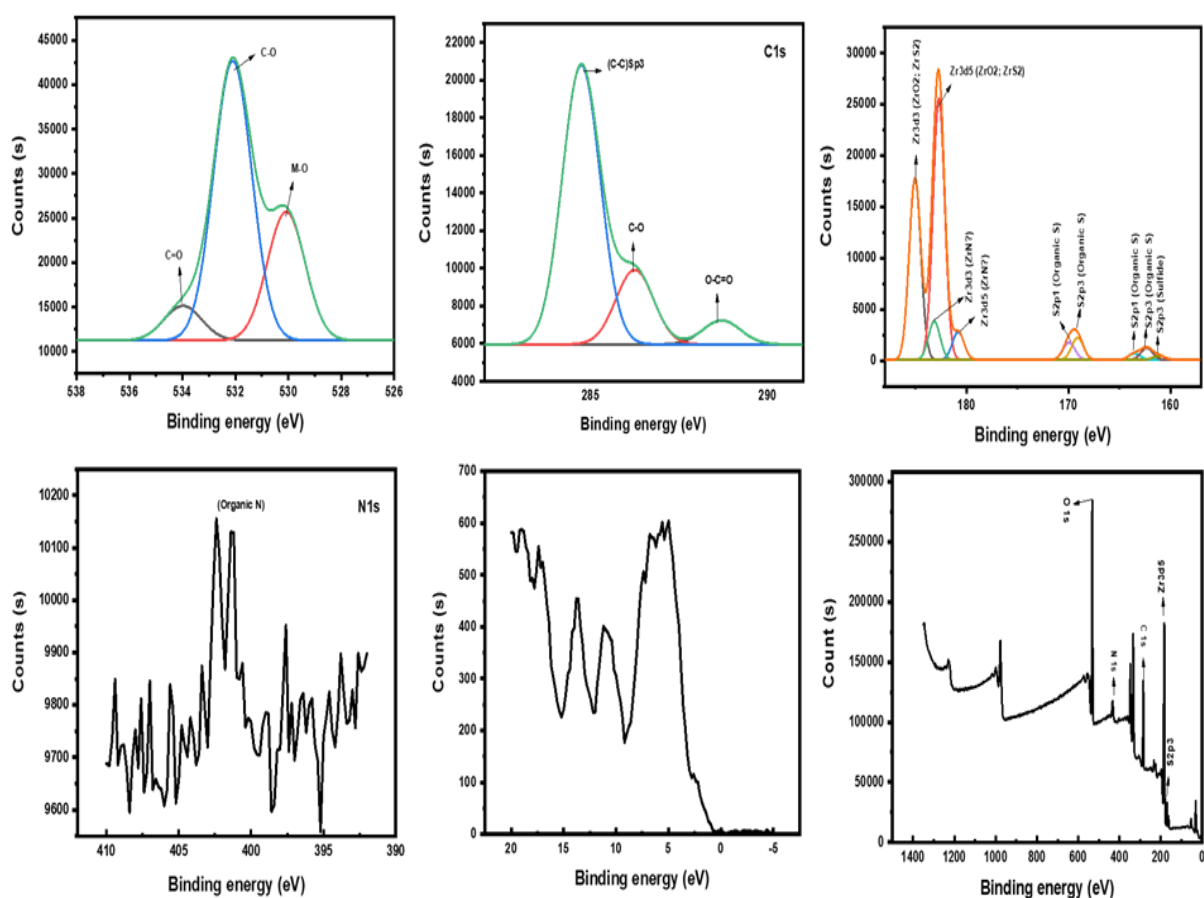


Figure 5.14: High resolution core level spectra of IPA exfoliated ZrS_2 nanosheets with focus on O1s, C1s, S2p+Zr3d, N1s, valence and survey spectrum.

5.6 Conclusion

In summary, we have illustrated a facile method of production of nanoparticles. Few layered nanosheets of ZrS_2 were satisfactorily exfoliated from bulk ZrS_2 sample via liquid exfoliation with CHP, NMP, IPA ethanol, methanol and water. The use of alcohols and water provided a green route of synthesis of few layers 2D materials with a direct band gap. IPA provided a good dispersion of the nanomaterial over other alcohols and water which were stable with no traces of degradation in ambient environment for several days. The nanomaterials could find great application in sensors, photodetectors, solar cells, fiber lasers, optics, tribology and catalysis.

5.7 References

1. Kaur, H., Yadav, S. and Srivastava, A.V., 2016. High Yield Synthesis and Chemical Exfoliation of Two- Dimensional Layered Hafnium Disulphide. *RSC Adv*, 9 (54) pp. 1-20.
2. Yin, J., Zhu, F. and Lai J., 2019. Hafnium Sulfide Nanosheets for Ultrafast Photonic Device. *J advanced optical materials*, 1801303, pp.1-8.
3. Pandit, A., and Hamad, B., 2021. The effect of finite-temperature and anharmonic lattice dynamics on the thermal conductivity of ZrS₂ monolayer: Self-consistent phonon calculations. *J Phys Condens Matter*, 33(42), pp.1-23.
4. Mattinen, M., Popov, G. and Vehkamäki, M., 2019. Atomic Layer Deposition of Emerging 2D Semiconductors, HfS₂ and ZrS₂, for Optoelectronics. *Chem Mater*, 31(15), pp. 5713-5724.
5. Wen, Y., Zhu, Y. and Zhang, S., 2015. Low temperature synthesis of ZrS₂ nanoflakes and their catalytic activity. *RSC Adv*, 5(81), pp. 66082-66085.
6. Li, L, Lv, R., and Wang, J., 2019. Optical nonlinearity of ZrS₂ and applications in fiber laser. *Nanomaterials*, 9(3), pp.315
7. Li, L., Fang, X. and Zhai, T., 2010. Electrical transport and high-Performance photoconductivity in individual ZrS₂ nanobelts. *Adv Mater*, 22 (37), pp. 4151-4156.
8. Nguyen, H.T.T., Hoang, D.Q. and Dao, T.P., 2020. The characteristics of defective ZrS₂ monolayers adsorbed various gases on S-vacancies: A first-principles study. *Superlattices Microstruct*, 140, pp. 106454
9. Ma, J., Liu, K. and Jiang, J., 2020. All optic-fiber coupled plasmon waveguide resonance sensor using ZrS₂ based dielectric layer. *Optical*, 28(8), pp.11280-11289.
10. Jana, M.K., and Rao, C.N.R., 2017. Transition Metal Dichalcogenides and Other Layered Materials. *2D Inorg Mater beyond Graphene*, pp.1-65.
11. Zhao, W., Jiang, T. and Shan, Y., 2018. Direct exfoliation of natural SiO₂-containing molybdenite in isopropanol: A cost efficient solution for large-scale production of MoS₂ nanosheetes. *Nanomaterials*, 8(10), pp. 843.

12. Yang, H. Li, W., Wang, G. and Sun, Y., 2020. Ultrafast mode-locked fiber laser with zirconium disulfide on D-shaped fiber. *Infrared Phys Technol*, 104, pp. 103143.
13. O'Neill, A., Khan, U., Nirmalraj, P.N., Boland, J., and Coleman, J.N., 2011. Graphene dispersion and exfoliation in low boiling point solvents. *J Phys Chem C*, 115(13), pp. 5422-5428.
14. Li, N., Wang, Y. and Sun, H., 2020. Resistive switching behaviors and mechanisms of HfS₂ film memory devices studied by experiments and density functional theory calculations. *Appl Phys Lett.*, 116(6), pp 63503.
15. Ahmad, H., Kahar., N.H.A., Yusoff, N., and Reduan, S.A., 2021. Thulium-holmium doped fiber laser mode-locking with hafnium disulfide (HfS₂) coated on D-shaped fiber. *Optik (Stuttg)*. 2021;246, pp.167785.
16. Vacacela Gomez, C., Guevara, M. and Tene, T., 2021. The liquid exfoliation of graphene in polar solvents. *Appl Surf Sci*, 546, pp.149046.
17. Vega-Mayoral, V., Tian, R. and Kelly, A.G., 2019. Solvent exfoliation stabilizes TiS₂ nanosheets against oxidation, facilitating lithium storage applications. *Nanoscale*, 2019;11(13), pp. 6206-6216.
18. Li, Y., Wang, H. and Chang, B., 2022. Intercalation assisted liquid phase production of disulfide zirconium nanosheets for efficient electrocatalytic dinitrogen reduction to ammonia. *Green Energy Environ*, 32, pp. 12-19.
19. Zhou, L.L., Wu, H.B., Li, X.M., Tang, L. B, and Guo, W. and Liang, J., 2019. ZrS₂ quantum dots: Preparation, structure, and optical properties. *Wuli Xuebao/Acta Phys Sin*, 68(14), pp. 148501.
20. Thiyagarajan, R., Beevi, M.M., and Anusuya. M., Nano structural characteristics of Zirconium Sulphide thin films. *American science*, 5(6), pp. 6-12.
21. Sherrell, P.C., Sharda, K. and Grotta, C., 2018. Thickness-Dependent Characterization of Chemically Exfoliated TiS₂ Nanosheets. *ACS Omega*, 3(8), pp. 8655-8662.
22. Mattinen, M., Popov, G. and Vehkamäki, M., 2019. Atomic Layer Deposition of Emerging 2D Semiconductors, HfS₂ and ZrS₂, for Optoelectronics. *Chem Mater*, 31(15), pp. 5713-5724

23. Mañas-Valero, S., García-López, V., Cantarero, A., and Galbiati, M., 2016. Raman spectra of ZrS₂ and ZrSe₂ from bulk to atomically thin layers. *Appl Sci*, 6(9), pp. 264.
24. Zhang, M., Zhu, Y. and Wang, X., 2015. Controlled Synthesis of ZrS₂ Monolayer and Few Layers on Hexagonal Boron Nitride. *J Am Chem Soc*, 137(22), pp. 7051-7054.
25. Hoffman D.M., 1994. Chemical vapour deposition of nitride thin films. *Polyhedron*, 13(8):1169-1179. doi:10.1016/S0277-5387(00)80253-3
26. Shimazu, Y., Fujisawa, Y., Arai, K., Iwabuchi, T., and Suzuki K., 2018. Synthesis and Characterization of Zirconium Disulfide Single Crystals and Thin-Film Transistors Based on Multilayer Zirconium Disulfide Flakes. *ChemNanoMat*, 4(10),1078-1082.
27. Zhu, Y., Wang, X., Zhang, M., Cai., C. and Xie. L., 2016. Thickness and temperature dependent electrical properties of ZrS₂ thin films directly grown on hexagonal boron nitride. *Nano Res.*, 9(10), pp.2931-2937.

CHAPTER 6: POLYANILINE AND ZIRCONIUM DISULPHIDE NANOCOMPOSITE AND ITS APPLICATION FOR CHEMICAL SENSING OF ALCOHOLS AND ACETONE

6.1 Introduction

It is about sixteen decades now ever since the existence of polyaniline (PANI); however, its conductive nature was only discovered just four decades ago. Polyaniline as a conducting organic polymer found a great application in sensors (chemical and biological) due to its ease of production, environmental stability, and reversible redox chemistry, redox capacitors, catalysis, batteries, fuel cells, display devices, separation membranes, and anticorrosion coatings^{1,2}. PANI is commonly fabricated using two methods: electrochemical polymerization and chemical polymerization methods. Moreover, the polymerization is commonly deployed in gas sensing applications since it can be easily tailored to fabricate nanostructures and various morphologies compared to the other method. 1D dimensional PANI are the mostly fabricated morphologies such as nanofibers, nanowires and nanorods by using aniline (monomer) and ammonium persulphate (APS) which plays the role of an oxidant in acidic mediums. The protonation of the polyaniline is very essential; this is the means in which PANI turns out to be electrically conductive. PANI is utilized in chemical sensing to serve as a replacement over metal oxide semiconducting nanomaterials, provides the advantages of low cost, ease of fabrication, tunable conductivity, high porosity, and sensitivity at room temperature. However, PANI based sensors have few demerits such as poor response time, weak selectivity, low reproducibility, and poor stability. To counter these drawbacks, nanocomposites of polyaniline with 2D materials, carbon materials and metals have been used and they reportedly improved the response time and stability of PANI based sensors. Hence, proffering a solution to these demerits is very essential by using novel nanomaterials with a proper attribute for chemical sensing. Functionalization of PANI with transition metal dichalcogenides (TMDCs) have been reported in literature to enhance the sensor attributes arising from synergetic effects. More research has been reported on group VI TMDCs compared to group V and group IV. Generally, few works are available on group IVB despite theoretical findings showing these nanomaterials as possessing astonishing properties. For instance in relating to chemical sensing application, it was speculated that TiS_2 has more active sites for gas absorption than MoS_2 owing to crystal structure and bonding that existed between the metal and the sulphur atoms³. It was also predicted that monolayer ZrS_2 will be suitable for gas sensing. The author reported that a defect ZrS_2 with S-vacancies will behave as a better sensor compared to ZrS_2 with no defect⁴.

TMDCs are a set of novel materials that are yet to be explored extensively, scarcely any reports are available on the chemical sensing of group IV TMDCs. The few available reports are on TiS_2 , and very few reports are available on conducting polymers nanocomposite with TMDCs, therefore more extensive research is very paramount. ZrS_2 has only been demonstrated as an optical coupled plasmon waveguide resonance (CPWR) sensor but not as a chemiresistive sensor⁵. ZrS_2 is a novel 2D layered material with exotic features when in mono or few layers; which include fast electron transport, high carrier mobility and sizeable band gap. The material is environmentally friendly, has good thermodynamic stability, very abundant in the earth's crust unlike rare earth metals which are not cost effective and very limited in nature^{4,6}. There are weak van der Waals forces that exist in between the layers and covalent bonds within the materials, it possesses outstanding electronic properties and large specific surface areas owing to high surface to volume-ratio. Kishoro *et al* was the first to report on chemical sensing of group IVB TMDCs in which TiS_2 was demonstrated for the sensing of O_2 and N_2 at temperature of 50 °C. The sensor displayed a short response time but a very poor recovery time.⁷ Shokouh *et al* reported a fascinating recovery with an ultra-fast response time of 2 s and response time of 60 s for ethanol sensing by a nanohybrid of TiS_2 and polyvinyl polymer (PVP)³. Manjunata *et al* demonstrated nanohybrid of titanium disulphide and polyaniline (PANI/TaS_2) for humidity sensing with good sensitivity, rapid response time and recovery time⁸. Sakhuja *et al* investigated TiS_2 nanosheets towards H_2S and O_2 at room temperature. The sensor showed high sensitivity of 111.8 %, quick response-recovery times of 19.7 and 48 s respectively towards 4 ppm of H_2S ⁹. Shaukat *et al* recently reported on ZrSe_2 towards humidity with a range of 15-80% RH. The sensor displayed good sensitivity of 68 $\text{K}\Omega$, fast response-recovery times, good reproducibility and good stability.¹⁰ So recently, Sharma *et al* demonstrated TiS_2 sheets toward ammonia vapour, the sensor showed response and recovery times of 72 and 175 s at room temperature¹¹. Extensive investigation has been reported on NH_3 and NO_2 vapour sensing based on TMDC sensors such as MoS_2 , MoSe_2 , WS_2 , WSe_2 , SnS_2 and SnSe_2 , however very few reports are available on alcohols and acetone vapours sensing^{12,13,14,15,16,17}.

6.2 Chemicals and materials

Zirconium disulphide [99 %, ZrS_2 , C.C. Imelmann (pty) ltd], isopropyl alcohol [99 %, IPA MK Chemicals], ammonium persulphate [99.9%, APS, Sigma-Aldrich], aniline [99.9%, Sigma-

Aldrich] HCl 32% [associated chemical enterprises] were used as received without further purification. A mortar and pestle, a PS-20A sonicator bath with a power of 100 W.

6.3 Methods

6.3.1 Synthesis of PANI

In a typical synthesis, as shown in Figure 1, 1.5 g of ammonium persulphate (APS) and 1 ml of aniline were dissolved in two separate 250 ml beakers containing 25 ml of HCl. The aqueous solution of APS was slowly transferred into the second beaker containing aniline with constant stirring of the solution and reaction maintained at about 0 °C. This is very essential as the reaction is very exothermic, it may lead to decomposition of the polyaniline polymer formed. After a few minutes, the reaction went to completion and a green precipitate of polyaniline formed was obtained by filtration. The polyaniline formed was then washed with a solution of 1 M HCl to remove any unreacted aniline followed by multiple washing with distilled water. Finally, the polymer was dried in an oven at a temperature of 40 °C.

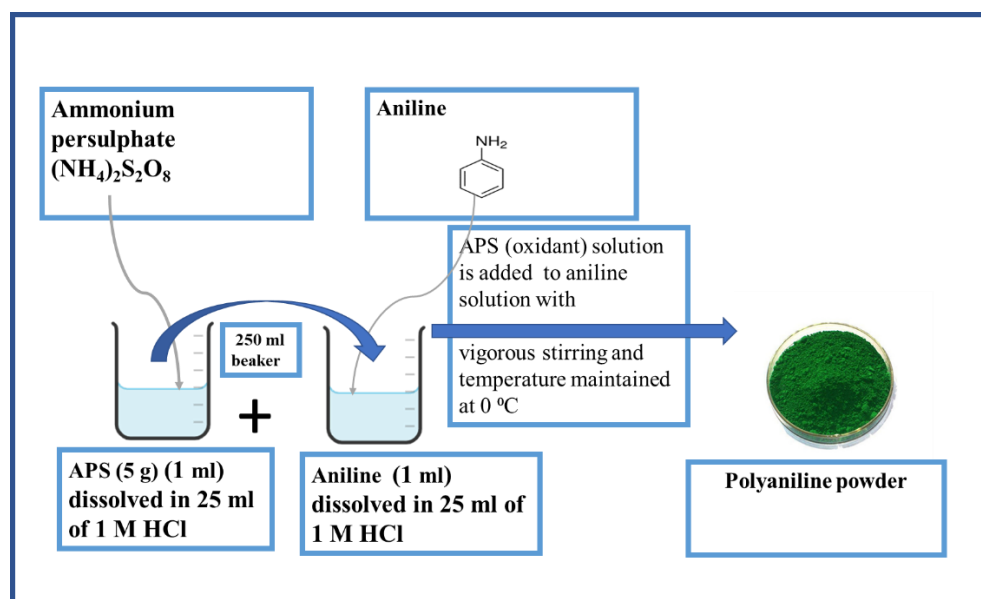


Figure 6.1: Schematic diagram of synthesis of PANI.

6.3.2 Synthesis of a nanocomposite of zirconium disulphide and polyaniline

A nanocomposite of zirconium disulphide and polyaniline was fabricated by introducing 5 mg of ZrS₂ into a vial containing 95 mg of polyaniline in isopropanol; and the vial was sealed and wrapped with parafilm. The vial was sonicated for 24 h after which the resulting solution was filtered, and the product dried at room temperature.

6.3.3 Sensor fabrication

The PANI-ZrS₂ based sensor was prepared on a printed circuit board (PCB) FR4 substrate. Interdigitated electrodes were patterned on the rectangular shaped PCB consisting of electroless nickel immersion gold electrodes of 18 pairs with a length of 7.9 mm and a space of 0.1 mm between each electrode. The sensing film was prepared by drop casting 15 µL of the film that was prepared by sonicating 5mg of nanocomposite of PANI-ZrS₂ in 500 µL of methanol for 10 min.

6.3.4 Gas sensing measurement

All electrical measurements were conducted at about 25 °C. An LCR-6300 10 Hz –300 KHz precision LCR meter coupled to a computer. The frequency and voltage were set at 10 KHz and 1.00 V respectively. The system was allowed to stand for few minutes before any measurement were done. The set-up for gas sensing is the same as the one reported in chapter four. The vapour sensing experiment was conducted at room temperature; the response values were recorded using a data logger (LCR). The vapour sensing properties were explored by injecting a measured volume of anhydrous alcohol (methanol) into a closed glass chamber (5 L) via a glass syringe. The concentration of the methanol vapour in the test chamber can be evaluated in ppm by using the following equation:

$$C = \frac{224\rho TV_s}{273MV} \times 100 \quad (6.0)$$

Where C represents concentration of methanol vapour (ppm), ρ is the density of the solvent (gML⁻¹), T is the temperature in Kelvin, V_s is the volume of the solvent, M is the molecular weight of the solvent. The response of the sensor is obtained as $S = (R_a - R_g) / R_a \times 100$, where R_a and R_g represented resistance in air and methanol vapour respectively. The duration involved by a sensor to complete 90% of the resistance change is known as response/recovery time. The sensor measurements were also conducted for ethanol, isopropanol, butanol, and acetone vapour. The sensor was exposed to methanol vapour at various concentrations. To ensure the

vapour reaches saturation point upon injection of the gas, the sensor was allowed to interact with the analyte gas for 300 s for proper adsorption and 200 s for the desorption of the vapour (recovery). The same procedure was conducted for ethanol, isopropanol, butanol, and acetone.

6.4 Characterization

Powder X-ray diffraction (PXRD) analysis was performed using a Bruker D2 phaser (D2-205530) diffractometer with Cu K α 1 radiation ($\lambda = 1.54060 \text{ \AA}$) at 30 kV and 10 mA. Measurements were taken using a glancing angle of the incident detector at an angle of 2° over 2θ angle range of $5\text{--}90^\circ$ in steps of 0.026° with a step time of 5 s at ambient temperature. Transmission electron microscopy (TEM) (Jeol JEM-2100F 200 kV) was used to analyse the morphology of the a-synthesized PANI and nanocomposite of PANI-ZrS₂. The surface area and porosity were measured using Micromeritics RS232 and porosity analyzer instrument. The surface area measurements were performed via N₂ adsorption/desorption and calculated by the Brunauer Emmett and Teller (BET) analysis method.

6.5 Results and discussions

6.5.1 XRD analysis

Figure 2 shows the XRD crystallographic structure of the ZrS₂/PANI nanocomposite. The ZrS₂ pattern matches hexagonal ZrS₂ indexed to the Joint committee on diffraction standard (JCPDS) card of 010605262. The following diffraction peaks: 15.45, 28.57, 32.34, 42.10, 46.25, 50.25, 52.68, 55.82, 60.94 and 67.58° which correspond to the (001) (100) (101) (102) (003) (110) (111) (103) (201) (202) planes of ZrS₂ respectively. Likewise, the XRD pattern of PANI shows diffraction peaks at 20.32 and 25.56° which correspond to (020) and (200) crystal planes of PANI in its emeraldine salt form¹⁸. The diffraction peaks at 35.20 and 44.20° are ascribed to the oxide of zirconium.

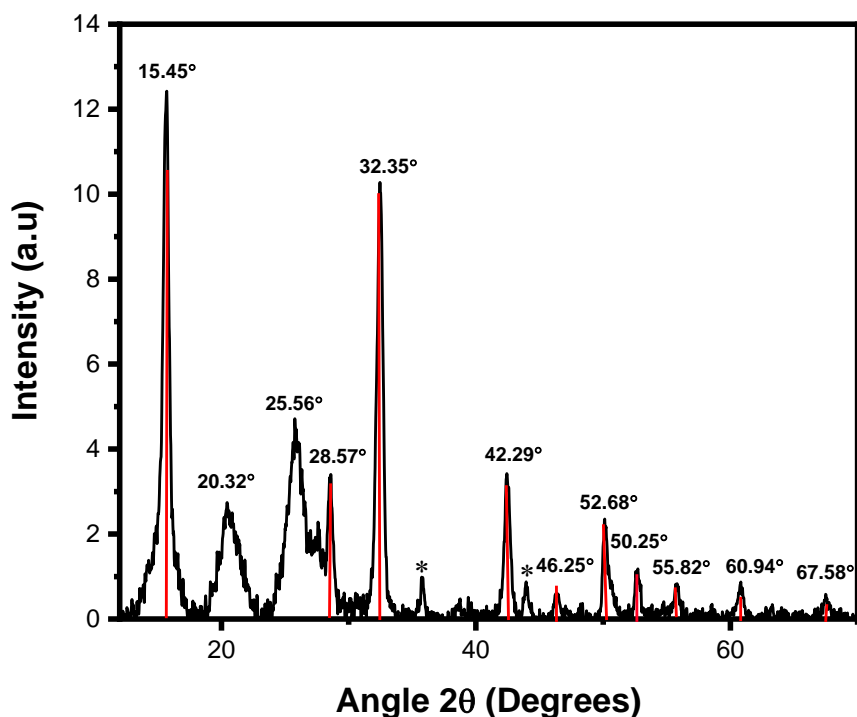


Figure 6.2 XRD pattern of PANI-ZrS₂ nanocomposite.

6.5.2 TEM analysis

The TEM micrographs show the morphologies of the pristine PANI and PANI-ZrS₂ nanocomposite. Both the pristine PANI and its nanocomposite exist in layers of nanosheets as shown in Figures 6.3 and 6.4A-6.4D, so it is quite difficult to distinguish between the two however, the dark stains represent nanosheets of ZrS₂ in PANI nanosheets. Several authors have reported on 1D PANI for different applications such as in gas sensing and supercapacitors compared to 2D dimensional PANI.

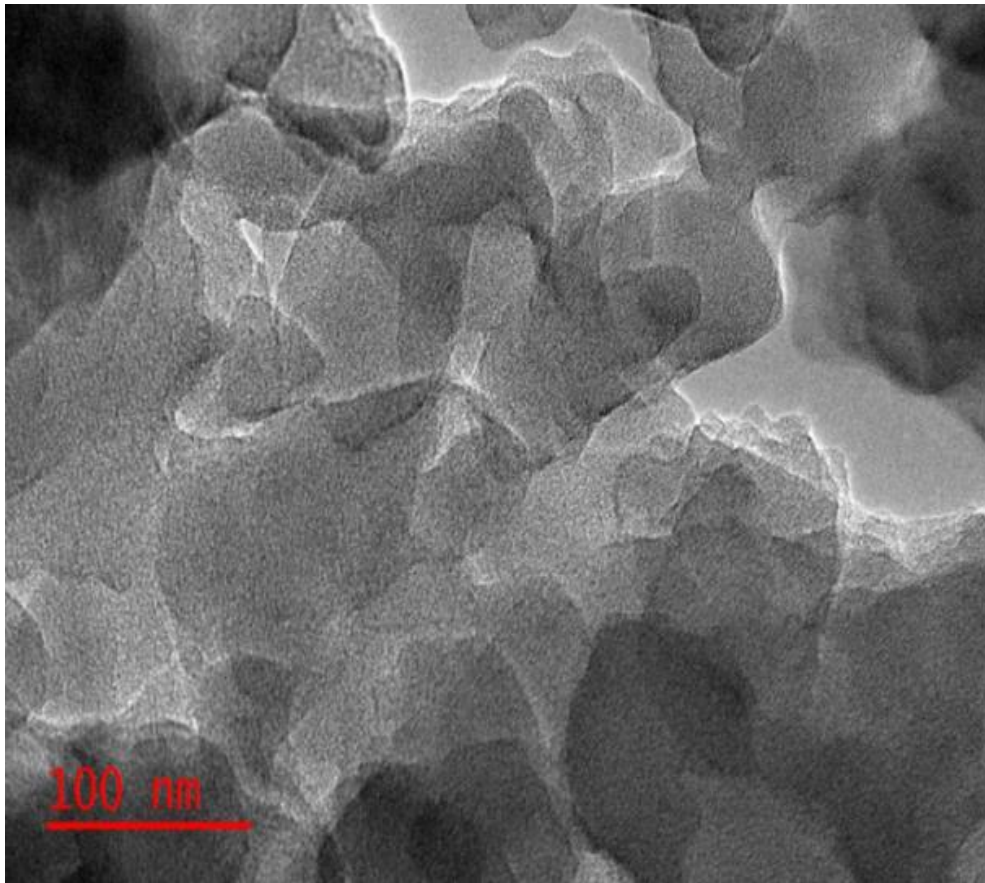


Figure 6.3: TEM image of PANI.

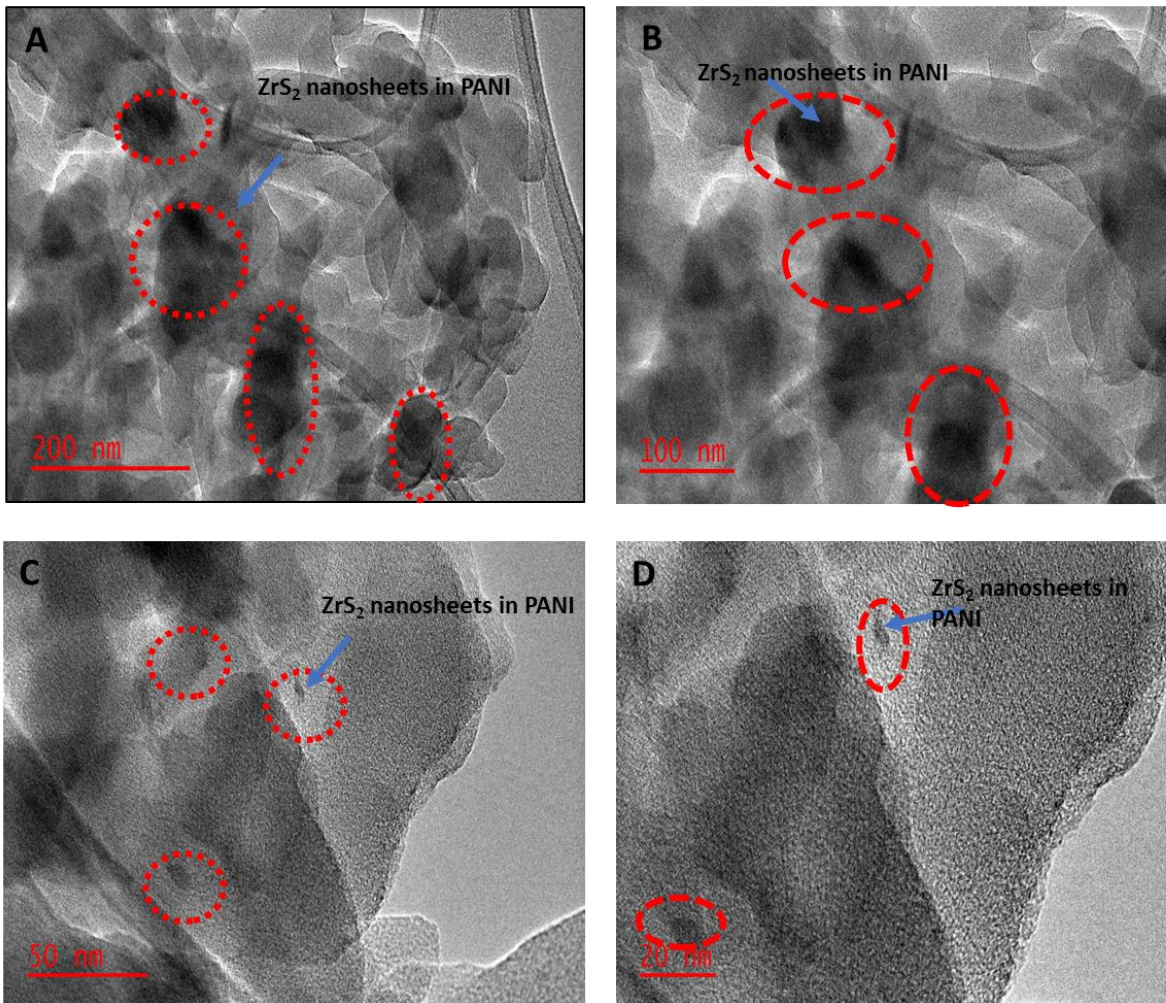


Figure 6.4 TEM images of PANI-ZrS₂ nanocomposite.

6.5.3 BET analysis

Figures 5A and 6A show nitrogen adsorption-desorption isotherms of PANI-ZrS₂ and PANI respectively; and 5B and 6B show pore-size distributions of PANI-ZrS₂ and PANI respectively. A steady increase in the volume of N₂ absorbed and desorbed definite can be noticed at about relative pressures at about 0.82-0.98 nm for the nanocomposite of PANI-ZrS₂ and pristine PANI, these represent type IV isotherm.¹⁹ The surface area of PANI increased from 27.87 m²/g to 28.95 m²/g with the nanocomposite and Barrett Joyner-Halenda (BJH) method was used to determine pore size distribution (PSD), the pore size increased from 0.18 to 0.19, these show the nanocomposite is microporous as well as pristine PANI. The improvement in the surface area and small pore size of the PANI-ZrS₂ contain plethora absorption sites to improve the interactions that exist with volatile organic molecules and the sensor.

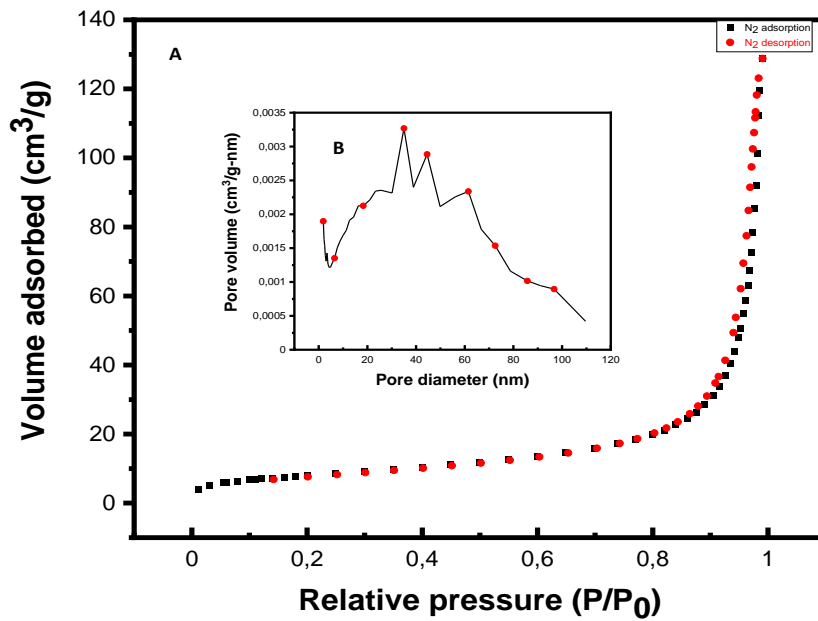


Figure 6.5 (A) Nitrogen adsorption-desorption isotherm for PANI-ZrS₂ (B) BJH pore size distributions of PANI-ZrS₂.

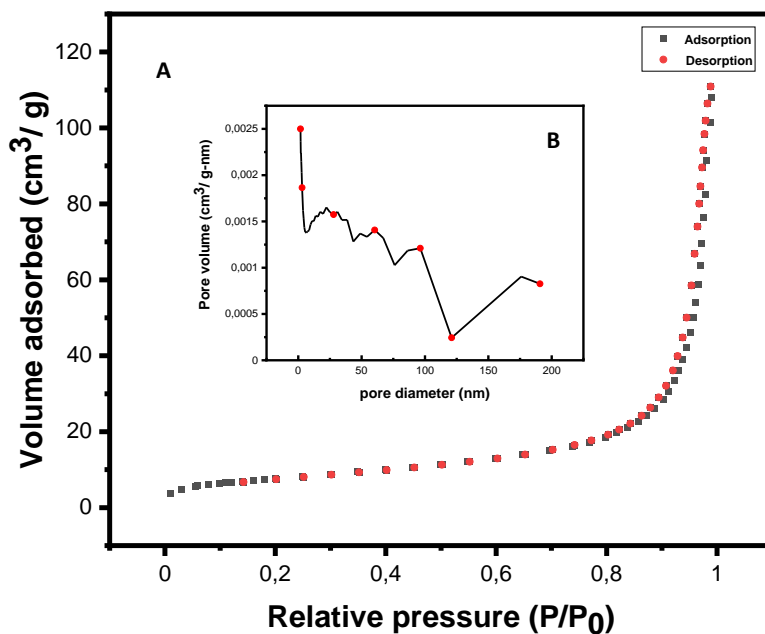


Figure 6.6 : (A) Nitrogen adsorption-desorption isotherm for PANI- ZrS₂ (B) : BJH pore size distributions of PANI.

6.6 Gas sensing of PANI-ZrS₂ nanocomposite

TMDCs and PANI sensors generally have the ability to sense chemical/gas vapours at room temperature, this gives them an advantage over metal oxide sensors that often require temperature that exceed room temperature. Operating a sensor at elevated temperature may lead to structural changes in the sensing material whose aftermath effects are instability and response disparity. PANI is an n-type chemiresistive sensor, PANI chains are made up of two structural units; a reduced [B-NH-B-NH] and oxidized [B-N=Q=N] repeating units, where B and Q represent benzenoid and quinoid rings respectively. Swelling of PANI is likely possible being a polymer with a rigid backbone. When a reducing chemical or gas such as alcohols is introduced to a PANI sensor, the reducing gas donates an electron to the polymer matrix, which leads to an increase in the resistance of the sensor as a result of change in the concentration of the sensing material holes. However, when reducing gases like NH₃, NO₂, H₂S and I₂ are injected, deprotonation of PANI occurs hence, the increase in resistance of the sensor. On exposure of the sensor to dry air, the opposite mechanism which is protonation of PANI occurs^{20,21}. There is change in conductance upon increase in vapour concentration. PANI and its substituted derivatives have been reported to be sensitive to first to fourth members of primary alcohols and heptanol vapours. Small chain alcohols result into a decrease in electrical resistance, however the reverse is the case with long chain alcohols. With ethanol, the doping or oxidation state remains the same and hence has negligible impact on the conductivity of PANI. Swelling of PANI backbones is very possible with ethanol therefore, there is an increase in the electrical resistance of the sensor. **Figure 6.7** shows the schematic representation of mechanism of PANI-ZrS₂ to ethanol vapour. Incorporating ZrS₂ with PANI provides a synergistic effect by improving the features of PANI sensor and enhancing the sensitivity of the sensor or boost its selectivity or both. ZrS₂ nanosheets integration with PANI, forms n-p heterojunction with a depletion layer. A change in depletion region will take place upon adsorption of gases by the nanocomposite²¹.

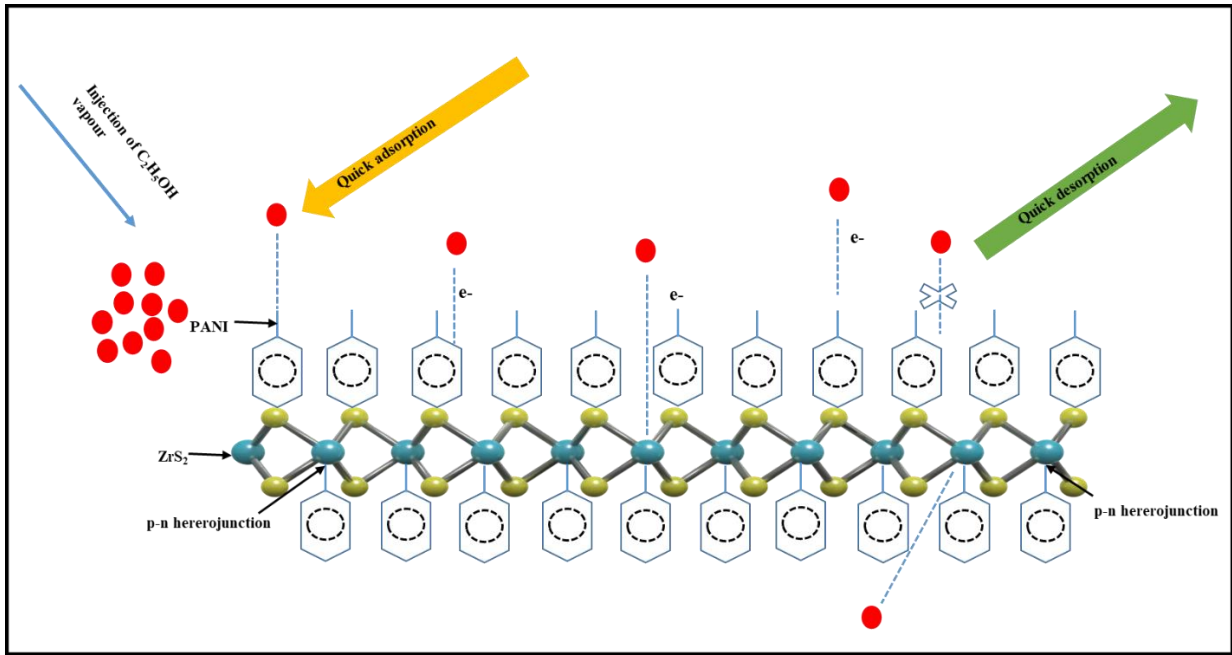


Figure 6.7: Schematic illustration of sensing mechanism of PANI-ZrS₂.

6.6.1 Primary alcohols and acetone sensing properties

Figure 6.8 depicts a static response curve of methanol vapour at room temperature in 45% RH to 555 ppm of methanol. A good signal with relatively weak noise to methanol gas can be deduced from the response curve. It took about 600 s for the sensor to attain saturation time upon exposure to the gas analyte. A total recovery of the sensor on exposure to air is also noticed.

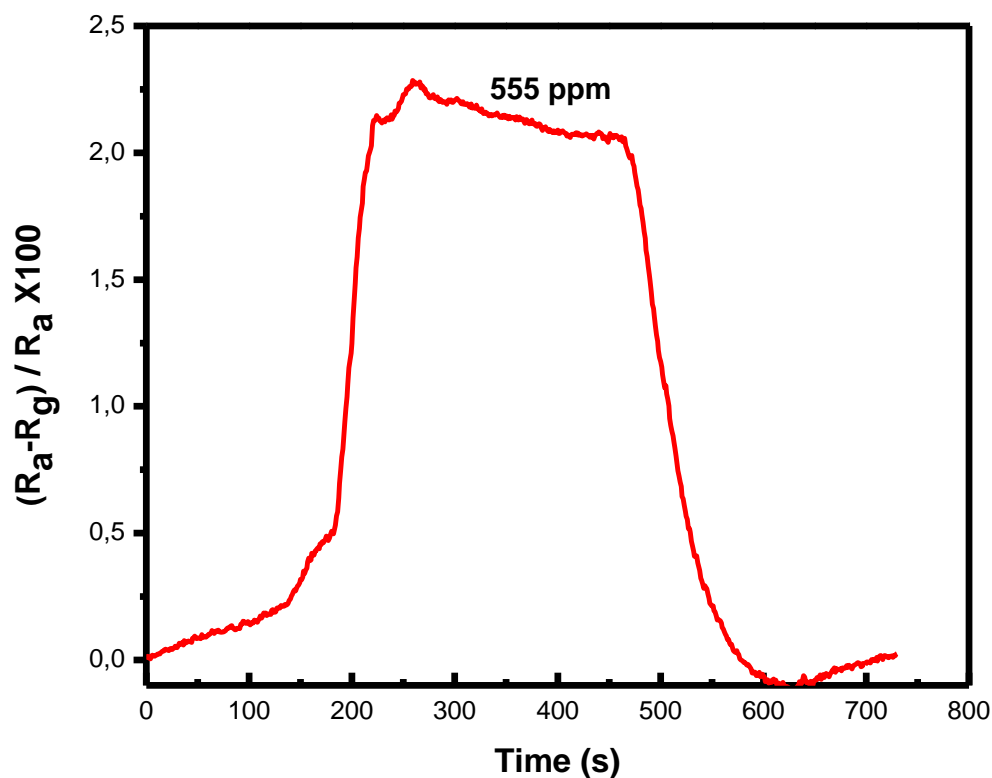


Figure 6.8: Static response of PANI-ZrS₂ towards methanol vapour at RT.

Figure 6.9A shows the static response curves of PANI and PANI-ZrS₂ sensors toward methanol vapour at different concentrations (111-555 ppm) at room temperature (RT) in 47% RH with exposure time of 300 s in gas and 200 s in air. **Figure 6.9B** shows response curves of the nanocomposite measured at different methanol concentrations (111-444 ppm). The measurement was conducted from low vapour concentration to high vapour concentration and vice versa.

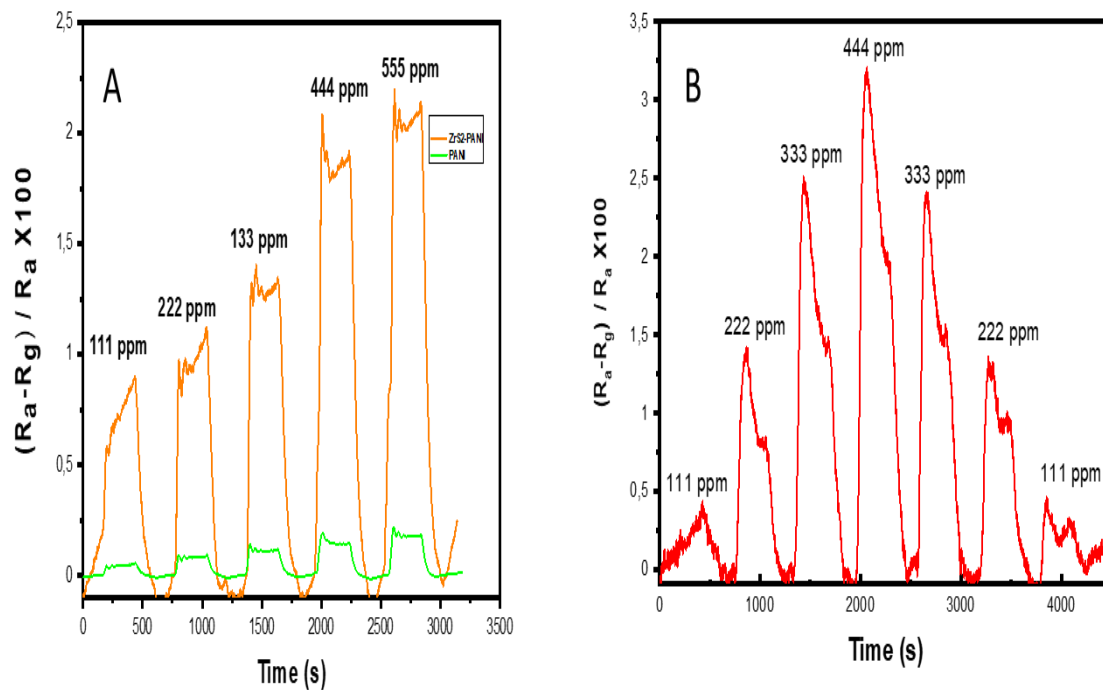


Figure 6.9: (A) Static response curves of PANI-ZrS₂ towards methanol vapour at RT (B) Response curves of the PANI-ZrS₂ sensor taken under various methanol vapour concentration.

Both sensors show a rise in response with increase in vapour concentration as seen in **Figure 6.10**.

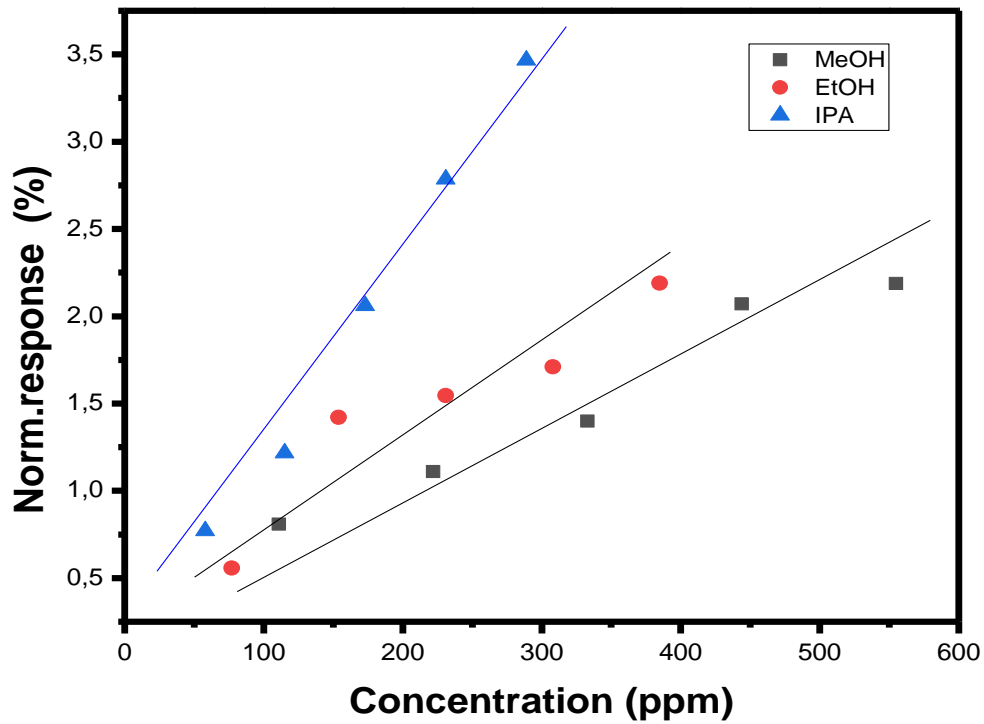


Figure 6.10: Normalized response of the PANI-ZrS₂ sensor towards methanol, ethanol, and isopropanol.

The PANI-ZrS₂ sensor showed a rapid response and recovery time 78 s and 69 s respectively to 555 ppm of methanol vapour (**Figure 6.11**).

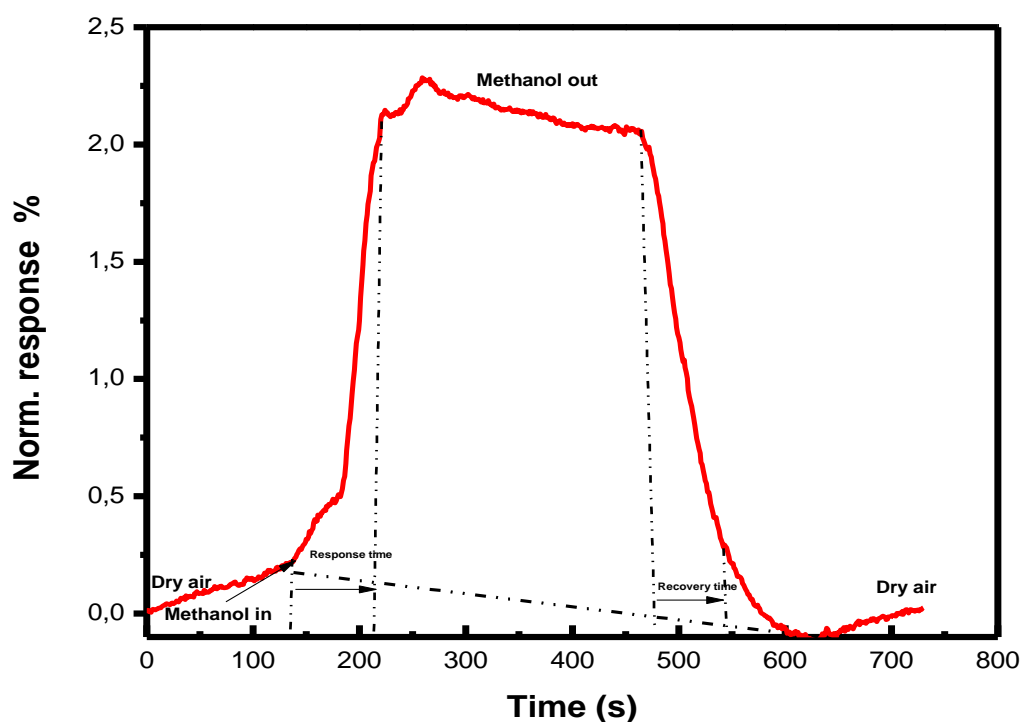


Figure 6.11: Response and recovery characteristic curve towards methanol.

There was a significant improvement on PANI response up to 9 folds due to the close interface that existed between the PANI and ZrS_2 . The enhanced response is due to synergistic effect. The time-dependent response and recovery curves of PANI- ZrS_2 to ethanol at 77 ppm and 385 ppm is depicted by **Figure 6.11**. The sensor response to 77 ppm ethanol vapour had a longer saturation time (> 600 s) while 385 ppm vapour concentration had a lesser saturation time (< 600 s). The sensor displayed a two - stage adsorption towards ethanol vapour which is shown by a rapid adsorption within the 180 s: thereafter a moderate adsorption at about saturation time of 600 s. This may be ascribed to possible defects of ZrS_2 or PANI or both resulting to differing affinity for ethanol vapour by the sensor giving rise to incremental saturation. Similar observation was reported by Mutuma *et al*, where untreated hollow carbon spheres resulted in two adsorption stages towards ammonia vapour ²².

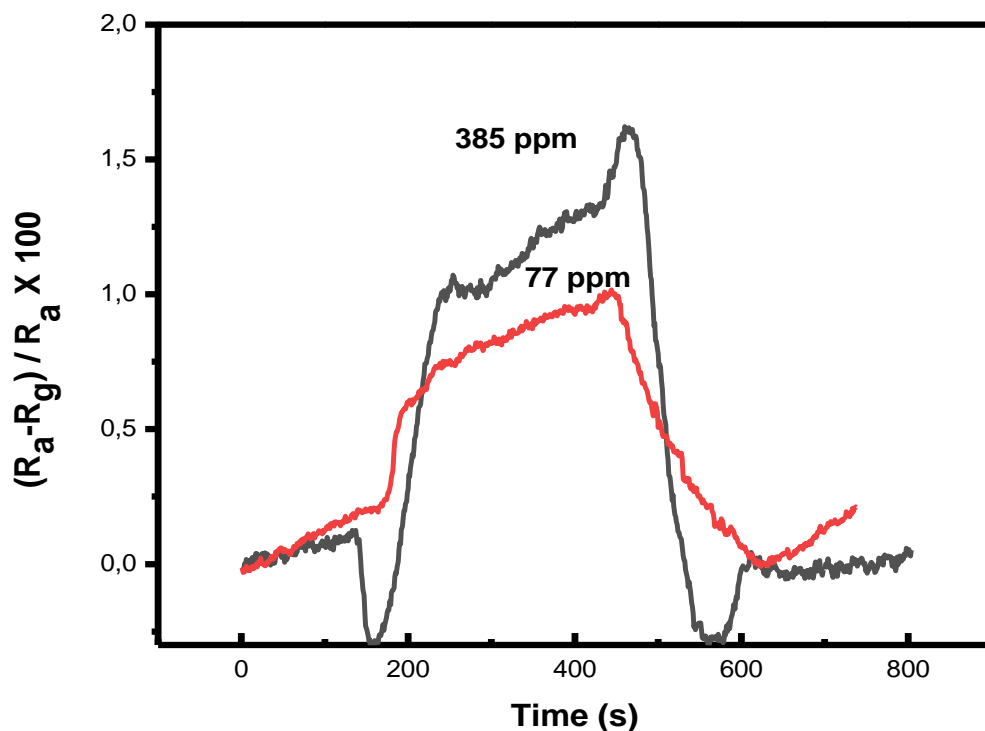


Figure 6.11: Typical response and recovery curves of PANI-ZrS₂ sensor to ethanol at 77 ppm and 385 ppm respectively.

Figure 6.12 depicts static response curves of PANI and PANI-ZrS₂ sensors toward ethanol vapour at varying concentrations (77-385 ppm) at RT in 50% RH with exposure time of 300 s and 200 s in gas and air respectively. Both sensors produced an increase in response with increase in vapour concentration introduced. The PANI-ZrS₂ nanocomposite amplified the performance of the sensor to ethanol vapour sensing characteristics in comparison to pristine PANI.

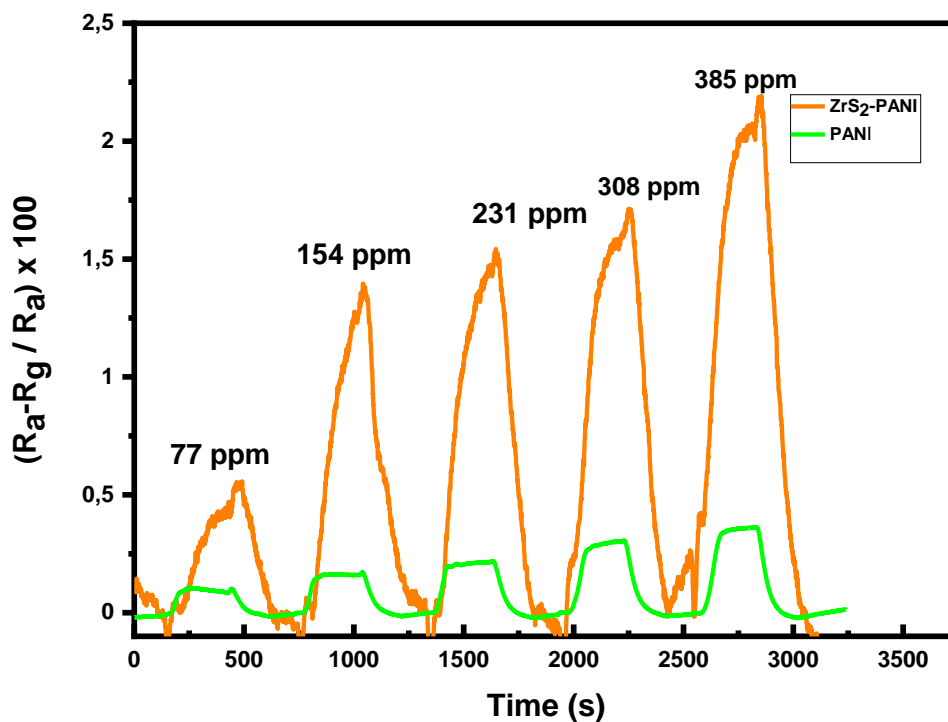


Figure 6.12: Static response and recovery curves of PANI-ZrS₂ towards ethanol vapour at RT.

The linear fitted plots linear is depicted in **Figure 6.10**, the response increases with increasing gas concentration. The sensor showed a quick response-recovery time of 83 s and 44 s to 385 ppm of ethanol vapour as shown in **Figure 6.13**.

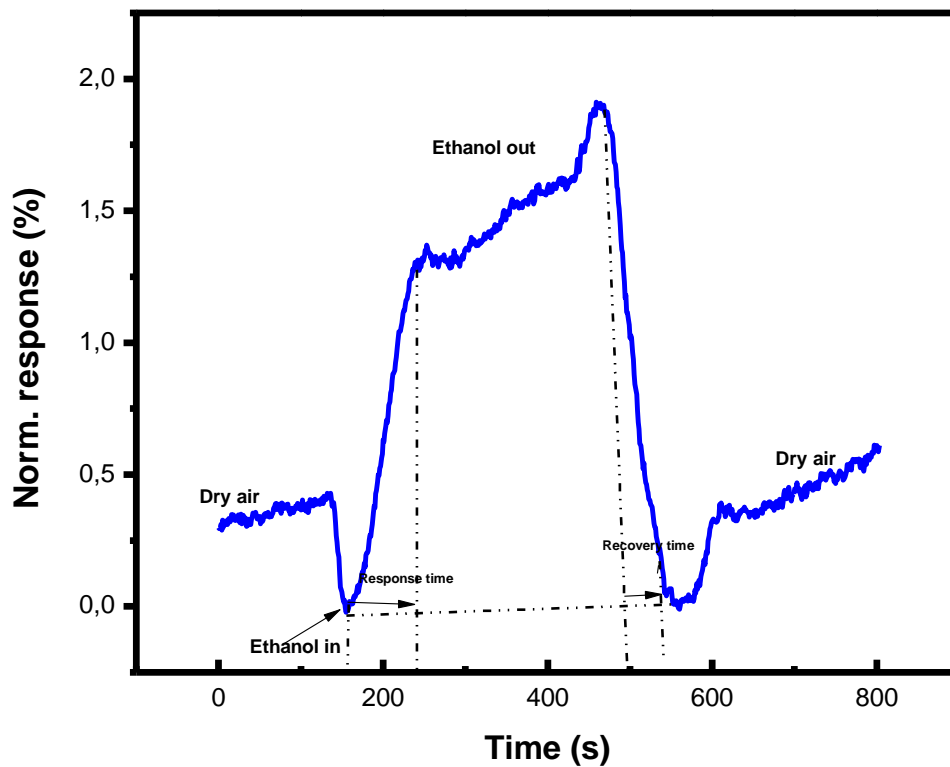


Figure 6.13: Response and recovery characteristic curves towards methanol.

The reproducibility of a sensor is a very paramount factor, as this determines the reliability of the chemical sensor for practical purposes. **Figure 6.14** depicts the reproducibility nature of the PANI-ZrS₂ film sensor to 385 ppm vapour at RT with three repetitive response-recovery curves. The sensor demonstrated a clear response-recovery output and stable three repetitive response-recovery curves for ethanol vapour sensing.

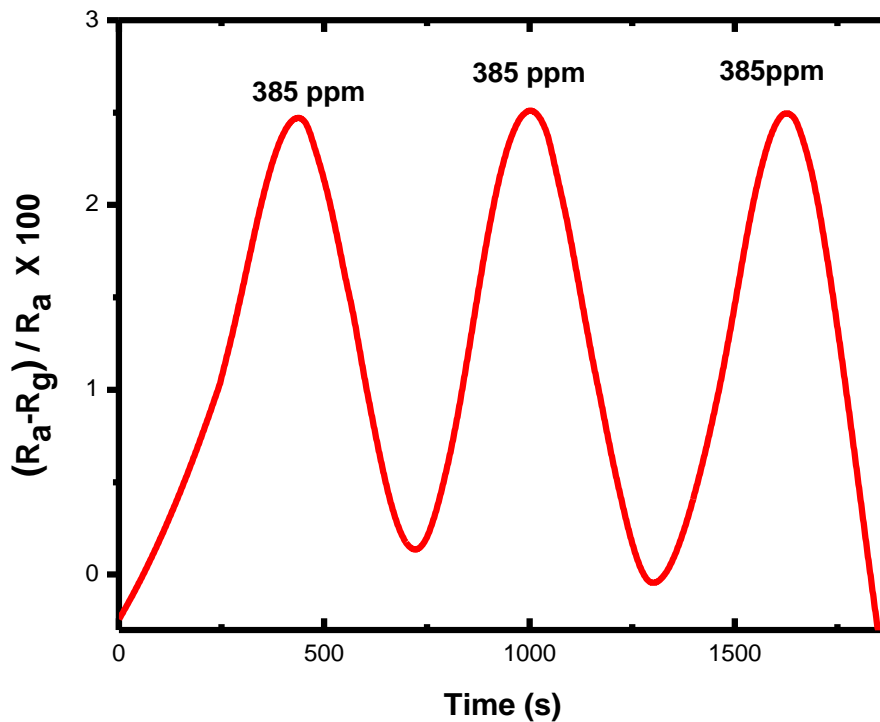


Figure 6.14 Repeatability of the PANI-ZrS₂ sensor to 385 ppm of ethanol vapour at RT.

Figure 6.15 depicts the static response curves of PANI and PANI-ZrS₂ sensors towards isopropanol vapour at distinct concentrations (58-289 ppm) at RT in 45% RH with exposure time of 300s in gas and 200 s in air. Both sensors show a rise in response with increase in vapour concentration as shown by the linear fitted plots (**Figure 6.10**). The sensitivity to methanol, ethanol and isopropanol was calculated from the slope of their linear fitted graphs in **Figure 6.10** as 0.43%, 0.58% and 1.04% respectively.

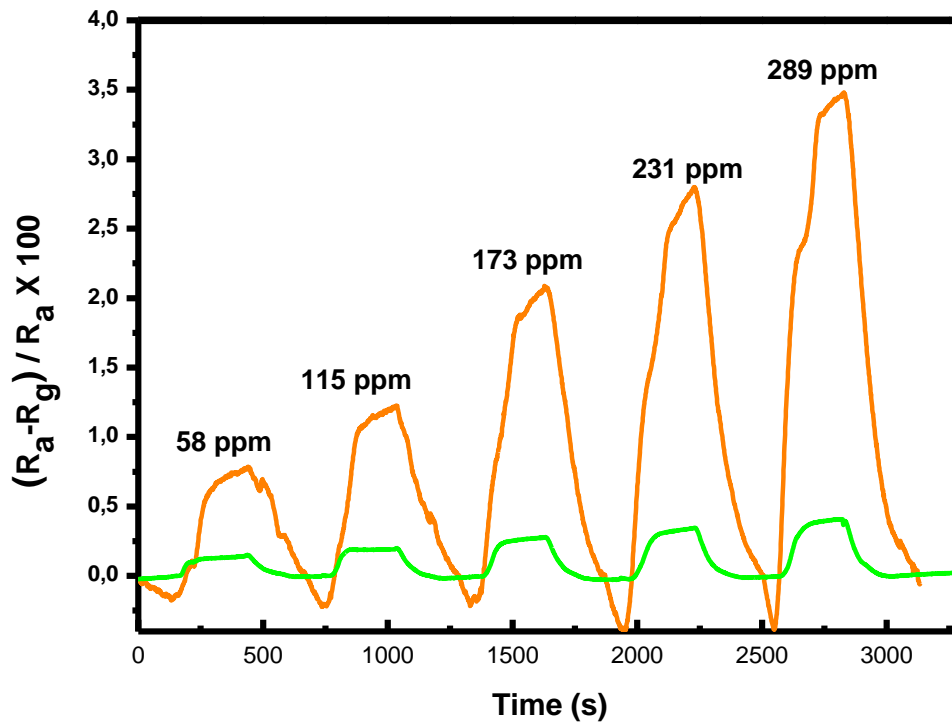


Figure 6.15: Static response and recovery curves of PANI-ZrS₂ towards isopropanol vapour at RT.

Figure 6.16 shows the sensitivity of the PANI-ZrS₂ sensor to different alcohols and acetone vapours. The sensitivity was extrapolated from their linear fitted plots. The response of the sensor to isopropanol is about a multiple of two compared to both ethanol and methanol vapours. The response to acetone vapour is the least.

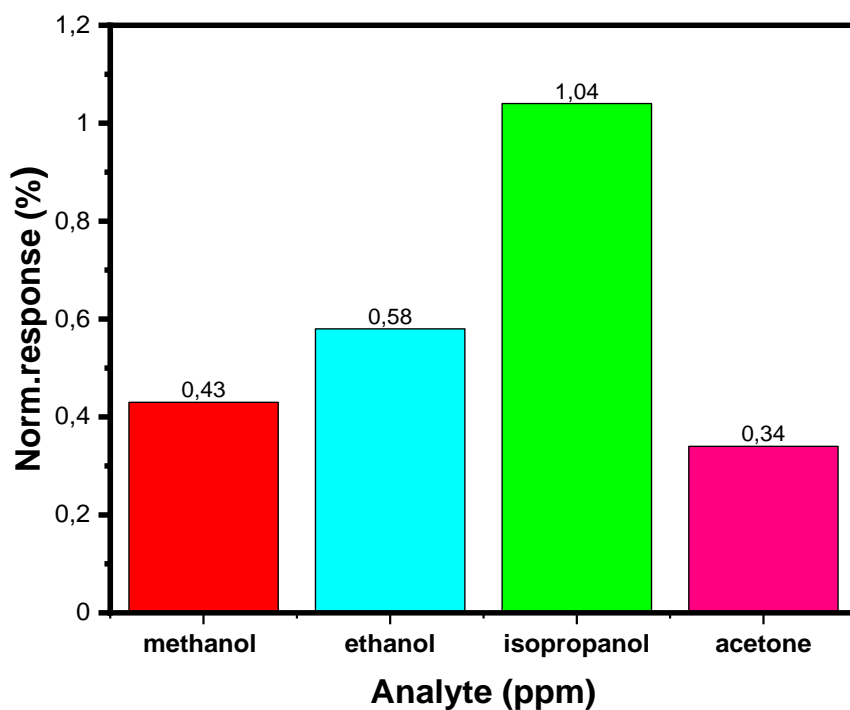


Figure 6.16 Comparison of PANI-ZrS₂ sensor towards methanol, ethanol and isopropanol vapour at RT.

Figure 6.17 showed static response curves of PANI and PANI-ZrS₂ sensors toward acetone vapour at varying concentrations (61-305 ppm) at RT in 50 % RH with exposure time of 300 s and 200 s in gas and air respectively.

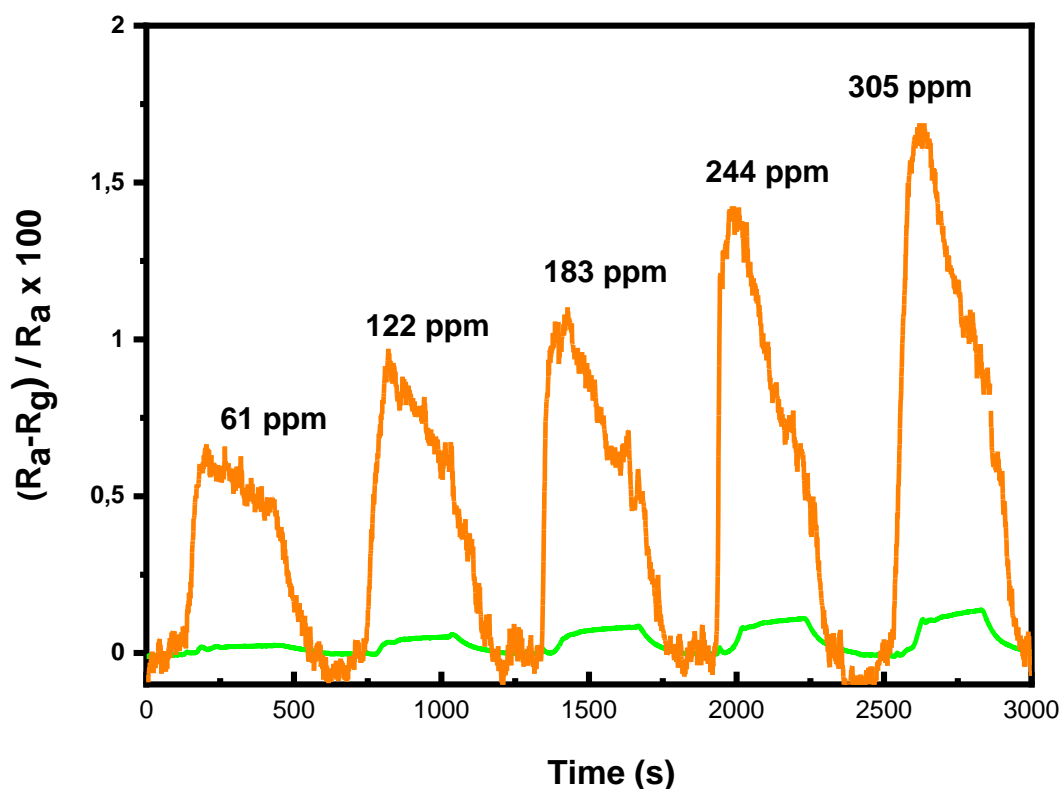


Figure 6.17: Static response and recovery curves of PANI-ZrS₂ towards acetone vapour at RT.

PANI sensor showed small response curve at 61 ppm to acetone vapour. The raw PANI sensor showed poor sensitivity towards acetone gas. A quick adsorption at the initial stage can be observed from the response curves after which a delayed adsorption towards the saturation time. An increase in response curves is observed with increasing vapour concentration for both PANI and PANI-ZrS₂ sensors. The nanocomposite produced far better sensing results towards acetone vapour up to seven times due to synergistic effect of p-n interface of PANI-ZrS₂ compared to raw PANI. An exponential linear dependence of the sensor is depicted in Figure 6.9, the response increases with increasing gas concentration (**Figure 6.18**). The chemical sensing was extended to hexane vapour at RT, the response was too poor. **Table 6.1** shows the performance of PANI-ZrS₂ sensor to other TMDCs and their nanocomposite with polymers for VOCs sensing and RH.

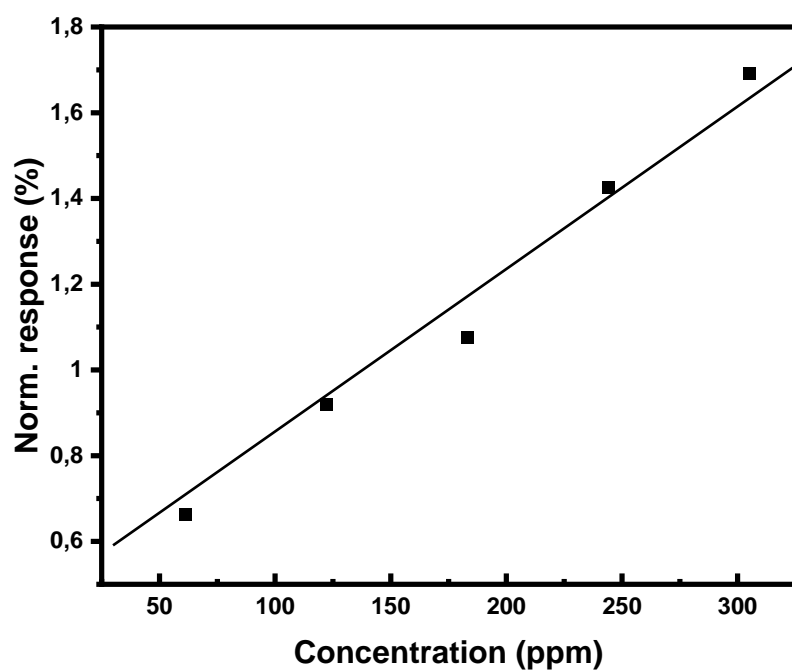


Figure 6.18: Normalized response of the PANI-ZrS₂ sensor towards acetone vapour.

Table 6.1: Group IVB TMDCs and TMDCs nanocomposite with polymers for VOC sensing.

T °C	Gas (ppm)	Sensitivity (%)	Response time (s)	Recovery time (s)	References
RT	H ₂ O	97	36	49	8
RT	NH ₃	75.6	-	-	23
RT	C ₂ H ₅ OH (2)	6800	60	2	3

RT	H ₂ S (4)	111.8	19.75	48	9
RT	H ₂ O	-	-	-	10
RT	NH ₃		72	175	11
RT	C ₂ H ₅ OH (385)	-	83	44	This work
		-	78	69	
	CH ₃ OH (555)				

with good sensitivity and rapid response-recovery times^{9,11} while pure ZrS₂ in this work manifested poor conductivity and has resulted in no response to VOCs at room temperature. This may be due to fact that the ZrS₂ nanosheets used in this work have many layers. Functionalization of PANI with ZrS₂ could be a good promoter for development of sensors with an enhanced performance at room temperature.

6.7 Relative Humidity

Relative humidity is another important factor which can affect the performance of a sensor, it either causes a rise or decline in response. This factor normally affects sensors at RT. The relative humidity of the sensor was conducted for methanol and ethanol vapours at RT as shown in **Figure 6.19 A and B**. The effect of humidity on methanol sensor was maximum at 64%; while for ethanol vapour at a pronounced humidity of 75% the sensor behaviour changed from

p- type to n- type and maximum response was observed at 96%. The mechanism for this change in behaviour from p-type to n-type at elevated humidity is yet to be understood.

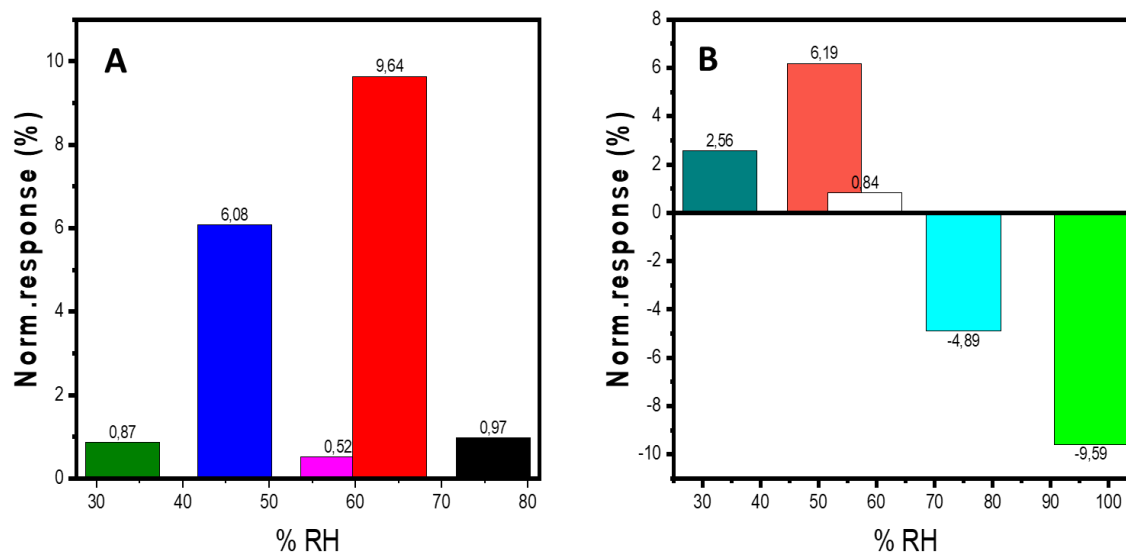


Figure 6.19: Response of PANI-ZrS₂ towards (A) 111 ppm of methanol vapour; (B) 77 ppm of ethanol vapour under different humidity conditions at 33, 46, 58, 64 and 76% for methanol and at 33, 51, 58, 75 and 96% for ethanol.

6.8 Conclusion

Group IVB TMDCs have exotic properties, which make them suitable for chemical sensing. The nanocomposite demonstrated sensing of primary alcohols and acetone. The sensor displayed more sensitivity towards isopropanol compared to methanol, ethanol, butanol and acetone. The behaviour of the sensor changed from p-type to n-type on exposure to ethanol vapour at elevated relative humidity. The sensor showed good response to low concentrations (7.7 ppm, 11 ppm, 5.8 ppm and 6.1 ppm), which correspond to methanol, ethanol, isopropanol and acetone respectively. The sensor can find application in breath analysis and medical purposes for monitoring diseases such as lung cancer and diabetes. The sensor displayed good sensitivity, reproducibility, rapid response and recovery times towards alcohols. The sensitivity and selectivity of the sensor can be improved at room temperature by fabricating nanofibers of PANI with monolayers of ZrS₂ or nanoparticles.

6.9 References

1. Song, E. and Choi, J.W., 2013. Conducting polyaniline nanowire and its applications in chemiresistive sensing. *Nanomaterials*, 3(3) pp.498-523.
2. Sayah, A. Habelhames, F. and Bahloul, A., 2018. Electrochemical synthesis of polyaniline-exfoliated graphene composite films and their capacitance properties. *J Electroanal Chem*, 818, pp.,26-34.
3. Hosseini-Shokouh, S.H., Fardindoost, S. and Zad AI., 2019. A High-Performance and Low-Cost Ethanol Vapor Sensor Based on a TiS₂/PVP Composite. *ChemistrySelect*, 4 (21), pp.6662-6666.
4. Nguyen, H.T.T. Hoang, D.Q. and Dao, T.P., 2020. The characteristics of defective ZrS₂ monolayers adsorbed various gases on S-vacancies: A first-principles study. *Superlattices Microstruct.*, 140: pp.106454.-106465.
5. Ma, J., Liu, K., Jiang, J. and Xu, T., 2020. All optic-fiber coupled plasmon waveguide resonance sensor using ZrS₂ based dielectric layer. *Optica*, 28(8), pp.11280-11289.
6. Shimazu, Y., Fujisawa, Y., Arai, K., Iwabuchi, T., and Suzuki, K., 2018. Synthesis and Characterization of Zirconium Disulfide Single Crystals and Thin-Film Transistors Based on Multilayer Zirconium Disulfide Flakes. *ChemNanoMat.*, 4(10),1078-1082.
7. Kishiro, K. Takemoto, S., Kuriyaki, H. and Hirakawa K., 1994. Resistivity response to oxygen of transition metal dichalcogenide TiS₂. *Japanese J Appl Physics, Part 1 Regul Pap Short Notes Rev Pap.*, 33(2),1069-1073.
8. Manjunatha, S., Machappa, T., Ravikiran, Y.T., Chethan., B. and Sunilkumar A. 2019. Polyaniline based stable humidity sensor operable at room temperature. *Phys B Condens Matter.*, 561, pp.170-178.
9. Sakhuja, N. Jha, R.K. Chaurasiya, R. Dixit, A. and Bhat, N., 2020. 1T-Phase Titanium Disulfide Nanosheets for Sensing H₂S and O₂. *ACS Appl Nano Mater.*, 3(4), pp.3382-3394.
10. Shaikat, R.A., Khan, M.U. and Saqib, Q.M., 2022. Two dimensional Zirconium Diselenide based humidity sensor for flexible electronics. *Sensors Actuators B Chem.* 358, pp.131507-131518.

11. Sharma, S., Singh, S., Singh, R.C. and Sharma, S., 2020. Structural transformation and room temperature ammonia sensing properties of TiS₂ nanostructures. *SN Appl Sci.*, 2(5), pp.1-12.
12. Late, D.J. Huang, Y.K. and Liu, B., 2013. Sensing behavior of atomically thin-layered MoS₂ transistors.. *ACS Nano.* 7(6), pp.4879-4891.
13. He, Q., Zeng, Z. and Yin, Z., 2012. Fabrication of flexible MoS₂ thin-film transistor arrays for practical gas-sensing applications. *Small.*, 8(19), pp.2994-2999.
14. Gqoba, S.S., Rodrigues, R. and Mphahlele, S.L., 2021. Hierarchical nanoflowers of colloidal WS₂ and their potential gas sensing properties for room temperature detection of ammonia. *Processes.*, 9(9), pp.1491-1496.
15. Yang, C., Xie, J., Lou, C., Zheng, W., Liu, X., and Zhang J., 2021. Flexible NO₂ sensors based on WSe₂ nanosheets with bifunctional selectivity and superior sensitivity under UV activation. *Sensors Actuators, B Chem.*, 333(2), pp.129571.
16. Shi, W., Huo, L., Wang, H., Zhang, H., Yang, J., and Wei P., 2006. Hydrothermal growth and gas sensing property of flower-shaped SnS₂ nanostructures. *Nanotechnology*, 17(12), pp.2918-2924.
17. Veeralingam, S., Sahatiya, P. and Badhulika, S., 2019. Low cost, flexible and disposable SnSe₂ based photoresponsive ammonia sensor for detection of ammonia in urine samples. *Sensors Actuators, B Chem.*, 297 (15), pp.126725.
18. Chen, H.Y., Wang, J., Meng, L., Yang, T., and Jiao, K., 2016. Thin-layered MoS₂/polyaniline nanocomposite for highly sensitive electrochemical detection of chloramphenicol. *Chinese Chem Lett.*, 27(2), pp.231-234.
19. Yoon, C.M. Lee, S., Hong, S.H., and Jang, J., 2015. Fabrication of density-controlled graphene oxide-coated mesoporous silica spheres and their electrorheological activity. *J Colloid Interface Sci.*, 438, pp.14-21.
20. Pirsa S., 2017. Chemiresistive gas sensors based on conducting polymers. *Mater Sci Eng Concepts, Methodol Tools, Appl.*, 1-3, pp.543-574
21. Fratoddi, I., Venditti, I., Cametti, C. and Russo, M.V., 2015. Chemiresistive polyaniline-based gas sensors: A mini review. *Sensors Actuators, B Chem.*, 220,

pp.534-548.

22. Mutuma, B.K, Rodrigues, and R. Ranganathan, K., 2017. Hollow carbon spheres and a hollow carbon sphere/polyvinylpyrrolidone composite as ammonia sensors. *J Mater Chem A.*, 5(6), 2539-2549.
23. Yan, H., Zhong, M., Lv, Z. and Wan, P. Stretchable Electronic Sensors of Nanocomposite Network Films for Ultrasensitive Chemical Vapor Sensing. *Small.*, 13(41), pp.1-8.

CHAPTER 7:

TITANIA-ZIRCONIUM DISULPHIDE NANOCOMPOSITE FOR SENSING ACETONE VAPOUR

7.1 Introduction

Transition metal dichalcogenides (TMDCs) are a class of 2D materials that are greatly explored recently in many applications, such as photocatalysis, solar cells, field effect transistors (FETs), thermoelectric devices, photodetectors, fibre lasers, optics, sensors, tribology, electrode materials and electrocatalysis¹. TMDCs have fantabulous attributes that make them useful as co-catalysts with semiconductors such as TiO₂, ZnO, WO₃, SnO₂ and to functionalize materials like carbon, graphene and polymers because they have exotic properties such as a plethora of available active sites, high mobility and large surface area. They are inexpensive and very abundant in nature unlike precious metal metals that are very rare and very costly. When fabricating proper nanostructures, there is a need for intimate and enormous contact interfaces with a plethora of active edge sites. Several authors have fabricated TMDCs with titania for photocatalytic reactions, however few reports are presently available on TMDCs/TiO₂ for sensor application². Group IVB TMDCs have been reported theoretically to possess immense mobility and great sheet current density. The method that is commonly deployed in obtaining a monolayer or few layers of group IVB TMDCs is mechanical exfoliation which has the disadvantages of non-scalability and this has not really help in exploring electrical measurements of these novel nanomaterials³. Group IVB TMDCs in their monolayer form have been reported to exist in non-centrosymmetric, which makes them to possess piezoelectric properties and negative poisson ratio. Until recently, most work reported on ZrS₂ and HfS₂ is majorly predictions based on density functional theory-based first principles calculations. 2D materials may forfeit the inversion symmetry when the number of layers is not even, thus having piezoelectric attribute. ZrS₂ nanomaterials are recently being explored in FETs and fibre laser applications due to exotic features these material possess in mono or few layers, however the available information on sensor application especially in gas/chemical sensing is very limited^{4,5,6,7}.

The layered structure, large surface-to-volume ratio of ZrS₂ and high mobilities make them suitable for gas sensing, however TMDC based sensors still have set backs such as poor sensitivity and recoverability. There is also a possibility of the nanomaterial being affected by

O₂ or moisture at ambient environment. Research conducted by several authors revealed that nanocomposites of TMDCs with semiconducting metal oxide could greatly improve the performance of TMDCs in gas sensing. The design of proper close interface between the composite will boost the electrical and chemical functionalities of the sensor. Functionalizing metal oxide with TMDCs provides a geometric advantage of the hybrid material. Blending of TMDCs with metal oxide such as titania is a new development to enhance the gas sensing activity of the nanomaterial because of combined effect of union of the nanohybrid. SnO₂ perhaps is the most investigated metal oxide for chemical sensing, after which ZnO is next. Han *et al* produced MoS₂-SnO₂ nanocomposite for sensing oxidizing gas (NO₂) at room temperature. The nanocomposite gas sensor produced a response of 18.7 % on exposure to 5 ppm of the gas. The sensor had good selectivity and stability. The hybridization of the heterostructures boosted the sensing activity of the sensor when compared to pristine MoS₂ sensor and this is attributed to proper p-n heterojunctions formed between the 2D and OD materials ⁸. In a similar experiment, Yan *et al* incorporated MoS₂ nanosheets with SnO₂ nanoparticles; this improved the gas sensing activity towards ethanol sensing. The improved achievement of the nanohybrid was attributed to increased surface area, which provided more active sites. Additionally, there is an internal electric field formed because of proper heterojunction formed which quickened the electron transfer ⁹. Proper research has been done on ZnO as a sensing material akin to SnO₂. Zhang *et al* reported on MoS₂-ZnO nanocomposite for NH₃ vapour sensing at room temperature. The activity of the nanohybrid was far better in comparison to pristine ZnO with a faster response and recovery time ¹⁰. Zhao *et al* functionalized MoS₂ nanosheets on TiO₂ nanotubes using hydrothermal method. The measurement was not operated at room temperature. The response value to ethanol (100 ppm) was great, the sensitivity of the nanohybrid outweigh pure TiO₂ by multiple of 11 times ¹¹.

Qin *et al* synthesized a nanohybrid of TiO₂-WS₂ by loading quantum dot of TiO₂ on WS₂ nanosheets for sensing NH₃ gas at RT. The sensor produced a good response (17 times) and rapid response - recovery times, selectivity, and stability towards 250 ppm NH₃ vapour compared to unloaded WS₂ ¹². Very recently Singh and Sharma also demonstrated MoS₂-TiO₂ for ethanol and methanol sensing with a good sensitivity, repeatability, and stability ¹³. Qiao *et al* constructed SnO₂-MoS₂ for chemical sensing of VOCs, the sensor displayed more sensitivity to trimethylamine (TEA) compared to other chemical vapours. The nanocomposite sensor was 11 folds far better in activity compared to raw SnO₂ with a sensitivity of 106.3 % towards 200 ppm of toward TEA ¹⁴.

7.2 Chemicals and materials

As-synthesized radially aligned nanorutile (RANR), exfoliated ZrS₂ nanosheets, isopropyl alcohol (99%, MK chemicals (RSA)) were used without further purification. vial, parafilm and sonicator bath with model name PS-20A with power of 100 W.

7.3 Methods

7.3.1 Synthesis of nanocomposite of titania with zirconium disulphide

The synthesis of radially aligned nanorutile titania (RANR) and nanosheets of ZrS₂ has been discussed in chapters four and five respectively. Nanocomposite of zirconium disulphide and titania was fabricated by introducing 5 mg of ZrS₂ into a vial containing 90 mg of RANR in isopropanol and the vial sealed and wrapped with parafilm. The vial was sonicated for 2 h after which the resulting solution was filtered, and the product dried at room temperature.

7.3.2 Sensor fabrication

The TiO₂-ZrS₂ based sensor was prepared on a printed circuit board (PCB) FR4 substrate. Interdigitated electrodes were patterned on the rectangular shaped PCB consisting of electroless nickel immersion gold electrodes of 18 pairs with a length of 7.9 mm and a space of 0.1 mm between each electrode. The sensing film was prepared by drop casting 12 µL of the film that was prepared by sonicating 5 mg of nanocomposite of TiO₂-ZrS₂ in 500 µL of methanol for 10 min.

7.3.3 Gas sensing measurement

All electrical measurements were conducted at about 25 °C. An LCR-6300 10 Hz –300 KHz precision LCR meter coupled to a computer. The frequency and voltage were set at 10 KHz and 1.00 V respectively. The system was allowed to stand for few minutes before any measurement were done. The set-up for gas sensing is the same as the one reported in Chapter four. The vapour sensing experiment was conducted at room temperature; the response values were recorded using data logger (LCR). The vapour sensing properties were explored by injecting measured volume of anhydrous acetone into a closed glass chamber (5 L) via a glass syringe. The concentration of the methanol vapour in the test chamber can be evaluated in ppm by using the following equation,

$$C = \frac{224\rho TVs}{273MV} \times 100 \quad (7.0)$$

Where C represents concentration of methanol vapour (ppm), ρ is the density of the solvent (gmL^{-1}), T is the temperature in Kelvin, Vs is the volume of the solvent, M is the molecular weight of the solvent. The response of the sensor is obtained as $S = (R_a - R_g) / R_a \times 100$, where R_a and R_g represented resistance in air and methanol vapour respectively. The duration involved by a sensor to complete 90 % of the resistance change is known as response/recovery time. The sensor was also conducted for acetone. The sensor was exposed to acetone at various concentrations. To ensure the vapour reaches saturation point upon injection of the gas, the sensor was allowed to interact with the analyte gas for 300 s for proper adsorption and 200 s for the desorption of the vapour (recovery). The same procedure was conducted for methanol and ethanol.

7.4 Characterization

Powder X-ray diffraction (PXRD) analysis was performed using a Bruker D2 phaser (D2-205530) diffractometer with Cu $K\alpha 1$ radiation ($\lambda = 1.54060 \text{ \AA}$) at 30 kV and 10 mA. Measurements were taken using a glancing angle of the incident detector at an angle of 2° over 2θ angle range of $5-90^\circ$ in steps of 0.026° with a step time of 5 s at ambient temperature. Transmission electron microscopy (TEM) (FEI Technai G2 Spirit 120 kV) was used to analyse the morphology of the synthesized titania nanomaterials. TEM samples were prepared by dissolving the material in isopropanol, sonicated for 10 min, after which they were deposited on a copper grid and allowed to dry at room temperature before analysis. The thermal stability of as-synthesized nanocomposite was monitored using a PerkinElmer 6000 thermogravimetric analyzer. The surface area and porosity were measured using Micromeritics RS232 and porosity analyzer instrument. The surface area measurements were performed via N_2 adsorption/desorption and calculated by the Brunauer Emmett and Teller (BET) analysis method. The diffuse reflectance (DR) UV-vis spectra were obtained in the range of 200–800 nm using a Cary 500 spectrophotometer equipped with a Praying Mantis diffuse reflectance accessory. Raman spectra were obtained using a Horiba LabRAM HR Raman spectrometer with an Olympus BX41 microscope attachment and the 514.5 nm line of a Lexel argon-ion laser as the excitation source.

7.5 Results and discussions

7.5.1 XRD analysis

Figure 7.1a shows the XRD crystallographic structure of the TiO_2/ZrS_2 nanocomposite. The TiO_2 matches tetragonal rutile phase indexed to the JCPDS card of no.21-1276. The following

diffraction peaks 27.5, 36, 41.5, 43, 54, 56, 64, and 69° correspond to the (110) (101) (111) (210) (211) (220) (310) and (311) planes of TiO₂. Furthermore, the XRD pattern of ZrS₂ shows diffraction peaks at 14.98, 32, 42.20, 49.80 and 62,15° which correspond to (001) and (101) (102) (110) and (201) crystal planes of ZrS₂ indexed to JCPDS card no: 010605262.

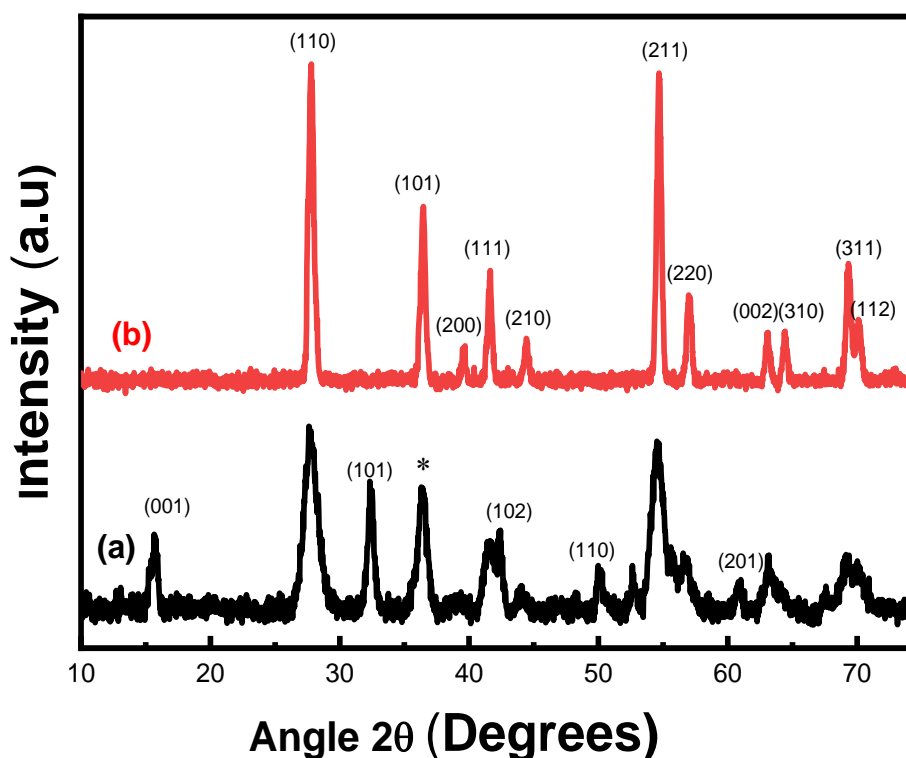


Figure 7.1: PXRD of (a) nanocomposite of TiO₂-ZrS₂ and (b) TiO₂.

7.5.2 Raman analysis

Raman spectroscopy is a proper tool and non-destructive approach which helps in distinguishing materials, certainty of their structural characteristics and phase of the material. Raman spectroscopy showed that the nanocomposite is made of both Rutile titania (D¹⁴_{4h}) and hexagonal ZrS₂ as depicted in Figure 7.2, E_g and A_{1g} raman active modes of rutile titania is observed at about 447 and 612 cm⁻¹ respectively. This corresponds to what is obtainable in literature^{15,16}. Likewise, the Raman active mode of ZrS₂ is observed at about 247 and 313 cm⁻¹ which represents E_g and dominant A_{1g} peaks respectively. This is in concordance with what Yang *et al* observed in their report⁶.

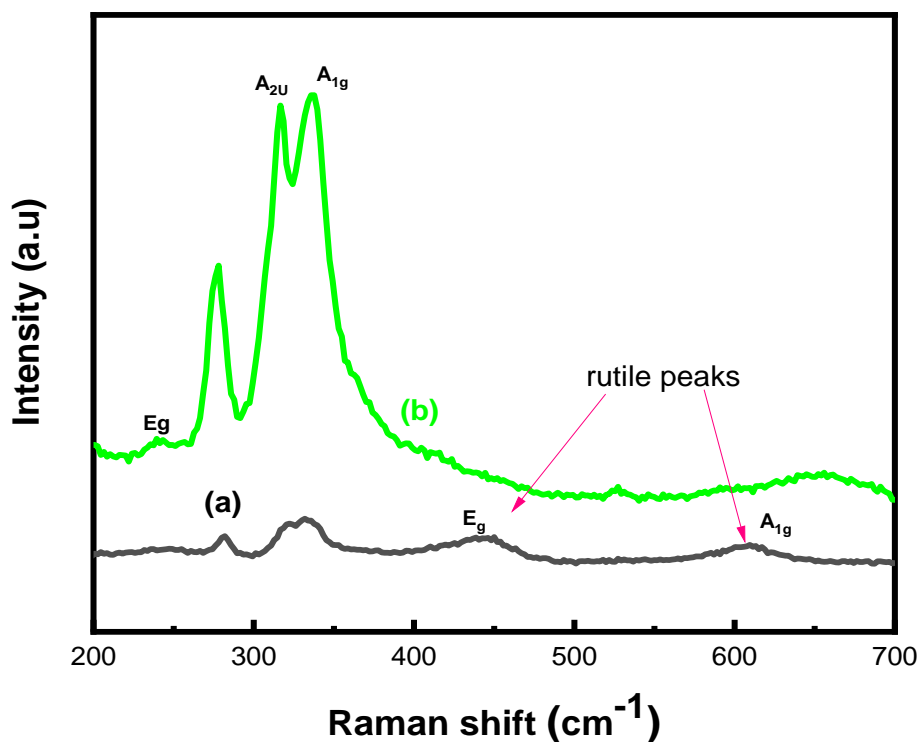


Figure 7.2: Raman of RANR and nanocomposite of ZrS₂ and with ZrS₂-TiO₂.

7.5.3 TEM analysis

The TEM micrographs in **Figure 7.3** show the nanocomposite of ZrS₂ nanosheets with TiO₂ at low magnification. The uniform decoration of ZrS₂ nanosheets in titania look as if they were nanoparticles in radially aligned nanorutile. The layered structure of ZrS₂ did not give room to observe the dandelion morphology of the titania or if the morphology has been distorted during the formation of the nanocomposite by the ultrasonication method. Radially aligned nanorutile are commonly decorated with precious metals or metals, hardly any information is available on RANR nanocomposite with other semiconductors^{17,18}. Similar observation is reported by Liu *et al*, the group decorated titanium dioxide with MoS₂ nanosheets. The nanosheets wrapped the nanobelts of titania evenly in which the surface morphology of titania nanobelts is evenly covered¹⁹. Comparable work is also reported by Wu *et al* in which nanosheets of MoS₂ are lying over quantum dots Fe₂O₃ to form a nanocomposite of MoS₂ with Fe₂O₃²⁰. **Figure 7.3** shows HRTEM of the nanocomposite of ZrS₂-TiO₂ in which even distribution of nanosheets of ZrS₂ is conspicuously observed in titania.

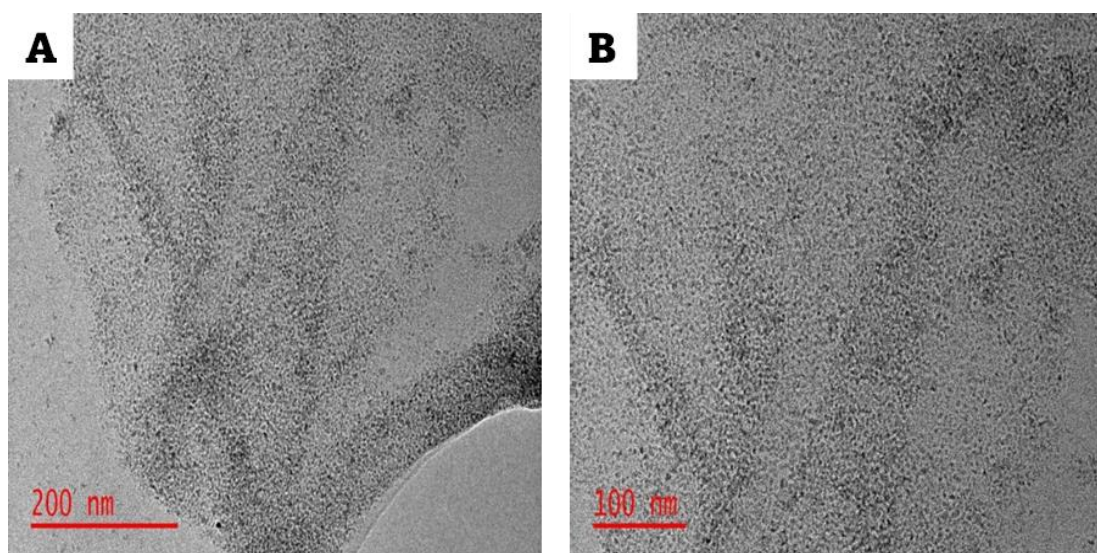


Figure 7.3: TEM micrographs of $\text{TiO}_2\text{-ZrS}_2$ nanocomposite.

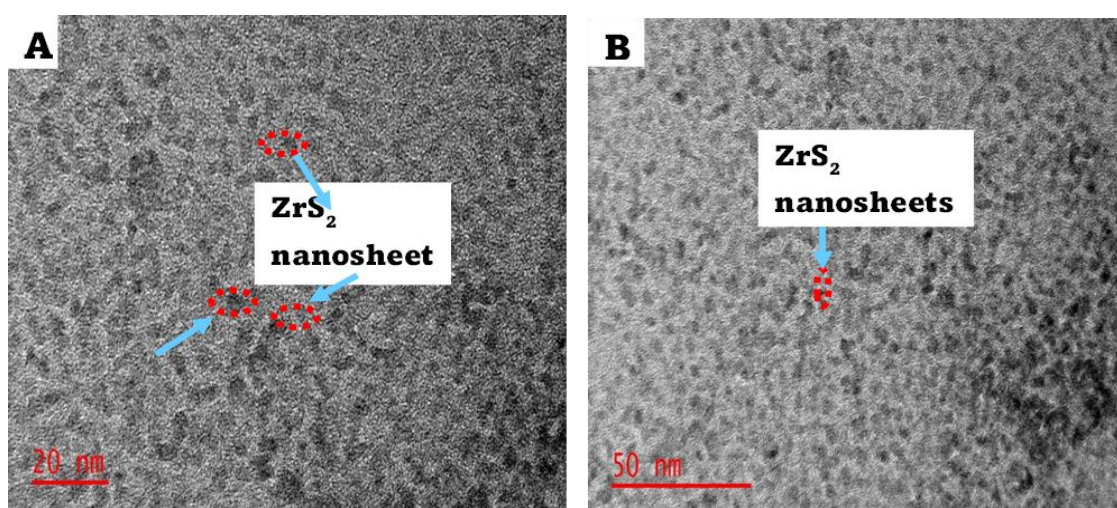


Figure 7.4: HRTEM of $\text{TiO}_2\text{-ZrS}_2$ nanocomposite.

7.5.4 UV-Vis spectroscopy

The solid-state UV-Vis DRS plots of RANR and nanocomposite of RANR- TiO_2 are shown in Figures 7.5a and 7.5b. The absorbance varies from 200-800 nm with a small absorption at about 350 nm while the absorption peak is not conspicuous for the nanocomposite of $\text{TiO}_2\text{-ZrS}_2$ unlike with pristine TiO_2 . The other absorption is observed at about 424 nm, while the absorption in nanocomposite is blue shifted at wavelength of 411 nm. This is in concordance with many authors who also reported absorption below or at about 400 nm for titania^{21,22}. The

band gap of the materials was extrapolated using Tauc plots to be 3.30 and 3.33 eV for RANR and TiO₂-ZrS₂ nanocomposite respectively.

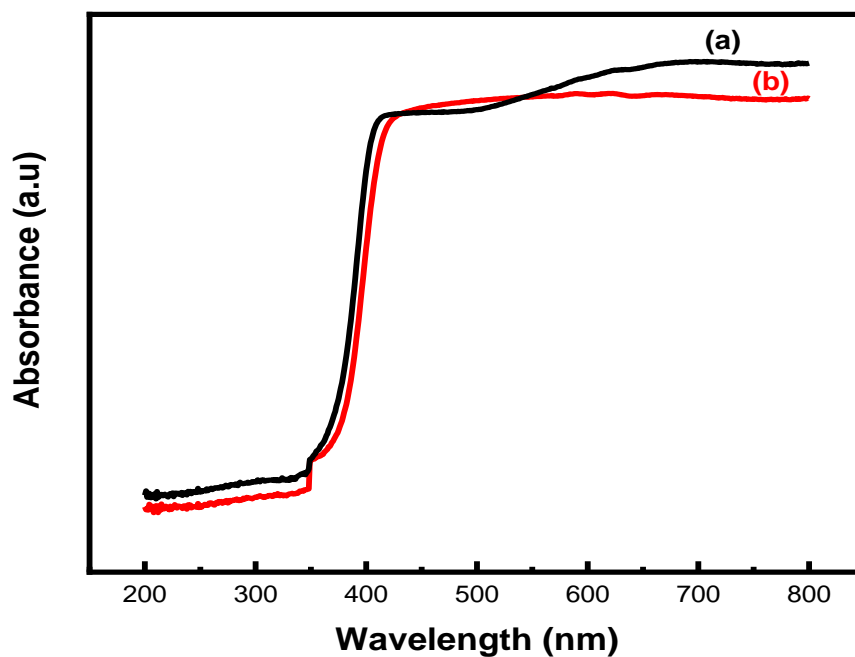


Figure 7.5: DRS-UV-Vis of (a) TiO₂-ZrS₂ and (b) TiO₂

7.5.5 Energy dispersive x-ray spectroscopy (EDS) analysis

The chemical composition of the nanocomposite was conducted with SEM-EDS. The EDS spectra shown in **Figure 7.6** confirm the presence of Ti, O₂, Zr and S atoms; the Pd and Au atoms are from the coating of the material prior to analysis. This would indicate the formation of TiO₂-ZrS₂ nanocomposite.

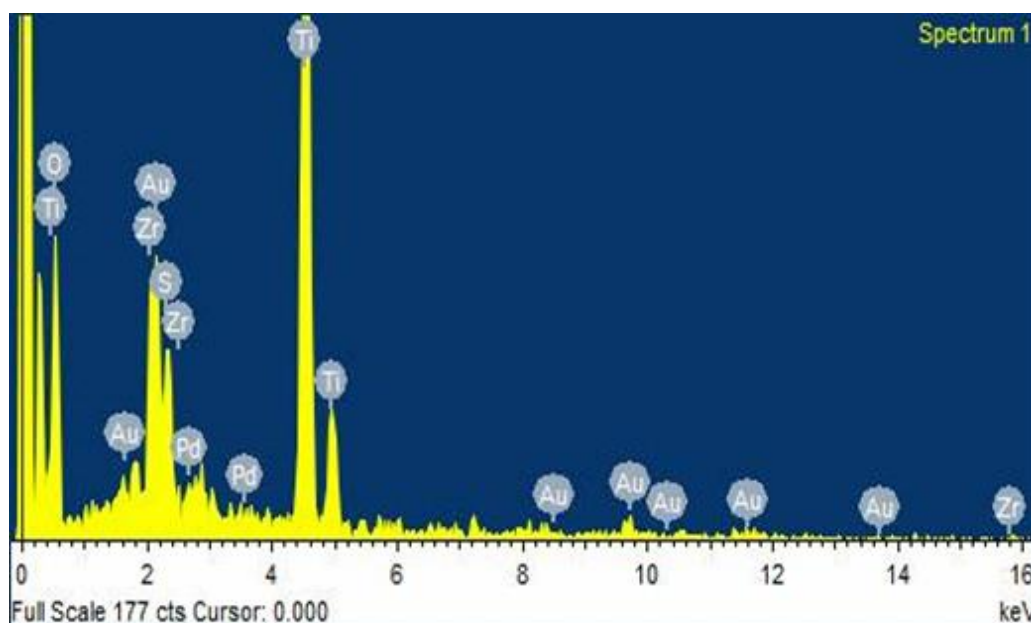


Figure 7.6: EDS of TiO₂-ZrS₂ nanocomposite

7.5.6 BET analysis

Textural characteristics of the nanocomposite was investigated by BET. The surface area and pore volume of TiO₂-ZrS₂ were lower than the pristine RANR as shown in **Table 7.1**, however an increase in pore size is observed. About 35% decrease in surface area was observed with the nanocomposite. This can be credited to the nanosheets of ZrS₂ covering the pores of RANR which contributed to the diminishing surface area of the nanocomposite. This is a drawback for the RANR, to enhance its surface area can be sometimes abortive. A similar observation was observed by Farai *et al* in which the surface area of RANR loaded independently with Au and Ni significantly reduced ¹⁸.

Table 7.1 The BET comparison between pristine RANR and nanocomposite of TiO₂-ZrS₂.

Sample	Surface area (m ² /g)	Pore volume (cm ³ /g)	Pore size (nm)
RANR	99.00	157.24	7.10
TiO ₂ -ZrS ₂	64.53	110.50	11.10

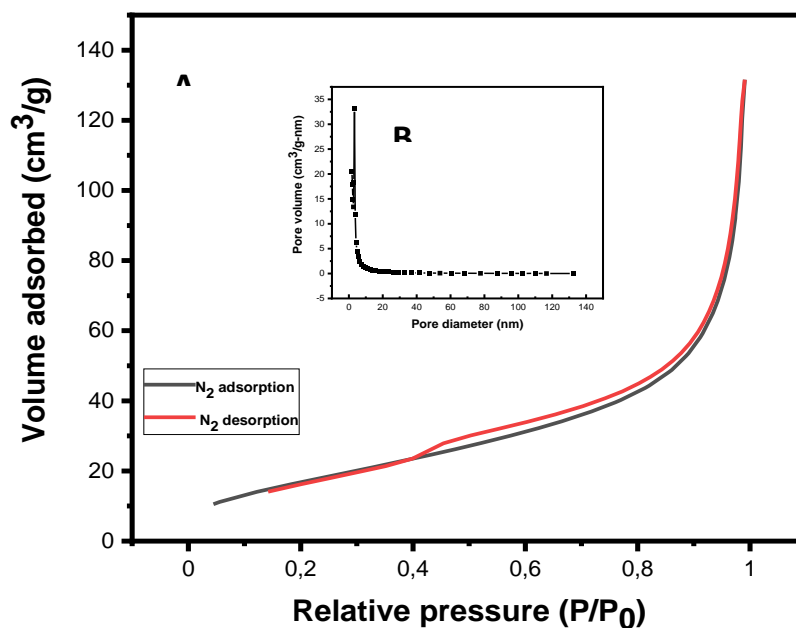


Figure 7.7: (a) Nitrogen adsorption/desorption isotherms of TiO₂-ZrS₂ nanocomposite; and (b) BJH pore size distribution of the TiO₂-ZrS₂ nanocomposite.

7.5.7 TGA analysis

The decomposition of titania nanomaterials and the nanocomposite of titania with zirconium disulphide was investigated using thermogravimetric analysis. The thermograms in **Figure 7.8** show both materials undergo initial decomposition from 0 to about 360 °C which is about 7% due to absorbed moisture from the ambient environment. From about 360 °C, there is no visible decomposition of the RANR which is in agreement with literature; rutile titania is stable even at elevated temperature whereas for the nanocomposite a slight oxidation is observed at 600 - 700 °C.

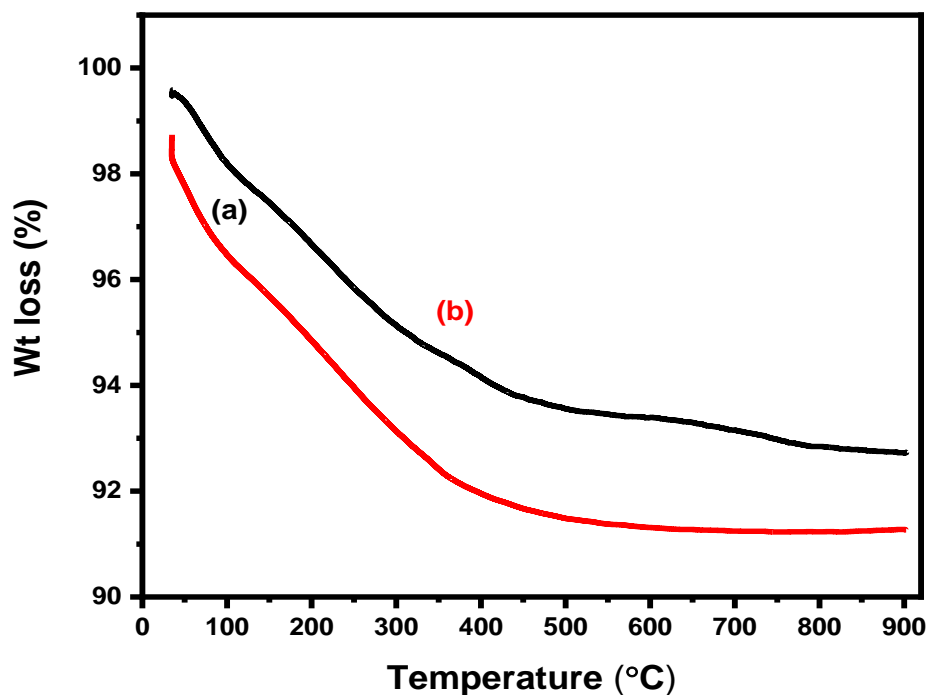


Figure 7.8: TGA of pristine RANR and $\text{TiO}_2\text{-ZrS}_2$ nanocomposite

7.6 Gas sensing performance of $\text{TiO}_2\text{-ZrS}_2$

Proposed gas sensing mechanism of TiO_2 with ZrS_2 is expected to form n-n heterojunction with should facilitates a quick electron transfer upon adsorption of vapour analyte on the sensor, however, the sensor performance was not enhanced with loading of ZrS_2 in titania at room temperature, however. No response was observed with nanocomposite of $\text{TiO}_2\text{-ZrS}_2$ at room temperature (RT). This could be attributed to reduction in the surface area with nanocomposite, low conductivity of as-synthesized ZrS_2 nanosheets at RT, temperature of sensing and the loading of ZrS_2 in titania. It is expected the performance of the sensor will be enhanced with TMDCs; however, parts of active sites are not available for sensing rather it was only titania that was responsible for the gas sensing at room temperature. **Figures 7.9 and 7.10** show the response of pristine RANR to acetone vapour. Details of the pristine RANR to volatile organic vapour have been discussed extensively in Chapter four. Singh and Sharma reported high sensitivity of $\text{MoS}_2\text{-TiO}_2$ towards ethanol and methanol at 300 and 240 °C. The loading of 2:1 of MoS_2 to TiO_2 produced surpassing gas adsorption to other compositions¹³. Moreover, 1:2 ratio of MoS_2 on titania have been reported to have better performance in sensing of gas

vapours. Nanohybrids of TMDCs with semiconductor metal oxide has been evaluated to enhance sensing activity of sensors with good sensor properties. Metal oxide with large particle size has been reported to be very difficult to decorate with TMDCs, hence metal oxide with small particles size such as quantum dots are very easy to decorate with TMDCs. Qin *et al* demonstrated WS₂ loaded in quantum dots TiO₂ for NH₃ sensing with superior performance in multiple of 17 times toward NH₃ vapour ¹².

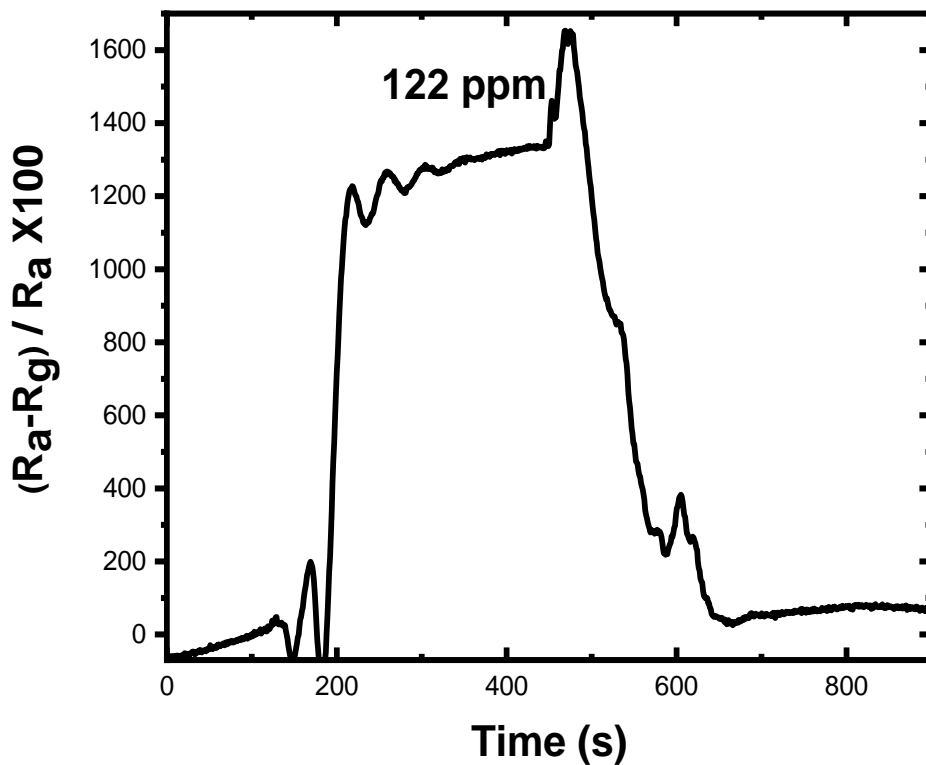


Figure 7.9: Static response of pristine RANR towards 122 ppm acetone vapour at RT.

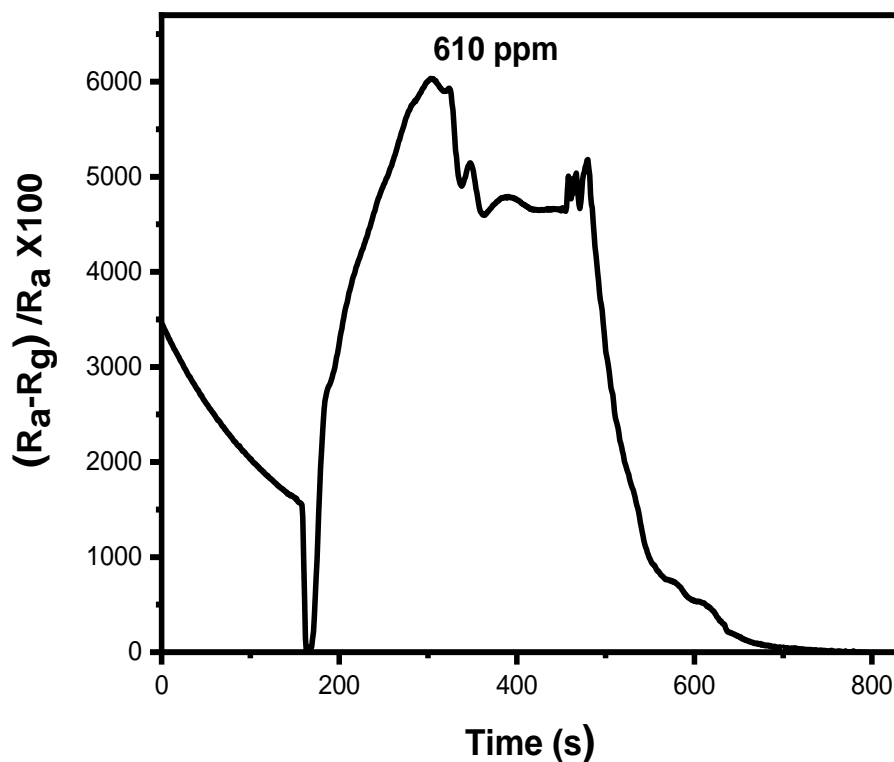


Figure 7.10: Static response of TiO₂-ZrS₂ towards 610 ppm acetone vapour at RT.

7.7 Conclusion

Nanocomposite TiO₂-ZrS₂ with n-n heterojunction was successfully fabricated for chemical sensing of VOCs at room temperature. Poor response or no response was observed at room temperature due to a drastic reduction of the surface area, only a few active sites are available for chemical sensing. In addition, poor conductivity of the exfoliated ZrS₂ nanosheets at room temperature also contributed to the poor sensing activity of the nanocomposite. Temperatures above RT may enhance the sensing characteristics of the nanocomposite sensor. Loading of precious metals on RANR will be more effective in chemical sensing compared to TMDCs which have the tendency to block or cover the pores of the RANR.

7.8 References

1. Wen, Y., Zhu Y. and Zhang, S., 2015. Low temperature synthesis of ZrS₂ nanoflakes and their catalytic activity. *RSC Adv*,5(81), pp.66082-66085.
2. Rahmanian, E., Malekfar, R. and Pumera, M., 2018. Nanohybrids of Two-Dimensional Transition-Metal Dichalcogenides and Titanium Dioxide for Photocatalytic Applications. *Chem - A Eur J*, 24(1), pp.18-31.
3. Zhu, Y., Wang, X., Zhang, M., Cai, C. and Xie, L., 2016. Thickness and temperature dependent electrical properties of ZrS₂ thin films directly grown on hexagonal boron nitride. *Nano Res*, 9(10), pp.2931-2937.
4. Dimple, J. N., Rawat, A. Ahammed, R., Mohanta, M.K., De Sarkar A., 2018. Emergence of high piezoelectricity along with robust electron mobility in Janus structures in semiconducting Group IVB dichalcogenide monolayers. *J Mater Chem A*, 6(48): pp. 24885-24898.
5. Gomes, L.C., Carvalho, A. and Castro Neto A.H., 2015. Enhanced piezoelectricity and modified dielectric screening of two-dimensional group-IV monochalcogenides. *Phys Rev B - Condens Matter Mater Phys*, 92(21), pp.1-8.
6. Yang, H., Li, W., Wang, G. and Sun, Y., 2020. Ultrafast mode-locked fiber laser with zirconium disulfide on D-shaped fiber. *Infrared Phys Technol*.104, pp.103143.
7. Zhang, M., Zhu, Y. and Wang, X., 2015. Controlled Synthesis of ZrS₂ Monolayer and Few Layers on Hexagonal Boron Nitride. *J Am Chem Soc*,137(22), pp.7051-7054.
8. Han, Y., Ma, Y. and Liu, Y., 2019. Construction of MoS₂/SnO₂ heterostructures for sensitive NO₂ detection at room temperature. *Appl Surf Sci*, 493, pp. 613-619.
9. Yan, H., Song, P., Zhang, S., Yang, Z. and Wang, Q., 2015. Dispersed SnO₂ nanoparticles on MoS₂ nanosheets for superior gas-sensing performances to ethanol. *RSC Adv*,5(97), pp.79593-79599.
10. Zhang, D., Jiang, C. and Sun, Y., 2017. Room-temperature high-performance ammonia gas sensor based on layer-by-layer self-assembled molybdenum disulfide/zinc oxide nanocomposite film. *J Alloys Compd*, 698, pp.476-483.
11. Zhao, P.X., Tang, Y. and Mao, J., 2016. One-Dimensional MoS₂-Decorated TiO₂

- nanotube gas sensors for efficient alcohol sensing. *J Alloys Compd*, 674, pp. 252-258.
12. Qin, Z., Ouyang, C. and Zhang, J., 2017. 2D WS₂ nanosheets with TiO₂ quantum dots decoration for high-performance ammonia gas sensing at room temperature. *Sensors Actuators, B Chem*, 253, pp.1034-1042.
 13. Singh, S. and Sharma, S., 2022. Temperature dependent selective detection of ethanol and methanol using MoS₂/TiO₂ composite. *Sensors Actuators B Chem*, 350, pp.130798
 14. Qiao, X.Q., Zhang, Z.W. and Hou, D.F., 2018. Tunable MoS₂/SnO₂ P-N Heterojunctions for an Efficient Trimethylamine Gas Sensor and 4-Nitrophenol Reduction Catalyst. *ACS Sustain Chem Eng*, 6 (9), pp.12375-12384.
 15. Bersani, D., Lottici, P.P. and Ding, X.Z., 1998. Phonon confinement effects in the Raman scattering by TiO₂ nanocrystals. *Appl Phys Lett*, 72 (1), pp.73-75.
 16. Singh, J., Sharma, S., Sharma, S. and Singh, R.C., 2019. Effect of tungsten doping on structural and optical properties of rutile TiO₂ and band gap narrowing. *Optik (Stuttg)*, 182, pp.538-547.
 17. Barrett, D.H., Scurrall, M.S., Rodella., C.B., Diaz ,B., Billing., DG. and Franklyn P.J., 2016. Achieving nano-gold stability through rational design. *Chem Sci*,7(11): pp.6815-6823.
 18. Dziike, F., Franklyn., P.J., Durbach., S.H., Maubane, M. and Hlekelele, L., 2018. Synthesis of radially aligned nano-rutile modified with Au and Ni for the photodegradation of methyl orange. *Mater Res Bull*,104, pp. 220-226.
 19. Liu, X., Li, D. and Liang, Y., 2021. Establishment of anti-oxidation platform based on few-layer molybdenum disulfide nanosheet-coated titanium dioxide nanobelt nanocomposite. *J Colloid Interface Sci*,60, pp.167-176.
 20. Wu, J., Zhang, D., and Cao, Y., 2018. Fabrication of iron-doped titanium dioxide quantum dots/molybdenum disulfide nanoflower for ethanol gas sensing. *J Colloid Interface Sci*, 529, pp.556-567.
 21. Ba-Abbad, M.M., Kadhum., A.A.H., Mohamad, A.B., Takriff, M.S., and Sopian, K., 2012. Synthesis and catalytic activity of TiO₂ nanoparticles for photochemical oxidation of concentrated chlorophenols under direct solar radiation. *Int J Electrochem*

Sci, 7(6), pp. 4871-4888.

22. Huang, C.W. and Wu, M.C., 2020. Photocatalytic degradation of methylene blue by UV-assistant TiO₂ and natural seriite composites. *J Chem Technol Biotechnol*, 95(10), pp.2715-2722

CHAPTER 8: GENERAL CONCLUSIONS AND RECOMMENDATIONS FOR FUTURE STUDIES

8.1 General Conclusions

Wet methods of synthesis of ZrS_2 is encouraged when heterostructures of ZrS_2 and ZrO_2 are to be fabricated for different applications. This will give the advantage of utilizing both properties of ZrS_2 and ZrO_2 . The performance of the semiconductor heterostructures is vastly superior when compared to individual semiconductor materials due to synergistic effect. However, if ZrS_2 with no contamination of ZrO_2 are required, gas phase of synthesis such as chemical vapour transport and chemical vapour deposition are to be deployed. Colloidal synthesis of ZrS_2 should be conducted with a capping agent of highest purity if possible 99% purity, the metal precursor and sulphur precursor should be stored in a glove box and all weighings should be done inside it. Every source of contaminant such as moisture, oxygen and oxides of carbon should be eradicated prior to the synthesis. A mixture of octadecene and oleic acid was used as co-ligand in this study via heat-up and hot injection methods to fabricate ZrS_2 nanostructures. The colloidal method helps in obtaining different morphologies by varying the reaction parameters. Morphologies such as nanospheres, nanorods, nanosheets, broken spheres, beeswax-like and hollow hemispheres were obtained using colloidal synthesis. However, the nanomaterials were not stable due to oxophilicity of the few layered group IVB transition metal dichalcogenides.

Exfoliation with amide solvents is more effective to obtain nanomaterials of 2D materials within a few minutes to 2h. Although amide solvents are effective, their use should be discouraged since they are not environmentally safe. Isopropanol and ethanol are more environmentally safe, their use in exfoliation of bulk materials should be more practiced.

2D nanomaterials are suitable in sensor applications because of their layered structures. They possess high surface area and special semiconducting features arising from the manipulation of their band gap. TMDCs are a new class of materials among the 2D materials. The group VIB TMDCs have received much investigation unlike the group IVB. Few reports are available on TiS_2 for chemical sensing, however, to the best of our knowledge ZrS_2 has not being reported as a chemiresistive sensor for sensing of gases or chemical vapours. Hardly any reports are available on TMDCs/polymer composites. Hence more research is required. This research showed that the performance of a conductive PANI is several folds boosted by integration of

ZrS₂ into the polymer matrix to form p-n heterojunction. The enhanced activity of the nanohybrid is a result of synergistic effect.

To the best of our knowledge, titania with dandelion morphology has not been reported for chemical sensing at room temperature. The synthesized dandelion TiO₂ morphology has a high surface area and high porosity with a plethora of active sites which facilitate ease of gas adsorption and desorption. The sensor showed high sensitivity towards primary alcohols and acetone vapours. Humidity served as a catalyst for the gas adsorption on the sensor, however the response declined at elevated humidity.

8.2 Recommendations

The following are recommended for further studies:

1. Both isopropanol and ethanol are suggested as good solvents for exfoliation of 2D bulk materials into few-layered nanomaterials. The use of co-solvent of ethanol and isopropanol is also suggested for exfoliation of bulk materials.
2. The sensing should be conducted in a more automated gas chamber system.
3. The sensing should be conducted in a large test chamber possibly 30 L glass cylinder to determine the efficacy of the sensor.
4. Electrospinning of ZrS₂/PANI nanocomposite to produce nanofibers of high specific surface area.
5. Different loading of ZrS₂ on PANI should be studied and applied for sensing of VOCs.
6. Formation of ternary composite by functionalizing ZrS₂/PANI with carbon materials such as carbon nanotubes, carbon dots and carbon nano-onions and applied for chemical sensing.
7. Introduction of defects into the zirconium disulphide such as sulphur deficiency.
8. Quantum dots, nanoparticles and single layered ZrS₂ should be exfoliated using green solvents and applied for chemical sensing.
9. The radially aligned nanorutile should be modified with precious metals or nanodiamonds and applied for chemical sensing.
10. Introduction of defects into the radially aligned nanorutile such as oxygen vacancies.

11. HRTEM of radially aligned nanorutile should be done to observe the 001 lattice fringes of the titania.

Supporting information

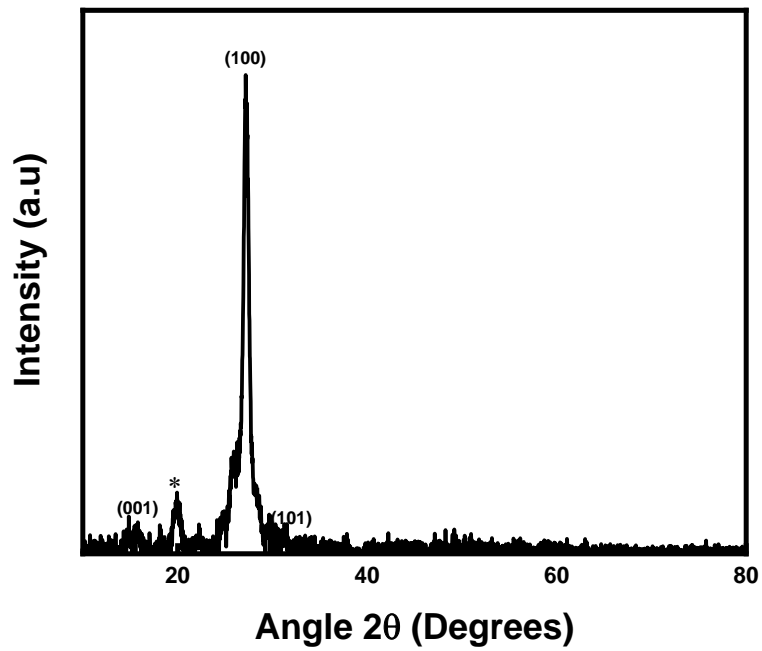


Figure S1: XRD patterns of ZrS₂ nanostructures prepared by hot injection method (9 ml ODE and 0.75 ml OA).

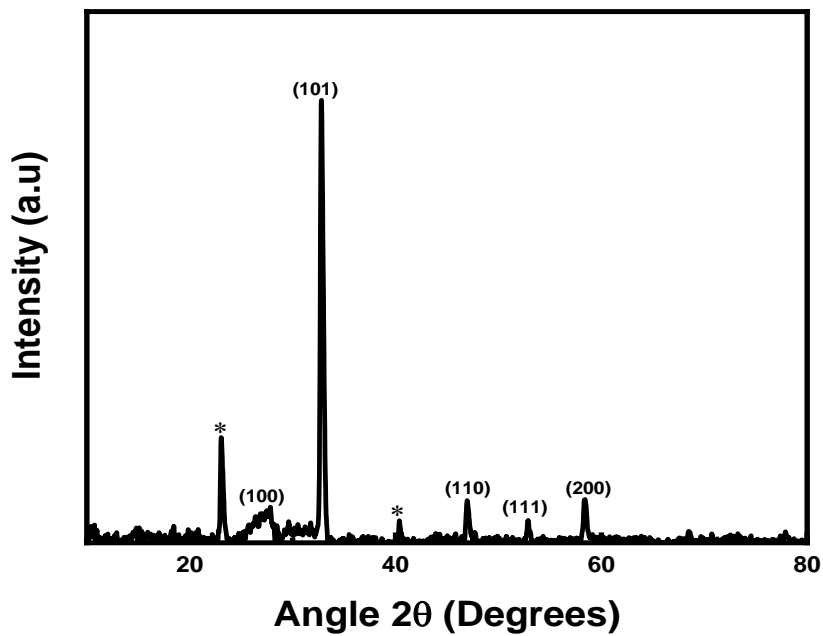


Figure S2: XRD patterns of ZrS₂ nanostructures prepared by the heat up method (9 ml ODE and 4 ml OA).

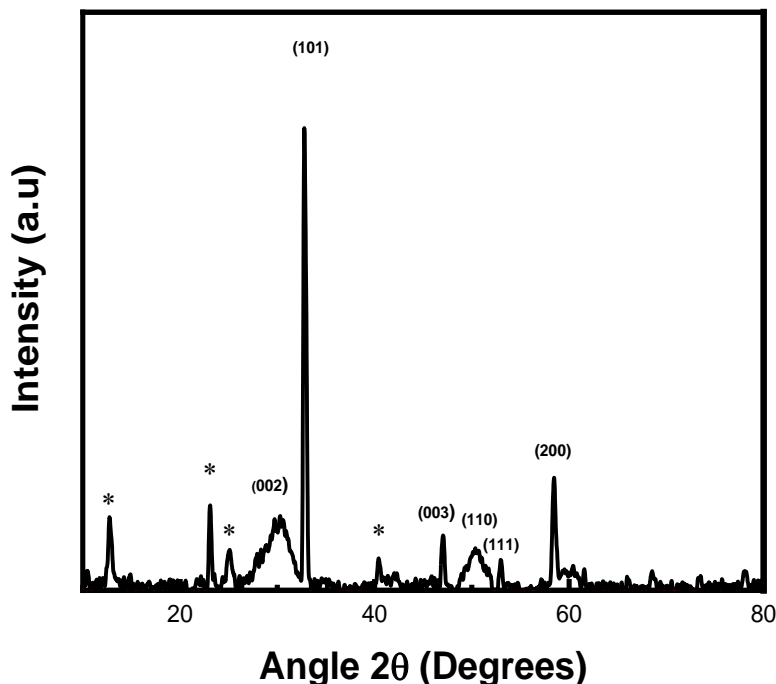


Figure S3: XRD patterns of ZrS_2 nanostructures prepared by the heat up method (9 ml ODE and 0.5 ml 1-DDT).

The use of octadecene (ODE), a non-coordinating and non-reducing solvent provided the opportunity to explore co-solvents in the synthesis of this nanomaterials. There was no nucleation with the use of sole capping agents such as oleic acid, oleylamine and oleyl alcohol even after several hours, hence no product was formed. However, with 1-dodecanethiol (1-DDT), the oxide of zirconium was formed instead of the disulphide. For the synthesis of ZrS_2 , a mixture of ODE and oleic acid (OA) were used as co-solvents where 4 ml of OA were mixed with 9 ml of ODE. It is important to note that no nucleation occurred when oleic acid was used in excess of 4 ml as co-solvent with ODE.

In attempt to use another ligand as co-solvent with ODE, 0.5 ml of 1-DDT with 9 ml of ODE were employed as described above for a typical one pot method of synthesis. From the XRD diffraction patterns in Figure S3, the (002), (101), (003), (110), (111) and (200) peaks were obtained which match the hexagonal ZrS_2 . Due to ease of formation of the ZrO_2 , the reproducibility of the result with ODE and 1-DDT was abortive. Similarly, ODE and ethane 1,2-diol were used as co-solvents for the synthesis, impurities were also formed along with

ZrS₂. A mixture of ODE, ethane 1,2-diol and octadecylamine was also experimented with and there was no improvement on the synthesis.

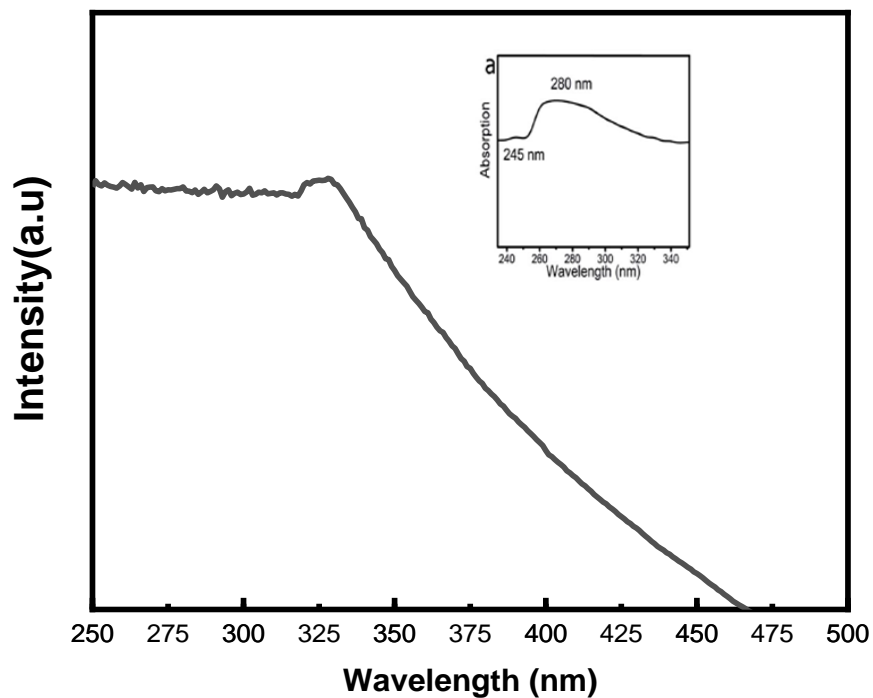


Figure S4: UV-Vis absorption spectrum of ZrS₂ nanostructures prepared by the heat up method (9 ml ODE and 4 ml OA). Inset is the absorption spectrum of ZrS₂ nanostructures fabricated by CVD by Wen *et al*¹.

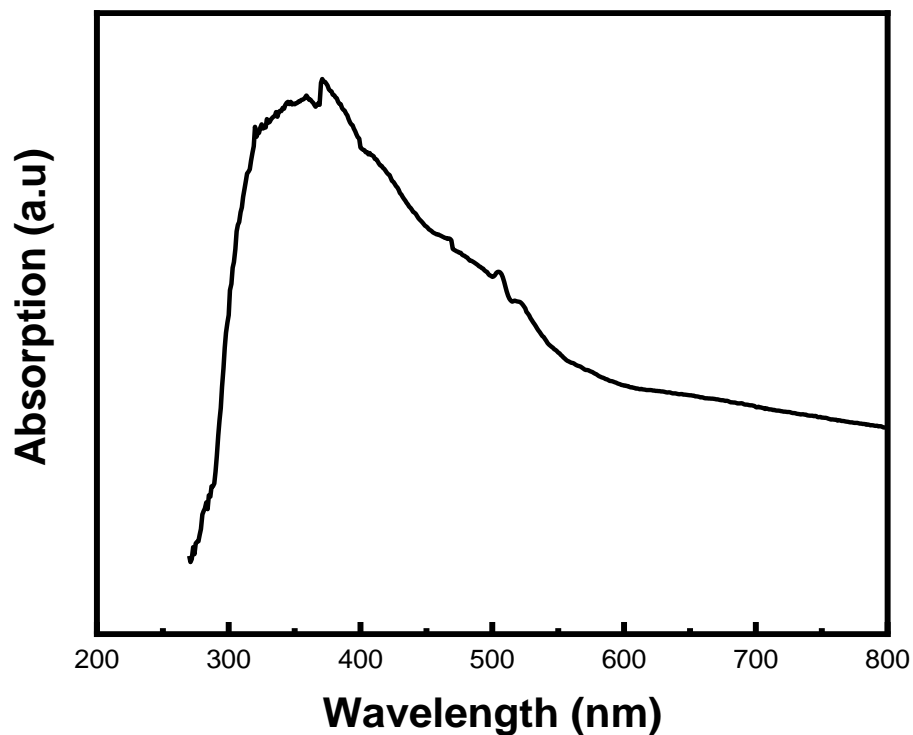


Figure S5: UV-Vis absorption of spectrum of ZrS₂ nanostructures prepared by the heat-up method (9 ml ODE ml).

Figure S5 shows a wide absorption peak from about 300 nm to about 450 nm with raw ODE as-synthesized ZrS₂, the wide absorption is attributed to oxidation of the ZrS₂ or mixed phase of ZrS₂ and ZrO₂. Singh and Nakate reported a very broad absorption peak for as-synthesized ZrO₂. The absorption peak for ZrS₂ has been reported to be at about 280 nm and 330 nm².

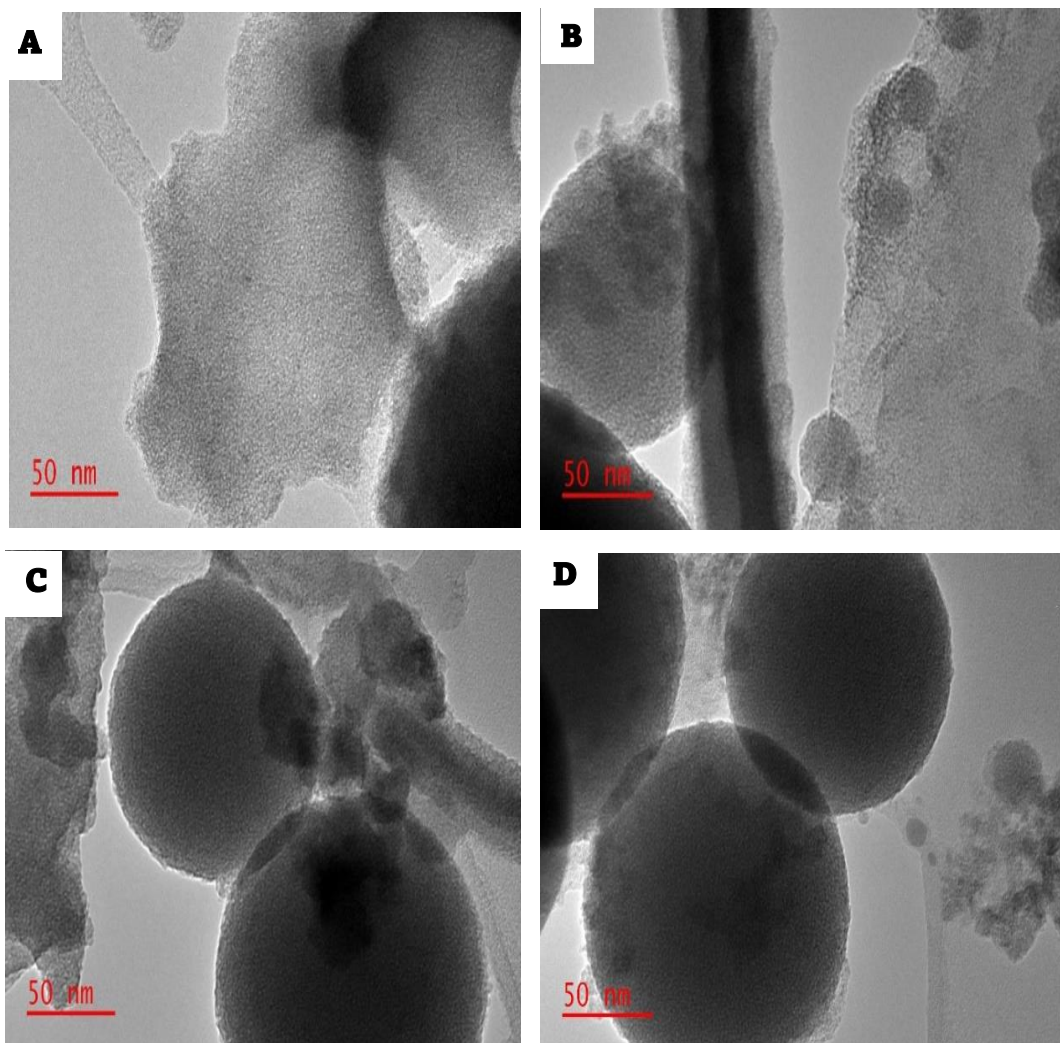


Figure S6: HRTEM images of ZrS₂ nanostructures prepared in a mixture of OA and ODE by the heat up method.

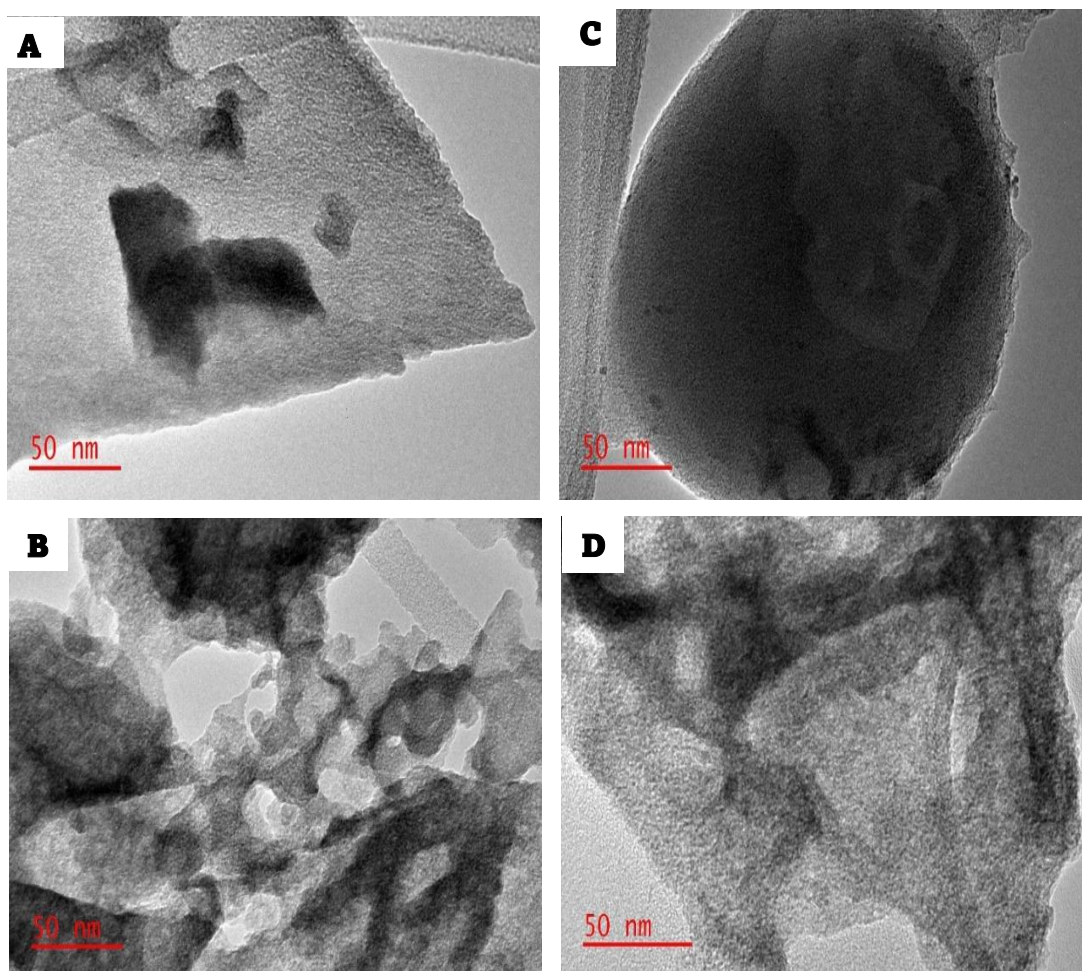


Figure S7: HRTEM images of ZrS₂ nanostructure prepared in mixture of OA and ODE by the hot injection method.

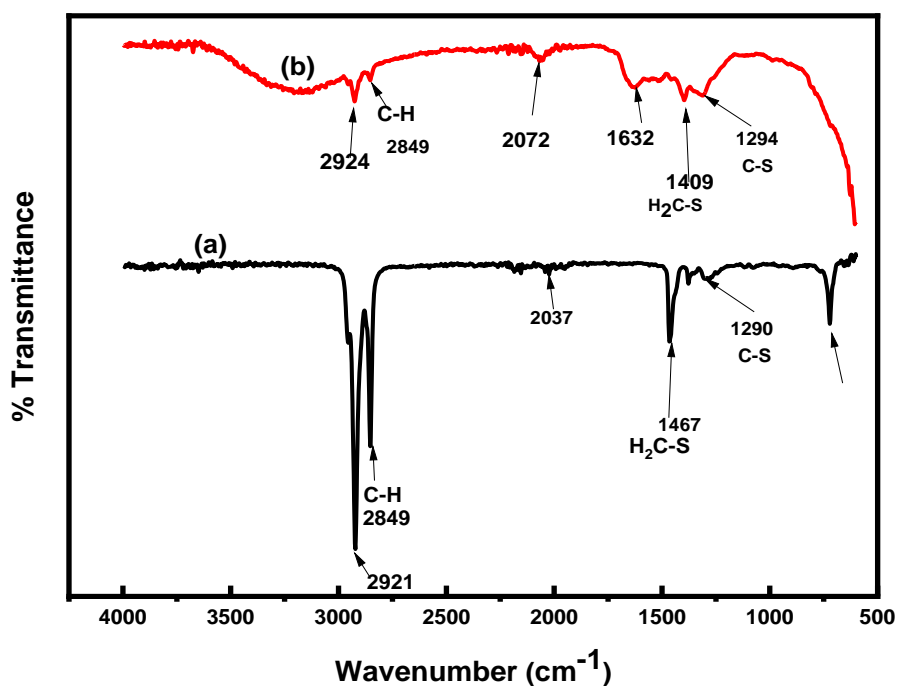


Figure S8: FTIR spectra of (a) Raw 1-DDT and (b) ZrS₂ nanostructure prepared by the heat up method (ODE/1-DDT).

From the spectra above, stretching vibrations of C-S at 1290 cm⁻¹ and CH₂-S at about 1467 cm⁻¹ can be seen. The same was observed for the as-synthesized though there there was a chemical shift which was observed at about 1409 cm⁻¹. The C-H vibration stretching could also be observed at 2921 cm⁻¹. It can be deduced that the 1-DDT capped the nanomaterials.

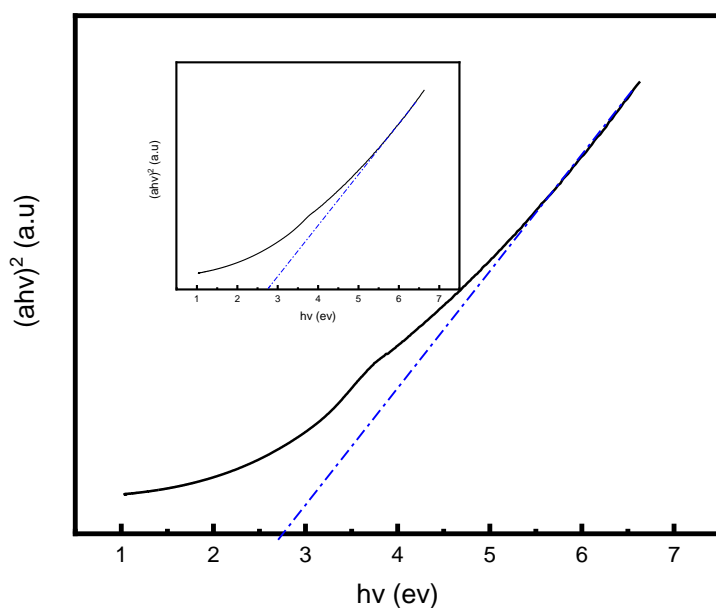


Figure S9 :Band gap of ZrS₂ heat up method and inset of hot injection method.

References

1. Wen, Y., Zhu, Y. and Zhang, S., 2015. Low temperature synthesis of ZrS₂ nanoflakes and their catalytic activity. *RSC Adv.*, 5(81), pp.66082-66085.
2. Singh, A. K. and Nakate, U.T., 2014. Microwave Synthesis, Characterization, and Photoluminescence Properties of Nanocrystalline. *Zirconia.Scientific world*, 2014, pp.349457-349464.

